AD_____

Award Number: W81XWH-04-01-0697

TITLE: Alpha-v Integrin Targeted PET Imaging of Breast Cancer Angiogenesis and Low-Dose Metronomic Anti-Angiogenic Chemotherapy Efficacy

PRINCIPAL INVESTIGATOR: Xiaoyuan Chen, Ph.D.

CONTRACTING ORGANIZATION: Leland Stanford Junior University
Stanford, CA 94305-4125

REPORT DATE: August 2005

TYPE OF REPORT: Annual

PREPARED FOR: U.S. Army Medical Research and Materiel Command
Fort Detrick, Maryland 21702-5012

DISTRIBUTION STATEMENT: Approved for Public Release;
Distribution Unlimited

The views, opinions and/or findings contained in this report are those of the author(s) and should not be construed as an official Department of the Army position, policy or decision unless so designated by other documentation.

20060207 001

REPORT DOCUMENTATION PAGE

Form Approved
OMB No. 0704-0188

1. REPORT DATE 01-08-2005	**2. REPORT TYPE** Annual	**3. DATES COVERED** 15 Jul 2004 – 14 Jul 2005

4. TITLE AND SUBTITLE

Alpha-v Integrin Targeted PET Imaging of Breast Cancer Angiogenesis and

Low-Dose Metronomic Anti-Angiogenic Chemotherapy Efficacy

5a. CONTRACT NUMBER

5b. GRANT NUMBER
W81XWH-04-1-0697

5c. PROGRAM ELEMENT NUMBER

6. AUTHOR(S)

Xiaoyuan Chen, Ph.D.

5d. PROJECT NUMBER

5e. TASK NUMBER

5f. WORK UNIT NUMBER

7. PERFORMING ORGANIZATION NAME(S) AND ADDRESS(ES)

Leland Stanford Junior University
Stanford, CA 94305-4125

8. PERFORMING ORGANIZATION REPORT NUMBER

9. SPONSORING / MONITORING AGENCY NAME(S) AND ADDRESS(ES)
U.S. Army Medical Research and Materiel Command
Fort Detrick, Maryland 21702-5012

10. SPONSOR/MONITOR'S ACRONYM(S)

11. SPONSOR/MONITOR'S REPORT NUMBER(S)

12. DISTRIBUTION / AVAILABILITY STATEMENT
Approved for Public Release; Distribution Unlimited

13. SUPPLEMENTARY NOTES

14. ABSTRACT

The overall objective of this project is to develop 18F-labeled RGD peptide derivatives for breast cancer imaging with prolonged tumor retention and improved in vivo kinetics to visualize and quantify αv-integrin expression and subsequently evaluate the metronomic anti-angiogenic chemotherapy efficacy on tumor regression, necrosis, and angiogenesis. Specific Aims: (1) To optimize 18F-labeled RGD peptide tracer for breast cancer imaging with prolonged tumor retention and improved in vivo kinetics. (2) To demonstrate the feasibility of PET/18F-RGD to image breast tumor growth, spread, and angiogenesis as well as quantifying αv-integrin expression level during breast tumor neovascularization over time. (3) To evaluate the efficacy of EMD 121974/paclitaxel combination on tumor regression, necrosis, and angiogenesis and demonstrate the feasibility of PET/18F-RGD to monitor the treatment outcomes. Major findings: We have developed a dimeric RGD peptide tracer [18F]FRGD2 that has high integrin $\alpha v \beta 3$ binding affinity and favorable in vivo kinetics. Furthermore, the binding potential calculated from simplified tracer kinetic modeling such as Logan plot appears to be an excellent indicator of tumor integrin density. We have also evaluated the antitumor activity of paclitaxel (PTX) conjugated with a bicyclic peptide E[c(RGDyK)]2 (RGD) in a metastatic breast cancer cell line (MDA-MB-435). Our results demonstrate the potential of tumor-targeted delivery of paclitaxel based on the specific recognition of cell adhesion molecule $\alpha v \beta 3$ integrin to reduce toxicity and enhance selective killing of cancer cells.

15. SUBJECT TERMS
Breast Cancer

16. SECURITY CLASSIFICATION OF:

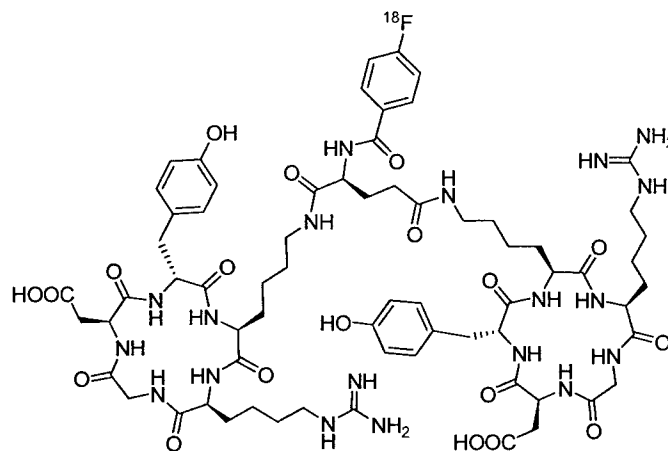| a. REPORT	b. ABSTRACT	c. THIS PAGE	17. LIMITATION OF ABSTRACT	18. NUMBER OF PAGES	19a. NAME OF RESPONSIBLE PERSON USAMRMC
U	U	U	UU	94	**19b. TELEPHONE NUMBER** (include area code)

Table of Contents

INTRODUCTION

We recently found that the receptor binding characteristics of dimeric and multimeric RGD peptides would be better than that of monomeric RGD peptide based upon polyvalency (*1-5*). The receptor binding of the one RGD domain significantly enhances the local concentration of the other RGD domain in the vicinity of the receptor, which may lead to a faster rate of receptor binding or a slower rate of dissociation from the radiolabeled RGD dimer. The dimeric RGD peptide with almost one order of magnitude higher integrin binding affinity than the monomeric analog is thus labeled with ^{18}F (*3*). [^{18}F]FB-E[c(RGDyK)]$_2$ (abbreviated as [^{18}F]FRGD$_2$) showed predominant renal excretion and almost twice as much tumor uptake in the same animal model as compared to the monomeric tracer [^{18}F]FB-c(RGDyK). In this study we will further evaluate this tracer in various preclinical animal models in order to measure the metabolic stability and to visualize and quantify integrin $\alpha_v\beta_3$ expression in vivo. We also used dimeric RGD peptide E[c(RGDyK)]$_2$ as carrier for paclitaxel to specifically target breast cancer cells and tumor blood vessels. The *in* vitro receptor binding, cytotoxicity and apoptosis results were observed in the MDA-MB-435 cell line and biodistribution data was performed in an orthotopic nude mouse breast cancer model.
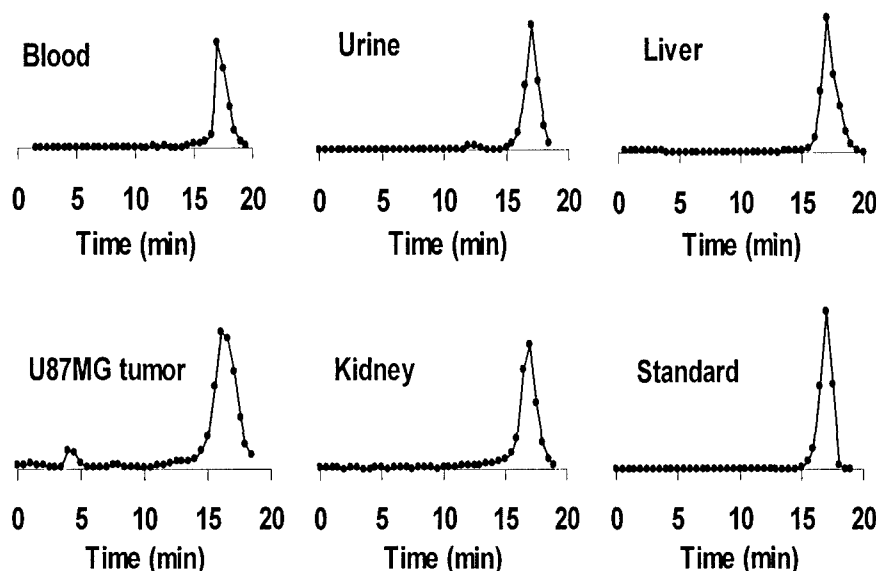
BODY

Part I: PET Imaging of Integrin Expression

^{18}F-fluorination of dimeric RGD (E[c(RGDyK)]$_2$) was carried out using *N*-succinimidyl 4-[^{18}F]fluorobenzoate ([^{18}F]SFB) (**Fig. 1**). Synthesis of [^{18}F]SFB followed a previously reported procedure except that [^{18}F]SFB was purified before coupling with an RGD dimer. It was found that the specific activity of [^{18}F]SFB with HPLC purification was higher than that with simple cartridge desalting. The subsequent purification of [^{18}F]FRGD2 *(3,6)* was also made easier. The yield of radiochemical acylation is dependent on peptide concentration, temperature, pH, and reaction time. Starting from ^{18}F$^-$ Kryptofix 2.2.2/K$_2$CO$_3$ solution, the total reaction time including final HPLC purification was about 200 ± 20 min. The maximum overall radiochemical yield with decay-correction was 23 ± 2 % (n = 20). The radiochemical purity of the labeled peptide was higher than 98% according to analytical HPLC analysis. The specific radioactivity of [^{18}F]SFB was estimated by radio-HPLC to be 200~250 TBq/mmol. Such yield was reached by using 200 μg of E[c(RGDyK)]$_2$ at pH = 8.0 and 40 °C within 20 min. Notice that this yield is significantly lower than that reported for monomeric RGD peptide c(RGDyK), which was > 40% *(7-9)*.

Fig. 1. Schematic structure of [^{18}F]FB-E[c(RGDyK)]$_2$ ([^{18}F]FRGD2).

The metabolic stability of [^{18}F]FRGD2 was determined in mouse blood and urine samples and in liver, kidneys, and tumor homogenates 60 min after tracer injection. For all organs extraction efficiency was between 78% and 93%. Between 0.2 and 20% of the total activity could not be trapped on the C$_{18}$ cartridges, which might be attributed to very hydrophilic metabolites or protein bound activity. The lowest extraction efficiency was found for the U87MG tumor and highest was found for the blood. HPLC analysis results of the soluble fractions of the different samples were shown in **Fig. 2**. The average fraction of intact tracer was between 80% and 95%. Highest metabolic stability of [^{18}F]FRGD2 was found in urine (95.5% intact tracer). Although we did not identify the composition of the metabolites, we found all of the metabolites eluted earlier from HPLC

4

column than the parent compound. There was a minor peak found at 12 min for all the samples. There was also another metabolite peak found at about 4 min for the tumor. No defluoridation of [^{18}F]FRGD2 was observed.
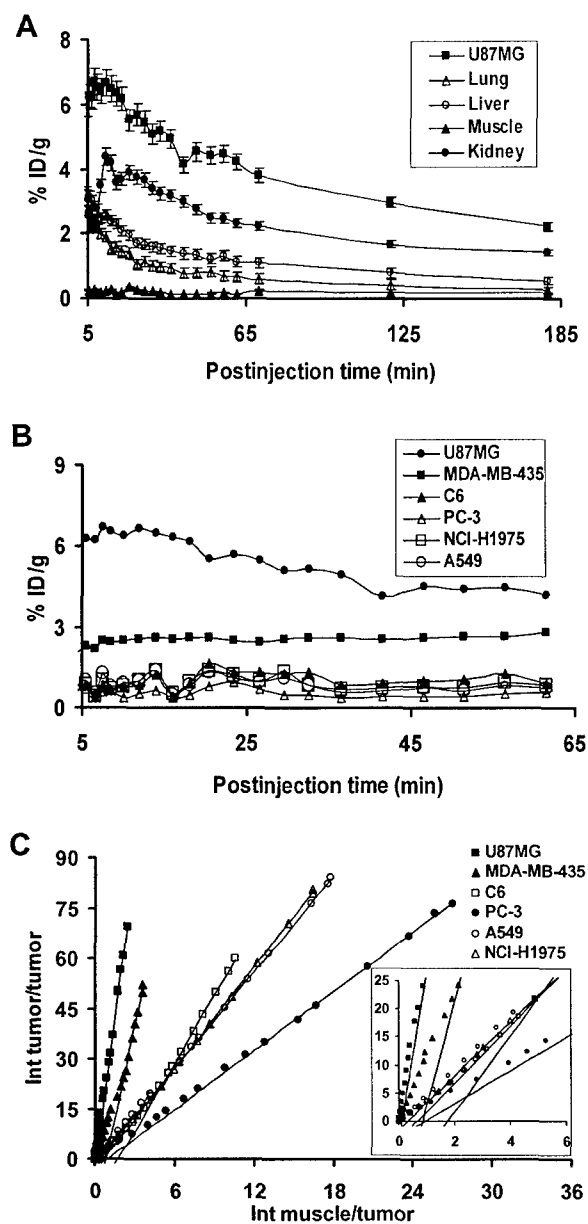

Fig. 2. Representative HPLC profiles of the reference compound [^{18}F]FRGD2, the soluble fractions of blood and urine samples, tumor, kidney, and liver homogenates collected 1 h after tracer injection. The dimeric RGD peptide tracer is metabolically stable in most organs and tissues.

The dynamic microPET scans were performed for six tumor models (U87MG, MDA-MB-435, PC-3, NCI-H1975, PC-3, and C6). Selected coronal images at different time points postinjection (p.i.) of [^{18}F]FRGD2 in a U87MG tumor mouse were showed in **Fig. 3**. High tumor activity accumulation was observed as early as 5 min p.i. Most of the radioactivity in non-target tissues were cleared at 70 min p.i. The uptakes in the U87MG tumor, kidneys, liver and lung were 3.81 ± 0.80, 2.25 ± 0.43, 1.10 ± 0.22, and 0.59 ± 0.18 %ID/g, respectively. Time-activity curves showed that this tracer excreted predominantly through the renal route (**Fig. 4A**). Diversified tumor uptake patterns of [^{18}F]FRGD2 were found in different xenograft models (**Fig. 4B**). The U87MG tumor had the highest tumor tissue integrin and tumor cell integrin levels and also had highest initial tumor uptake but also had the most rapid tumor washout, reaching a plateau after 50 min p.i. The tumors with low magnitude of tumor uptake had minimal tumor washout, providing reasonably high tumor contrast at late time points when non-specific activity accumulation in the normal organs had been mostly cleared.
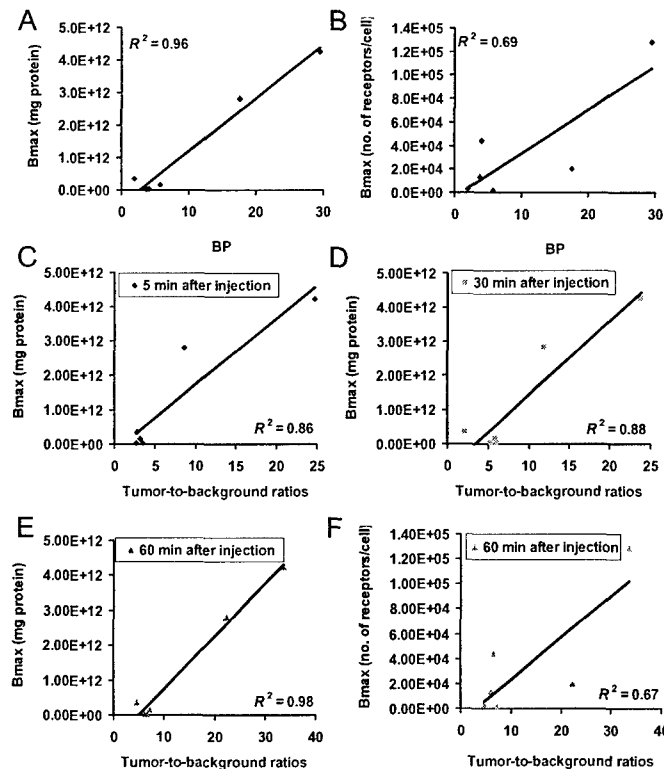
Fig. 3. Dynamic microPET study of U87MG tumor bearing mouse over 60 min after injection of [^{18}F]FRGD2 (100 μCi), static scans at 2 h and 3 h time points were also conducted to complete the tracer kinetic study. Decay-corrected whole-body coronal images that contain the tumor were shown.

Fig. 4. (A) Time activity curves derived from the 60 min dynamic and 70 min, 120 min, 180 min static microPET imaging study. The regions of interests (ROIs) are shown as mean % ID/g ± SD (n = 3). (B) Comparison of tumor uptake in nude mice derived from the 60 min dynamic microPET scans. (C) Logan plots derived from 60 min dynamic microPET imaging data, which showed excellent linearity of normalized integrated (Int) tumor activity versus normalized integrated muscle tissue activity effective for t > 25 min. The slopes of the fits represent the distribution volume ratios (DVR).

Logan plot is a graphical method of analysis, applicable to ligands that bind reversibly to receptors or enzymes (*10,11*). This method can calculate the DV for dynamic PET data before steady state is actually reached. We used 26.5 min as starting point for linear regression of the dynamic microPET studies since all graphs became linear after that point with the slope being DVR (**Fig. 4C**). The calculated binding potentials (B_{max}/K_d) for [^{18}F]FRGD2 in the U87MG, MDA-MB-435, C6, PC-3, NCI-H1975, and A549 tumors using muscle as reference tissue were found to be 29.5, 17.5, 5.8, 1.9, 4.1 and 3.8, respectively.

A linear relationship was found between the BP values calculated from graphical analysis of dynamic microPET imaging and the B_{max} values measured from SDS-PAGE/autoradiograms ($R^2 = 0.96$, $P = 0.005$) (**Fig. 5A**). The tumor to contralateral background ratios did not provide the same level of correlation with the tumor tissue integrin density at early time points (e.g. Pearson's correlation coefficient R^2 was 0.86 at 5 min and 0.88 at 30 min p.i.) (**Fig. 5C and D**). At 1 h p.i., a good linear relationship was found between tumor/background ratio and tumor integrin level (**Fig. 5E**). Interestingly, tumor cell integrin level did not have the same level of correlation with tumor contrast or binding potential (**Fig. 5B and F**).

7

Fig. 5. Correlation analysis between: (A) tumor tissue receptor density (# receptors/mg protein measured from SDS-PAGE/autoradiography using ^{125}I-echistatin as radioligand) vs. binding potential (BP) (calculated from Logan plot transformation of dynamic microPET imaging data) (R^2 = 0.96); (B) tumor cell integrin expression (# receptors/cell measured from whole-cell receptor binding assay) vs. binding potential (BP) (R^2 = 0.69); (C-E) tumor tissue receptor density vs. tumor/background ratios (calculated from time-activity curves derived from dynamic microPET imaging). The coefficient of determination R^2 is about 0.86, 0.87, and 0.98 at 5 min, 30 min, and 60 min postinjection of [^{18}F]FRGD2, respectively; (F) tumor cell receptor density vs. tumor/background ratio at 60 min postinjection of [^{18}F]FRGD2. The coefficient of determination R^2 is 0.67. Data derived from six tumor models (U87MG, C6, MDA-MB-435, PC-3, NCI-H1975, and A549) illustrated excellent linear relationship between tumor tissue receptor density vs. binding potential, and tumor tissue receptor density vs. tumor/background ratio at 1 h p.i..

Part II: RGD-Paclitaxel for Integrin Targeted Drug Delivery

The conjugate of paclitaxel (PTX) with dimeric RGD peptide (**Fig. 6**) (*1*) was prepared by derivatizing the 2'-hydroxy function of paclitaxel with succinic anhydride, according to reported procedure (*12*). The paclitaxel hemisuccinate ester (PTXSX) was activated using EDC and NHS, followed by coupling with RGD peptide glutamate amino group under slightly basic conditions.

Fig. 6. Schematic representation of the molecular structure of dimeric RGD peptide-paclitaxel conjugate. The succinate linkage is through the 2'-hydroxy group of paclitaxel and amino group of RGD glutamate residue.

The cytotoxic effect of PTX, PTXSX, RGD and PTX-RGD conjugate administered as single agents was assessed by MTT (3-(4,5-dimethylthiazole-2-yl)-2,5-diphenyltetrazoliumbromide)-assay (*13*) in MDA-MB-435 breast cancer cells after 48 h continuous drug exposure (**Fig. 7**). PTXSX with the IC_{50} of 67 ± 9 nM showed similar potency to PTX (IC_{50} = 34 ± 5 nM). However, PTX-RGD conjugate with the IC_{50} value of 134 ± 28 nM was slightly less potent than free PTX. Cyclic RGD peptide was the least potent (IC_{50} = 2.9 ± 0.1 μM).

8

Fig. 7. Cytotoxic effect of PTX , PTXSX, PTX-RGD conjugate, and RGD peptide. MDA-MB-435 cells were treated with continuous exposure of each drug for 48 h and cytotoxicity were assessed by MTT assay as described in the Method Section. Data are presented as a measure of percent survival normalized against the untreated population. Each data point is from an average of 3 to 4 independent experiments performed in triplicate. IC_{50} values for PTX, PTXSX, PTX-RGD, and RGD are 34 ± 5, 67 ± 9, 134 ± 28, and 2940 ± 15 nM, respectively.

Flow cytometric analysis was performed to analyze the cell cycle perturbations and apoptosis. As expected, RGD administered as a single agent induced cell cycle arrest in G_0/G_1-phase. No apoptotic fraction (as determined by the sub-G_1 peak) was observed even at longer exposures to high concentrations of the drug (IC_{80}), which correlates well with the cytostatic effect observed in the drug sensitivity test. A G_2/M cell cycle arrest was observed for PTX, PTXSX and PTX-RGD conjugate (**Fig. 8**). The appearance of apoptotic cells (as calculated by sub- G_0/G_1 population) was evident at 24 h for all drugs. PTX-RGD conjugate and PTXSX showed similar mitotic arrest and apoptotic cell death to that of PTX. In all cases, the apoptotic events seemed to occur after G_2/M arrest.
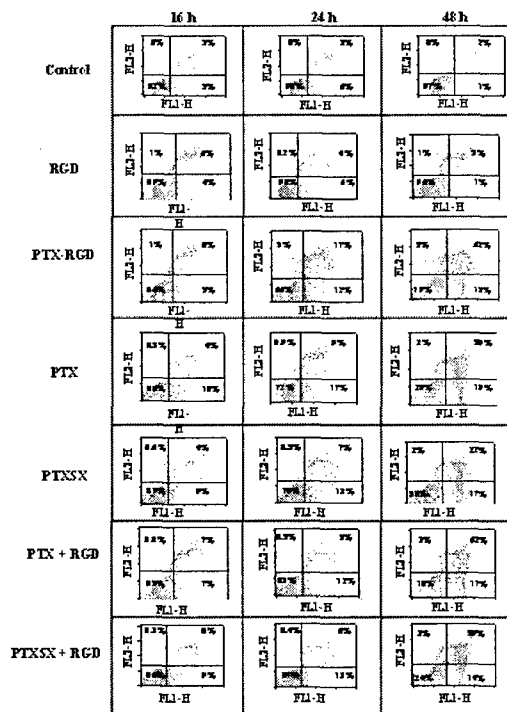
9

Fig. 8. Flow cytometric analysis of the cell cycle profiles of treated MDA-MB-435 cells. RGD peptide induces cell cycle arrest in G_0/G_1-phase with no apoptosis even at high drug concentration and prolonged exposure. All three PTX derivatives resulted in G_2/M cell cycle arrest with distinct apoptosis (sub-G_0/G_1 population) 24 h after drug treatment.

Simultaneous combination of PTX, PTXSX and RGD first induced a slight G_2/M-phase arrest at 16 h followed by the progressive appearance of a sub-G_1 peak characteristic of apoptosis. Levels of apoptotic fractions increased up to 35% and 57% with PTX/RGD and PTXSX /RGD combination, respectively. Our findings also demonstrate that the PTX-RGD conjugate is as efficacious as the combination of PTX or PTXSX and RGD.

An early event in apoptotic cell death is the translocation of the phosphatidyl-serine (PS) residues to the outer part of the cytoplasmatic cell membrane. In the presence of calcium, rapid high affinity binding of annexin V to PS occurs. PS translocation to the cell surface precedes nuclear breakdown, DNA fragmentation and the appearance of most apoptosis-associated molecules, making annexin V binding a marker of early-stage apoptosis. By using this method, we determined the ability of PTX-RGD conjugate to induce apoptosis and compared it to the ability of PTX and RGD used as a single agents or in simultaneous combination (PTX+RGD). As shown in **Fig. 9**, PTX-RGD conjugate caused a strong apoptotic effect comparable to that induced by PTX as a single agent. At 24 h, 17% of PTX-RGD conjugate treated cells appeared to be in early-apoptosis as compared to 9% for PTX. An increase in late-apoptosis/necrosis was also apparent at 48 h for both drugs. No significant changes in the percentage of apoptotic cells were observed in RGD treated

10

cells, data that correlates with the results obtained in the cell cycle analysis. Moreover, as we previously observed in the cell cycle profile for the simultaneous combination of PTX and RGD, the presence of RGD significantly reduced the percentage of apoptotic cells as compared to PTX as a single agent.
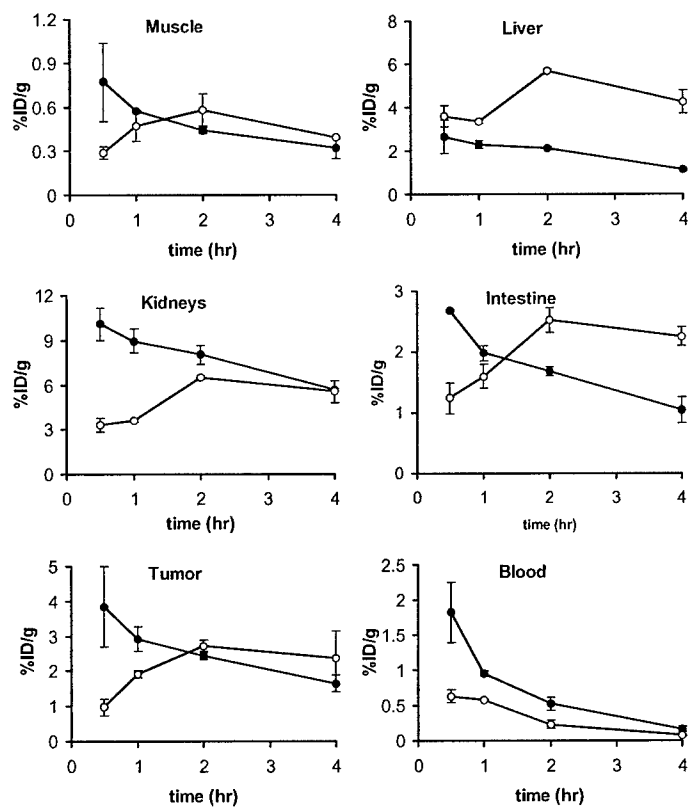

Fig. 9. Apoptosis analysis of MDA-MB-435 treated cells with RGD, PTX-RGD conjugate. Cells stained with annexinV/propidium iodide and analyzed by flow cytometry.

To assess the effect of conjugation and the presence of drug moiety on the MDA-MB-435 tumor and normal tissue uptake, the biodistribution of the ^{125}I-labeled conjugate (^{125}I-RGD-PTX) was compared to that of ^{125}I-RGD. Radioiodination of both compounds through a standard Chloramine-T method afforded the labeled molecules as evidenced by radio-HPLC with high specific activity (1,500 to 2,000 Ci/mmol). Typical radiochemical yield after HPLC purification for both radioligands was about 50-60% with radiochemical purity over 95%. The labeled RGD and conjugate were injected intravenously (i.v.) into athymic nude mice carrying orthotopic MDA-MB-435 xenografts. Tissues were removed at different time-points postinjection (p.i.) and the radioactivity uptakes, expressed in %ID/g were measured. Both RGD and PTX-RGD conjugate revealed fast blood clearance. Tumor activity accumulation was rapid for ^{125}I-RGD (e.g., 3.85 ± 1.15% ID/g at 30 min p.i.) and was quickly washed out, resulting in only 1.64 ± 0.24 %ID/g at 4 h p.i. The maximum tumor uptake for the conjugate appeared at 2 h p.i. (2.72 ± 0.16 %ID/g), and remained constant at 4 h p.i. (2.37 ± 0.76 %ID/g). The best tumor-to-blood and tumor-to-muscle ratios were achieved after 4 h p.i. To demonstrate that the RGD and RGD-PTX conjugate uptakes in MDA-MB-435 tumors were specific and receptor mediated, biodistribution studies were performed by co-injecting of c(RGDyK) (10 mg/kg) with the iodinated radiotracers. Uptake values of 0.87

11

± 0.17 and 0.42 ± 0.07 %ID/g were observed at 1 h p.i. for RGD and the conjugate, respectively (**Fig. 10**). These values were 4-5 times lower than the tumor uptake of the radiotracers when no blocking agent was coinjected.

Fig. 10. Comparison of biodistribution data for ^{125}I-E[c(RGDyK)]2 (●) and ^{125}I-RGD-PTXSX (○) in orthotopic MDA-MB-435 breast cancer xenograft model. Error bars denote SD (n = 4).

KEY RESEARCH ACCOMPLISHMENTS

- Developed a dimeric RGD peptide tracer [^{18}F]FRGD2 for PET imaging of tumor integrine expression;
- Established a tracer kinetic modeling protocol for quantification of tumor inetgrin receptor density;
- Applied polyvalency principle to develop dimeric and multimeric RGD peptides in order to increase the receptor avidity of the resulting RGD multimers;
- Synthesized a dimeric RGD peptide-paclitaxel conjugate for breast cancer targeting;
- Established procedures for analyzing breast cancer treatment efficacy in vitro.

REPORTABLE OUTCOMES

1. Wu Y, Zhang X, Xiong Z, Cheng Z, Fisher Dr, Liu S, Gambhir SS, <u>Chen X</u>.
   MicroPET Imaging of Glioma alpha(v)-Integrin Expression Using ^{64}Cu-Labeled
   Tetrameric RGD Peptide.
   *J Nucl Med.*2005;46:1707-1718.

2. Zhang X, Xiong Z, Wu Y, Tseng JR, Gambhir SS, <u>Chen X</u>.
   Quantitative PET Imaging of Tumor Integrin $\alpha_v\beta_3$ Expression with [^{18}F]FRGD2.
   J Nucl Med. Accepted.

3. Cheng Z, Wu Y, Xiong Z, Gambhir SS, <u>Chen X</u>.
   Near-Infrared Fluorescent RGD Peptides for Optical Imaging of Integrin $\alpha_v\beta_3$
   Expression in Living Mice.
   Bioconj Chem. In press.

4. Cai W, Gambhir SS, Chen X
   Multimodality tumor imaging targeting integrin $\alpha v\beta 3$.
   Biotechniques. In press.

5. <u>Chen X</u>, Tohme M, Park R, Hou Y, Bading JR, Conti PS.
   MicroPET Imaging of $\alpha_v\beta_3$ Integrin Expression with ^{18}F-Labeled Dimeric RGD
   Peptide.
   Mol Imaging 2004;3:96-104.

6. <u>Chen X</u>, Conti PS, Moats RA.
   In Vivo Near-Infrared Fluorescence Imaging of Integrin $\alpha_v\beta_3$ in Brain Tumor
   Xenografts.
   Cancer Res 2004;64:8009-8014.

7. <u>Chen X</u>, Sievers E, Hou Y, Park R, Tohme M, Bart R, Bremner R, Bading JR,
   Conti PS.
   Integrin $\alpha_v\beta_3$ Targeted Imaging of Lung Cancer.
   Neoplasia 2005;7:271-279.

8. <u>Chen X</u>, Plasencia C, Hou Y, Neamati N.
   Synthesis and Biological Evaluation of Dimeric RGD Peptide-Paclitaxel
   Conjugate as Model for Integrin Targeted Drug Delivery.
   J Med Chem 2005;48:1098-106.

9. <u>Chen X</u>, Hou Y, Tohme M, Park R, Khankaldyyan V, Gonzales-Gomez I, Bading
   JR, Laug WE, Conti PS.
   PEGylated RGD Peptide: ^{64}Cu-Labeling and PET Imaging of Brain Tumor
   Angiogenesis
   J Nucl Med 2004;45:1776-1783.

Abstracts:

1. Xiong Z, Cheng Z, Zhang X, Wu Y, Subbarayan M, Wu JC, Gambhir SS, <u>Chen X</u>
   MicroPET Imaging of Chemically Modified Adenovirus for Integrin $\alpha_v\beta_3$
   Retargeting.
   AMI International Conference 2005, Orlando, FL, March, 2005. (Abstract #: 108, oral)

2. Zhang X, Wu Y, Xiong Z, Yang Y, Cheng Z, <u>Chen X</u>
   Preparation and Characterization of $^{99m}Tc(CO)_3$-Bpy-RGD Complex as $\alpha_v\beta_3$ Integrin Receptor Targeted Imaging Agent.
   AMI International Conference 2005, Orlando, FL, March, 2005. (Abstract #: 330, poster)

3. Wu Y, Zhang X, Xiong Z, Yang Y, Cheng Z, Liu S, <u>Chen X</u>
   MicroPET Imaging of Brain Tumor Angiogenesis with ^{64}Cu-Tetra-c(RGDfK) Peptide
   AMI International Conference 2005, Orlando, FL, March, 2005. (Abstract #: 315, poster)

4. Cheng Z, Wu Y, Xiong Z, Gambhir SS, <u>Chen X</u>
   Cyanine Dye Conjugated RGD Monomer, Dimer, and Tetramer for Optical Imaging of Integrin Alpha(v)Beta(3) in Living Mice.
   AMI International Conference 2005, Orlando, FL, March, 2005. (Abstract #: 368, poster)

5. Wu Y, Fisher DR, Liu S, <u>Chen X</u>
   Evaluation of Copper-64 Labeled Tetrameric RGD Peptide for Tumor Imaging.
   SNM 52nd Annual meeting, Toronto, Canada, June 2005 (Abstract #: 79, oral)

6. Zhang X, Wu Y, <u>Chen X</u>
   Evaluation of ^{18}F-Labeled Dimeric RGD Peptide for PET Imaging of Tumor $\alpha_v\beta_3$-Integrin Expression.
   SNM 52nd Annual meeting, Toronto, Canada, June 2005 (Abstract #: 408, oral)

7. Zhang X, Wu Y, <u>Chen X</u>
   ^{18}F-Labeled Bombesin Analogs for Targeting GRP Receptor-Expressing Tumors.
   SNM 52nd Annual meeting, Toronto, Canada, June 2005 (Abstract #: 409, oral)

8. Wu Y, <u>Chen X</u>
   RGD-Cy7 Conjugate as NIR Fluorescence Probe to Image $\alpha_v\beta_3$ Integrin Expression in Brain Tumor Xenografts
   19th American Peptide Symposium, San Diego, June 2005 (Abstract #: PY37)

9. Cai W, <u>Chen X</u>
   RGD-Labeled Quantum Dot for Imaging Tumor Cells Overexpressing $\alpha_v\beta_3$ Integrin
   19th American Peptide Symposium, San Diego, June 2005 (Abstract #: P237)

10. Cai W, <u>Chen X</u>
    RGD Peptide-Labeled Quantum Dots for Optical Imaging of Integrin $\alpha_v\beta_3$ Expression
    The 4th Annual Meeting of the Society for Molecular Imaging, Cologne, Germany, September, 2005 (Travel Award) (Abstract #: 159)

11. Wu Y, <u>Chen X</u>
    In Vivo Near-Infrared Fluorescent Imaging of $\alpha_v\beta_3$ Integrin Expression in Brain Tumor Xenografts by Cy7-labeled Multimeric RGD Peptides
    The 4th Annual Meeting of the Society for Molecular Imaging, Cologne, Germany, September, 2005 (Abstract #: 489)

12. Cai W, <u>Chen X</u>
    PET Imaging of Tumor Integrin Expression
    2005 IEEE Computational Systems Bioinformatics Conference, Stanford, CA, August, 2005

13. <u>Chen X</u>
    PET Imaging of Tumor Integrin Expression: From Bench to Bedside
    2005 Animal Molecular Imaging International Symposium, Taipei, ROC, November, 2005

14. <u>Chen X</u>
    αv Integrin Targeted Delivery of Paclitaxel
    Era of Hope Department of Defense Breast Cancer Research Program Meeting, 2005 Proceedings, June 8-11, Philadelphia, PA

CONCLUSIONS

Part I: This study demonstrates that ^{18}F-labeled dimeric RGD peptide [^{18}F]FB-E[(c(RGDyK)]$_2$ ([^{18}F]FRGD2) has initial high activity accumulation in $\alpha_v\beta_3$-integrin rich tumors and some washout with time, providing high tumor/background ratio even at early time points. [^{18}F]FRGD2 uptake in tumors with medium or low $\alpha_v\beta_3$ levels was also low but minimal tumor washout was observed, and consequently clear tumor contrast is observable at late time points. The binding potential calculated from graphical analysis of dynamic PET imaging data is a better indicator than the tumor/background contrast for tumor integrin level in various preclinical tumor models.

Part II: In conclusion, this study demonstrates that a paclitaxel-RGD peptide conjugate can be used as an antitumor agent. By targeting integrin $\alpha_v\beta_3$, it is possible to improve the tumor specificity and cytotoxic effect of paclitaxel, resulting in lower systemic doses to obtain anitumor efficacy and reduced toxicity. It is unknown if and when the free paclitaxel is released during the time course of the assay. The possibility of partial distribution of free drug generated through either extracellular or intracellular proteases cannot be completely ruled out. Nevertheless, an improved therapeutic index could be expected by tumor integrin specific delivery of at least a part of targeted pacliatxel, resulting in lower and therefore less toxic systemic doses that are necessary to obtain antitumor efficacy. Further evaluation of this lead compound in preclinical animal models for tumor growth inhibition and acute toxicity studies is currently in progress.

REFERENCES

1. Chen X, Plasencia C, Hou Y, Neamati N. Synthesis and biological evaluation of dimeric RGD peptide-paclitaxel conjugate as a model for integrin-targeted drug delivery. *J Med Chem*. 2005;48:1098-1106.
2. Chen X, Sievers E, Hou Y, et al. Integrin $\alpha_v\beta_3$-targeted imaging of lung cancer. *Neoplasia*. 2005;7:271-279.
3. Chen X, Tohme M, Park R, Hou Y, Bading JR, Conti PS. Micro-PET imaging of $\alpha_v\beta_3$-integrin expression with ^{18}F-labeled dimeric RGD peptide. *Mol Imaging*. 2004;3:96-104.
4. Chen X, Liu S, Hou Y, et al. MicroPET imaging of breast cancer α_v-integrin expression with ^{64}Cu-labeled dimeric RGD peptides. *Mol Imaging Biol*. 2004;6:350-359.
5. Wu Y, Zhang X, Xiong Z, et al. MicroPET imaging of glioma α_v-integrin expression using ^{64}Cu-labeled tetrameric RGD peptide. *J Nucl Med*. 2005;46:1707-1718.
6. Zhang X, Xiong Z, Wu Y, et al. Quantitative PET Imaging of Tumor Integrin $\alpha_v\beta_3$ Expression with [^{18}F]FRGD2. *J Nucl Med*. In press.
7. Chen X, Park R, Shahinian AH, et al. ^{18}F-labeled RGD peptide: initial evaluation for imaging brain tumor angiogenesis. *Nucl Med Biol*. 2004;31:179-189.
8. Chen X, Park R, Tohme M, Shahinian AH, Bading JR, Conti PS. MicroPET and autoradiographic imaging of breast cancer α_v-integrin expression using [18]F- and ^{64}Cu-labeled RGD peptide. *Bioconjug Chem*. 2004;15:41-49.
9. Chen X, Park R, Hou Y, et al. MicroPET imaging of brain tumor angiogenesis with ^{18}F-labeled PEGylated RGD peptide. *Eur J Nucl Med Mol Imaging*. 2004;31:1081-1089.
10. Logan J. Graphical analysis of PET data applied to reversible and irreversible tracers. *Nucl Med Biol*. 2000;27:661-670.
11. Logan J. A review of graphical methods for tracer studies and strategies to reduce bias. *Nucl Med Biol*. 2003;30:833-844.
12. Deutsch HM, Glinski JA, Hernandez M, et al. Synthesis of congeners and prodrugs. 3. Water-soluble prodrugs of PTX with potent antitumor activity. *J Med Chem*. 1989;32:788-792.
13. Alley MC, Scudieron DA, Monks A, et al. Feasibility of drug screening with panels of human tumour cell lines using microculture tetrazolium assay. *Cancer Res*. 1988;48:589-601.

APPENDICES

1. Wu Y, Zhang X, Xiong Z, Cheng Z, Fisher Dr, Liu S, Gambhir SS, Chen X.
   MicroPET Imaging of Glioma alpha(v)-Integrin Expression Using ^{64}Cu-Labeled Tetrameric RGD Peptide.
   *J Nucl Med.*2005;46:1707-1718.

2. Cheng Z, Wu Y, Xiong Z, Gambhir SS, Chen X.
   Near-Infrared Fluorescent RGD Peptides for Optical Imaging of Integrin $\alpha_v\beta_3$ Expression in Living Mice.
   Bioconj Chem. In press.

3. Cai W, Gambhir SS, Chen X
   Multimodality tumor imaging targeting integrin $\alpha v\beta3$.
   Biotechniques. In press.

4. Chen X, Tohme M, Park R, Hou Y, Bading JR, Conti PS.
   MicroPET Imaging of $\alpha_v\beta_3$ Integrin Expression with ^{18}F-Labeled Dimeric RGD Peptide.
   Mol Imaging 2004;3:96-104.

6. Chen X, Conti PS, Moats RA.
   In Vivo Near-Infrared Fluorescence Imaging of Integrin $\alpha_v\beta_3$ in Brain Tumor Xenografts.
   Cancer Res 2004;64:8009-8014.

5. Chen X, Sievers E, Hou Y, Park R, Tohme M, Bart R, Bremner R, Bading JR, Conti PS.
   Integrin $\alpha_v\beta_3$ Targeted Imaging of Lung Cancer.
   Neoplasia 2005;7:271-279.

6. Chen X, Plasencia C, Hou Y, Neamati N.
   Synthesis and Biological Evaluation of Dimeric RGD Peptide-Paclitaxel Conjugate as Model for Integrin Targeted Drug Delivery.
   J Med Chem 2005;48:1098-106.

7. Chen X, Hou Y, Tohme M, Park R, Khankaldyyan V, Gonzales-Gomez I, Bading JR, Laug WE, Conti PS.
   PEGylated RGD Peptide: ^{64}Cu-Labeling and PET Imaging of Brain Tumor Angiogenesis
   J Nucl Med 2004;45:1776-1783.

microPET Imaging of Glioma Integrin $\alpha_v\beta_3$ Expression Using ^{64}Cu-Labeled Tetrameric RGD Peptide

Yun Wu, PhD[1]; Xianzhong Zhang, PhD[1]; Zhengming Xiong, MD, PhD[1]; Zhen Cheng, PhD[1]; Darrell R. Fisher, PhD[2]; Shuang Liu, PhD[3]; Sanjiv S. Gambhir, MD, PhD[1]; and Xiaoyuan Chen, PhD[1]

[1]Molecular Imaging Program at Stanford (MIPS), Department of Radiology and Bio-X Program, Stanford University, Stanford, California; [2]Radioisotopes Program, Pacific Northwest National Laboratory, Richland, Washington; and [3]Industrial and Physical Pharmacy, School of Health Sciences, Purdue University, West Lafayette, Indiana

Integrin $\alpha_v\beta_3$ plays a critical role in tumor-induced angiogenesis and metastasis and has become a promising diagnostic indicator and therapeutic target for various solid tumors. Radiolabeled RGD peptides that are integrin specific can be used for noninvasive imaging of integrin expression level as well as for integrin-targeted radionuclide therapy. **Methods:** In this study we developed a tetrameric RGD peptide tracer ^{64}Cu-DOTA-E{E[c(RGDfK)]$_2$}$_2$ (DOTA is 1,4,7,10-tetraazacyclododecane-N,N',N'',N'''-tetraacetic acid) for PET imaging of integrin $\alpha_v\beta_3$ expression in female athymic nude mice bearing the subcutaneous UG87MG glioma xenografts. **Results:** The RGD tetramer showed significantly higher integrin binding affinity than the corresponding monomeric and dimeric RGD analogs, most likely due to a polyvalency effect. The radiolabeled peptide showed rapid blood clearance (0.61 ± 0.01 %ID/g at 30 min and 0.21 ± 0.01 %ID/g at 4 h after injection, respectively [%ID/g is percentage injected dose per gram]) and predominantly renal excretion. Tumor uptake was rapid and high, and the tumor washout was slow (9.93 ± 1.05 %ID/g at 30 min after injection and 4.56 ± 0.51 %ID/g at 24 h after injection). The metabolic stability of ^{64}Cu-DOTA-E{E[c(RGDfK)]$_2$}$_2$ was determined in mouse blood, urine, and liver and kidney homogenates at different times after tracer injection. The average fractions of intact tracer in these organs at 1 h were approximately 70%, 58%, 51%, and 26%, respectively. Noninvasive microPET studies showed significant tumor uptake and good contrast in the subcutaneous tumor-bearing mice, which agreed well with the biodistribution results. Integrin $\alpha_v\beta_3$ specificity was demonstrated by successful blocking of tumor uptake of ^{64}Cu-DOTA-E{E[c(RGDfK)]$_2$}$_2$ in the presence of excess c(RGDyK) at 1 h after injection. The highest absorbed radiation doses determined for the human reference adult were received by the urinary bladder wall (0.262 mGy/MBq), kidneys (0.0296 mGy/MBq), and liver (0.0242 mGy/MBq). The average effective dose resulting from a single ^{64}Cu-DOTA-E{E[c(RGDfK)]$_2$}$_2$ injection was estimated to be 0.0164 mSv/MBq. **Conclusion:** The high integrin and avidity and favorable biokinetics make ^{64}Cu-DOTA-E{E[c(RGDfK)]$_2$}$_2$ a promising agent for peptide receptor radionuclide imaging and therapy of integrin-positive tumors.

Key Words: tumor angiogenesis; integrin; RGD peptide; microPET; multimeric peptide; [64]Cu

Malignant gliomas are the most common types of brain tumors and are the second leading cause of cancer death in children under 15 y old and also in young adults up to 34 y old (*1,2*). With a high proliferation rate, marked neovascularization, and extensive local invasion of tumor cells into the normal brain parenchyma, gliomas are resistant to traditional radiation and chemotherapy, which leads to patient mortality over months or years (*3*). Recent clinical and experimental evidence suggests that the tumor growth and progression are dependent on angiogenesis and invasion, which share common regulatory mechanisms (*4*). Angiogenesis is an invasive process characterized by endothelial cell proliferation, modulation of the extracellular matrix (ECM), and cell adhesion and migration (*5*). Among many angiogenic factors, the cell adhesion molecule integrin is a mediator of angiogenesis in many tumor types, including gliomas (*6*). Integrins are part of a family of heterodimeric transmembrane receptors involved in multiple steps of angiogenesis and metastasis. Integrins on endothelial cells bind to and respond to the ECM components, and this interaction is accompanied by the transduction of positional cues from the ECM to the intracellular signaling machinery (*7*). The function of these protein receptors during angiogenesis has been studied with integrin $\alpha_v\beta_3$, which is not readily detectable in quiescent vessels but becomes highly expressed in angiogenic vessels and tumor cells (*8,9*). The $\alpha_v\beta_3$ integrin is necessary for the formation, survival, and maturation of newly formed blood vessels (*10*) and its expression correlates with tumor grade and histologic type (*11*).

.,Recent data both in preclinical tumor models and in phase I/II clinical trials suggest that antagonists of $\alpha_v\beta_3$ integrin inhibit tumor angiogenesis and metastasis (12,13). The ability to noninvasively visualize and quantify $\alpha_v\beta_3$ integrin expression level provides opportunities to document tumor (tumor cells and sprouting tumor vasculature) receptor expression, to more appropriately select patients considered for antiintegrin treatment, and to monitor treatment efficacy in integrin-positive patients. Several molecular probes have been developed for MRI (14), ultrasound (15), optical imaging (16), PET, and SPECT applications (17). Although most of the RGD peptide-based probes could target tumors by binding integrin $\alpha_v\beta_3$, they suffer from modest tumor uptake and unfavorable pharmacokinetics that limit their applications for imaging and internal radiotherapy.

We and others have reported radiolabeled RGD-containing peptide dimers as radiopharmaceuticals for diagnosis of rapidly growing solid tumors (18–23). It was hypothesized that the receptor binding of one RGD cyclic peptide will significantly enhance the "local concentration" of the other RGD peptide in the vicinity of the receptor, which may lead to a faster rate of receptor binding or a slower rate of dissociation of radiolabeled RGD dimer from the integrin $\alpha_v\beta_3$ and result in higher uptake and longer retention time in the tumor. A multimeric RGD peptide with >2 repeating cyclic RGD units is thus expected to further enhance the affinity of the receptor–ligand interactions even more significantly through the phenomenon of a polyvalency effect. The apparent increase in molecular size may also prolong circulation time of the multimer and consequently reduce tumor washout rate.

In this investigation we applied the polyvalency principle and developed a novel tetrameric RGD peptide using glutamate as the branching unit. The resulting RGD peptide tetramer was conjugated with the macrocylic chelator 1,4,7,10-tetraazacyclododecane-N,N',N'',N'''-tetraacetic acid (DOTA) and labeled with ^{64}Cu for microPET imaging of integrin expression in a subcutaneous U87MG glioblastoma xenograft model in female athymic nude mice. The aim of this study was to investigate integrin targeting characteristics of ^{64}Cu-DOTA-E{E[c(RGDfK)]$_2$}$_2$ as a potential agent for diagnosis and receptor-mediated internal radiotherapy of integrin receptor–expressing tumors.

MATERIALS AND METHODS

All commercially available chemical reagents were used without further purification. DOTA was purchased from Macrocyclics, Inc. Dicyclcohexylcarbodiimide (DCC), 1-ethyl-3-[3-(dimethylamino)propyl]carbodiimide (EDC), N-hydroxysulfonosuccinimide (SNHS), and Chelex 100 resin (50–100 mesh) were purchased from Aldrich. Water and all buffers were passed over a Chelex 100 column (1 × 15 cm) before use in radiolabeling procedures. Reversed-phase extraction C-18 Sep-Pak cartridges were obtained from Waters. The syringe filter and polyethersulfone membranes (pore size, 0.2 μm; diameter, 13 mm) were obtained from Nalge Nunc International. ^{125}I-echistatin, labeled by the lactoperoxidase

method to a specific activity of 74,000 GBq/mmol (2,000 Ci/mmol), was purchased from Amersham Biosciences. The female athymic nude mice were supplied from Harlran at 4–5 wk of age. ^{64}Cu (half-life [$t_{1/2}$] = 12.7 h, β^+ = 655 keV [17.4%], β^- = 573 keV [30%]) was obtained form Mallinckrodt Institute of Radiology, Washington University School of Medicine (St. Louis, MO). ^{64}Cu was produced in a CS-15 biomedical cyclotron using the ^{64}Ni(p,n,)^{64}Cu nuclear reaction and supplied in high specific activity as CuCl$_2$ in 0.1 mol/L of HCl. The monomeric cyclic RGD peptide, c(RGDfK), was prepared via solution cyclization of the linear peptide H-Gly-Asp(OtBu)-D-Phe-Lys(Boc)-Arg(Pbf)-OH. Trifluoroacetic acid (TFA) deprotection in the presence of the free radical scavenger triisopropylsilane produced the desired cyclic pentapeptide c(RGDfK) (24–27). The RGD peptide dimer E[c(RGDfK)]$_2$ was prepared according to the literature method (18).

Analytic as well as semipreparative reversed-phase high-performance liquid chromatography (RP-HPLC) were performed on a Dionex 680 chromatography system with a UVD 170U absorbance detector and model 105S single-channel radiation detector (Carroll & Ramsey Associates). The recorded data were processed using Chromeleon version 6.50 software. Isolation of DOTA-conjugated peptide and ^{64}Cu-labeled peptide was performed using a Vydac protein and peptide column (218TP510; 5 μm, 250 × 10 mm). The flow was 5 mL/min, with the mobile phase starting from 95% solvent A (0.1% TFA in water) and 5% solvent B (0.1% TFA in acetonitrile) (0–3 min) to 35% solvent A and 65% solvent B at 33 min. The analytic HPLC was performed using the same gradient system, but with a Vydac 218TP54 column (5 μm, 250 × 4.6 mm) and flow of 1 mL/min. Ultraviolet (UV) absorbance was monitored at 218 nm.

Preparation of Boc-Glu(OSu)-OSu

To a solution of the Boc-protected glutamic acid (0.247 g, 1.0 mmol) in 5 mL of N,N-dimethylforamide (DMF) were added N-hydroxysuccinimide (NHS) (0.253 g, 2.2 mmol) and DCC (0.453 g, 2.2 mmol). The resulting mixture was stirred at room temperature for 10 h. The dicyclohexylurea (DCU) by-product was filtered off. The filtrate was evaporated to dryness under vacuum to give a crude product, which was then taken up in 3 mL of methylene chloride. The insoluble solid was filtered off. The filtrate was concentrated to about 1 mL. The solution was added dropwise into 30 mL of ether. The desired product was precipitated as white solid, which was dried in vacuo. The yield was 0.27 g (~61%). ^{1}H NMR (CDCl$_3$) δ-5.23 (br s, 1H, NH), 4.82 (m, 1H, CH), 2.85 (m, 8H, succinimide group), 2.44–2.25 (m, 2H, CH$_2$CO), 1.52 (m, 2H, CH$_2$CH$_2$CO), 1.46 (s, 9H, t-Bu).

Preparation of Cyclic RGD Peptide Tetramer: E{E[c(RGDfK)]$_2$}$_2$

To a solution of the Boc-protected glutamic acid activated ester Boc-E(OSu)$_2$ (4.4 mg, 0.01 mmol) in anhydrous DMF (1 mL) was added the cyclic RGD peptide dimer E[c(RGDfK)]$_2$ (39.4 mg, 0.03 mmol). The pH of the resulting mixture was adjusted to 8.5–9.0 with diisopropylethyl amine (DIPEA). The reaction was stirred at room temperature overnight and the desired product, Boc-E{E[c(RGDfK)]$_2$}$_2$, was isolated by semipreparative HPLC. The collected fractions were combined and lyophilized to give a fluffy white powder. The yield was 15 mg (~53%). Electrospray ionization mass spectroscopy (ESI-MS) (positive mode): m/z = 2,848 for [M + H]$^+$ (C$_{128}$H$_{187}$N$_{39}$O$_{56}$, calculated molecular weight [MW] = 2.847). The Boc-group was readily removed by treating Boc-

E{E[c(RGDfK)]₂}₂ with anhydrous TFA for 5 min. The crude product was purified by HPLC. The collected fractions were combined and lyophilized to afford E{E[c(RGDfK)]₂}₂ as a white powder. The yield was 98%. ESI-MS (positive mode): m/z = 2,748 for [M + H]⁺ ($C_{123}H_{181}N_{39}O_{34}$, calculated MW = 2,747).

DOTA Conjugation and ⁶⁴Cu Radiolabeling

DOTA-E{E[c(RGDfK)]₂}₂ was synthesized in a manner similar to that described before (18,26,28,29). Briefly, DOTA was activated by EDC and SNHS at pH 5.5 for 30 min with a molar ratio of DOTA:EDC:SNHS = 10:5:4. The DOTA-OSSu reaction mixture (15 μmol, calculated on the basis of SNHS) was cooled to 4°C and added to E{E[c(RGDfK)]₂}₂ (2 mg, 0.6 μmol) dissolved in 500 μL of water. The reaction mixture was adjusted to pH 8.5 with 0.1N of NaOH and was allowed to incubate overnight at 4°C. The DOTA-coupled peptide was purified by semipreparative HPLC. The peak containing the tetramer conjugate was collected, lyophilized, and dissolved in water (2 mg/mL) for use in radiolabeling reactions. The yield was 1.4 mg (~75%). Matrix-assisted laser desorption ionization time-of-flight mass spectroscopy (MALDI-TOF MS): m/z = 3,135.3 for [M + H]⁺ ($C_{139}H_{205}N_{43}O_{41}$, calculated MW = 3,135.5)

DOTA-E{E[c(RGDfK)]₂}₂ was radiolabeled with ⁶⁴Cu to obtain ⁶⁴Cu-DOTA-E{E[c(RGDfK)]₂}₂. In brief, ⁶⁴CuCl₂ (74 MBq) was diluted in 400 μL of 0.1 mol/L sodium acetate and added to the DOTA conjugate (5 μg peptide per mCi ⁶⁴Cu). The reaction mixture was incubated for 1 h at 50°C. ⁶⁴Cu-DOTA-E{E[c(RGDfK)]₂}₂ was then purified by semipreparative HPLC. The radioactive peak containing ⁶⁴Cu-DOTA-E{E[c(RGDfK)]₂}₂ was collected, the solvent was evaporated, and the activity was reconstituted in phosphate-buffered saline (PBS) and passed through a 0.22-μm syringe filter for in vivo animal experiments.

Octanol–Water Partition Coefficient

Approximately 111 kBq of ⁶⁴Cu-DOTA-E{E[c(RGDfK)]₂}₂ in 500 μL of PBS (pH 7.4) were added to 500 μL of octanol in an Eppendorf microcentrifuge tube. The 2 layers were mixed for 5 min at room temperature, the tubes were centrifuged at 12,500 rpm for 5 min (model 5415R Eppendorf microcentrifuge; Brinkman), and 200-μL aliquots of both layers were counted in a γ-counter (Packard Instruments). The experiment was repeated 3 times.

Cell Integrin Receptor-Binding Assay

In vitro integrin-binding affinities and specificities of DOTA-conjugated RGD peptides were assessed via displacement cell-binding assays using ¹²⁵I-echistatin as the integrin-specific radioligand. Experiments were performed on human glioblastoma U87MG cell line by modification of a method previously described (28). Cells were grown in Dulbecco's medium (Gibco) supplemented with 10% fetal bovine serum (FBS), 100 IU/mL penicillin, and 100 μg/mL streptomycin (Invitrogen Co.), at 37°C in a humidified atmosphere containing 5% CO₂. During the cell-binding assay experiment, the cells were harvested, washed twice with PBS, and resuspended (2 × 10⁶ cells/mL) in binding buffer (20 mmol/L Tris, pH 7.4, 150 mmol/L NaCl, 2 mmol/L CaCl₂, 1 mmol/L MgCl₂, 1 mmol/L MnCl₂, 0.1% bovine serum albumin). Filter multiscreen DV plates (96-well; pore size, 0.65 μm; Millipore) were seeded with 10⁵ cells and incubated with ¹²⁵I-echistatin (30,000 cpm/well) in the presence of increasing concentrations of different RGD peptide analogs (0–1,000 nmol/L). The total incubation volume was adjusted to 200 μL. After the cells were incubated for 2 h at room temperature, the plates were filtered

through a multiscreen vacuum manifold and washed twice with cold binding buffer. The hydrophilic polyvinylidenedifluoride (PVDF) filters were collected and the radioactivity was determined using a NaI(Tl) γ-counter (Packard Instruments). The best-fit 50% inhibitory concentration (IC₅₀) values for the U87MG cells were calculated by fitting the data by nonlinear regression using GraphPad Prism (GraphPad Software, Inc.). Experiments were performed twice with triplicate samples.

Animal Models

Animal procedures were performed according to a protocol approved by Stanford University Institutional Animal Care and Use Committee. Human brain cancer carcinoma xenografts were induced by subcutaneous injection of 10⁷ U87MG cells into the right front leg of female athymic nude mice. Three weeks after inoculation of the tumor cells, when the tumor reached 0.4–0.6 cm in diameter, the mice were used for biodistribution and microPET (Concorde Microsystems Inc.) experiments.

In Vivo Metabolic Stability Studies

The metabolic stability of ⁶⁴Cu-DOTA-E{E[c(RGDfK)]₂}₂ was evaluated in normal athymic nude mice using the method described in the literature with some modifications (29). Animals were sacrificed and dissected at 30 min, 1 h, and 2 h after injection of 7.4 MBq of activity into the tail vein. Blood was immediately centrifuged for 5 min at 15,000g. Liver and kidneys were homogenized, extracted with 500 μL PBS, and centrifuged at 15,000g for 5 min. After removal of the supernatants, the pellets were washed with 1 mL PBS. For each sample, supernatants of both centrifugation steps of blood, liver, and kidneys were combined and passed through Sep-Pak C-18 cartridges. The urine sample was diluted with 1 mL PBS and passed through a C-18 cartridge. The cartridges were washed with 2 mL of water and eluted with 2 mL acetonitrile containing 0.1% TFA. After evaporation of the solvent, the residues were redissolved in 1 mL PBS. Aliquots of 400 μL were injected onto analytic RP-HPLC.

Biodistribution Studies

Female nude mice bearing tumor xenography of human glioblastoma U87MG were injected with 0.74–1.11 MBq of ⁶⁴Cu-DOTA-E{E[c(RGDfK)]₂}₂. The mice were sacrificed and dissected at 30 min, 1, 2, 4, and 24 h after injection of ⁶⁴Cu-labeled tetrameric RGD peptide. The blocking experiment was performed by coinjecting radiotracer with a saturating dose of c(RGDyK) (10 mg/kg) and sacrificed at 1 h after injection. Blood, tumor, major organs, and tissues were collected and wet weighted. The radioactivity in the tissues was measured using a γ-counter. The results are presented as the percentage injected dose per gram (%ID/g). For each mouse, the radioactivity of the tissue samples was calibrated against a known aliquot of the injectate and normalized to a body mass of 20 g. Values are expressed as mean ± SD for a group of 3 animals.

Calibration of microPET

Scanner activity calibration was performed to map between microPET image units and units of radioactivity concentration. A preweighed 50-mL centrifuge tube was filled with distilled water and ⁶⁴CuCl₂ (~9.3 MBq [~250 μCi] as determined by the dose calibrator) was used to simulate the whole body of the mouse. This tube was weighed, centered in the scanner aperture, and imaged for a 30-min static image, single bed position. From the sample weight and assuming a density of 1 g/mL, the activity concentration in the

bottle was calculated in units of μCi/mL. Eight planes were acquired in the coronal section. A rectangular region of interest (ROI) (counts/pixel/s) was drawn on the middle of 8 coronal planes. Using these data, a calibration factor (C) was obtained by dividing the known radioactivity in the cylinder (μCi/mL) by the image ROI. This calibration factor was determined periodically and did not vary significantly with time.

microPET Studies

PET of tumor-bearing mice was performed on a microPET R4 rodent model scanner (Concorde Microsystems Inc.). The scanner has computer-controlled vertical and horizontal bed motion, with an effective axial field of view (FOV) of 7.8 cm and a transaxial FOV of 10 cm. U87MG tumor-bearing mice ($n = 3$) were imaged in the prone position in the microPET scanner. The mice were injected with about 9.3 MBq of ^{64}Cu-DOTA-E{E[c(RGDfK)]$_2$}$_2$ via the tail vein and then anesthetized with 2% isoflurane and placed near the center of the FOV of the microPET where the highest image resolution and sensitivity are obtained. The 10-min static scans were obtained at 15 min, 30 min and 1, 2, 4, and 18 h after injection. The images were reconstructed by a 2-dimensional ordered-subsets expectation maximum (OSEM) algorithm. No correction was necessary for attenuation and scattering. At each microPET scan, ROIs were drawn over each tumor, normal tissue, and major organs on decay-corrected whole-body coronal images. The average radioactivity concentration (accumulation) within a tumor or an organ was obtained from mean pixel values within the multiple ROI volumes, which were converted to counts/mL/min by using the calibration constant C. Assuming a tissue density of 1 g/mL, the ROIs were then converted to counts/g/min, and then divided by the administered activity to obtain an imaging ROI-derived percentage administered activity per gram of tissue (%ID/g). For a receptor-blocking experiment, mice bearing U87MG tumors on the right front leg were imaged at 1 h (10-min static scan) after administration of 9.3 MBq of ^{64}Cu-DOTA-E{E[c(RGDfK)]$_2$}$_2$ coinjected with 10 mg/kg c(RGDyK).

Radiation Dose Extrapolations to the Human

Radiation-absorbed doses were not estimated for our U87MG tumor-bearing mice. However, the mouse biodistribution data (uptake, retention, and clearance) were used to project radiation-absorbed doses that could be expected in human subjects administered ^{64}Cu-DOTA-E{E[c(RGDfK)]$_2$}$_2$. Projected radiation-absorbed doses for humans were made by assuming that, for the purpose of this exercise, the metabolism rates and pharmacokinetics of ^{64}Cu-DOTA-E{E[c(RGDfK)]$_2$}$_2$ in man and mouse were equivalent. Therefore, the biodistribution data were assumed to apply to a reference adult human subject. Time–activity curves were generated from the mean values obtained in mice for each organ of interest. We then calculated source organ residence times for the human model by integrating a monoexponential fit to the experimental biodistribution data for each organ or tissue by standard methods. The whole-body time–activity curve was integrated by fitting the whole-body retention data to a biphasic exponential decay curve, which represented the retention data more closely than a single exponential equation. The source organ residence times obtained forthwith were used with a standard quantitation platform Organ Level Internal Dose Assessment (OLINDA; Vanderbilt University) (30). Note that the residence time for the urinary bladder was calculated without incorporating a dynamic bladder model.

Statistical Analysis

The data were expressed as means ± SD. One-way ANOVA was used for statistical evaluation. Means were compared using the Student t test. P values < 0.05 were considered significant.

RESULTS

Chemistry and Radiochemistry

The synthesis of DOTA-E{E[c(RGDfK)]$_2$}$_2$ (Fig. 1) was performed through an active ester method by coupling Boc-Glu(OSu)-OSu with dimeric RGD peptide E[c(RGDfK)]$_2$ followed by TFA deprotection. In aqueous solution, DOTA

FIGURE 1. Schematic structure of DOTA-E{E[c(RGDfK)]$_2$}$_2$. The tetrameric RGD peptide was synthesized by coupling Boc-Glu(OSu)-OSu with dimeric RGD peptide E[c(RGDfK)]$_2$ followed by removal of Boc protecting group. DOTA conjugation was realized by reacting monoactive ester of DOTA with the free amino group on the N-terminal glutamate.

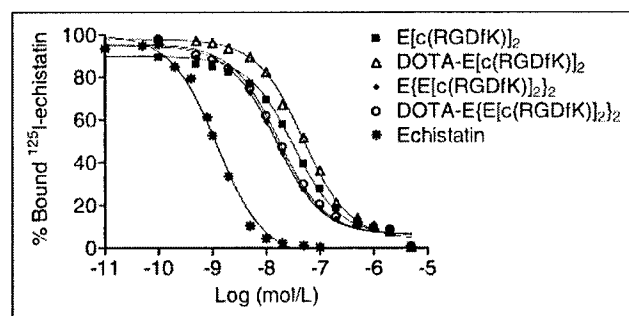was activated with SNHS/EDC, and the resulting DOTA-OSSu ester was conjugated with tetrameric cyclic RGD peptide. The overall yield of DOTA-E{E[c(RGDfK)]$_2$}$_2$ was about 25% starting from Boc-Glu. ^{64}Cu labeling of DOTA-RGD tetramer conjugate was performed using ^{64}Cu having a measured specific activity of 1 Ci/μmol (37 MBq/nmol) at >95% radiochemical purity as determined by analytic HPLC (decay corrected). The ^{64}Cu-DOTA-E{E[c(RGDfK)]$_2$}$_2$ was purified by semipreparative HPLC. On the analytic HPLC, we observed no significant difference between ^{64}Cu-radiolabeled tracer and unlabeled conjugate. The tetrameric peptide tracer showed intermediate hydrophilicity, as indicated from octanol–water partition coefficient measurements, with a log P value of -1.60 ± 0.10.

Cell Integrin Receptor-Binding Assay

The receptor-binding affinity studies of DOTA-E{E[c(RGDfK)]$_2$}$_2$ for α_v integrin were performed using α_v integrin–positive U87MG cells rather than isolated receptors $\alpha_v\beta_3$. Binding on the cell membrane allows cross-linking and integrin receptor multimerization, by which multivalent binding and clustering of receptor is studied in the natural context of the integrin (31). We compared the receptor-binding affinity of DOTA conjugated tetrameric RGD peptide with that of unlabeled echistatin, E{E[c(RGDfK)]$_2$}$_2$, E[c(RGDfK)]$_2$, and DOTA-E[c(RGDfK)]$_2$ by performing competitive displacement studies with ^{125}I-echistatin (Fig. 2). All the peptides inhibited the binding of ^{125}I-echistatin to α_v integrin–positive U87MG cells. The IC$_{50}$ values for echistatin, E{E[c(RGDfK)]$_2$}$_2$, and E[c(RGDfK)]$_2$, were 1.2 ± 0.1, 15.0 ± 1.1, and 32.2 ± 2.1 nmol/L, respectively. DOTA chelation had minimal effect on the receptor avidity of dimeric and tetrameric RGDs. The IC$_{50}$ values for DOTA-E{E[c(RGDfK)]$_2$}$_2$ and DOTA-E[c(RGDfK)]$_2$ were 16.6 ± 1.3 and 48.4 ± 2.8 nmol/L, respectively. The cell-binding assay demonstrated that RGD tetramer had about 3-fold and almost 10-fold higher integrin avidity than the corresponding dimeric (19) and monomeric (25) RGD peptide analogs, respectively.

FIGURE 2. In vitro inhibition of ^{125}I-echistatin binding to α_v integrin on human glioblastoma cell line U87MG by echistatin, E[c(EGDfK)]$_2$, DOTA-E[c(EGDfK)]$_2$, E{E[c(RGDfK)]$_2$}$_2$, and DOTA-E{E[c(RGDfK)]$_2$}$_2$. Results are means of 3 experiments.
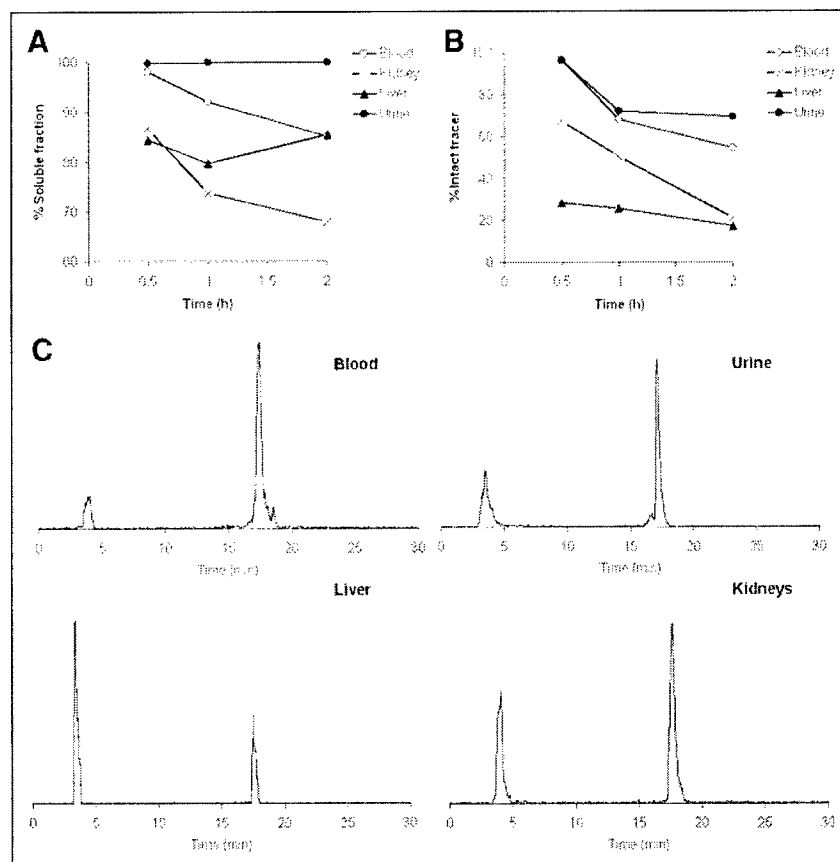
In Vivo Metabolism of ^{64}Cu-DOTA-E{E[c(RGDfK)]$_2$}$_2$

The metabolic stability of ^{64}Cu-DOTA-E{E[c(RGDfK)]$_2$}$_2$ was determined in mouse blood and urine and in liver and kidney homogenates at 30 min, 1 h, and 2 h after tracer injection. The extraction efficiency of all organs was between 65% and 100% (Fig. 3A). The lowest extraction efficiency was found for the kidney homogenates. Between 5% and 10% of the total activity could not be fixed on the C-18 cartridges, which can be related to very hydrophilic metabolites and protein-bound activity. The HPLC analyses of the soluble fraction of all organs and tissues allowed detection of only one major radiolabeled metabolite with the retention time between 3.3 to 4.0 min. The retention time for ^{64}Cu-DOTA-E{E[c(RGDfK)]$_2$}$_2$ was about 17.5 min (Fig. 3B). The tracer was stable in both blood (96.3% $\pm$ 3.5% intact tracer) and urine (95.3% $\pm$ 4.8% intact tracer) samples at 30 min after injection, but some degradation was found at late time points. The amount of intact tracer in the kidneys was approximately 70% at 30 min after injection and rapidly dropped to 21% over 2 h. This tracer in the liver showed rapid metabolism. Representative HPLC profiles of the soluble fractions of the different samples are shown in Figure 3C.

Biodistribution Studies

The biodistribution data of ^{64}Cu-DOTA-E{E[c(RGDfK)]$_2$}$_2$ in human U87MG glioma tumor-bearing athymic nude mice are shown in Figure 4A as the percentage administered activity (injected dose) per gram of tissue (%ID/g). This radiolabeled peptide displayed rapid blood clearance (0.61 ± 0.01 %ID/g at 30 min after injection and 0.21 ± 0.01 %ID/g at 4 h after injection). Rapid and high activity accumulation in the $\alpha_v\beta_3$-positive U87MG tumors was observed at early time points (9.93 ± 1.05 %ID/g at 30 min after injection). Tumor uptake slowly decreased to 7.61 ± 0.68 %ID/g at 2 h after injection, and 4.56 ± 0.51 %ID/g over 24 h. The biologic retention half-time $t_{1/2}$ of the ^{64}Cu-labeled tetrameric RGD peptide tracer was 4.3 h ($R^2 = 0.99$) in the tumor. The renal associated activity was initially high (9.02 ± 0.56 %ID/g, 30 min after injection), but fell to 2.83 ± 0.22 %ID/g at the end of 24 h (biologic retention $t_{1/2} = 1.72$ h, $R^2 = 0.99$) (Table 1). Moderate liver activity accumulation (e.g., 4.38 ± 0.39 %ID/g at 1 h and 2.34 ± 0.18 %ID/g, respectively) was also observed at all times.

A receptor specificity was demonstrated by coinjection of c(RGDyK) (10 mg/kg), which is integrin $\alpha_v\beta_3$ positive, with ^{64}Cu-DOTA-E{E[c(RGDfK)]$_2$}$_2$ and measuring the biodistribution at 1 h after injection A significant decrease of radioactivity in all dissected tissues is shown in Figure 4B. Uptake in tumor was reduced most markedly from 9.70 %ID/g to 1.75 %ID/g. This experiment showed that the uptake and retention of ^{64}Cu-DOTA-E{E[c(RGDfK)]$_2$}$_2$ can be blocked in the presence of excess of nonradioactive RGD peptide in the U87MG tumor as well as in other organs, except blood and kidney. This simple blocking

FIGURE 3. (A) Extraction efficiency of liver and kidney homogenates, blood, and urine samples at 30 min, 1 h, and 2 h after tracer injection in normal athymic nude mice ($n = 3$). (B) Time course of intact tracer in soluble fraction of blood, urine, and organ homogenates. (C) Representative HPLC elution profiles of soluble fraction of blood and urine samples, liver, and kidney homogenates collected 1 h after tracer injection.
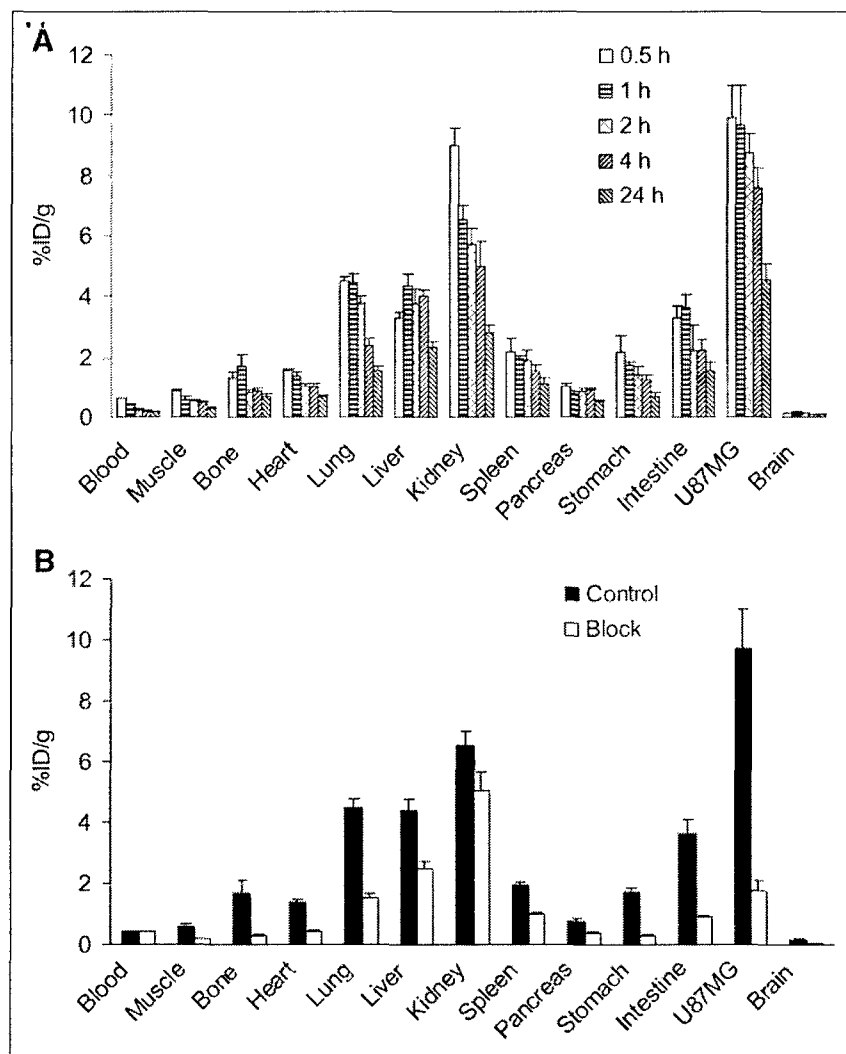
experiment does not allow us to conclude with absolute certainty that tumor uptake of ^{64}Cu-DOTA-E{E[c(RGDfK)]$_2$}$_2$ is attributed to specific peptide–receptor interaction unless dose-dependent inhibition of tumor uptake is observed by coinjecting varying amounts of competing agents.

A comparison of the kinetics of excretion of ^{64}Cu-DOTA-E[c(RGDfK)]$_2$ and ^{64}Cu-DOTA-E{E[c(RGDfK)]$_2$}$_2$ from the blood, liver, kidneys, and U87MG tumors is shown in Figure 5. Both tracers demonstrated rapid blood clearance with the tetramer (biologic $t_{1/2} = 0.56$ h; $R^2 = 0.99$) slower than the dimer (biologic $t_{1/2} = 0.20$ h; $R^2 = 0.99$). The renal uptake of the tetramer was significantly higher than that of the dimer at all time points ($P < 0.0001$), presumably because of the charge differences of these 2 conjugates. No significant difference was seen between 2 tracers in the liver uptake at early time points ($P > 0.1$), but the tetramer displayed persistent activity accumulation in the liver while liver activity for the dimer was slowly excreted. The relatively lipophilic character of the cyclic RGDfK tetramer (log P $= -1.6 \pm 0.1$) may be responsible for the hepatic residualization of this tracer. The uptake for ^{64}Cu-DOTA-E{E[c(RGDfK)]$_2$}$_2$ in the integrin-positive U87MG tumor was more than 2-fold higher

than for ^{64}Cu-DOTA-E[c(RGDfK)]$_2$ ($P < 0.001$). Altogether, the prolonged tumor retention and rapid clearance from nontarget organs led to very high tumor-to-nontumor ratios for the tetrameric RGD peptide tracer (e.g., at 2 h time point, tumor-to-blood ratio $= 34.8 \pm 2.7$; tumor-to-muscle ratio $= 15.9 \pm 1.2$; tumor-to-liver ratio $= 2.32 \pm 0.18$; tumor-to-kidney ratio $= 1.54 \pm 0.12$; and tumor-to-small intestine ratio $= 3.95 \pm 0.30$).

microPET Studies

The localization of ^{64}Cu-DOTA-E{E[c(RGDfK)]$_2$}$_2$ in human U87MG tumor-bearing nude mice ($n = 3$) was performed by multiple time-point static microPET scans. Figure 6A shows coronal microPET images of a female mouse at different times after injection following administration of 9.1 MBq (245 μCi) of the radiotracer. All microPET images were decay corrected. The tumor was clearly visualized with high tumor-to-contralateral background contrast, with the ratio higher than 5 at all times examined. Quantification of activity accumulation in the tumor and major organs (Fig. 6B) agreed well with that obtained from direct tissue sampling, except that the tumor-to-muscle ratio obtained from microPET was lower than that from biodis-

FIGURE 4. (A) Biodistribution data for ^{64}Cu-DOTA-E{E[c(RGDfK)]$_2$}$_2$ in athymic nude mice bearing subcutaneously xeno-transplanted U87MG tumors. Data are expressed as normalized accumulation of activity in %ID/g ± SD ($n = 3$). (B) Biodistributions of ^{64}Cu-DOTA-E{E[c(RGDfK)]$_2$}$_2$ in U87MG tumor-bearing athymic nude mice at 1 h with and without coinjection of 10 mg/kg of c(RGDyK) as a blocking agent ($n = 3$).

tribution studies ($P < 0.002$). No activity accumulation was observed in the normal brain, presumably because of a low α_v integrin expression level and an intact blood–brain barrier (BBB). Comparison of tumor uptakes in mice with and without coinjection of blocking dose of nonradioactive RGD peptide c(RGDyK) is illustrated in Figure 6C. Tumor-to-background contrasts at 1 h after injection for the control group and blocked group were 8.7 ± 1.5 and 2.3 ± 0.6, respectively.

Radiation Dosimetry

Table 1 shows the fractional uptake at time zero together with the biologic half-times for each organ of the mouse based on monoexponential clearance. Also shown are the biologic half-times and applicable fractions for the remainder of body based on a biexponential clearance function. The fractional uptakes (%ID) were greatest for the urinary bladder, tumor, and liver. These parameters were used to project radiation-absorbed doses per unit administered activity in an adult human (Table 2). These results predict that the highest radiation-absorbed doses will be to the urinary

TABLE 1
Average Fractional Uptake at Time Zero and Biologic Half-Times for Each Organ of Tumor-Bearing Mice According to Biodistribution Data ($n = 3$)

Organ	Fractional uptake (%)	Biologic half-times (h)
Heart	0.19	3.52
Lung	0.76	3.11
Liver	3.48	10.45
Kidneys	2.49	2.95
Spleen	0.19	6.00
Pancreas	0.09	9.32
Brain	0.05	8.52
Urine*†	25.0	0.05; 1.85
Remainder of body*	9.2	0.07; 4.40

*Biologic half-times were calculated based on a biexponential clearance function.
†Urinary bladder fraction calculated assuming no excretion.

FIGURE 5. Comparison of biodistributions of ^{64}Cu-DOTA-E{E[c(RGDfK)]$_2$}$_2$ (●) and ^{64}Cu-DOTA-E[c(RGDfK)]$_2$ (○) in U87MG tumor-bearing athymic nude mice. Error bars denote SDs (n = 3).

bladder wall (0.262 mGy/MBq), kidneys (0.0296 mGy/MBq), and liver (0.0242 mGy/MBq). The whole-body absorbed dose was found to be 0.0164 mSv/MBq administered.

DISCUSSION

This study describes the synthesis of a tetrameric RGD peptide ligand for radiolabeling with the positron-emitting radionuclide ^{64}Cu for imaging tumor integrin expression. The new tracer ^{64}Cu-DOTA-E{E[c(RGDfK)]$_2$}$_2$ (Fig. 1) shows a very high tumor-to-nontumor contrast and should be useful for targeted diagnosis and radiotherapy of integrin $\alpha_v\beta_3$–positive tumors.

A variety of radiolabeled peptides are being evaluated for tumor localization and therapy. Radiolabeled RGD peptides are of particular interest because they bind to the integrin $\alpha_v\beta_3$ overexpressed on newly formed blood vessels and cells of many common cancer types. However, most small cyclic RGD peptides tracers result in fast blood clearance accompanied by low tumor uptake and rapid tumor washout, presumably due to suboptimal receptor-binding affinity and inadequate contact with cell-surface integrin receptors (*17,24–29,32–34*).
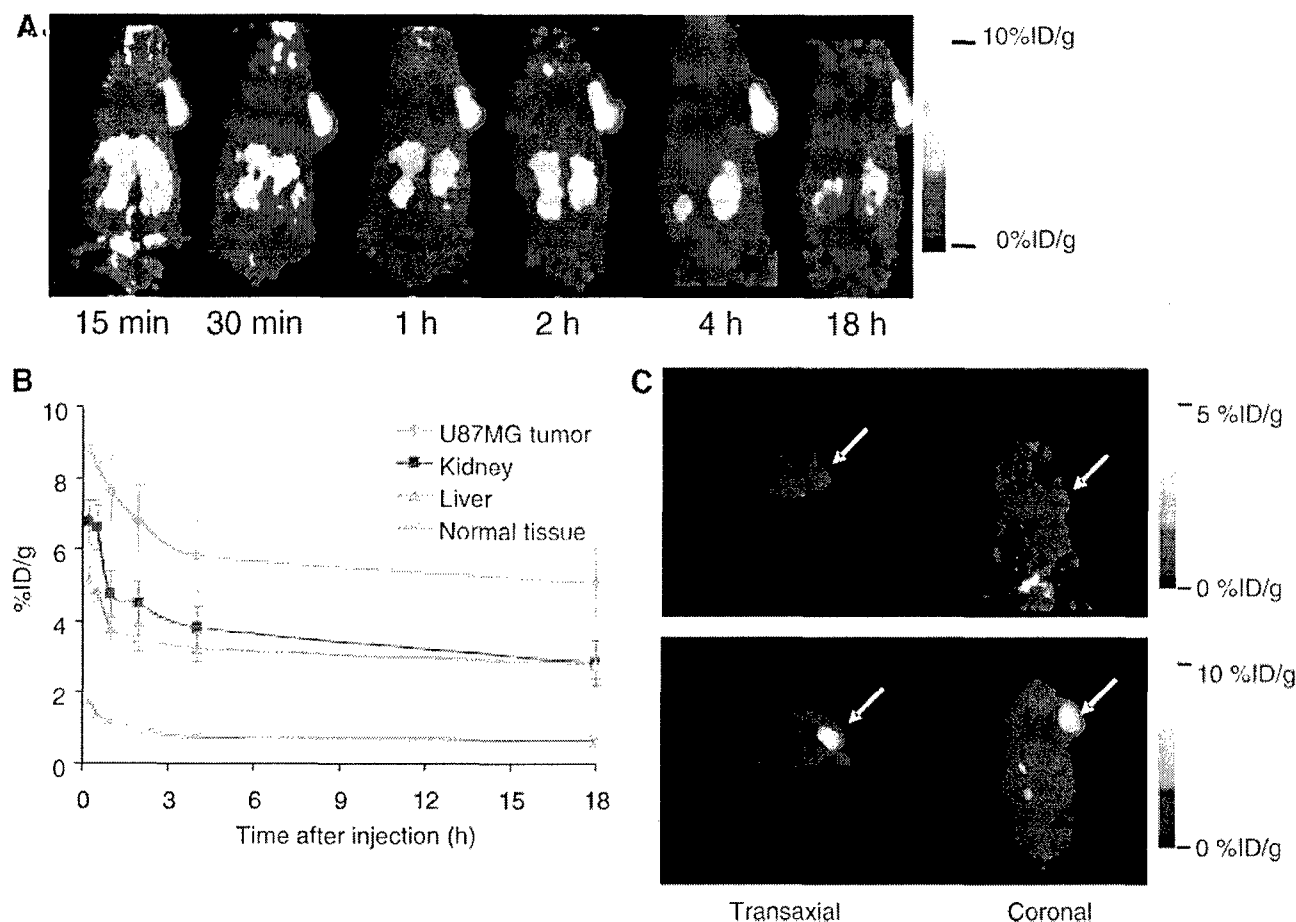
We and others (*18–23*) have previously applied the concept of bivalency to develop dimeric RGD peptides for improved tumor targeting over that of the corresponding monomeric RGD peptide analogs. In principle, the introduction of the homogeneous dimeric RGD peptide system is expected to improve integrin targeting by cooperative receptor interactions and receptor shielding to endogenous

competition. Dimeric RGD peptide E[c(RGDfK)]$_2$ was conjugated with DOTA or HYNIC, which enables labeling with ^{111}In (*21*), ^{90}Y (*21,23*), ^{64}Cu (*19*), and ^{99m}Tc (*18,22*). The dimeric RGD peptide tracer showed higher receptor-binding affinity and specificity for integrin $\alpha_v\beta_3$ in vitro and enhanced tumor uptake and retention in vivo as compared with the monomeric RGD peptide analog. A single injection of ^{90}Y-DOTA-E[c(RGDfK)]$_2$ at maximum tolerated dose caused a significant delay in tumor growth in a small subcutaneous OVCAR-3 ovarian xenograft tumor model (*21*). We found that replacing D-phenylalanine with D-tyrosine increased the hydrophilicity of the dimeric RGD peptide and, consequently, resulted in increased integrin-mediated tumor uptake and more favorable biokinetics in an orthotopic MDA-MB-435 breast cancer model (*19*). E[c(RGDyK)]$_2$ was also labeled with ^{18}F by using a prosthetic 4-^{18}F-fluorobenzoyl group and showed significantly higher tumor uptake and prolonged tumor retention in comparison with the ^{18}F-labeled monomeric RGD peptide because of the synergistic effect of bivalency and improved pharmacokinetics (*20*).

Although the dimeric RGD peptide tracers had some incremental improvement on tumor targeting and pharmacokinetics as compared with the monomeric RGD peptide analogs, the intermediate tumor uptake and persistent renal activity accumulation of this type of radioligand prevent their translation into human beings for diagnostic or therapeutic applications.

We hypothesize that multimerization to introduce tetrameric RGD peptides might further increase the re-

FIGURE 6. (A) Decay-corrected whole-body coronal microPET images of nude mouse bearing human U87MG tumor at 15 and 30 min and at 1, 2, 4, and 18 h (10-min static image) after injection of 9.1 MBq (245 μCi) of ^{64}Cu-DOTA-E{E[c(RGDfK)]$_2$}$_2$. (B) Time–activity curves derived from multiple time-point microPET study. ROIs are shown as the mean %ID/g ± SD ($n = 4$). (C) Comparison of tumor uptakes in mice injected with ^{64}Cu-DOTA-E{E[c(RGDfK)]$_2$}$_2$ at a dose of 9.3 MBq with (top) or without (bottom) 10 mg/kg c(RGDyK).

ceptor-binding affinity presumably because of the poly-valency effect. In this study, we designed a new tetrameric RGD peptide with repeating c(RGDfK) units connected through glutamate linkers. A cell receptor–binding assay using integrin-positive U87MG cells and ^{125}I-echistatin as the radioligand found integrin avidity of E{E[c(RGDfK)]$_2$}$_2$ > E[c(RGDfK)]$_2$ > c(RGDfK) (Fig. 2). DOTA conjugation had a minimal effect on the integrin affinity of the RGD peptides. When applied to the subcutaneous U87MG glioblastoma xenogarft model, ^{64}Cu-DOTA-E{E[c(RGDfK)]$_2$}$_2$ showed high tumor uptake and primarily renal and secondarily hepatic excretion routes (Figs. 4 and 6). The initial high tumor uptake might be attributed to the high integrin affinity of the tracer. The increased molecular size resulting in longer blood circulation time might be responsible for the prolonged tumor retention. At any given time, the in vivo tumor signal not only is attributed to specific binding but also presents contributions from nonspecific binding, free ligand in tissue, and intravascular activity. Kinetic modeling (e.g., Logan plot) (35) of the noninvasive dynamic

PET data may be applied to directly measure affinity constants and binding potential in vivo.

Kidney retention of ^{64}Cu was much longer for ^{64}Cu-DOTA-E{E[c(RGDfK)]$_2$}$_2$ than for ^{64}Cu-DOTA-E[c(RGDfK)]$_2$ (Fig. 5). Differences in renal uptake and excretion may be related to the charge differences of these 2 conjugates. The tetrameric RGD peptide tracer is more positively charged than the dimeric RGD peptide tracer because of the presence of more secondary amino groups, similar to what is observed for the difference between dimers and monomers (18–23). The positively charged radiopeptides or metabolites are usually retained in the kidney after resorption by renal tubular cells and lysosomal proteolysis (36). We also note from Figure 5 that the enhanced tumor uptake of the tetramer compared with the dimer is accompanied by a similar increase in renal uptake. Thus, tumor-to-kidney ratios do not increase significantly when using the tetrameric RGD peptide tracer and, consequently, the therapeutic window may not be increased and the advantage of a tetramer over a dimer might be modest. Blocking cationic binding sites in the kidneys

TABLE 2
Estimated Radiation-Absorbed Doses to Adult Human After Intravenous Injection of ^{64}Cu-DOTA-E{E[c(RGDfK)]$_2$}$_2$ Based on Average Biodistribution Data Obtained in U87MG Glioblastoma-Bearing Nude Mice ($n = 3$)

Target organ	mGy/MBq (SD)	rad/mCi (SD)
Adrenals	2.07E−03 (3.31E−04)	7.67E−03 (1.23E−03)
Brain	4.73E−04 (3.64E−05)	1.75E−03 (1.35E−04)
Breasts	6.58E−04 (1.05E−04)	2.43E−03 (3.89E−04)
Gallbladder wall	3.00E−03 (4.80E−04)	1.11E−02 (1.78E−03)
Lower large intestine	3.94E−03 (6.30E−04)	1.46E−02 (2.34E−03)
Small intestine	2.19E−03 (3.50E−04)	8.10E−03 (1.30E−03)
Stomach wall	1.28E−03 (2.05E−04)	4.74E−03 (7.58E−04)
Upper large intestine	2.04E−03 (3.26E−04)	7.53E−03 (1.20E−03)
Heart wall	3.22E−03 (6.15E−05)	1.19E−02 (2.27E−04)
Kidneys	2.96E−02 (1.84E−03)	1.10E−01 (6.84E−03)
Liver	2.43E−02 (1.56E−03)	8.98E−02 (5.76E−03)
Lungs	9.57E−04 (2.34E−05)	3.54E−03 (8.66E−05)
Muscle	1.55E−03 (8.90E−05)	5.74E−03 (3.30E−04)
Ovaries	3.74E−03 (5.98E−04)	1.38E−02 (2.21E−03)
Pancreas	1.15E−02 (4.73E−04)	4.24E−02 (1.74E−03)
Red marrow	1.28E−03 (2.05E−04)	4.75E−03 (7.60E−04)
Osteogenic cells	1.46E−03 (2.34E−04)	5.41E−03 (8.66E−04)
Skin	8.32E−04 (1.33E−04)	3.08E−03 (4.93E−04)
Spleen	8.16E−03 (1.64E−03)	3.02E−02 (6.07E−03)
Testes	2.72E−03 (4.35E−04)	1.01E−02 (1.62E−03)
Thymus	6.80E−04 (1.09E−04)	2.51E−03 (4.02E−04)
Thyroid	5.05E−04 (8.08E−05)	1.87E−03 (2.99E−04)
Urinary bladder wall	2.62E−01 (4.72E−02)	9.69E−01 (1.75E−01)
Uterus	7.92E−03 (1.27E−03)	2.93E−02 (4.69E−03)
Total body dose	2.35E−03 (3.76E−04)	8.69E−03 (1.39E−03)
Effective dose*	1.64E−02 (2.95E−03)	6.06E−02 (1.09E−02)

*In unit of mSv/MBq or rem/mCi.

with cationic amino acid infusion was reported to reduce renal uptake without compromising the tumor activity accumulation in both mice and humans (37). We expect that renal uptake of ^{64}Cu-DOTA-E{E[c(RGDfK)]$_2$}$_2$ may be blocked by coadministration of D- or L-lysines (37). Modification of DOTA-E{E[c(RGDfK)]$_2$}$_2$ conjugation by inserting a pharmacokinetic modifier to make the ^{64}Cu-labeled complex neutral or negatively charged may also improve the biokinetics of the tracer. Tetrameric RGD peptide tracer had moderate but persistent liver uptake. Although the factors that exert this influence are not fully understood, it is clear that the charge, lipophilicity, and stability of the copper complex play major roles. Our pervious experience with ^{64}Cu-labeled dimeric RGD peptide found that replacing D-Phe with D-Tyr increased the hydrophilicity of the resulting radiotracer and subsequently reduced liver uptake (19). We suggest that ^{64}Cu-DOTA-E{E[c(RGDyK)]$_2$}$_2$ may exhibit less liver uptake than ^{64}Cu-DOTA-E{E[c(RGDfK)]$_2$}$_2$.

In addition to U87MG tumor, ^{64}Cu-labeled RGD tetramer uptake in some normal organs and tissues was also inhibited by coadministration of an excess amount of monomeric RGD peptide c(RGDyK) (Fig. 4B). Western blot analysis of the tissue lysates suggested that these organs express a low amount of integrin $\alpha_v\beta_3$ (data not shown). Whether integrin-mediated localization of ^{64}Cu-DOTA-E{E[c(RGDyK)]$_2$}$_2$ in nontumor tissues will affect its imaging as well therapeutic application requires further investigation.

The OLINDA software (30), as a replacement for MIRDOSE3, provides a calculation of the effective dose for human adults as defined in ICRP Publication 60 (38). The urinary bladder received the highest absorbed doses, reflecting rapid clearance of most of the injected ^{64}Cu-DOTA-E{E[c(RGDyK)]$_2$}$_2$ into the bladder and making it the limiting organ as far as the amount of ^{64}Cu-DOTA-E{E[c(RGDyK)]$_2$}$_2$ that can be injected. However, the patient's voiding interval affects the radiation dose absorbed by the urinary bladder and, because the urinary bladder is the limiting organ, the patient's frequency of urination will change the bladder dose. Previous nonhuman primate imaging studies with ^{64}Cu-labeled octreotide ^{64}Cu-TETA-Y3-TATE found that the bladder dose could be reduced >7-fold by a normal voiding scheme as compared with no excretion assumption (39). If this is also true for our tetrameric RGD peptide tracer, then the kidneys appear to be the most affected and dose-limiting organs in human studies with regard to toxicity. The human kidney and liver doses of ^{64}Cu-DOTA-E{E[c(RGDfK)]$_2$}$_2$ calculated from mouse biodistribution data (0.030 and 0.024 mGy/MBq, respec-

tively) were significantly lower than those of ^{64}Cu-labeled octreotide ^{64}Cu-DOTA-OC calculated from clinical PET (0.078 and 0.091 mGy/MBq, respectively) (40). The use of rodent biodistribution data is generally thought to give a worst-scenario estimate of absorbed doses to normal organs. Whether this is true for ^{64}Cu-DOTA-E{E[c(RGDfK)]$_2$}$_2$ remains to be tested in human patients. Nevertheless, methods to decrease the uptake of radioligand in the kidneys, such as coadministration of cationic amino acids (37) or modifying the structure to render the overall neutral or negatively charged molecule, may be able to minimize long-term damage to this organ if a particle ray-emitting isotope is used for the therapy.

Previous clinical investigations demonstrated the expression of integrin $\alpha_v\beta_3$ in glioma-associated angiogenesis (11). We have also shown that both subcutaneous and orthotopic U87MG glioblastoma xenografts (20,24,26,27) had high level of integrin. However, the subcutaneous tumor model used in this study does not accurately represent the growth, invasion, histology, gene expression profiling, vasculature, and stromal interactions or intracranial tumors.

In addition, the tumor model from the established U87MG glioblastoma cell line does not necessarily reflect the biology, heterogeneity, or therapeutic response of the primary tumor from which it was derived. Genetically accurate animal models for brain tumors such as those described in the Mouse Models of Human Cancers Consortium (MMHCC) (http://emice.nci.nih.gov/) that are more likely to parallel the human situation may be used in the future to test the clinical potential of the tetrameric RGD peptide tracer.

CONCLUSION

[64]Cu-DOTA-E{E[c(RGDfK)]$_2$}$_2$ was shown to bind with high affinity and specificity with integrin-positive U87MG glioma cells in vitro and in vivo and has the right characteristics for further pursuit as an imaging agent with PET. The presumed polyvalency effect and suitable apparent size of this tetrameric RGD peptide tracer make it a superior ligand for integrin targeting in vivo. Although the effectiveness of this copper complex to eradicate integrin-positive tumors was untested, high and prolonged tumor uptake and favorable pharmacokinetics suggest that the this tetrameric RGD peptide tracer has great potential as a clinical PET radiopharmaceutical for imaging tumor integrin expression and as a therapeutic radiopharmaceutical to treat integrin-positive tumors. Because DOTA is a universal chelator capable of forming stable complexes with a variety of metals, such as ^{111}In, [67/68]Ga, [64/67]Cu, [86/90]Y, and ^{177}Lu, the same peptide conjugate used for ^{64}Cu labeling in this study can also be applied to label other radiometals for tumor localization and therapy.

REFERENCES

1. Davis FG, Freels S, Grutsch J, Barlas S, Brem S. Survival rates in patients with primary malignant brain tumors stratified by patient age and tumor histological type: an analysis based on Surveillance, Epidemiology, and End Results (SEER) data, 1973–1991. *J Neurosurg.* 1998;88:1–10.
2. Jemal A, Tiwari RC, Murray T, et al. Cancer statistics, 2004. *CA Cancer J Clin.* 2004;54:8–29.
3. Grossman SA, Batara JF. Current management of glioblastoma multiforme. *Semin Oncol.* 2004;31:635–644.
4. Folkman J. Role of angiogenesis in tumor growth and metastasis. *Semin Oncol.* 2002;29:15–18.
5. Brook PC, Clark RAF, Cheresh DA. Requirement of vascular integrin $\alpha_v\beta_3$ for angiogenesis. *Science.* 1994;264:569–571.
6. Puduvali VK. Inhibition of angiogenesis as a therapeutic strategy against brain tumor. *Cancer Treat Res.* 2004;117:307–336.
7. Friedlander M, Brooks PC, Shiller RW, Kincaid CH, Varner JA, Cheresh DA. Definition of two angiogenic pathways by distinct α_v integrin. *Science.* 1995;270:1500–1502.
8. Horton MA. The $\alpha_v\beta_3$ integrin "vitronectin receptor". *Int J Biochem Cell Biol.* 1997;29:721–725.
9. Brooks PC, Montgomery AM, Rosenfeld M, et al. Integrin $\alpha_v\beta_3$ antagonists promote tumor regression by inducing apoptosis of angiogenic blood vessels. *Cell.* 1994;79:1157–1164.
10. Hwang R, Varner JV. The role of integrins in tumor angiogenesis. *Hematol Oncol Clin North Am.* 2004;18:991–1006.
11. Bello L, Francolini M, Marthyn P, et al. $\alpha_v\beta_3$ and $\alpha_v\beta_5$ integrin expression in glioma periphery. *Neurosurgery.* 2001;49:380–390.
12. Jin H, Varner J. Integrins: roles in cancer development and as treatment targets. *Br J Cancer.* 2004;90:561–565.
13. Kumar CC. Integrin $\alpha_v\beta_3$ as a therapeutic target for blocking tumor-induced angiogenesis. *Curr Drug Targets.* 2003;4:123–131.
14. Sipkins DA, Cheresh DA, Kazemi MR, Nevin LM, Bednarski MD, Li KC. Detection of tumor angiogenesis in vivo by $\alpha_v\beta_3$-targeted magnetic resonance imaging. *Nat Med.* 1998;4:623–626.
15. Ellegala DB, Leong-Poi H, Carpenter JE, et al. Imaging tumor angiogenesis with contrast ultrasound and microbubbles targeted to $\alpha_v\beta_3$. *Circulation.* 2003;108:336–341.
16. Chen X, Conti PS, Moats RA. In vivo near-infrared fluorescence imaging of integrin $\alpha_v\beta_3$ in brain tumor xenografts. *Cancer Res.* 2004;64:8009–8014.
17. Haubner R, Wester HJ. Radiolabeled tracers for imaging of tumor angiogenesis and evaluation of anti-angiogenic therapies. *Curr Pharm Des.* 2004;10:1439–1455.
18. Liu S, Edwards DS, Ziegler MC, Harris AR, Hemingway SJ, Barrett JA. ^{99m}Tc-Labeling of a hydrazinonicotinamide-conjugated vitronectin receptor antagonist useful for imaging tumors. *Bioconjug Chem.* 2001;12:624–629.
19. Chen X, Liu S, Hou Y, et al. MicroPET imaging of breast cancer α_v-integrin expression with ^{64}Cu-labeled dimeric RGD peptides. *Mol Imaging Biol.* 2004;6:350–359.
20. Chen X, Tohme M, Park R, Hou Y, Bading JR, Conti PS. Micro-PET imaging of $\alpha_v\beta_3$-integrin expression with ^{18}F-labeled dimeric RGD peptide. *Mol Imaging.* 2004;3:96–104.
21. Janssen ML, Oyen WJ, Dijkgraaf I, et al. Tumor targeting with radiolabeled $\alpha_v\beta_3$

integrin binding peptides in a nude mouse model. *Cancer Res.* 2002;62:6146–6151.

22. Janssen M, Oyen WJ, Massuger LF, et al. Comparison of a monomeric and dimeric radiolabeled RGD-peptide for tumor targeting. *Cancer Biother Radiopharm.* 2002;17:641–646.

23. Janssen M, Frielink C, Dijkgraaf I, et al. Improved tumor targeting of radiolabeled RGD peptides using rapid dose fractionation. *Cancer Biother Radiopharm.* 2004;19:399–404.

24. Chen X, Park R, Shahinian AH, Bading JR, Conti PS. Pharmacokinetics and tumor retention of ^{125}I-labeled RGD peptide are improved by PEGylation. *Nucl Med Biol.* 2004;31:11–19.

25. Chen X, Park R, Tohme M, Shahinian AH, Bading JR, Conti PS. MicroPET and autoradiographic imaging of breast cancer α_v-integrin expression using ^{18}F- and ^{64}Cu-labeled RGD peptide. *Bioconjug Chem.* 2004;15:41–49.

26. Chen X, Park R, Shahinian AH, et al. ^{18}F-Labeled RGD peptide: initial evaluation for imaging brain tumor angiogenesis. *Nucl Med Biol.* 2004;31:179–189.

27. Chen X, Hou Y, Tohme M, et al. Pegylated Arg-Gly-Asp peptide: ^{64}Cu labeling and PET imaging of brain tumor $\alpha_v\beta_3$-integrin expression. *J Nucl Med.* 2004;45:1776–1783.

28. Chen X, Sievers E, Hou Y, et al. Integrin $\alpha_v\beta_3$-targeted imaging of lung cancer. *Neoplasia.* 2005;7:271–279.

29. Haubner R, Kuhnast B, Mang C, et al. [^{18}F]Galacto-RGD: synthesis, radiolabeling, metabolic stability, and radiation dose estimates. *Bioconjug Chem.* 2004;15:61–69.

30. Sgouros G. Dosimetry of internal emitters. *J Nucl Med.* 2005;46(suppl):18S–27S.

31. Hynes RO. Integrins: bidirectional, allosteric signaling machines. *Cell.* 2002;110:673–687.

32. Haubner R, Wester HJ, Burkhart F, et al. Glycosylated RGD-containing peptides: tracer for tumor targeting and angiogenesis imaging with improved biokinetics. *J Nucl Med.* 2001;42:326–336.

33. Haubner R, Wester HJ, Weber WA, et al. Noninvasive imaging of $\alpha_v\beta_3$ integrin expression using ^{18}F-labeled RGD-containing glycopeptide and positron emission tomography. *Cancer Res.* 2001;61:1781–1785.

34. van Hagen PM, Breeman WA, Bernard HF, et al. Evaluation of a radiolabelled cyclic DTPA-RGD analogue for tumour imaging and radionuclide therapy. *Int J Cancer.* 2000;90:186–198.

35. Logan J. Graphical analysis of PET data applied to reversible and irreversible tracers. *Nucl Med Biol.* 2000;27:661–670.

36. Akizawa H, Arano Y, Mifune M, et al. Effect of molecular charges on renal uptake of ^{111}In-DTPA-conjugated peptides. *Nucl Med Biol.* 2001;28:761–768.

37. Jamar F, Barone R, Mathieu I, et al. ^{86}Y-DOTA-D-Phe^1-Tyr^3-octreotide (SMT487): a phase I clinical study—pharmacokinetics, biodistribution and renal protective effect of different regimens of amino acid co-infusion. *Eur J Nucl Med Mol Imaging.* 2003;30:510–518.

38. International Commission on Radiological Protection. 1990 Recommendations of the International Commission on Radiological Protection: ICRP Publication 60. *Ann ICRP.* 1991;21:6–10.

39. Lewis JS, Lewis MR, Cutler PD, et al. Radiotherapy and dosimetry of ^{64}Cu-TETA-Tyr^3-octreotate in a somatostatin receptor-positive, tumor-bearing rat model. *Clin Cancer Res.* 1999;5:3608–3616.

40. Anderson CJ, Dehdashti F, Cutler PD, et al. ^{64}Cu-TETA-octreotide as a PET imaging agent for patients with neuroendocrine tumors. *J Nucl Med.* 2001;42:213–221.

Near-Infrared Fluorescent RGD Peptides for Optical Imaging of Integrin $\alpha_v\beta_3$ Expression in Living Mice

Zhen Cheng,[†] Yun Wu,[†] Zhengming Xiong,[†,‡] Sanjiv Sam Gambhir,[†] and Xiaoyuan Chen[*,†]

Molecular Imaging Program at Stanford (MIPS), Department of Radiology and Bio-X Program, Stanford University, California, California, 94305-5344, and Department of Pediatrics, Tongji Medical College, Huazhong University of Science and Technology & Tongji Hospital, Wuhan, China, 430030. Received June 14, 2005; Revised Manuscript Received August 25, 2005

Near-infrared fluorescence optical imaging is a powerful technique for studying diseases at the molecular level in preclinical models. We recently reported that monomeric RGD peptide c(RGDyK) conjugated to the NIR fluorescent dye specifically targets integrin receptor both in cell culture and in living subjects. In this report, Cy5.5-conjugated mono-, di-, and tetrameric RGD peptides were evaluated in a subcutaneous U87MG glioblastoma xenograft model in order to investigate the effect of multimerization of RGD peptide on integrin avidity and tumor targeting efficacy. The binding affinities of Cy5.5-conjugated RGD monomer, dimer, and tetramer for $\alpha_v\beta_3$ integrin expressed on U87MG cell surface were determined to be 42.9 ± 1.2, 27.5 ± 1.2, and 12.1 ± 1.3 nmol/L, respectively. All three peptide–dye conjugates had integrin specific uptake both in vitro and in vivo. The subcutaneous U87MG tumor can be clearly visualized with each of these three fluorescent probes. Among them, tetramer displayed highest tumor uptake and tumor-to-normal tissue ratio from 0.5 to 4 h postinjection. Tumor-to-normal tissue ratio for Cy5.5-conjugated RGD monomer, dimer, and tetramer are found to be 3.18 ± 0.16, 2.98 ± 0.05, and 3.63 ± 0.09, respectively, at 4 h postinjection. These results suggest that Cy5.5-conjugated monomeric, dimeric, and tetrameric RGD peptides are all suitable for integrin expression imaging. The multimerization of RGD peptide results in moderate improvement of imaging characteristics of the tetramer, compared to that of the monomer and dimeric counterparts.

INTRODUCTION

Near-infrared fluorescence (NIRF)[1] optical imaging is emerging as a powerful technology for studying diseases at molecular level in small animal models (1–5). Water and biological tissues have minimal absorbance and autofluorescence in the NIR window (650–900 nm), thus allowing efficient photon penetration into, and out of tissue with low intra-tissue scattering. Recent advances in the field of molecular imaging have demonstrated that this technology can be used for monitoring the biological activity of a wide variety of molecular targets such as intracellular enzymes (6–10), cell surface receptors (11–16), and antigens (17–18), as well as other targets (19–20), providing a unique opportunity to achieve insight into the biological events involved with these molecules of interest. Moreover, NIR optical imaging technology is a highly sensitive imaging modality, which does not require use of ionizing radiation or radioactive materials (1–5). It is expected that NIR optical imaging will make a significant impact in disease detection and staging, drug development, and treatment assessment.

The cell adhesion molecule integrin $\alpha_v\beta_3$ is a very important factor involved in angiogenesis and metastasis in many tumor types (20–22). It is found that $\alpha_v\beta_3$ is significantly up-regulated in activated endothelial cells and fast-growing solid tumor cells, compared to its minimum expression in quiescent blood vessels and most normal tissues (22, 23). The ability to noninvasively image the integrin $\alpha_v\beta_3$ expression in living subjects would render a novel approach to diagnose tumor and its metastasis and to help to better understand tumor biology of angiogenesis, as well as to greatly facilitate the development of integrin targeted therapy. For this purpose, numerous molecular probes have been developed for imaging integrin expression using different modalities such as magnetic resonance imaging (24), ultrasound (25–27), optical imaging (28–30), positron emission tomography (PET) (31–40), and single-photon emission computed tomography (SPECT) (41–44).
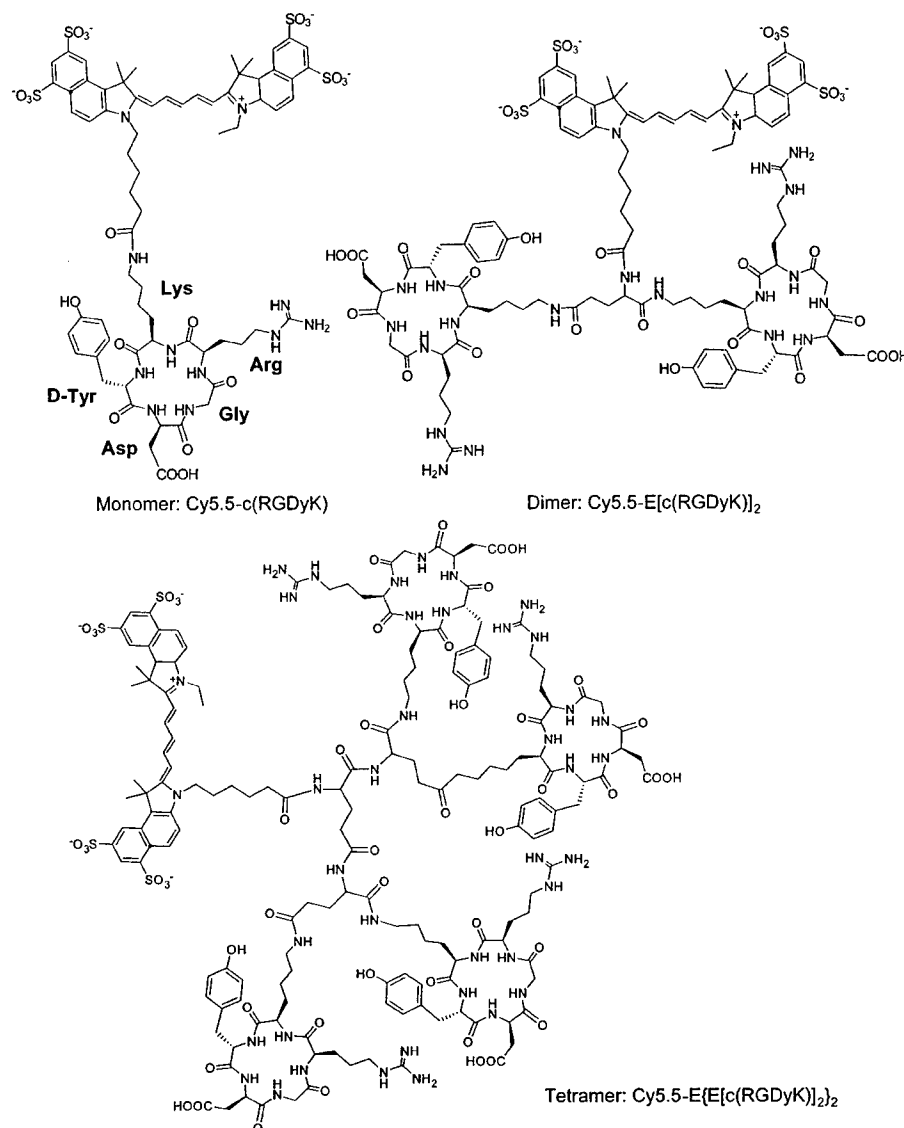
We reported recently that NIRF dye Cy5.5-labeled monomeric arginine-glycine-aspartic acid (RGD) peptide c(RGDyK) specifically targets integrin $\alpha_v\beta_3$ both in cell culture and in living subjects (28). Cy5.5-c(RGDyK), however, had only moderate integrin binding affinity and thus might provide suboptimal tumor targeting efficacy. We and others found that dimeric and multimeric RGD peptides, consisting of multiple cyclic RGD monomer appropriately linked together, have significantly higher integrin avidity than the monomeric counterpart, presumably due to the polyvalency effect (35–37, 43, 44). It was hypothesized that the receptor binding of one RGD cyclic peptide moiety will significantly enhance the "local concentration" of the other RGD peptide moieties in the vicinity of the receptor, which may lead to a faster rate of receptor binding or a slower rate of dissociation of the oligomer from the integrin $\alpha_v\beta_3$ receptor. In this report, we evaluate the effect that multimerization of RGD

* To whom correspondence should be addressed. Phone: (650)725-0950, Fax: (650)736-7925, E-mail: shawchen@stanford.edu.
† Stanford University.
‡ Huazhong University of Science and Technology & Tongji Hospital.

[1] Abbreviations used: NIRF, near-infrared fluorescence; RGD, arginine-glycine-aspartic acid; HPLC, high-performance liquid chromatography; PET, positron emission tomography; SPECT, single photon emission spectroscopy; pi, postinjection.

Figure 1. Schematic structures of Cy5.5-conjugated RGD monomer Cy5.5-c(RGDyK), dimer Cy5.5-E[c(RGDyK)]₂, and tetramer Cy5.5-E{E[c(RGDyK)]₂}₂.

peptide has on integrin binding affinity and tumor targeting efficacy in three novel NIRF probes: Cy5.5-labeled monomer c(RGDyK), dimer E[c(RGDyK)]₂, and tetramer E{E[c(RGDyK)]₂}₂ (structures are shown in Figure 1).

MATERIALS AND METHODS

General. All commercially available chemical reagents were used without further purification. 9-Fluorenyl-methoxycarbonyl (Fmoc) amino acids and 2-chlorotrityl chloride resin were purchased from Novabiochem (San Diego, CA). Arginine and lysine were protected by the 2,2,4,6,7-pentamethyldihydrobenzofuran-5-sulfonyl (Pbf) and *tert*-butoxycarbonyl (Boc) groups, respectively, while D-tyrosine and aspartic acid were protected as a *tert*-butyl ester. Cy5.5 monofunctional *N*-hydroxysuccinimide (NHS) ester (Cy5.5-NHS) and ¹²⁵I-echistatin labeled by the lactoperoxidase method to a specific activity of 2000 Ci/mmol were purchased from Amersham Biosciences (Piscataway, NJ). Echistatin was purchased from Sigma (St. Louis, MO). The purification of the crude product was carried out on a semipreparative reversed-phase high-performance liquid chromatography (HPLC) system

equipped with a 170U 4-Channel UV–Vis absorbance detector (Dionex Summit HPLC system, Dionex Corporation, Sunnyvale, CA) using a Vydac protein and peptide column (218TP510, 5 μm 250 × 10 mm). The flow was 5 mL/min, with the mobile phase starting from 95% solvent A (0.1% TFA in water) and 5% solvent B (0.1% TFA in acetonitrile) (0−3 min) to 35% solvent A and 65% solvent B at 33 min. The analytical HPLC method was performed with the same gradient system, but with a Vydac 218TP54 column (5 μm, 250 × 4.6 mm) and flow rate of 1 mL/min.

Peptide Synthesis. Monomeric cyclic RGD peptide c(RGDyK) (MW = 617.6) was synthesized via solution cyclization of the fully protected linear pentapeptide H-Gly-Asp(OtBu)-D-Tyr(OtBu)-Lys(Boc)-Arg(Pbf)-OH, followed by trifluoroacetic acid (TFA) deprotection (*45*). Dimeric RGD peptide, E[c(RGDyK)]₂, was prepared according to the literature method (*37*). The tetrameric RGD peptide E{E[c(RGDyK)]₂}₂ was obtained by coupling Boc-protected glutamic acid activated ester Boc-E(OSu)₂ with RGD dimer E[c(RGDyK)]₂ in the presence of diiso-propylethylamine (DIPEA) (pH = 8.5−9) followed by semipreparative HPLC purification (*46*).

Cy5.5-RGD Conjugates Synthesis. Appropriate RGD peptide (monomer, dimer, or tetramer) (5 μmol) was dissolved in 1 mL of 0.1 M sodium borate ($Na_2B_4O_7$) buffer (pH = 8.3) and then mixed with 1.2 equiv of Cy5.5-NHS (6.7 mg, 6 μmol) in H_2O (1 mL). The reaction mixture (pH = 8.1) was incubated in the dark at 4 °C overnight and then quenched by adding 200 μL of 5% acetic acid (HOAc). The crude product was purified by a semipreparative reversed-phase HPLC and characterized by an analytical HPLC and matrix-assisted laser desorption/ionization time-of-flight mass spectrometry (MALDI-TOF-MS). α-Cyano-4-hydroxycinnamic acid (α-CHCA, prepared as 10 g/L in 33.3% CH_3CN: 33.3% EtOH: 33.3% H_2O: 0.1% TFA) was used as solid matrix. Fractions containing RGD-Cy5.5 conjugates were collected, lyophilized, redissolved in saline at a concentration of 1 mg/mL, and stored in the dark at −20 °C until use.

U87MG Glioblastoma Xenograft Model. U87MG human glioblastoma cell line was obtained from American Type Culture Collection (Manassas, VA) and was maintained at 37 °C in a humidified atmosphere containing 5% CO_2 in Iscove's modified Dulbecco's medium and 5% fetal bovine serum (Life Technologies, Inc., Grand island, NY). Animal procedures were performed according to a protocol approved by the Stanford University Administrative Panels on Laboratory Animal Care (A-PLAC). Female athymic nude mice (*nu/nu*), obtained from Charles River Laboratories, Inc. (Cambridge, MA) at 4−6 weeks of age, were injected subcutaneously in the right foreleg with 5 × 10⁶ U87MG glioblastoma cells suspended in 100 μL of phosphate-buffered saline (PBS). The tumor bearing mice were subjected to in vivo imaging studies when the tumors reached 0.4−0.6 cm in diameter (14−21 d after implant).

Receptor Binding Assay. The $\alpha_v\beta_3$ receptor binding assay was performed to determine binding affinities of NIR fluorescent RGD conjugates. Briefly, 2 × 10⁵ U87MG cells/well in a 96-well plate were incubated with ¹²⁵I-echistatin (0.06 nM) in the binding buffer [25 mM 2-amino-2-(hydroxymethyl)-1,3-propanediol, hydrochloride (Tris-HCl), pH 7.4, 150 mM NaCl, 1 mM $CaCl_2$, 0.5 mM $MgCl_2$ and 1 mM $MnCl_2$, 0.1% bovine serum albumin (BSA)] in the presence of different concentrations of Cy5.5-RGD conjugates at room temperature for 3 h. After incubation, the plate was washed three times with binding buffer, and the radioactivity was solubilized with 2 N NaOH followed by γ-counting. Nonspecific binding of ¹²⁵I-echistatin to $\alpha_v\beta_3$ was determined in the presence of 100 nM echistatin. The IC_{50} values were calculated by nonlinear regression analysis using the GraphPad Prism computer-fitting program (GraphPad Software, Inc., San Diego, CA). Each data point is a result of the average of triplicate wells.

Fluorescence Microscopic Studies. For fluorescence microscopic studies, 1 × 10⁴ cells were cultured on 35 mm MatTek glass bottom culture dishes (cat. no.: P35G-0-14-C, Ashland, MA). After 24 h, the cells were washed with PBS and then incubated at 37 °C with appropriate Cy5.5-RGD conjugate (10 nM) for 30 min. Integrin specificity of the RGD-Cy5.5 conjugates in cell culture was verified by incubating U87MG cells with or without blocking dose of the nonfluorescent monomeric RGD peptide c(RGDyK) (10 μmol/L). After the incubation period, cells were washed three times with ice-cold PBS. The fluorescence signal of the cells was recorded using an Axiovert 200M fluorescence microscope (Carl Zeiss MicroImaging, Inc., Thornwood, NY) equipped with a Cy5.5 filter set (Exciter, HQ 650/20 nm; Emitter, HQ 675/35 nm). An AttoArc HBO 100W microscopic illuminator

was used as a light source for fluorescence excitation. Images were taken using a thermoelectrically cooled charge-coupled device (CCD) (Micromax, model RTE/CCD-576, Princeton Instruments Inc., Trenton, NJ) and analyzed using MetaMorph Software version 6.2r4 (Molecular Devices Corporation, Downingtown, PA).
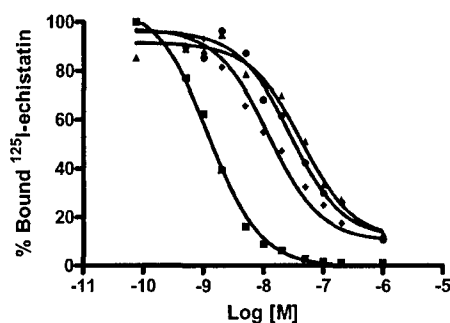
In Vivo Optical Imaging of Tumors. In vivo fluorescence imaging was performed with an IVIS 200 small animal imaging system (Xenogen, Alameda, CA). A Cy5.5 filter set was used for acquiring Cy5.5-conjugated RGD monomer, dimer, and tetramer fluorescence in vivo. Identical illumination settings (lamp voltage, filters, f/stop, field of views, binning) were used for acquiring all images, and fluorescence emission was normalized to photons per second per centimeter squared per steradian (p/s/cm²/sr). Images were acquired and analyzed using Living Image 2.5 software (Xenogen, Alameda, CA). For the control experiment, mice ($n = 3$ for each probe) were injected via tail vein with 500 pmol Cy5.5-RGD (monomer, dimer, or tetramer) and subjected to optical imaging at various time points postinjection (pi). For the blocking experiment, mice ($n = 3$ for each probe also) were injected with the mixture of 10 mg/kg of c(RGDyK) and 500 pmol Cy5.5-conjugated RGD peptides. All NIRF images were acquired using 1 s exposure time (f/stop = 4). The mice in the control experiment were euthanized at 24 h pi. The tumor and major tissues and organs were dissected, wet weighted, and placed on black papers. The fluorescence images were acquired, and total fluorescence flux (p/s/cm²/sr) for each sample was obtained. Aliquots with known amount of the injectates were also put on the black papers and imaged together with the samples. The results were presented as the percentage injected dose per gram (%ID/g). Values were quoted as mean ± standard deviation (SD) for a group of three animals.

Data Processing and Statistics. All the data are given as means ± SD of n independent measurements. Statistical analysis was performed using a Student's t-test. Statistical significance was assigned for P values < 0.05. For determining tumor contrast, mean fluorescence intensities of the tumor area (T) at the right foreleg of the animal and of the area (N) at the right flank (normal tissue) were calculated by the region-of-interest (ROI) function of Living Image software integrated with Igor (Wavemetrics, Lake Oswego, OR). Dividing T by N yielded the contrast between tumor tissue and normal tissue.

RESULTS

Conjugation and Purification of Cy5.5-RGD Conjugates. The synthesis of Cy5.5-RGD conjugates was achieved through conjugation of Cy5.5-NHS ester with the ϵ-amino group of the lysine residue (in case of monomer) or glutamate amine (in the case of dimer and tetramer) of the RGD peptides. The desired products were purified by semipreparative HPLC. The purity of Cy5.5-labeled peptides were over 95% from analytical HPLC analysis. The retention times on analytical HPLC for monomer, dimer, and tetramer are found to be: 15.5, 15.8, and 16.2 min, respectively. The yields of Cy5.5-RGD conjugates were typically over 70%. The purified RGD-Cy5.5 conjugates were characterized by MALDI-TOF-MS. Cy5.5-c(RGDyK) (monomer): m/z = 1518.4 for $[M + H]^+$ ($C_{68}H_{83}N_{11}O_{21}S_4$, Calculated MW= 1518.7); Cy5.5-E[c(RGDyK)]₂ (dimer): m/z = 2249.0 for $[M + H]^+$ ($C_{100}H_{129}N_{21}O_{31}S_4$, calculated MW= 2249.5); Cy5.5-E{E[c(RGDfK]₂}₂ (tetramer): m/z = 3711.8 for $[M + H]^+$ ($C_{165}H_{222}N_{40}O_{51}S_4$, calculated MW = 3710.02); The absorption and fluores-

Figure 2. Competitive integrin receptor assay of unlabeled echistatin (■), monomer Cy5.5-c(RGDyK) (▲), dimer Cy5.5-E[c(RGDyK)]₂ (●), and tetramer Cy5.5-E{E[c(RGDyK)]₂}₂ (◆) to U87MG human glioma cells. All experiments were done in triplicate. The IC_{50} values for echistatin, Cy5.5-monomer, dimer, and tetramer were determined to be 1.2 ± 0.1, 12.1 ± 1.3, 27.5 ± 1.2, and 42.9 ± 1.2 nmol/L, respectively.
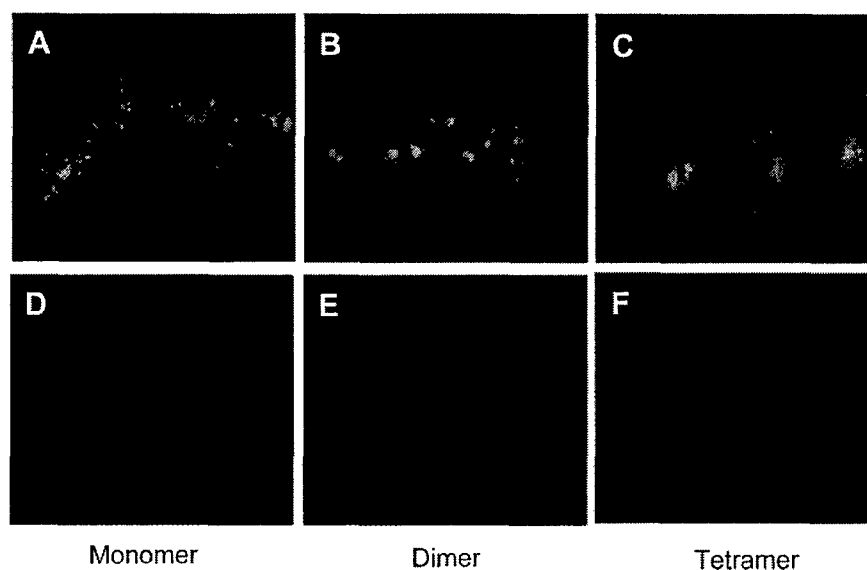
cence emission characteristics of Cy5.5-RGD conjugates were identical to those of free Cy5.5, as apparent from the spectrums measured in H_2O (data not shown).

Integrin Binding Characteristics in Vitro. The receptor binding affinity study of Cy5.5-RGD conjugates for integrin $\alpha_v\beta_3$ was carried out using $\alpha_v\beta_3$ positive U87MG cells. We compared the receptor binding affinity of the three probes by performing competitive displacement studies with ^{125}I-echistatin as radioligand (Figure 2). All the peptides inhibited the binding of ^{125}I-echistatin to U87MG cells in a dose dependent manner. The IC_{50} values for echistatin, Cy5.5-E{E[c(RGDyK)]₂}₂, Cy5.5-E[c(RGDyK)]₂, and Cy5.5-c(RGDyK) were 1.2 ± 0.1, 12.1 ± 1.3, 27.5 ± 1.2, and 42.9 ± 1.2 nmol/L, respectively.

To demonstrate the $\alpha_v\beta_3$ integrin specificity and subcellular localization of the Cy5.5-RGD conjugates, cyanine dye-labeled RGD peptides were incubated with U87MG tumor cells and images taken with a fluorescent microscope. Receptor-mediated endocytosis of the fluorescent dye was observed for all three RGD peptide conjugates (Figure 3 A–C) after 30 min of incubation at 37 °C as indicated by the appearance of fluorescence in the perinuclear region. Integrin receptor specificity of the Cy5.5-
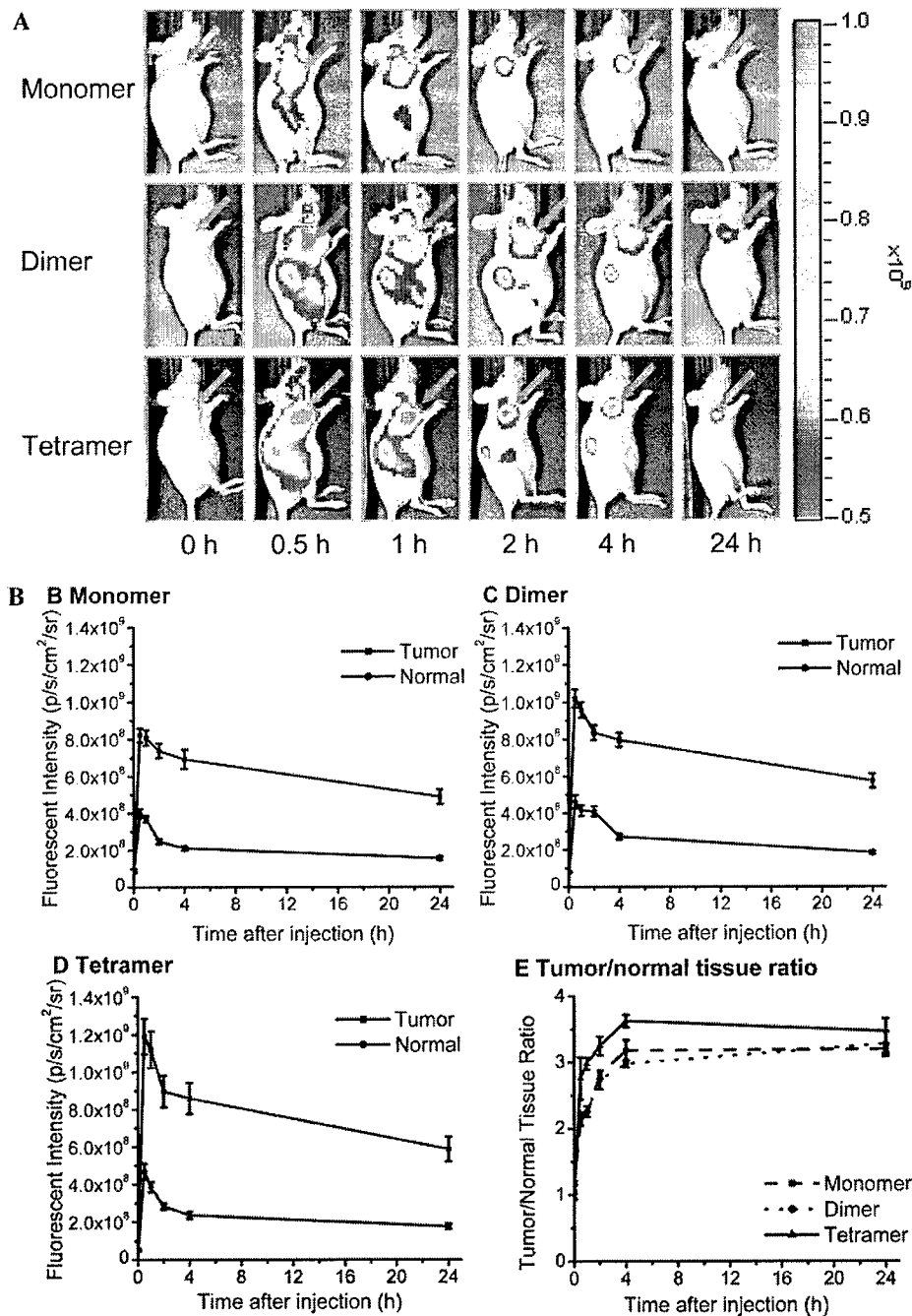
RGD conjugates was further demonstrated by the absence of the cell associated fluorecscence in the presence of a blocking dose of monomeric RGD peptide c(RGDyK) (1 μmol/L) (Figure 3D–F).

Imaging of U87MG Tumor in Vivo. Whole-body imaging of subcutaneous U87MG tumor xenografted mice was accomplished by using tungsten–halogen lamp light source to excite the probe at 610–665 nm wavelength and monitoring the distribution of the imaging agents with IVIS200 system equipped with a cooled charged-coupled device (CCD) camera. Figure 4A shows typical NIRF images of athymic nude mice bearing subcutaneous U87MG glioblastoma tumor after intravenous (iv) injection of 500 pmol of Cy5.5-RGD monomer, dimer, and tetramer, respectively. For all three probes, the subcutaneous U87MG tumor could be clearly visualized from the surrounding background tissue from 30 min to 24 h pi. Quantification analysis of these images was performed using software Living Image2.5. The fluorescence intensities in the tumor and the normal tissues as a function of time for monomer, dimer, and tetramer are depicted in Figure 4B–D, respectively. Monomer, dimer, and tetramer all exhibited fast tumor targeting character in vivo. The tumor uptake reached a maximum at 30 min pi and slowly washed out over time. Most importantly, at early time points (from 0.5 to 4 h) pi, both tetramer and dimer had significantly higher accumulation in tumor than monomer ($P < 0.05$). Tetramer also showed higher tumor uptake than dimer, although the difference is not significant ($P > 0.05$). The differences in tumor uptakes among the three probes were minimal at 24 h pi. The fluorescence intensity ratio between the tumor and normal tissue (T/N) for Cy5.5-conjugated RGD peptides were calculated and shown in Figure 4E. The tetramer shows significantly higher T/N value than both monomer and dimer at early time points (0.5, 1, 2, and 4 h) ($P < 0.05$). For example, T/N ratio for tetramer, dimer, and monomer are found to be 3.63 ± 0.09, 2.98 ± 0.05, and 3.18 ± 0.16, respectively, at 4 h pi, while the difference diminished at 24 h time point ($P > 0.05$). No significant difference in T/N is observed between dimeric and monomeric peptide probes ($P > 0.05$ for all time

Figure 3. Specific binding and endocytosis of the Cy5.5-labeled cyclic RGD peptides. NIRF images of U87MG were obtained after the cells were incubated for 30 min at 37 °C in the presence of 10 nmol/L monomer Cy5.5-c(RGDyK), dimer Cy5.5-E[c(RGDyK)]₂, tetramer Cy5.5-E{E[c(RGDyK)]₂}₂ with (D, E, F) or without (A, B, C) blocking dose of nonfluorescent RGD peptide c(RGDyK) (10 μmol/L). Complete blocking of NIR fluorescence of U87MG cells demonstrating high $\alpha_v\beta_3$ integrin specificity of these NIR dye-labeled RGD peptides.
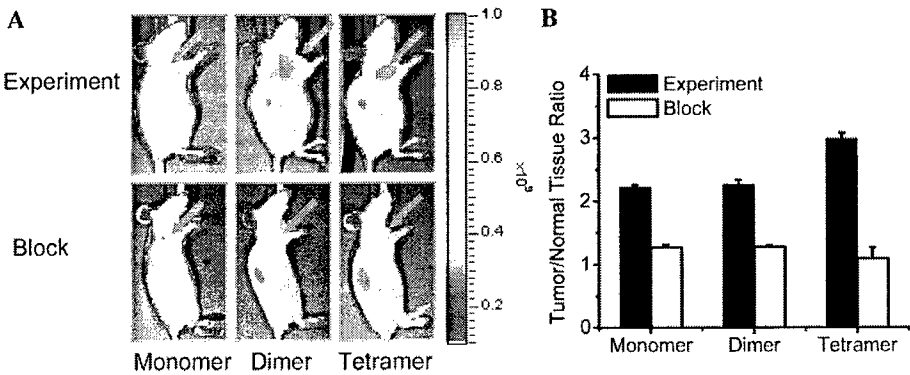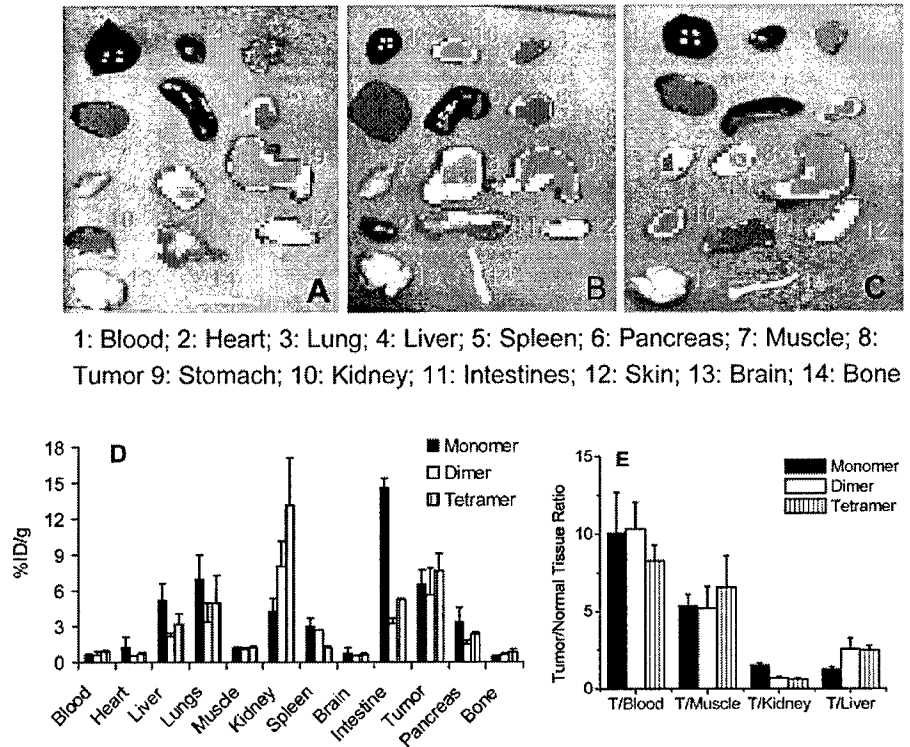
Figure 4. (A) In vivo fluorescence imaging of athymic nude mice bearing subcutaneous U87MG glioblastoma xenografts after intravenous injection of 500 pmol Cy5.5-RGD monomer, dimer, or tetramer. The location of the tumor was indicated by an arrow. Fluorescence signal from Cy5.5 was pseudo-colored red. The tetramer and dimer displayer higher tumor uptake and tumor/normal contrast than that of monomer from 0.5 to 4 h pi (B–D) in vivo targeting characters of Cy5.5-RGD monomer, dimer, and tetramer, respectively. Both tetramer and dimer had significantly higher accumulation in tumor than monomer ($P < 0.05$) at early time points (from 0.5 to 4 h) pi. But the differences in tumor uptakes among the three probes were minimal at 24 h pi. (E) Tumor contrast (tumor-to-normal tissue ratio) as a function of time post-administration of Cy5.5-RGD monomer (■), dimer (●), and tetramer (▲). The fluorescence intensity for the region of interest was recorded as photons per second per centimeter squared per steradian (p/s/cm2/sr). The tumor contrast of Cy5.5-RGD-tetramer from 0.5 to 4 h postinjection is significantly higher than that of Cy5.5-RGD-dimer and monomer ($P < 0.05$).

points examined in this experiment). Kidneys were clearly visualized for dimeric and tetarmeric peptides, indicating that dimer and tetramer have significantly higher renal activity accumulation than the monomer.

Receptor specificities of these probes were validated by a blocking experiment. Unlabeled monomeric RGD peptide, c(RGDyK), successfully reduced tumor contrast for all three tracers (Figure 5). Tumor contrast as quantified by ROI analysis of noninvasive optical imaging

indicated that the T/N was reduced from 2.22 ± 0.04 to 1.27 ± 0.05 for monomer, 2.26 ± 0.27 to 1.28 ± 0.02 for dimer, and 2.98 ± 0.09 to 1.09 ± 0.18 for tetramer, respectively.

To further characterize the distribution of RGD peptide–dye conjugates in U87MG in vivo, the tumor-bearing mice were sacrificed right after noninvasive imaging at 24 h pi. Tumors and other normal organs and tissues were removed and subjected to IVIS200 imaging

Figure 5. Representative NIRF images of mice bearing subcutaneous U87MG tumor on the right foreleg demonstrating blocking of Cy5.5-RGD conjugates (500 pmol) uptake in the tumors by coinjection with 10 mg/kg of c(RGDyK). Pseudo-color fluorescence images of tumor-bearing mice were acquired 1 h after intravenous injection of Cy5.5-RGD conjugates (experiment) or Cy5.5-RGD conjugates + c(RGDyK) (block). (B) Tumor contrast (tumor-to-normal tissue ratio) calculated from region of interest measurement at 1 h postadministration of Cy5.5-RGD conjugates.

1: Blood; 2: Heart; 3: Lung; 4: Liver; 5: Spleen; 6: Pancreas; 7: Muscle; 8: Tumor 9: Stomach; 10: Kidney; 11: Intestines; 12: Skin; 13: Brain; 14: Bone

Figure 6. Representative images of dissected organs of mice bearing U87MG tumor sacrificed 24 h after intravenous injection of Cy5.5-RGD monomer (A), dimer (B), and tetramer (C) at a dose of 500 pmol per mouse. (D) Biodistribution of the probes at 24 h postinjection. (E) Tumor-to-normal organ ratios.

(Figure 6). The total fluorescence of the whole organ was obtained, and %ID/g was calculated for each organ. The biodistribution of the probes at 24 h pi is shown in the Figure 6B. Tumor-to-blood, tumor-to-muscle, tumor-to-kidney, and tumor-to-liver ratios are illustrated in Figure 6C. The renal uptake for tetramer and dimer are much higher than monomer, consistent with the imaging data obtained in living mice. The tumor accumulation and tumor/muscle and tumor/blood ratios for monomer are similar to that of dimer and tetramer. This corroborated the noninvasive imaging data obtained in living mice.

DISCUSSION

NIRF imaging, which uses neither ionizing radiation nor radioactive materials, is emerging as a complement to nuclear imaging methods. A relatively low-cost, safe, and easy-to-use NIRF imaging system has been proven to be a very powerful tool for noninvasive imaging diseases in preclinical models such as rodents (3). Furthermore, NIRF imaging may provide both surgical anatomy and functional/molecular information when exogenous fluorescent probes are used; thus, it has a potential in the clinical setting by allowing easy visualization and guidance in surgery (47). We are very interested in applying this NIRF imaging technique for studying an important molecular target integrin $\alpha_v\beta_3$, so we can better understand tumor angiogenesis and eventually develop methods for integrin-directed tumor therapy. To achieve this goal, a highly specific and sensitive NIRF agent needs to be developed first.

We have previously demonstrated that Cy5.5-labeled monomeric RGD peptide c(RGDyK) targets integrin $\alpha_v\beta_3$-expressed tumor in vivo (28). However, this agent only provides moderate tumor contrast in a highly integrin

positive U87MG tumor model. Cell receptor binding assay using ^{125}I-echistatin as radioligand indicated that the IC_{50} value for c(RGDyK) was approximately 50 nM. Because the cyclic pentatpeptide c(RGDyK) has already been optimized for receptor–ligand interactions (48), it is very unlikely that one can significantly improve receptor avidity of monomeric RGD peptide by fine-tuning of the peptide configuration. An alternative is to apply the concept of multivalency or multimerization and to develop oligomeric RGD peptide probes. In principle, the introduction of a homogeneous multimeric RGD peptide system is expected to improve integrin targeting by cooperative receptor interactions and receptor shield-ing to endogenous competition. We and others have previously reported that suitably labeled dimeric RGD peptide tracers had incremental improvement on tumor targeting efficiency and pharmacokinetics, compared to the monomeric RGD peptide analogues (35–37, 43, 44). We hypothesize that multimerization to introduce tet-rameric RGD peptides might further increase the recep-tor binding affinity. In this study, we designed a new Cy5.5-labeled tetrameric RGD peptide with repeating c(RGDyK) units connected through glutamate linkers (Figure 1). As expected, integrin affinity followed the order of tetramer > dimer > monomer. Fluorescence microscope imaging studies also confirmed the effective-ness of all three probes for integrin positive U87MG cell staining and receptor mediated endocytosis.

We recently radiolabeled DOTA-conjugated RGD mono-mer, dimer, and tetramer with ^{64}Cu and compared their tumor targeting efficacy and in vivo kinetics (33, 37, 46). Tetrameric RGD peptide tracer had almost twice as much tumor uptake than the corresponding dimer. The dimer also had significantly higher tumor uptake than the monomeric counterpart. Renal and hepatic activity ac-cumulation of tetramer was also somewhat higher than that of dimer and monomer. In agreement with these data, we observed significant ($P < 0.05$) increase of tumor fluorescence intensity for Cy5.5-conjugated tetramer and dimer, compared to the monomic analogue at early time points (from 0.5 to 4 h) pi (Figure 4). However, between tetramer and dimer, no significant difference in tumor accumulation is observed. Another important finding in this research is that tetramer demonstrated the highest T/N contrast from 0.5 to 4 h pi (Figure 4). This attribute is apparent from the high tumor uptake and relatively low normal tissue uptake. The monomer displayed low uptake in the tumor, but it was quickly cleared from normal tissue. This results in a moderate T/N contrast. For the dimer, although it showed a higher tumor uptake thanthat of the monomer, the relatively high uptake in normal tissue reduced its T/N contrast. We did not observe significant differences in the magnitude of tumor uptake or T/N contrast at 24 h after administration of the NIRF probes by which most of the tumor uptake has been cleared. Moreover, the tumor uptake of NIRF RGD peptides could be specifically inhibited by the unlabeled c(RGDyK) (Figure 5). This demonstrates that Cy5.5-conjugated monomeric, dimeric, and tetrameric RGD peptides are all specific agents for NIR fluorescence imaging of integrin expression. Overall, these data sug-gest that based on the highest tumor uptake and contrast at early time points pi, the tetramer appears to be the best integrin $\alpha_v\beta_3$ targeting agent among these three compounds. However, only moderate improvement was achieved through multimerization of the peptide strategy. Compared to the monomer, the tetramer only shows 1.20–1.45-fold increase in tumor accumulation and 1.08–1.30-fold increase in T/N ratio at different time points postinjection.

The small animal optical imaging studies above also highlight the importance of evaluation of polyvalency effects of the contrast agents in vivo. Initially we expected that higher tumor uptake, retention, and T/N ratio would be achieved for Cy5.5-labeled RGD multimers due to their increased binding affinities. However, although it was found that the absolute tumor uptake of Cy5.5-labeled RGD probes was generally enhanced with increasing number of RGDs in each probe, multimerization of RGD also changes the molecular size, overall molecular charge, and hydrophilicity of the resulting peptides, thus altering their in vivo pharmacokinetics and clearance from non-target tissues. These results are consistent with the data reported in the literature (43, 46). In both reports, the multimeric RGD peptides showed significantly higher IC_{50} values in vitro and the magnitude of tumor uptake in vivo; however, the improvement of tumor-to-back-ground ratio is marginal. Apparently, for applying the strategy of peptide multimerization extensively and ef-ficiently, more studies are needed to investigate what the essential effects are required to improve the biodistribu-tion and achieve greater targeting selectivity.

Fluorescence intensities of the dissected tumors and normal organs and tissues agreed well with the afore-mentioned in vivo observations, except that the ex vivo tumor-to-muscle ratio was substantially higher than that observed noninvasively, which might be attributed to the minimal loss of excitation and emission of light density without the need of penetration in and out of skin in addition to the scatter caused by the skin. Quantification analysis verified there were no significant differences in tumor/blood and tumor/muscle ratios for these NIRF probes at 24 h pi. Furthermore, both dimer and tetramer had much lower tumor-to-kidney ratios than the mono-mer, likely reflecting the more net positive charge character of the dimer and tetramer than the monomer. The membranes of the renal tabular cells contain nega-tively charged sites to which the positively charged groups (such as guanidines in the RGD sequence) are expected to bind. There is no significant difference in liver uptake of the three probes.

To further optimize the NIRF RGD probes, it also should carefully choose fluorescent labels itself. The emission maximum of Cy5.5 at 694 nm is at the lower limit of NIRF window. It is expected that fluorescent dyes with more red-absorbing character may provide deeper tissue penetration and thus a closer reflection of an actual distribution of the probe in vivo. Another major problem with Cy5.5 dye is the very small Stokes shift (20 nm). Development of fluorescent dyes with a large Stokes shift would provide better fluorescence detection sensitivity by eliminating the interference with the excitation source, minimizing the rejection of excitation light by the emis-sion filter, and reducing the error by excitation light and scattered light. A good alternative to the fluorescent dyes would be quantum dots (QDs) as fluorescent biolabeling reagents. In comparison with organic fluorophores, QDs have unique optical and electronic properties, such as size- and composition-tunable fluorescence emission from visible to NIR wavelengths, a large absorption coefficient across a wide spectral range, and very high level of brightness and photostability (49). Because of their broad excitation profiles and narrow, symmetric emission spec-tra, high-quality QDs are suited for optical multiplexing. Whether conjugation of RGD peptides with novel reporter components such as fluorescent dyes with a large Stokes

shift or QDs could generate better NIRF imaging agents for integrin $\alpha_v\beta_3$ requires further investigation.

Initially we also expected that NIRF imaging using Cy5.5-labeled RGD peptides might provide the opportunity for rapid and cost-effective structure–activity studies to screen newly developed ligands, rather than the more costly radionuclide-based imaging studies such as SPECT and PET. However, this hypothesis oversimplifies the complex effect that a fairly bulky Cy 5.5 label has on the pharmacokinetics of a probe. The in vivo behavior is the combination of many factors, including, but not limited, to the receptor affinity and specificity, molecular size, overall molecular charge, hydrophilicity, and metabolic stability. Cy5.5 is a rather large chromophore with a molecular weight of ca. 1000. Tumor contrast obtained with a Cy5.5-RGD conjugate may not truly reflect the same RGD peptide labeled with a radionuclide. Additional studies to evaluate the impact of cyanine dye structure on the receptor targeting properties of RGD peptide in vivo is needed to elucidate the discrepancy between NIRF imaging and radionuclide imaging.

CONCLUSION

Cy5.5-RGD monomer, dimer, and tetramer all exhibit specific uptake in the U87MG glioblastoma both in vitro and in vivo. Among these three probes, Cy5.5-RGD tetramer displays the highest tumor uptake and tumor-to-background ratio up to 4 h postinjection and as such appears to be the most promising probe for integrin receptor NIRF imaging. However, the improvement of imaging character of tetramer is only moderate, compared to that of monomer. More research is needed to further optimize such probes.

ACKNOWLEDGMENT

LITERATURE CITED

(1) Massoud, T. F., and Gambhir, S. S. (2003) Molecular imaging in living subjects: seeing fundamental biological processes in a new light. *Genes Dev. 17*, 545–80.

(2) Sevick-Muraca, E. M., Houston, J. P., and Gurfinkel, M. (2002) Fluorescence-enhanced, near infrared diagnostic imaging with contrast agents. *Curr. Opin. Chem. Biol. 6*, 642–50.

(3) Ntziachristos, V., Bremer, C., and Weissleder, R. (2003) Fluorescence imaging with near- infrared light: new technological advances that enable in vivo molecular imaging. *Eur. Radiol. 13*, 195–208.

(4) Tung, C. H. (2004) Fluorescent peptide probes for in vivo diagnostic imaging. *Biopolymers 76*, 391–403.

(5) Weissleder, R., and Mahmood, U. (2001) Molecular imaging. *Radiology 219*, 316–33.

(6) Weissleder, R., Tung, C. H., Mahmood, U., and Bogdanov, A., Jr. (1999) In vivo imaging of tumors with protease-activated near-infrared fluorescent probes. *Nat. Biotechnol. 17*, 375–8.

(7) Tung, C. H., Mahmood, U., Bredow, S., and Weissleder, R. (2000) In vivo imaging of proteolytic enzyme activity using a novel molecular reporter. *Cancer Res. 60*, 4953–8.

(8) Tung, C. H., Zeng, Q., Shah, K., Kim, D. E., Schellingerhout, D., and Weissleder, R. (2004) In Vivo Imaging of β-Galactosidase Activity Using Far Red Fluorescent Switch. *Cancer Res. 64*, 1579–83.

(9) Wunder, A., Tung, C. H., Muller-Ladner, U., Weissleder, R., and Mahmood, U. (2004) In vivo imaging of protease activity in arthritis: a novel approach for monitoring treatment response. *Arthritis Rheum. 50*, 2459–65.

(10) Mahmood U., and Weissleder, R. (2003) Near-Infrared Optical Imaging of Proteases in Cancer. *Mol. Cancer Ther. 2*, 489–496.

(11) Ke, S., Wen, X., Gurfinkel, M., Charnsangavej, C., Wallace, S., Sevick-Muraca, E. M., and Li, C. (2003) Near-infrared optical imaging of epidermal growth factor receptor in breast cancer xenografts. *Cancer Res. 63*, 7870–5.

(12) Moon, W. K., Lin, Y., O'Loughlin, T., Tang, Y., Kim, D. E, Weissleder, R., and Tung, C. H. (2003) Enhanced tumor detection using a folate receptor-targeted near-infrared fluorochrome conjugate. *Bioconjugate Chem. 14*, 539–45.

(13) Licha, K., Hessenius, C., Becker, A., Henklein, P., Bauer, M., Wisniewski, S., Wiedenmann, and B., Semmler, W. (2001) Synthesis, characterization, and biological properties of cyanine-labeled somatostatin analogues as receptor-targeted fluorescent probes. *Bioconjugate Chem. 12*, 44–50.

(14) Achilefu, S., Jimenez, H. N., Dorshow, R. B., Bugaj, J. E., Webb, E. G., Wilhelm, R. R., Rajagopalan, R., Johler, J., and Erion, J. L. (2002) Synthesis, in vitro receptor binding, and in vivo evaluation of fluorescein and carbocyanine peptide-based optical contrast agents. *J. Med. Chem. 45*, 2003–15.

(15) Achilefu, S., Dorshow, R. B., Bugaj, J. E., and Rajagopalan, R. (2000) Novel receptor-targeted fluorescent contrast agents for in vivo tumor imaging. *Invest. Radiol. 35*, 479–85.

(16) Bugaj, J. E., Achilefu, S., Dorshow, R. B., and Rajagopalan, R. (2001) Novel fluorescent contrast agents for optical imaging of in vivo tumors based on a receptor- targeted dye-peptide conjugate platform. *J. Biomed. Opt. 6*, 122–133.

(17) Moore, A., Medarova, Z., Potthast, A., and Dai, G. (2004) In vivo targeting of underglycosylated MUC-1 tumor antigen using a multimodal imaging probe. *Cancer Res. 64*, 1821–7.

(18) Ballou, B., Fisher, G. W., Hakala, T. R., and Farkas, D. L. (1997) Tumor detection and visualization using cyanine fluorochrome-labeled antibodies. *Biotechnol. Prog. 13*, 649–58.

(19) Zaheer, A., Lenkinski, R. E., Mahmood, A., Jones, A. G., Cantley, L. C, and Frangioni, J. V. (2001) In vivo near-infrared fluorescence imaging of osteoblastic activity. *Nat. Biotechnol. 19*, 1148–54.

(20) Ntziachristos, V., Schellenberger, E. A., Ripoll, J., Yessayan, D., Graves, E., Bogdanov, A., Jr., Josephson, L., and Weissleder R. (2004) Visualization of antitumor treatment by means of fluorescence molecular tomography with an annexin V–Cy5.5 conjugate. *Proc. Natl. Acad. Sci. U.S.A. 101*, 12294–9.

(21) Jin, H., and Varner, J. (2004) Integrins: roles in cancer development and as treatment targets. *Br. J. Cancer 90*, 561–5.

(22) Cairns, R. A., Khokha, R., and Hill, R. P. (2003) Molecular mechanisms of tumor invasion and metastasis: an integrated view. *Curr. Mol. Med. 3*, 659–71.

(23) Felding-Habermann, B. (2003) Integrin adhesion receptors in tumor metastasis. *Clin. Exp. Metastasis 20*, 203–13.

(24) Schmieder, A. H., Winter, P. M., Caruthers, S. D., Harris, T. D., Williams, T. A., Allen, J. S., Lacy, E. K., Zhang, H., Scott, M. J., Hu, G., Robertson, J. D, Wickline, S. A., and Lanza, G. M. (2005) Molecular MR imaging of melanoma angiogenesis with $\alpha_v\beta_3$-targeted paramagnetic nanoparticles. *Magn. Reson. Med. 53*, 621–7.

(25) Ellegala, D. B., Leong-Poi, H., Carpenter, J. E., Klibanov, A. L., Kaul, S., Shaffrey, M. E., Sklenar, J., and Lindner, J. R. (2003) Imaging tumor angiogenesis with contrast ultrasound and microbubbles targeted to $\alpha_v\beta_3$. *Circulation 108*, 336–41.

(26) Leong-Poi, H., Christiansen, J., Klibanov, A. L., Kaul, S., and Lindner, J. R. (2003) Noninvasive assessment of angiogenesis by ultrasound and microbubbles targeted to $\alpha_v\beta_3$-integrins. *Circulation 107*, 455–60.

(27) Dayton, P. A., Pearson, D., Clark, J., Simon, S., Schumann, P. A., Zutshi, R., Matsunaga, T. O., and Ferrara, K. W. (2004) Ultrasonic analysis of peptide- and antibody-targeted microbubble contrast agents for molecular imaging of $\alpha_v\beta_3$-expressing cells. *Mol. Imaging 3*, 125–34.

(28) Chen, X., Conti, P. S., and Moats, R. A. (2004) In vivo near-infrared fluorescence imaging of integrin $\alpha_v\beta_3$ in brain tumor xenografts. *Cancer Res. 64*, 8009–14.

(29) Wang, W., Ke, S., Wu, Q., Charnsangavej, C., Gurfinkel, M., Gelovani, J. G., Abbruzzese, J. L., Sevick-Muraca, E. M., and Li, C. (2004) Near-infrared optical imaging of integrin $\alpha_v\beta_3$ in human tumor xenografts. *Mol. Imaging 3*, 343–51.

(30) Achilefu, S., Bloch, S., Markiewicz, M. A., Zhong, T., Ye, Y., Dorshow, R. B., Chance, B., and Liang, K. (2005) Synergistic effects of light-emitting probes and peptides for targeting and monitoring integrin expression. *Proc. Natl. Acad. Sci. U.S.A. 102*, 7976–81.

(31) Chen, X., Park, R., Shahinian, A. H., Tohme, M., Khankaldyyan, V., Bozorgzadeh, M. H., Bading, J. R., Moats, R., Laug, W. E., and Conti, P. S. (2004) ^{18}F-labeled RGD peptide: initial evaluation for imaging brain tumor angiogenesis. *Nucl. Med. Biol. 31*, 179–89.

(32) Chen, X., Hou, Y., Tohme, M., Park, R., Khankaldyyan, V., Gonzales-Gomez, I., Bading, J. R., Laug, W. E., and Conti, P. S. (2004) Pegylated Arg-Gly-Asp peptide: ^{64}Cu labeling and PET imaging of brain tumor $\alpha_v\beta_3$-integrin expression. *J. Nucl. Med. 45*, 1776–83.

(33) Chen, X., Park, R., Tohme, M., Shahinian, A. H., Bading, J. R., and Conti, P. S. (2004) MicroPET and autoradiographic imaging of breast cancer α_v-integrin expression using ^{18}F- and ^{64}Cu-labeled RGD peptide. *Bioconjug. Chem. 15*, 41–9.

(34) Chen, X., Park, R., Hou, Y., Khankaldyyan, V., Gonzales-Gomez, I., Tohme, M., Bading, J. R., Laug, W. E., and Conti, P. S. (2004) MicroPET imaging of brain tumor angiogenesis with ^{18}F-labeled PEGylated RGD peptide. *Eur. J. Nucl. Med. Mol. Imaging 31*, 1081–9.

(35) Chen, X., Sievers, E., Hou, Y., Park, R., Tohme, M., Bart, R., Bremner, R., Bading, J. R., and Conti, P. S. (2005) Integrin $\alpha_v\beta_3$-targeted imaging of lung cancer *Neoplasia 7*, 271–9.

(36) Chen, X., Tohme, M., Park, R., Hou, Y., Bading, J. R., and Conti, P. S. (2004) Micro-PET imaging of $\alpha_v\beta_3$-integrin expression with ^{18}F-labeled dimeric RGD peptide. *Mol. Imaging 3*, 96–104.

(37) Chen, X., Liu, S., Hou, Y., Tohme, M., Park, R., Bading, J. R., and Conti, P. S. (2004) MicroPET imaging of breast cancer α_v-integrin expression with ^{64}Cu-labeled dimeric RGD peptides. *Mol. Imaging Biol. 6*, 350–9.

(38) Haubner, R., Kuhnast, B., Mang, C., Weber, W. A., Kessler, H., Wester, H. J., and Schwaiger, M. (2004) [^{18}F]Galacto-RGD: synthesis, radiolabeling, metabolic stability, and radiation dose estimates. *Bioconjugate Chem. 15*, 61–9.

(39) Haubner, R., Wester, H. J., Weber, W. A., Mang, C., Ziegler, S. I., Goodman, S. L., Senekowitsch-Schmidtke, R., Kessler, H., and Schwaiger, M. (2001) Noninvasive imaging of $\alpha_v\beta_3$ integrin expression using ^{18}F-labeled RGD-containing glycopeptide and positron emission tomography. *Cancer Res. 61*, 1781–5.

(40) Haubner, R., Weber, W. A., Beer, A. J., Vabuliene, E., Reim, D., Sarbia, M., Becker, K. F., Goebel, M., Hein, R., Wester, H. J., Kessler, H., and Schwaiger, M. (2005) Noninvasive Visualization of the Activated $\alpha_v\beta_3$ Integrin in Cancer Patients by Positron Emission Tomography and [^{18}F]Galacto-RGD. *PLoS Med. 2*, 0244–51.

(41) Sadeghi, M. M., Krassilnikova, S., Zhang, J., Gharaei, A. A., Fassaei, H. R., Esmailzadeh, L., Kooshkabadi, A., Edwards, S., Yalamanchili, P., Harris, T. D., Sinusas, A. J., Zaret, B. L., and Bender, J. R. (2004) Detection of injury-induced vascular remodeling by targeting activated $\alpha_v\beta_3$ integrin in vivo. *Circulation 110*, 84–90.

(42) Meoli, D. F., Sadeghi, M. M., Krassilnikova, S., Bourke, B. N., Giordano, F. J., Dione, D. P., Su, H., Edwards, D. S., Liu, S., Harris, T. D., Madri, J. A., Zaret, B. L., and Sinusas, A. J. (2004) Noninvasive imaging of myocardial angiogenesis following experimental myocardial infarction. *J. Clin. Invest. 113*, 1684–91.

(43) Janssen, M., Oyen, W. J., Massuger, L. F., Frielink, C., Dijkgraaf, I., Edwards, D. S., Radjopadhye, M., Corstens, F. H., and Boerman, O. C.(2002) Comparison of a Monomeric and dimeric radiolabeled RGD-peptide for tumor targeting. *Cancer Biother. Radiopharm. 17*, 641–6.

(44) Janssen, M. L., Oyen, W. J., Dijkgraaf, I., Massuger, L. F., Frielink, C., Edwards, D. S., Rajopadhye, M., Boonstra, H., Corstens, F. H., and Boerman, O. C. (2002) Tumor targeting with radiolabeled $\alpha_v\beta_3$ integrin binding peptides in a nude mouse model. *Cancer Res. 62*, 6146–51.

(45) Chen, X., Park, R., Shahinian, A. H., Bading, J. R., and Conti, P. S. (2004) Pharmacokinetics and tumor retention of ^{125}I-labeled RGD peptide are improved by PEGylation. *Nucl. Med. Biol. 31*, 11–9.

(46) Wu, Y., Zhang, X., Xiong, Z., Cheng, Z., Fisher, D. R., Liu, S., Gambhir, S. S., and Chen, X. (2005) MicroPET Imaging of Glioma α_v-Integrin Expression Using ^{64}Cu Labeled Tetrameric RGD Peptide. *J. Nucl. Med. 46*, Accepted.

(47) Nakayama, A., del Monte, F., Hajjar, R. J., and Frangioni, J. V. (2002) Functional near-infrared fluorescence imaging for cardiac surgery and targeted gene therapy. *Mol. Imaging 1*, 365–77.

(48) Xiong, J. P., Stehle, T., Zhang, R., Joachimiak, A., Frech, M., Goodman, S. L., and Arnaout, M. A. (2002) Crystal structure of the extracellular segment of integrin $\alpha_v\beta_3$ in complex with an Arg-Gly-Asp ligand. *Science 296*, 151–5.

(49) Gao, X., and Nie, S. (2005) Quantum dot-encoded beads. *Methods Mol. Biol. 303*, 61–72.

Multimodality tumor imaging targeting integrin $\alpha_v\beta_3$

Weibo Cai, Sanjiv Sam Gambhir, and Xiaoyuan Chen

Stanford University School of Medicine, Stanford, CA, USA

The cell adhesion molecule integrin $\alpha_v\beta_3$ is an important player in the process of tumor angiogenesis and metastasis. Antibodies, peptides, peptidomimetics, and small molecule antagonists against integrin $\alpha_v\beta_3$ have been shown to induce endothelial apoptosis, to inhibit tumor angiogenesis, and to increase endothelial permeability. The ability to quantitatively image integrin $\alpha_v\beta_3$ expression in vivo in a noninvasive manner may shed new light into the mechanism of angiogenesis and antiangiogenic treatment efficacy based on integrin antagonism. Tumor integrin expression imaging will also aid in lesion detection, patient stratification, new anti-integrin drug development/validation, as well as treatment monitoring and optimization. This review summarizes the recent advances in multimodality imaging of tumor integrin $\alpha_v\beta_3$ expression using magnetic resonance imaging (MRI), ultrasound, near-infrared (NIR) fluorescence, single photon emission computed tomography (SPECT), and positron emission tomography (PET).

INTRODUCTION

Molecular Imaging

Molecular imaging refers to the characterization and measurement of biological processes at the molecular level (1,2). Conventional imaging modalities that detect anatomical and functional changes of tumor vascularity during angiogenesis, tumor growth, and upon antiangiogenic treatment provide little or no information regarding the specific molecular markers on newly formed blood vessels, tumor cells, and the molecular changes upon therapy. Molecular imaging takes advantage of traditional diagnostic imaging techniques and introduces molecular probes to determine the expression of indicative molecular markers of the tumor development at different stages (2–4). Detection of these molecular markers permits much earlier diagnosis, earlier treatment, and better prognosis. Subsequent profiling to identify suitable treatment targets could lead to individualized therapy and treatment monitoring. Molecular imaging technologies include, but are not limited to, positron emission tomography (PET), single photon emission computed tomography (SPECT), magnetic resonance imaging (MRI), magnetic resonance spectroscopy (MRS), optical bioluminescence, optical fluorescence, and ultrasound (2,5). In computed tomography (CT), the images are obtained because tissues absorb X-rays differently as they pass through the body, therefore providing mainly anatomical information. Since CT signal is rarely specific at the molecular level, it will not be discussed here.

Since many tumors are quite heterogeneous, tissue sampling does not always represent the biochemical or pathological processes of the disease. Furthermore, temporal studies usually need large numbers of animals to be sacrificed at various time points to obtain statistically significant results. Noninvasive imaging of genetic and cellular processes at the molecular level will compliment the established ex vivo molecular biological assays and provide both spatial and temporal dimensions to our understanding of various diseases. Two prerequisites need to be satisfied in order to image and quantify biological processes in vivo noninvasively: *(i)* a probe composed of a label that can be detected with high sensitivity and a ligand that binds specifically and with high affinity to the target and *(ii)* a sensitive, high-resolution imaging instrument to detect the signal noninvasively. In this review, we will highlight the recent advances in developing molecular imaging probes and techniques targeting a tumor-specific molecular marker, integrin $\alpha_v\beta_3$.

Tumor Angiogenesis and Metastasis

Angiogenesis, the formation of new blood vessels from preexisting blood vessels, is a fundamental process occurring during tumor progression (6). Angiogenesis depends on the balance between pro-angiogenic molecules [vascular endothelial growth factor (VEGF), fibroblast growth factor (FGF), epidermal growth factor (EGF)] and antiangiogenic molecules (angiostatin, endostatin) (7,8). The fact that tumors are dependent on blood supply has inspired many scientists to search for antiangiogenic molecules and to design antiangiogenic strategies for cancer treatment and prevention of cancer recurrence and metastasis (9–11). Tumor angiogenesis differs significantly from physiological angiogenesis. The differences include aberrant vascular structure, altered endothelial cell-pericyte interactions, abnormal blood flow, increased permeability, and delayed maturation (6,12). Most tumors start growing as avascular dormant nodules until they reach a steady-state level of proliferating and apoptosing cells. Angiogenesis begins with perivascular detachment and vessel dilation, followed by angiogenic sprouting, new vessel formation and maturation, and the recruitment of perivascular cells. Blood-vessel formation continues as the tumor grows, feeding on hypoxic and necrotic areas of the tumor for essential nutrients and oxygen.

Cancer cells spread throughout the body by metastasis (13–16). Metastasis occurs through several steps. First, cancer cells lose E-cadherin-dependent intercellular adhesions, acquire a migratory phenotype, detach from neighboring cells, penetrate the basement membrane, and invade the interstitial matrix. Second, tumor cells penetrate into blood vessels and lymphatic vessels and enter the circulatory system, a process called intravasation. After reaching the bloodstream, tumor cells often adhere to platelets and leukocytes, forming emboli that stop in the microcirculation of target organs more easily than individual tumor cells. Finally, metastatic cells exit the bloodstream (extravasation) and undergo expansive growth within the parenchyma of the target organ.

Role of Integrin $\alpha_v\beta_3$ During Tumor Progression

Molecules regulating angiogenesis include growth factor receptors, tyrosine kinase receptors, G protein-coupled receptors for angiogenesis modulating proteins, and integrins (6–8). Integrins are a family of adhesion molecules consisting of two noncovalently bound transmembrane subunits (α and β), both type I membrane proteins with large extracellular segments that pair to create heterodimers with distinct adhesive capabilities (17,18). In mammals, 18 α and 8 β subunits assemble into 24 different receptors. Increasing amounts of evidence now imply that integrin signaling plays a key role in tumor angiogenesis and metastasis (19–21). Integrins expressed on endothelial cells modulate cell migration and survival during angiogenesis, while integrins expressed on carcinoma cells potentiate metastasis by facilitating invasion and movement across blood vessels. Efficient tumor invasion requires partial degradation of the extracellular matrix (ECM) at the invasion front. The matrix metalloproteinases (MMPs)

are the major proteases involved in remodeling the ECM (15). The $\alpha_v\beta_3$ integrin, which binds to arginine-glycine-aspartic acid (RGD)-containing components of the interstitial matrix, such as vitronectin, fibronectin, and thrombospondin, is significantly up-regulated on endothelium during angiogenesis but not on quiescent endothelium (21–23). The special role of integrin $\alpha_v\beta_3$ in tumor invasion and metastasis arises from its ability to recruit and activate MMP-2 and plasmin, which degrade components of the basement membrane and interstitial matrix (24). Research has shown that tumor expression of integrin $\alpha_v\beta_3$ correlates well with tumor progression in several malignancies such as melanoma (25), glioma (26), ovarian cancer (27), and breast cancer (28,29). Inhibition of αv integrin activity by monoclonal antibodies (MAbs), cyclic RGD peptide antagonists, and peptidomimetics has also been shown to induce endothelial cell apoptosis (30), to inhibit angiogenesis (20), and to increase endothelial monolayer permeability (31).

Integrin $\alpha_v\beta_3$ as the Imaging Target

For a targeting approach aimed at monitoring tumor angiogenesis and metastasis, the sufficient level of accessible tumor specific targets is essential for the detection and delineation of lesions from background by imaging technologies. Integrin $\alpha_v\beta_3$, the most extensively studied in the integrin family, serves as an excellent molecular marker for tumor angiogenesis and metastasis imaging, since it is not readily detectable in quiescent vessels but becomes highly expressed in angiogenic vessels (19). The ability to noninvasively visualize and quantify integrin $\alpha_v\beta_3$ expression level will provide new opportunities to document tumor (tumor cells and sprouting tumor vasculature) integrin expression, to more appropriately select patients for anti-integrin treatment, and to monitor treatment efficacy in integrin-positive patients. Several review articles on tumor angiogenesis imaging have partially covered some integrin targeting approaches (32,33). In this review article, recent advances in both nonradionuclide (MRI, ultrasound, and optical) and radionuclide imaging (SPECT and PET) of tumor integrin $\alpha_v\beta_3$ will be summarized.

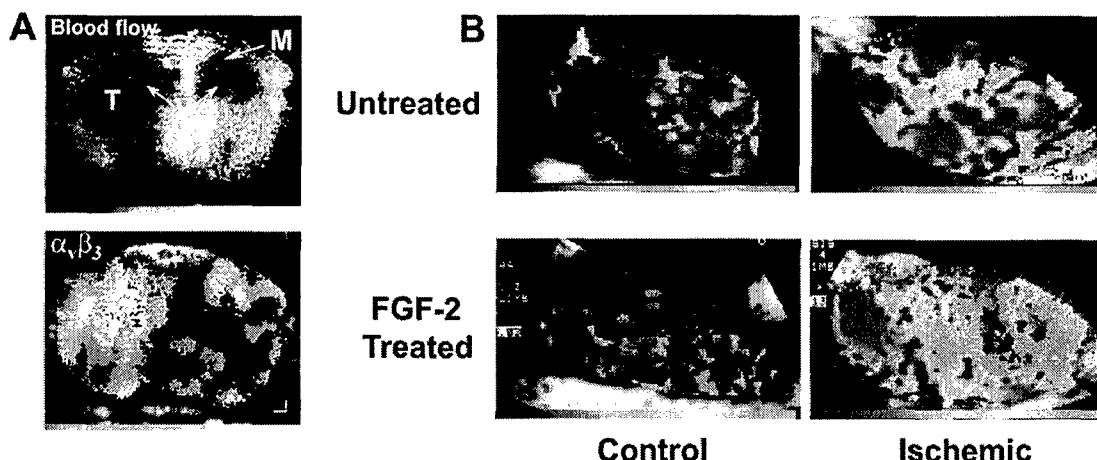## NONRADIONUCLIDE IMAGING OF INTEGRIN $\alpha_v\beta_3$ EXPRESSION

Magnetic Resonance Imaging

The major advantage of MRI over radionuclide or optical imaging is its higher spatial resolution (usually submillimeter level). However, MRI is many orders of magnitude less sensitive than radionuclide and optical techniques, which means that much larger amounts of molecular probes must be retained at the target for detectable MRI signal (34). High mass amounts of probe can be toxic, and this must be carefully studied before any MRI probe is translated into the clinic. The inherent low sensitivity of MRI can be only partially compensated by working at relatively high magnetic fields (4.7–14 T), using hardware and software dedicated to small animal imaging and much longer acquisition times during imaging.

In an animal model, Sipkins et al. first demonstrated the use of antibody-coated paramagnetic liposomes (300–350 nm in diameter) containing Gd3+ for MRI imaging of integrin $\alpha_v\beta_3$ expression (35). Imaging of a rabbit model of squamous cell carcinomas (V2) was achieved by directly targeting paramagnetic agents to the angiogenic vasculature using LM609, a mouse anti-human integrin $\alpha_v\beta_3$ MAb. Anderson et. al. (36) also reported site-directed contrast enhancement of angiogenic vessels in vivo using antibody-coated MRI contrast agent. The targeted contrast agent consists of Gd-perfluorocarbon nanoparticles conjugated to integrin $\alpha v\beta3$ antibody DM101 (400–700 nm in diameter). The study was carried out in a rabbit corneal micropocket model, where neovasculature was induced in the cornea using basic FGF. However, only a modest increase (<25%) in the average MR signal intensity was observed after 90 min.

Winter et al. attached peptidomimetic integrin $\alpha_v\beta_3$ antagonist to magnetic nanoparticles for MRI imaging under common clinical field strength of 1.5 T (37,38). Two animal models were used, New Zealand white rabbits implanted with Vx-2 tumors and an atherosclerosis model. In the Vx-2 model, integrin $\alpha_v\beta_3$-targeted paramagnetic nanoparticles increased MRI signal dramatically in the periphery of the tumor at 2 h postinjection (p.i.). Similar increases in MR contrast were also observed within the walls of some vessels proximate to the tumor. Despite the relatively large size (about 270 nm in diameter), these nanoparticles penetrated into the leaky tumor neovasculature but did not migrate into the interstitium in an appreciable amount, since only marginal increase in MR signal was observed at 2 h (characteristic of passive targeting rather than integrin-specific targeting). Immunohistochemistry of integrin $\alpha_v\beta_3$ confirmed the extent and distribution of neovascularity observed by MRI. In the atherosclerosis model, enhancement in the MRI signal was also observed among rabbits that received integrin-targeted nanoparticles. Histology and immunohistochemistry confirmed the

Figure 1. (A) (Top) contrast-enhanced ultrasound (CEU) images from a rat 28 days after U87MG implantation using nontargeted microbubbles. Tumor (T), ventricles (V), and a periventricular metastasis (M) are pointed out. (Bottom) Signal enhancement from integrin $\alpha_v\beta_3$-targeted microbubbles. (B) Color-coded CEU images of integrin $\alpha_v\beta_3$-targeted microbubbles in control (left) and ischemic (right) proximal hind limb adductor muscles from untreated (top) and fibroblast growth factor 2 (FGF-2) treated (bottom) rat 4 days after iliac artery ligation. Adapted from References 40 and 42.

proliferation of angiogenic vessels within the aortic adventitia of the atherosclerotic rabbits as compared with control animals. Since this integrin-targeting nanoparticle system can carry a variety of drugs in its lipid membrane, it may have potential for simultaneous molecular imaging and site-directed drug delivery for early atherosclerotic disease.

Very recently, athymic nude mice bearing human melanoma tumors were also imaged using systemically injected $\alpha_v\beta_3$ integrin-targeted paramagnetic nanoparticles (25). Contrast enhancement of neovascularity in animals that received targeted nanoparticles increased significantly by 2 h as compared with nontargeted paramagnetic nanoparticles. MRI results were also supported by histology. This technique may be employed to noninvasively detect small regions of angiogenesis associated with nascent melanoma tumors, as well as to phenotype and to stage other integrin-positive tumors in a clinical setting.

In all these studies, the targeted paramagnetic nanoparticles are coated with either antibodies or small peptidic/peptidomimetic integrin $\alpha_v\beta_3$ antagonists. Coating the paramagnetic nanoparticles with peptides or peptidomimetics is potentially better than antibodies, since hundreds even thousands of peptides/peptidomimetics can be attached to the nanoparticles, which leads to much higher local concentration of the ligand and higher binding affinity. Moreover, not only do antibodies add to the already large size of the nanoparticle contrast agents, antibody-coated contrast agents also stay in the circulation system much longer while peptide- or peptidomimetics-coated contrast agents home to the target faster and that gives better contrast.
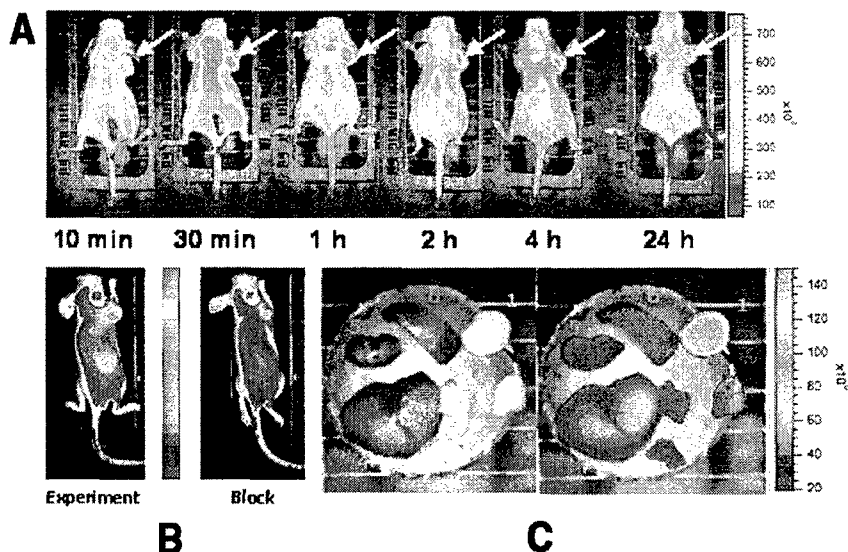
Ultrasound

Because of its low cost, high availability, and safety, ultrasonography is the most commonly used clinical imaging modality. High-frequency (>20 kHz) sound waves are emitted from a transducer placed against the skin, and ultrasound images are obtained based on the sound wave reflected back from the internal organs (39).

The ultrasound contrast is dependent on the sound speed, sound attenuation, backscatter, and the imaging algorithm. Ultrasound imaging using diagnostic ultrasound instrumentation operated in the 7.5–15 MHz frequency range has been applied to several small animal models.

Ellegala et al. reported the ultrasound imaging of tumor angiogenesis using integrin $\alpha_v\beta_3$-targeted microbubbles (40). Athymic nude rats were inoculated intracerebrally with U87MG human glioma cells. On 2 or 4 weeks after implantation, contrast-enhanced ultrasound (CEU) was performed using microbubbles (3–4 μm in diameter) targeted to integrin $\alpha_v\beta_3$ by surface conjugation of echistatin, a disintegrin containing an RGD sequence that can be recognized by many membrane-associated adhesion receptors including integrin $\alpha_v\beta_3$ (Figure 1A). CEU perfusion imaging using nontargeted microbubbles was also performed to determine tumor microvascular blood volume and blood velocity. It was found that CEU signal from targeted microbubbles in tumors increased significantly from 2 to 4 weeks. The signal was highest at the periphery of tumors, where αv-integrin expression was most prominent based on immunohistochemistry, which correlated well with tumor microvascular blood volume. In another study, the integrin α_v-targeting microbubbles were prepared by conjugating echistatin (MBE) or the MAb against murine α_v (MBA) to the surface (41). Control microbubbles (MBC) were also prepared. The microvascular behavior of these microbubbles was assessed by intravital microscopy of the cremaster muscle in mice treated for 4 days with the sustained release of FGF-2. It was observed that microvascular retention was much greater for MBE and MBA than MBC, where the microbubble retention was minimal. The signal from targeted microbubbles (MBE and MBA) also correlated quite well with the blood volume determined by CEU perfusion imaging. In yet another study, hindlimb ischemia was produced in rats by ligation of an iliac artery (42). Immediately after ligation and at subsequent intervals from 4 to 28 days, targeted CEU imaging of integrin expression was performed using microbubbles conjugated with echistatin (Figure 1B). It was observed that iliac artery ligation led to a 65%–70% reduction in blood flow and oxygen tension. In untreated ischemic muscle, blood flow and oxygen tension partially recovered by weeks 2 to 4, and signal from integrin-targeted microbubbles reached maximum between 4 to 7 days, which was before the blood flow increase. FGF-2-treated muscle had a greater rate and extent of blood flow recovery and greater signal intensity from integrin-targeted microbubbles as compared to control animals.

Since acoustic destruction of "payload-bearing" microbubbles may be used to deliver drugs or to augment gene transfection (43), angiogenesis-targeted microbubbles may also have applications in site-specific therapy for ischemic tissues or tumors. Of course, further characterization of integrin α_v-targeted microbubbles in physiological models of ischemia or tumor angiogenesis is needed to validate these potential applications. So far, it is still unclear whether this approach will lead to additional diagnostic and prognostic information compared to those already used in the clinic.

10 min   30 min   1 h   2 h   4 h   24 h

Experiment   Block

B   **C**

Figure 2. (A) In vivo near-infrared (NIR) fluorescence imaging of subcutaneously (s.c.) U87MG tumor bearing athymic nude mice after intravenously (i.v.) injection of arginine-glycine-aspartic acid (RGD)-Cy5.5 conjugate (3 nmol). (B) Representative NIR images (60° mounting angle) of tumor mice demonstrating blocking of RGD-Cy5.5 (0.5 nmol) uptake in the tumors by co-injection of 10 mg/kg mice body weight of c(RGDyK). Pseudocolor fluorescence images of tumor bearing mice were acquired 4 h postinjection (p.i.) of RGD-Cy5.5 (left, experiment) or RGD-Cy5.5 + RGD (right, block). (C) Representative images of dissected organs of a tumor mouse sacrificed 4 h p.i.. 1, U87MG tumor; 2, muscle; 3, pancreas; 4, liver; 5, kidney; 6, spleen; 7, lung. Adapted from Reference 47.

Optical Imaging

One advantage of optical imaging is that multiple probes with different spectral character could potentially be used for multichannel imaging. The major drawback of optical imaging of living subjects is the poor tissue penetration of light. Due to the limited penetration and intense scattering of light, optical imaging will be only possible in humans in limited sites such as the tissues and lesions close to the surface of the skin, tissues accessible by endoscopy, and intraoperative visualization. Even though optical imaging may not be widely used in clinical settings, near-infrared (NIR; 700–900 nm) approaches provide opportunities for rapid and cost-effective preclinical evaluation in small animal models before the more costly radionuclide-based imaging studies, since the absorbance spectra for all biomolecules reach minima in the NIR region, which provides a clear window for in vivo optical imaging (44). Charged-coupled device (CCD) cameras have been developed to more efficiently detect the light emitted from the body (45), and fluorescence-mediated tomography has also been developed recently (46). The subject is exposed to continuous wave or pulsed light from different sources, and multiple detectors arranged in a spatially defined order in an imaging chamber are used to capture the emitted light. Mathematical processing of this information gives the reconstructed tomographic image. Improvement in the algorithm and extensive mathematical validation is needed for practical implementation.
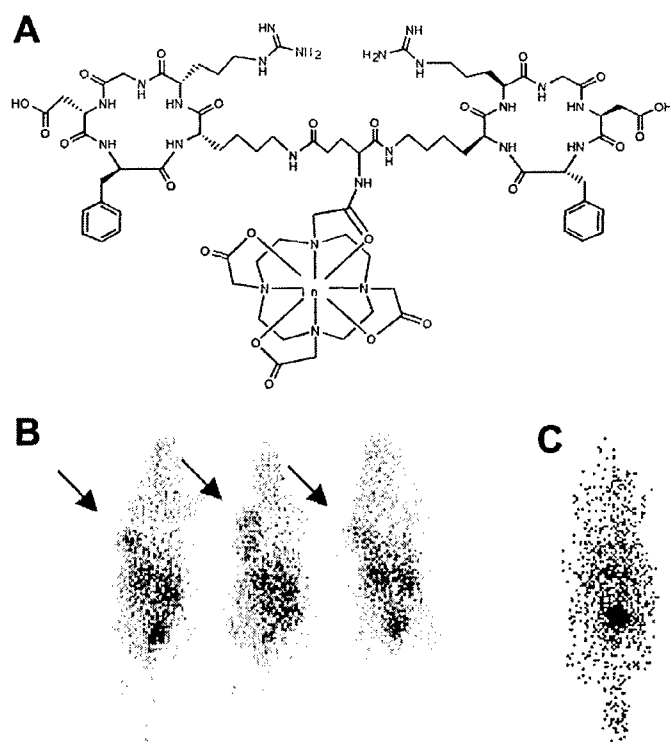
We first demonstrated that NIR fluorescent dye Cy™5.5 conjugated cyclic RGD peptide could be used to visualize subcutaneously (s.c.) inoculated integrin-positive tumors (Figure 2) (47). In vivo imaging with a prototype three-dimensional (3-D) small-animal imaging system visualized subcutaneously U87MG glioblastoma xenograft with a broad range of concentrations of fluorescent probe

administered via the tail vein. The intermediate dose (0.5 nmol) produced better tumor contrast than the high dose (3 nmol) and the low dose (0.1 nmol) during 30 min to 24 h p.i., because of partial self-inhibition of receptor-specific tumor uptake at high dose and the presence of significant amount of background fluorescence at low dose, respectively. Subsequently, Wang et al. also reported optical imaging of tumor xenografts using an integrin $\alpha_v\beta_3$-targeted peptide c(KRGDf) labeled with fluorescent dyes Cy5.5 and IRDye800 (48,49). In vitro, the peptide-dye conjugates bound specifically to integrin $\alpha_v\beta_3$-positive tumor cells. When administered intravenously (i.v.) into mice, dynamic imaging revealed that Cy5.5-c(KRGDf) was rapidly taken up by KS1767 tumor (human Kaposi's sarcoma) after bolus injection, and the uptake of Cy5.5-c(KRGDf) in tumor regions were linearly increased with a dose of up to 1.5 nmol/mouse (possibly integrin receptor saturation above this dose). However, the tumor-to-background ratio was modest, and very low contrast was observed in another integrin $\alpha_v\beta_3$-positive M21 human melanoma tumor.

Burnett et al. (50) also reported the use of integrin $\alpha_v\beta_3$-targeted optical probes both in vitro and in vivo. A series of aliphatic carbamate derivatives of the nonpeptide integrin antagonists were synthesized, and the binding affinity was determined by enzyme-linked immunoabsorbent assay (ELISA) and cell adhesion inhibition assays. They observed that a hydrophobic carbamate linker increased the binding affinity of the parent compound for integrin $\alpha_v\beta_3$ by 2- to 20-fold and demonstrated that the probe with a neopentyl linker exhibited increased binding affinity and significant tumor cell uptake in vitro as well as specific tumor accumulation and retention in vivo. Very recently, Achilefu et al. (51) discovered that conjugating a presumably inactive linear hexapeptide GRDSPK with an NIR carbocyanine molecular probe yielded Cyp-GRD that targets integrin $\alpha_v\beta_3$-positive tumors. In vivo, Cyp-GRD selectively accumulated in tumors. Blocking studies with c(RGDfV) inhibited the uptake of Cyp-GRD, suggesting that both compounds target the same site of integrin $\alpha_v\beta_3$. Surprisingly, neither a Cypate-labeled linear RGD peptide nor an ^{111}In-labeled DOTA-GRD conjugate exhibited specific tumor targeting. Ex vivo redox studies suggested that the probe accumulation level in integrin $\alpha_v\beta_3$-positive tumors might be correlated with mitochondrial NADH concentration. More experiments need to be carried out to fully understand this phenomenon, and a docking experiment is needed to confirm whether Cyp-RGD actually binds to the RGD binding domain in integrin $\alpha_v\beta_3$.

Quantum dots (QDs) with size- and composition-tunable fluorescence emission have high quantum yields and photostability suitable for optical imaging and multiplexing (52). Cai et al. (53) labeled QD705 (emission wavelength 705 nm) with a monomeric RGD peptide c(RGDyK), and the resulting conjugate QD705-RGD was tested for in vitro staining of several cancer cell lines, ex vivo tissue staining, and in vivo tumor targeting. The in vitro cell staining experiments demonstrated the specific integrin targeting ability of QD705-RGD, and the fluorescence intensity correlated well with the integrin level of the cell lines. The tumor signal of QD705-RGD in nude mice U87MG xenografts steadily increased during the first several hours and reached a peak at 6 h (tumor-to-muscle ratio of about 3.6). QD705 had minimal tumor uptake, and no enhancement was found throughout the study as compared to muscle. Most of the injected particles accumulated in the liver, spleen, bone marrow, and lymphatic systems, suggesting that the mononuclear phagocytes of the reticuloendothelial system (RES), which can mediate nonspecific uptake of circulating particulates are involved in the clearance of some of the circulating QD705 and QD705-RGD particles in the mice (54). Based on these results, an approach that

Figure 3. (A) Structure of ^{111}In-DOTA-E-[c(RGDfK)]$_2$. (B) Scintigraphic image of three athymic BALB/c mice with a subcutaneous NIH:OVCAR-3 tumor 2 h after injection of 1.8 MBq ^{111}In-DOTA-E-[c(RGDfK)]$_2$, tumors are pointed out by arrows. Prominent activity accumulations in the kidneys, liver, and intestines are also obvious. (C) Mouse injected with 1.8 MBq of the ^{111}In-labeled scrambled peptide DOTA-E-[c(RGKfD)]$_2$ showed no significant tumor uptake. Adapted from Reference 56.

takes advantage of the high integrin targeting efficacy of the cyclic RGD peptides, high stability and brightness of QD, and emission wavelength in the NIR window will have great potential in cancer diagnosis and imaging as well as imaging-guided surgery and therapy.

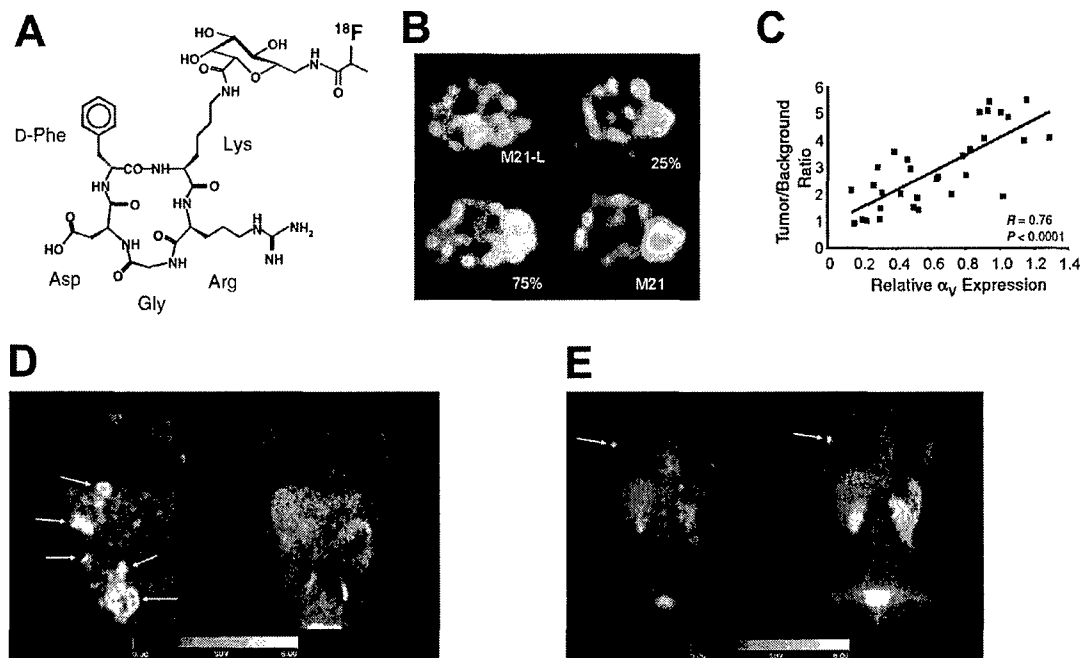## RADIONUCLIDE IMAGING OF INTEGRIN $\alpha_v\beta_3$ EXPRESSION

Single Photon Emission Computed Tomography

As its name suggests (single photon emission), the source of SPECT images are γ-ray emissions (55). Internal radiation is administered through a low mass amount of pharmaceutical labeled with a radioactive isotope, which is then inhaled, ingested, or injected. The radioactive isotope decays and emits γ-rays, which can be detected by a γ-camera. The γ-camera can be used in planar imaging to obtain two-dimensional (2-D) images, or in SPECT imaging, to obtain 3-D images. The first object that an emitted γ-photon encounters after exiting the body is the collimator that allows it to travel only along certain directions to reach the detector, to ensure that the position on the detector accurately represents the source of the γ-ray. SPECT imaging has a very low detection efficiency of $<10^{-4}$ times the emitted number of γ-rays because of the use of lead collimators to define the angle of incidence. However, the advantage of SPECT imaging is that it allows simultaneous imaging of multiple radionuclides since γ-rays emitted from different radioisotopes can be differentiated based on the energy.

Janssen and coworkers (56) studied the in vivo behavior of the radiolabeled dimeric RGD peptide E[c(RGDfK)]$_2$ in the subcutaneous NIH:OVCAR-3 ovarian carcinoma xenograft model in BALB/c nude mice. ^{111}In/^{90}Y and ^{99m}Tc were incorporated through DOTA and hydrazinonicotinamide (HYNIC) chelators, respectively (Figure 3).

Tumor uptake was as high as 7.5% injected dose (ID)/g (^{111}In-DOTA-E[c(RGDfK)]$_2$) at 2 h p.i. or 6.0% ID/g (^{99m}Tc-HYNIC-E-[c(RGDfK)]$_2$) at 1 h p.i.. A single injection of ^{90}Y-DOTA-E[c(RGDfK)]$_2$ at 37 MBq in mice with small subcutaneous tumors caused a significant growth delay as compared with control mice. However, increasing the number of injections did not improve the therapeutic efficacy (57,58). Moreover, the prominent renal uptake limits its potential in clinical applications. Multimeric RGD peptides with even higher receptor affinity and longer tumor retention time might be more suitable for clinical translation.

RP748, an ^{111}In-labeled quinolone that binds to integrin $\alpha_v\beta_3$ with high affinity, was recently studied both in vitro and in vivo to track injury-induced vascular proliferation in rodents (59). This tracer exhibits selective binding to activated $\alpha_v\beta_3$ integrin, and activation of integrin $\alpha_v\beta_3$ by Mn^{2+} led to increased cell binding. RP748 was then injected into mice at 1, 3, or 4 weeks after left carotid injury, and carotids were harvested for autoradiography. It was found that the relative autographic intensity was higher at 1 and 3 weeks and decreased significantly by 4 weeks after injury. Carotid α_v and β_3 integrin expression peaked at 1 week and decreased by 4 weeks after injury. The proliferation index obtained from Ki67 staining exhibited a temporal pattern that correlates to RP748 uptake. In vivo imaging of this radiolabeled integrin $\alpha_v\beta_3$-targeting agent was performed in a canine model of postinfarction angiogenesis (60). Serial in vivo dual-isotope SPECT imaging with RP748 and ^{99m}Tc-MIBI demonstrated focal radiotracer uptake in hypoperfused regions where angiogenesis was stimulated. A 4-fold increase in myocardial radiotracer uptake in the infarct region was observed, which was confirmed by histological staining of $\alpha_v\beta_3$ integrin. These results demonstrated in vivo imaging of vascular cell proliferation-associated states, whether focal, as in postangioplasty re-stenosis, or diffuse, as in pulmonary hypertension, which may lead to better understanding of pathophysiology, development of novel paradigms

Figure 4. (A) Structure of [^{18}F]Galacto-RGD. (B) Transaxial images of nude mice bearing tumors with increasing amounts of $\alpha_v\beta_3$-positive M21 cells (0% [M21-L], 25%, 75%, and 100% [M21]) 90 min postinjection (p.i.) obtained from a small-animal positron emission tomography (PET) scanner show increasing tracer uptake in the tumor. (C) The correlation between tumor/background ratios (obtained from PET) and relative integrin $\alpha_v\beta_3$ expression (obtained from Western blot analyses). (D) A patient with malignant melanoma stage IV and multiple metastases in the liver, skin, and lower abdomen (arrows) showed marked uptake of [^{18}F]FDG (left panel) but virtually no uptake of [^{18}F]Galacto-RGD (right panel) using a clinical PET camera. (E) A patient with malignant melanoma stage IIIb and a solitary lymph node metastasis in the right axilla can be detected by both [^{18}F]FDG (left panel) and [^{18}F]Galacto-RGD (right panel). RGD, arginine-glycine-aspartic acid. Adapted from Reference 62.

for management of cardiovascular disease, as well as better risk stratification of patients following myocardial infarction.

Positron Emission Tomography

To date, most of integrin targeted PET studies have been focused on the radiolabeling of RGD peptide antagonists of integrin $\alpha_v\beta_3$ due to its high binding affinity (nanomolar to subnanomolar range for monomeric and multimeric RGD peptides) (61–64). For early lesion detection, acquisition of higher count statistics is particularly valuable for detecting the fewest possible cells per unit volume with the least amount of radio-activity. The sensitivity of PET is very high (10^{-11}–10^{-12} M), and there is no depth limitation for detecting tumor signal (1,65). Therefore, PET imaging of tumor integrin expression is the most extensively studied among all the modalities described above. The current status of RGD-based PET probe development is reviewed next.

¹⁸F-Labeled RGD Peptides

Monomeric RGD peptide c(RGDyV) was first labeled by Haubner et al. (61) with ^{125}I. This tracer had rapid tumor washout and unfavorable hepatobiliary excretion due to its high lipophilicity, which limited its further application. Glycosylation on the lysine side chain of a similar RGD peptide c(RGDyK) decreased the lipophi-licity and the hepatic uptake (66). Another glycopeptide based on c(RGDfK) was then labeled with ^{18}F via 2-[^{18}F]fluoropropionate prosthetic group, and the resulting [^{18}F]galacto-RGD (Figure 4A) exhibited integrin $\alpha_v\beta_3$-specific tumor uptake in integrin-positive M21 melanoma xenograft model (62,67,68). It was also demon-strated that [^{18}F]galacto-RGD is sensitive enough to visualize $\alpha_v\beta_3$ expression resulting exclusively from the tumor vasculature using
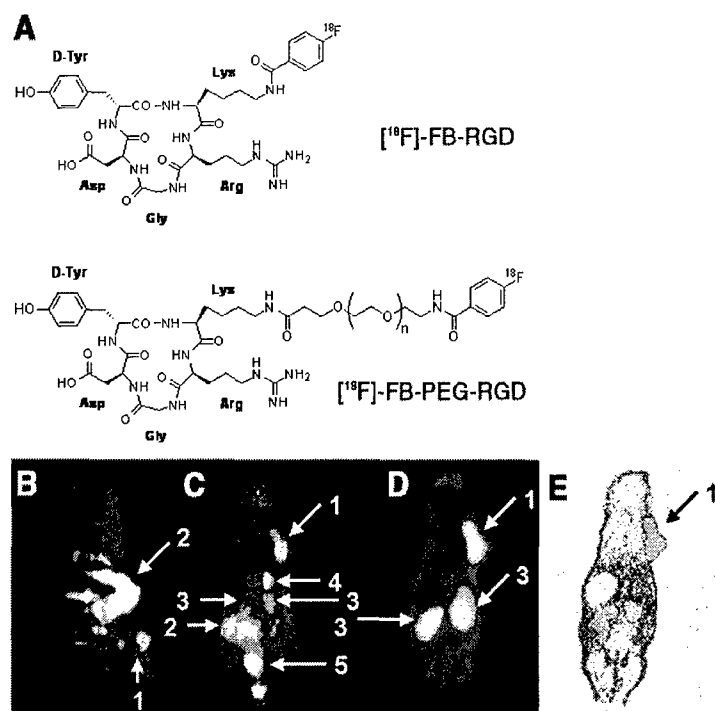
an A431 human squamous cell carcinoma model, in which the tumor cells are integrin negative. Quantitative analysis showed that uptake of [^{18}F]Galacto-RGD in the melanoma model is related to $\alpha_v\beta_3$ expression as determined by Western blot analyses. Initial clinical trials in healthy volunteers and a limited number of cancer patients revealed that this tracer can be safely administered to patients and is able to delineate certain lesions that are integrin-positive with reasonable contrast (62,69). Therefore, this approach may help in planning and optimizing therapeutic strategies targeting the $\alpha_v\beta_3$ integrin.

Despite the successful translation of [^{18}F]Galacto-RGD into clinical trials, several key issues remain to be resolved. (i) Tumor targeting efficacy—as a monomeric RGD peptide tracer, it has relatively low integrin binding affinity and only modest tumor standard uptake values (SUVs). Therefore, tumors with low integrin expression level may not be detectable. (ii) Pharmacokinetics—although glycosylation improved the pharmacokinetic behavior of the tracer to a certain degree, prominent activity accumulation in the liver, kidneys, spleen, and intestines was still observed in both preclinical models and human studies, which makes it difficult to visualize lesions in the abdomen. (iii) Quantification of integrin density—it is unclear whether the tumor contrast from [^{18}F]galacto-RGD/PET is a true reflection of tumor integrin $\alpha_v\beta_3$ expression level in vivo. In the preclinical M21/M21-L model, there is moderate correlation between tumor/background ratios (obtained from PET) and relative integrin $\alpha_v\beta_3$ expression level (from Western blot analyses) (Figure 4, B and C). In the clinical trial, the kinetic modeling was carried out using a two-tissue compartment model for the tumors and a one-tissue compartment model for the muscle. The tracer uptake does not seem to correlate with melanoma patient tumor grading and the tumor metastatic potential. As shown in Figure 4D, a patient with malignant melanoma stage IV and multiple metastases in the liver, skin, and lower abdomen showed virtually no uptake of [^{18}F]Galacto-RGD, while in Figure 4E, a patient with malignant melanoma stage IIIb and a solitary lymph node metastasis in the right axilla can be detected.

Sutcliffe-Goulden et al. (70) labeled a linear RGD peptide with ^{18}F via solid-phase synthesis. Unfortu-nately, low metabolic stability and low avidity of the linear RGD peptide did not give tumor contrast. RGD peptides have also been labeled with ^{18}F through electrophilic substitution method (71). The direct fluorination strategy resulted in multiple side products that were difficult to purify by high-performance liquid chromatography (HPLC). The low specific activity of the carrier-added product, in particular, makes such tracers unsuitable for in vivo integrin imaging.

We labeled c(RGDyK) with ^{18}F through a fluoro-benzoyl prosthetic group (Figure 5) (26,29,72). The resulting [^{18}F]FB-RGD had good tumor-to-blood and tumor-to-muscle ratios but also rapid tumor washout and unfavorable hepatobiliary excretion, making it only suitable for visualizing lesions above the liver (e.g., breast cancer, head and neck cancer, and brain tumor). Rather than introducing an amino sugar moiety to increase the hydrophilicity (62,67), an amphiphilic polyethylene glycol (PEG) linker (MW = 3400) was incorporated to improve the pharmacokinetics (26,73). PEGylation significantly prolonged tumor retention without compromising the desired rapid clearance of radioactivity from liver and kidneys, yet it also reduced the receptor binding affinity of the RGD peptide. The overall effect is that the tumor uptake is comparable to the unmodified monomeric RGD peptide but with
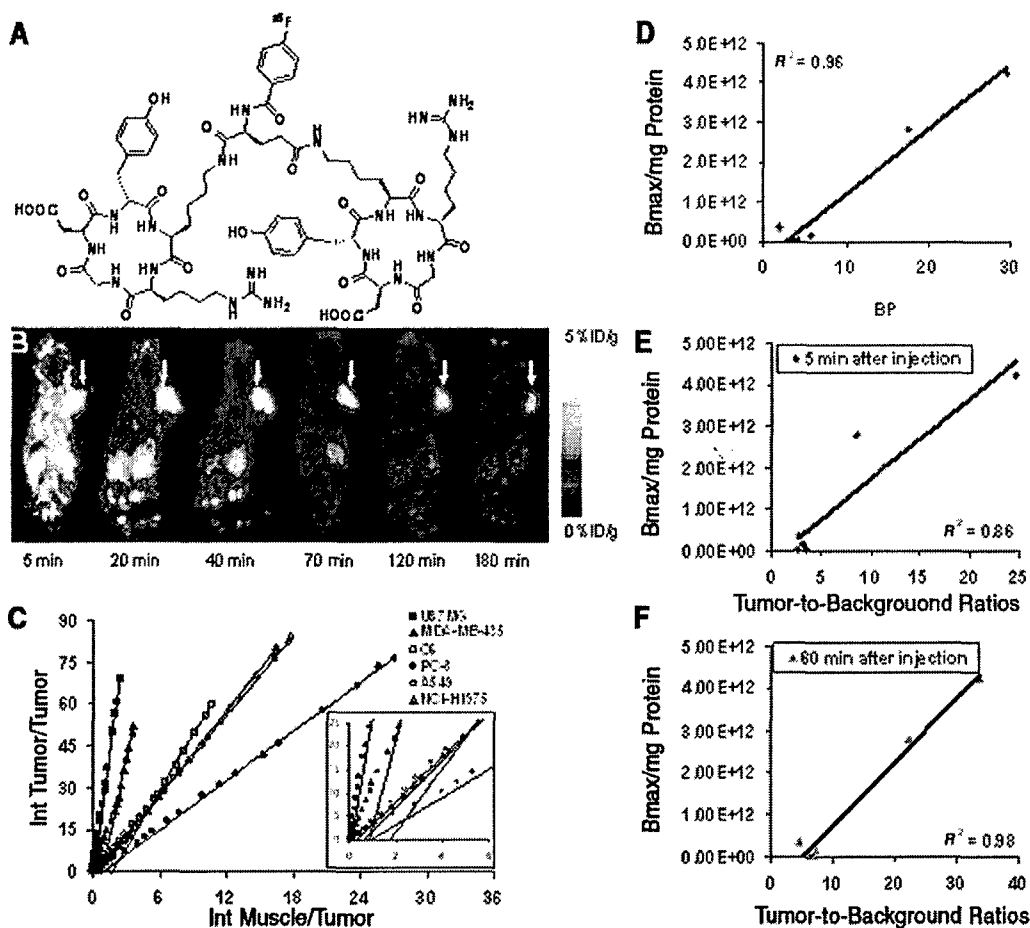

Figure 5. (A) Structure of [^{18}F]FB-RGD and [^{18}F]FB-PEG-RGD. The polyethylene glycol (PEG) linker has a molecular weight of 3400. (B) Coronal microPET image of U87MG tumor-bearing mouse 30 min after injection of [^{18}F]FB-RGD (10-min static image). (C) 2-D projec-tion of U87MG tumor-bearing mouse 60 min after injection of [^{18}F]FB-PEG-RGD (10-min static image). (D) Coronal image of the mouse shown in panel C. (E) Digital autoradiograph of the section containing tumor after microPET imaging. 1, U87MG tumor; 2, intestines; 3, kidney; 4, gallbladder; 5, bladder; PET, positron emission tomography; RGD, arginine-glycine-aspartic acid. Adapted from Reference 26.

improved pharmacokinetics. One disadvantage is that PEG is not a monodisperse compound, which makes complete characterization of the tracer more difficult.

Since c(RGDyK) gives better in vivo imaging results than c(RGDfK), due to its increased hydrophilicity (D-Tyr is more hydrophilic than D-Phe), which gives lower liver uptake, and the bent conformation of both peptides has been optimized to fit into the deep cleft between the α and β units of integrin $\alpha_v\beta_3$, it is unlikely that one can further improve integrin affinity and selectivity of the monomeric RGD peptide by fine-tuning the pentapeptide configuration (22,74). Polyvalency effects have been applied to develop dimeric and multimeric RGD peptides, with repeating cyclic pentapeptide units connected by glutamates (28,56–58,63,75,76). Indeed, the dimeric RGD peptide E[c(RGDyK)]₂ exhibited one order of magnitude higher binding affinity than the corresponding monomer c(RGDyK). [18F]FB-E[c(RGDyK)]₂ (abbreviated as [18F]FRGD2) (Figure 6A) had predominant renal excretion and almost twice as much tumor uptake in the same animal model as compared to the monomeric tracer [18F]FB-c(RGDyK). The synergistic effect of polyvalency (77) and improved pharmacokinetics may be responsible for the excellent imaging characteristics of [18F]FRGD2 (Figure 6B).

In order to quantify integrin $\alpha_v\beta_3$ expression level in vivo, graphical analyses of the dynamic microPET scans in several tumor xenograft models, such as glioma, breast cancer, prostate cancer, and non-small cell lung cancers were performed (78). The Logan plot (79) (Figure 6C) gave better fit than the Patlak analysis (80), reflecting the reversible binding characteristics of [18F]FRGD2. Since 125I-echistatin forms a sodium dodecyl sulfate (SDS)-stable complex with integrin $\alpha_v\beta_3$ (resistant to 0.6% SDS) in the absence of chemical cross-linkers, reducing conditions and heating (81), the tumor integrin density can be quantified by SDS polyacrylamide gel electrophoresis (SDS-PAGE)/autoradiography using 125I-echistatin as radioligand. The binding potential (BP) thus calculated from the Logan plot correlated well with the receptor density measured from receptor autoradiography (Figure 6D). Most importantly, at late time points when most of the nonspecific binding had been cleared, the tumor-to-background ratio also had a linear relationship with the tumor integrin levels (Figure 6F), thus making it possible to quantify tumor integrin expression level in vivo with static PET scans and [18F]FRGD2. Whether this tracer [18F]FRGD2 will be translated into the clinic to correlate between tumor-to-background ratios or SUVs and tumor integrin expression level remains to be determined.

Figure 6. (A) Structure of [18F]FB-E[c(RGDyK)]2 (abbreviated as [18F]FRGD2). (B) Dynamic microPET study of U87MG tumor-bearing mouse over 60 min after injection of [18F]FRGD2, static scans at 120 min and 180-min time points were also conducted to complete the tracer kinetic study. Decay-corrected whole-body coronal images containing the tumor are shown. (C) Logan plots derived from 60-min dynamic microPET imaging data showed excellent linearity of normalized integrated (Int) tumor activity versus normalized integrated muscle tissue activity effective for t > 25 min. The curves for t < 25 min are shown in the inset. (D) Correlation analysis between tumor tissue receptor density [Bmax/mg protein measured from sodium dodecyl sulfate polyacrylamide gel electrophoresis (SDS-PAGE)/autoradiography using 125I-echistatin as the radioligand] versus binding potential (BP; calculated from the Logan plot transformation of dynamic microPET imaging data). (E) Tumor tissue receptor density versus tumor-to-background ratio at 5 min postinjection (p.i.) of [18F]FRGD2. (F) Tumor tissue receptor density versus tumor-to-background ratio at 60 min p.i. of [18F]FRGD2. PET, positron emission tomography. Adapted from References 63 and 78.

The initial clinical trial of [18F]Galacto-RGD boasts promising future of RGD-based PET tracer for in vivo tumor imaging. This tracer gives good contrast in most regions of the body except for the urogenital tract and the liver and spleen, even though the tracer itself is not quite optimal. Multimeric RGD peptides have been reported to exhibit increased binding affinities in vitro and improved tumor accumulation and tumor-to-background ratios in preclinical rodent models as compared with the monomeric compounds (28,58,63,64,78). Therefore, it is necessary to perform a side-by-side comparison to determine whether multimeric RGD-based tracers such as [18F]FRGD2 may exhibit more specific and more sensitive tumor targeting in both the preclinical rodent model and in clinical trials. It is very likely that the multimeric ligand approach will be used for performance optimization of RGD-based PET tracer development.

64Cu-Labeled RGD Peptides

For PET imaging of integrin $\alpha_v\beta_3$ expression, 18F-labeled RGD peptides will likely be the first choice, since [18F]F- is readily available from most medical cyclotron facilities. In addition to 18F-labeled RGD peptides, 64Cu- and 86Y-labeled RGD peptides are also of considerable interest. 64Cu [$t_{1/2}$ = 12.7 h; β^+ = 655 keV (19%); β^- = 573 keV (40%)] is an attractive radionuclide for both PET imaging and targeted radiotherapy of cancer (82) while 86Y ($t_{1/2}$ = 14.7 h) is usually used as a substitute of 90Y for pharmacokinetics

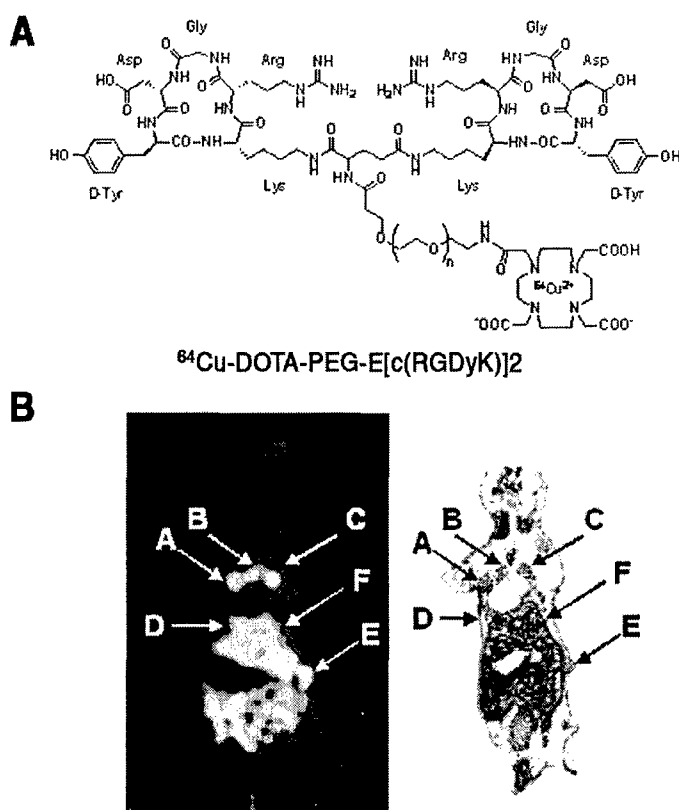and dosimetry studies (83). PET imaging of tumors with low doses of 64Cu-labeled RGD peptides could also be utilized to determine individual radiation dosimetry prior to therapy with either high dose 64Cu- or 67Cu-labeled RGD peptides.

We initially labeled the DOTA-c(RGDyK) conjugate with 64Cu for breast cancer imaging (29). The radiotracer exhibited moderate tumor uptake with prominent liver and kidney retention. The PEGylated analog, 64Cu-DOTA-PEG-c(RGDyK) showed significantly reduced hepatic activity accumulation, higher renal uptake at early time points, but more rapid clearance compared with 64Cu-DOTA-c(RGDyK) (84). Although PEGylation at the lysine side chain reduced the integrin binding affinity of the RGD peptide, the tumor activity accumulation was virtually unaltered. However, the suboptimal tumor uptake and retention of this PEGylated tracer limited its further application for receptor radionuclide therapy.

Dimeric RGD peptides were then labeled with 64Cu, and their tumor targeting efficacy in murine xenograft models was tested (Figure 7A) (28). At all time points, activity accumulation of 64Cu-DOTA-E[c(RGDyK)]2 in tumors was significantly higher than that of the D-Phe analog. Liver uptake of 64Cu-DOTA-E[c(RGDyK)]2 was lower than the D-Phe derivative 64Cu-DOTA-E[c(RGDfK)]2 at early time points but the difference became marginal over time. Overall, 64Cu-DOTA-E[c(RGDyK)]2 yielded better PET images in orthotopic MDA-MB-435 bearing mice than did 64Cu-DOTA-E[c(RGDfK)]2, most likely attributed to the increased hydrophilicity of D-Tyr over D-Phe. Both dimeric peptides showed better tumor retention than the previously tested monomeric RGD counterparts, presumably because of bivalency and the increase in apparent molecular size. In both cases, the tumor uptake can be efficiently blocked by injection of the unlabeled RGD peptide. PEGylated RGD dimer 64Cu-DOTA-PEG-E[c(RGDyK)]2 had similar blood clearance, more rapid renal clearance, and significantly reduced hepatic uptake as compared with 64Cu-DOTA-E[c(RGDyK)]2 (75). Rapid tumor localization and high tumor-to-background contrast makes 64Cu-DOTA-PEG-E[c(RGDyK)]2 a promising agent for integrin $\alpha_v\beta_3$-positive tumor imaging. One striking observation is that it accumulated specifically in both primary and metastatic lung tumor lesions (Figure 7B), while FDG only delineates the primary tumor but none of the metastatic sites because of high uptake of FDG in the heart area. However, the significance of this finding may be slightly diluted by the fact that the magnitude of tumor uptake is too low (<3% ID/g) for peptide receptor radiotherapy applications.

Janssen et al. first applied the polyvalency strategy for SPECT imaging using 99mTc and 111In-labeled dimeric RGD peptides (56,58). Various reports have since demonstrated that the dimer gives better in vivo kinetics as well as much improved imaging results. Very recently, Wu et al. (64) developed a tetrameric RGD peptide tracer 64Cu-DOTA-E(E[c(RGDfK)]2)2 (Figure 8A) for integrin $\alpha_v\beta_3$ imaging in a subcutaneous U87MG glioma xenograft model. The RGD tetramer showed significantly higher integrin binding affinity than the corresponding mono- and dimeric RGD analogs. The radiolabeled peptide showed rapid blood clearance, predominant renal excretion, significant receptor-mediated tumor uptake, and good contrast in tumor mice. Tumor uptake was rapid and high, and the tumor washout was slow (9.93 ± 1.05% ID/g at 30 min p.i. and 4.56 ± 0.51% ID/g at 24 h p.i.) (Figure 8B). This tracer was metabolically stable. The high integrin avidity and favorable biokinetics make 64Cu-DOTA-E(E[c(RGDfK)]2)2 a promising agent for peptide receptor radionuclide imaging as well as radiotherapy of integrin-positive tumors.
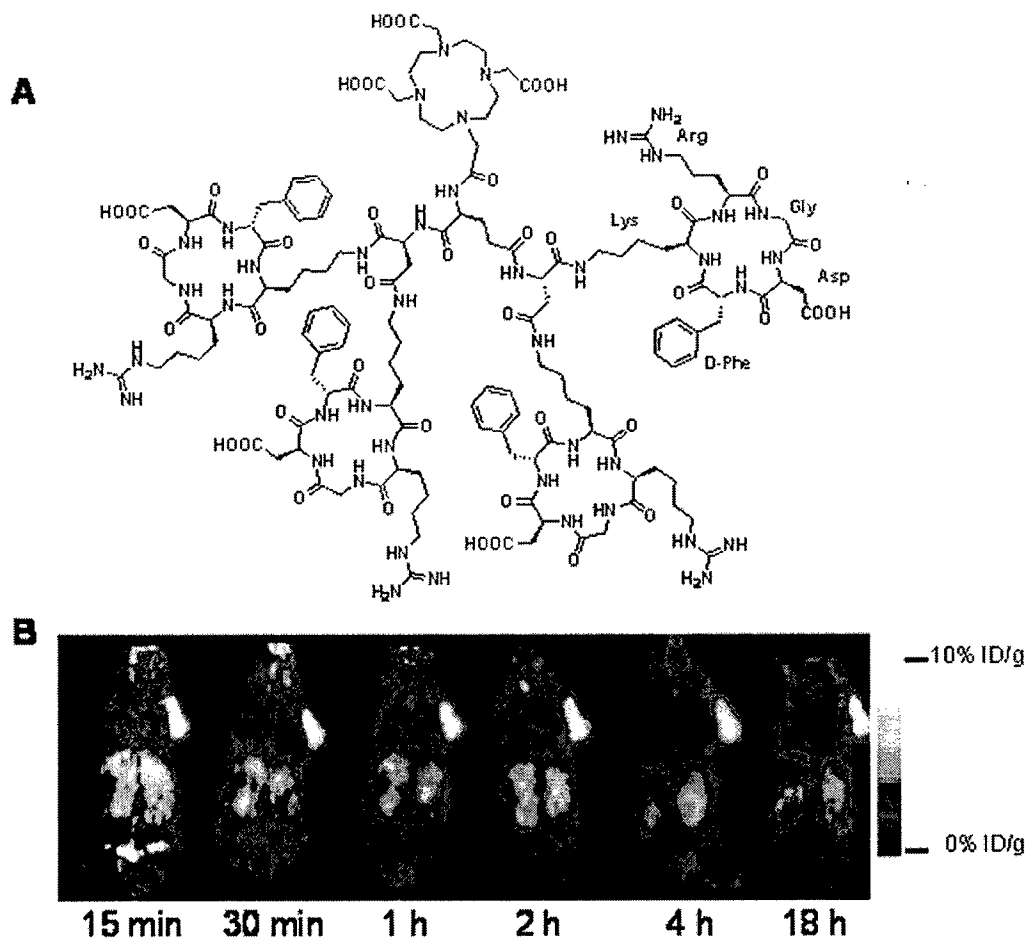
A

64Cu-DOTA-PEG-E[c(RGDyK)]2

B

Figure 7. (A) The structure of 64Cu-DOTA-PEG-E[c(RGDyK)]2. (B, left panel) coronal image (15-min static scan) of severe combined immunodeficiency (SCID)-bg mouse bearing both subcutaneous and orthotopic NCI-H1975 tumors at 2 h after injection of 64Cu-DOTA-PEG-E[c(RGDyK)]2. Both primary tumors and metastases are clearly identified. (B, right panel) Whole body digital autoradiograph of a 50-μm-thick section correlating well with the coronal microPET image shown on the left. (B, panel labels) A, primary orthotopic tumor in the upper lobe of the left lung; B, local metastasis of the primary tumor; C, contralateral lung metastasis; D, metastasis in the diaphragm; E, subcutaneous tumor; F, liver. PET, positron emission tomography. Adapted from Reference 75.

CONCLUSION AND FUTURE PERSPECTIVE

Significant advances have been achieved in developing novel probes for multimodality molecular imaging of tumor integrin expression. Small molecules, peptides, peptidomimetic integrin $\alpha_v\beta_3$ antagonists, and antibodies have been labeled with radioisotopes, superparamagnetic nanoparticles, fluorescent dyes, QDs, and microbubbles for PET, SPECT, MRI, NIR fluorescence, and ultrasound imaging of small animals, mostly tumor models. The nanoparticles or microbubbles used for MRI or ultrasound imaging has relatively large particle sizes (usually >200 nm) and typically can not extravasate from the blood vessels. Therefore, they may only be suitable for tumor vasculature imaging rendering limited potential in the clinic due to less available targets as compared to the small molecule tracers that can extravasate and therefore target not only the tumor vasculature but also the tumor cells. Because of the high sensitivity and adequate spatial and temporal resolution of PET, development of PET probes for integrin expression imaging is currently the most active among all these modalities. [^{18}F]Galacto-RGD is already in clinical trials for cancer imaging. ^{18}F-labeled RGD dimer [^{18}F]FRGD2 may outperform [^{18}F]Galacto-RGD because of its higher receptor avidity and more favorable pharmacokinetics as well as the ability to quantify integrin expression in vivo. ^{64}Cu-labeled tetramer exhibited high and prolonged tumor retention and rapid liver and kidney clearance resulting in good tumor-to-normal organ ratios, which not only makes this tracer suitable for early

lesion detection but also for integrin-targeted radiotherapy. RGD peptides may also be labeled with less common PET isotopes such as ^{124}I and ^{86}Y, which can help guide ^{131}I and ^{90}Y-RGD therapy, respectively. Radiolabeled antibodies against integrin $\alpha_v\beta_3$ have not been well studied despite the fact that a humanized monoclonal antibody Vitaxin® is already in phase II clinical trials for treatment of melanoma and prostate cancer patients (85,86). Development of suitably labeled Vitaxin for imaging the pharmacokinetics and pharmacodynamic of the systemically administered antibody or for integrin-targeted radioimmunotherapy may need to be emphasized for future studies.

Despite the fact that [^{18}F]galacto-RGD is already in early clinical trials for documentation of integrin expression in cancer patients, many other relevant integrin $\alpha_v\beta_3$-specific imaging probes discussed in this review suffer from the slow translation from bench to bedside. Multiple steps in preclinical development, such as pharmacokinetics, dosimetry, imaging feasibility, and investigational new drug (IND)-directed toxicology, are necessary to convert a potential new agent into a diagnostic drug candidate suitable for early clinical testing. Emphasis on highly specific molecular targets and processes has led to products with increased complexity and higher costs of development but smaller market potential. This trend has effectively created a class of agents that investors consider too risky for commercial development, but these agents may have the potential to influence diagnosis and treatment significantly. A general

Figure 8. (A) Structure of DOTA-E(E[c(RGDfK)]₂)₂. (B) Decay-corrected whole-body coronal microPET images of a nude mouse bearing human U87MG tumor at various time points (10-min static image) after injection of ⁶⁴Cu-DOTA-E(E[c(RGDfK)]₂)₂. PET, positron emission tomography. Adapted from Reference 64.

strategy of angiogenesis imaging may thus be more practical in the long run than very specific protein targets (e.g., Her-2/Neu).

Tumor integrin expression imaging has potential clinical applications in many aspects. The first aspect is lesion detection. Despite the clinical success with [^{18}F]FDG/PET imaging, this tracer has several limitations. The tracer can be nonspecifically taken up by several benign conditions such as inflammatory disease, pneumonia, brown fat, muscle, bowel uptake, and granulomatous disease. Also, slow growing indolent tumors may exhibit only a mild increase in glucose metabolism and therefore can be missed by FDG PET (1,87). As most tumor vasculature endothelial cells and many tumor cells express integrin $\alpha_v\beta_3$, suitably labeled RGD peptides might be a potentially more advantageous surrogate marker than FDG for more sensitive detection or detecting lower tumor burden. The second aspect is patient stratification. Differences in tracer accumulation in various tumor types suggest a great diversity in integrin receptor expression. In light of the differences in receptor expression and tracer accumulation, quantitative imaging of tumor integrin becomes very important as a mechanism to stratify and select patients to enter clinical trials focused on anti-integrin treatment. The third aspect is new drug development and/or validation. Rapid characterization of pharmacokinetics and pharmacodynamics by multimodality in vivo imaging of new tracers or anti-integrin drugs can improve data quality, reduce costs, reduce number of animals used, and most importantly, decrease the work-up for new compounds. Fourth is treatment monitoring and optimization. Visualization and quantification of tumor integrin levels by noninvasive molecular imaging can be applied to detect early response to anti-integrin treatment and to elucidate the mechanisms of treatment efficacy underlying integrin signaling, therefore providing important information for treatment optimization. Finally, the fifth aspect is the combination of molecular and functional imaging. As the molecular imaging probes get more specific regarding which leads to a visible signal in only the tumor or other targeted tissue, anatomical and/or functional imaging techniques are needed to identify the exact location of the signal. The combination of molecular and anatomical and/or functional imaging techniques in assessing tumor angiogenesis and in response to antiangiogenic-based therapy will be a powerful tool, and the new generation clinical PET-CT and microPET/microCT will likely play a major role in cancer imaging for the years to come.

Tumor integrin $\alpha_v\beta_3$ expression imaging is given as an example here to demonstrate how molecular imaging can provide a robust platform for understanding the mechanisms of tumor angiogenesis and evaluating the efficacy of novel antiangiogenic therapies. Further progress is needed to improve the sensitivity and resolution of molecular imaging technologies and to develop optimal molecular imaging probes as surrogate markers to pinpoint and monitor specific molecular and cellular actions of angiogenesis inhibitors. Development of multimodality probes, for example, probes that can give both PET and MRI signals, will be of significant value but are currently unexplored. Other targets besides integrins, such as VEGFR, MMP-2, etc., are also being studied for multimodality in vivo imaging of tumor angiogenesis.

ACKNOWLEDGMENTS

COMPETING INTERESTS STATEMENT

REFERENCES

1. Gambhir, S.S. 2002. Molecular imaging of cancer with positron emission tomography. Nat. Rev. Cancer 2:683-693.
2. Massoud, T.F. and S.S. Gambhir. 2003. Molecular imaging in living subjects: seeing fundamental biological processes in a new light. Genes Dev. 17:545-580.
3. Herschman, H.R. 2003. Molecular imaging: looking at problems, seeing solutions. Science 302:605-608.
4. Gross, S. and D. Piwnica-Worms. 2005. Spying on cancer: molecular imaging in vivo with genetically encoded reporters. Cancer Cell 7:5-15.
5. Weissleder, R. and U. Mahmood. 2001. Molecular imaging. Radiology 219:316-333.
6. Bergers, G. and L.E. Benjamin. 2003. Tumorigenesis and the angiogenic switch. Nat. Rev. Cancer 3:401-410.
7. Ferrara, N. 2002. VEGF and the quest for tumour angiogenesis factors. Nat. Rev. Cancer 2:795-803.
8. Nyberg, P., L. Xie, and R. Kalluri. 2005. Endogenous inhibitors of angiogenesis. Cancer Res. 65:3967-3979.
9. Kerbel, R. and J. Folkman. 2002. Clinical translation of angiogenesis inhibitors. Nat. Rev. Cancer 2:727-739.
10. Tucker, G.C. 2003. α_v integrin inhibitors and cancer therapy. Curr. Opin. Investig. Drugs 4:722-731.
11. Jain, R.K. 2005. Normalization of tumor vasculature: an emerging concept in antiangiogenic therapy. Science 307:58-62.
12. Hanahan, D. and J. Folkman. 1996. Patterns and emerging mechanisms of the angiogenic switch during tumorigenesis. Cell 86:353-364.
13. Friedl, P. and K. Wolf. 2003. Tumour-cell invasion and migration: diversity and escape mechanisms. Nat. Rev. Cancer 3:362-374.
14. Sahai, E. 2005. Mechanisms of cancer cell invasion. Curr. Opin. Genet. Dev. 15:87-96.
15. Egeblad, M. and Z. Werb. 2002. New functions for the matrix metalloproteinases in cancer progression. Nat. Rev. Cancer 2:161-174.
16. Bogenrieder, T. and M. Herlyn. 2003. Axis of evil: molecular mechanisms of cancer metastasis. Oncogene 22:6524-6536.
17. Ruoslahti, E. 1996. RGD and other recognition sequences for integrins. Annu. Rev. Cell Dev. Biol. 12:697-715.
18. Xiong, J.P., T. Stehle, B. Diefenbach, R. Zhang, R. Dunker, D.L. Scott, A. Joachimiak, S.L. Goodman, and M.A. Arnaout. 2001. Crystal structure of the extracellular segment of integrin $\alpha_v\beta_3$. Science 294:339-345.
19. Brooks, P.C., R.A. Clark, and D.A. Cheresh. 1994. Requirement of vascular integrin $\alpha_v\beta_3$ for angiogenesis. Science 264:569-571.
20. Kumar, C.C. 2003. Integrin $\alpha_v\beta_3$ as a therapeutic target for blocking tumor-induced angiogenesis. Curr. Drug Targets 4:123-131.
21. Hood, J.D. and D.A. Cheresh. 2002. Role of integrins in cell invasion and migration. Nat. Rev. Cancer 2:91-100.
22. Xiong, J.P., T. Stehle, R. Zhang, A. Joachimiak, M. Frech, S.L. Goodman, M.A. Arnaout, B. Diefenbach, et al. 2002. Crystal structure of the extracellular segment of integrin $\alpha_v\beta_3$ in complex with an Arg-Gly-Asp ligand. Science 296:151-155.
23. Jin, H. and J. Varner. 2004. Integrins: roles in cancer development and as treatment targets. Br. J. Cancer 90:561-565.
24. Brooks, P.C., S. Stromblad, L.C. Sanders, T.L. von Schalscha, R.T. Aimes, W.G. Stetler-Stevenson, J.P. Quigley, and D.A. Cheresh. 1996. Localization of matrix metalloproteinase MMP-2 to the surface of invasive cells by interaction with integrin $\alpha_v\beta_3$. Cell 85:683-693.
25. Schmieder, A.H., P.M. Winter, S.D. Caruthers, T.D. Harris, T.A. Williams, J.S. Allen, E.K. Lacy, H. Zhang, et al. 2005. Molecular MR imaging of melanoma angiogenesis with $\alpha_v\beta_3$-targeted paramagnetic nanoparticles. Magn. Reson. Med. 53:621-627.
26. Chen, X., R. Park, Y. Hou, V. Khankaldyyan, I. Gonzales-Gomez, M. Tohme, J.R. Bading, W.E. Laug, and P.S. Conti. 2004. MicroPET imaging of brain tumor angiogenesis with ^{18}F-labeled PEGylated RGD peptide. Eur. J. Nucl. Med. Mol. Imaging 31:1081-1089.
27. Beck, V., H. Herold, A. Benge, B. Luber, P. Hutzler, H. Tschesche, H. Kessler, M. Schmitt, et al. 2005. ADAM15 decreases integrin $\alpha_v\beta_3$/vitronectin-mediated ovarian cancer cell adhesion and motility in an RGD-dependent fashion. Int. J. Biochem. Cell Biol. 37:590-603.

28. Chen, X., S. Liu, Y. Hou, M. Tohme, R. Park, J.R. Bading, and P.S. Conti. 2004. MicroPET imaging of breast cancer α_v-integrin expression with ^{64}Cu-labeled dimeric RGD peptides. Mol. Imaging Biol. 6:350-359.

29. Chen, X., R. Park, M. Tohme, A.H. Shahinian, J.R. Bading, and P.S. Conti. 2004. MicroPET and autoradiographic imaging of breast cancer α_v-integrin expression using [18]F- and ^{64}Cu-labeled RGD peptide. Bioconjug. Chem. 15:41-49.

30. Meerovitch, K., F. Bergeron, L. Leblond, B. Grouix, C. Poirier, M. Bubenik, L. Chan, H. Gourdeau, et al. 2003. A novel RGD antagonist that targets both $\alpha_v\beta_3$ and $\alpha_5\beta_1$ induces apoptosis of angiogenic endothelial cells on type I collagen. Vascul. Pharmacol. 40:77-89.

31. Qiao, R., W. Yan, H. Lum, and A.B. Malik. 1995. Arg-Gly-Asp peptide increases endothelial hydraulic conductivity: comparison with thrombin response. Am. J. Physiol. 269:C110-117.

32. Haubner, R.H., H.J. Wester, W.A. Weber, and M. Schwaiger. 2003. Radiotracer-based strategies to image angiogenesis. Q. J. Nucl. Med. 47:189-199.

33. Haubner, R. and H.J. Wester. 2004. Radiolabeled tracers for imaging of tumor angiogenesis and evaluation of anti-angiogenic therapies. Curr. Pharm. Des. 10:1439-1455.

34. Pathak, A.P., B. Gimi, K. Glunde, E. Ackerstaff, D. Artemov, and Z.M. Bhujwalla. 2004. Molecular and functional imaging of cancer: advances in MRI and MRS. Methods Enzymol. 386:3-60.

35. Sipkins, D.A., D.A. Cheresh, M.R. Kazemi, L.M. Nevin, M.D. Bednarski, and K.C. Li. 1998. Detection of tumor angiogenesis in vivo by $\alpha_v\beta_3$-targeted magnetic resonance imaging. Nat. Med. 4:623-626.

36. Anderson, S.A., R.K. Rader, W.F. Westlin, C. Null, D. Jackson, G.M. Lanza, S.A. Wickline, and J.J. Kotyk. 2000. Magnetic resonance contrast enhancement of neovasculature with $\alpha_v\beta_3$-targeted nanoparticles. Magn. Reson. Med. 44:433-439.

37. Winter, P.M., S.D. Caruthers, A. Kassner, T.D. Harris, L.K. Chinen, J.S. Allen, E.K. Lacy, H. Zhang, et al. 2003. Molecular imaging of angiogenesis in nascent Vx-2 rabbit tumors using a novel $\alpha_v\beta_3$-targeted nanoparticle and 1.5 tesla magnetic resonance imaging. Cancer Res. 63:5838-5843.

38. Winter, P.M., A.M. Morawski, S.D. Caruthers, R.W. Fuhrhop, H. Zhang, T.A. Williams, J.S. Allen, E.K. Lacy, et al. 2003. Molecular imaging of angiogenesis in early-stage atherosclerosis with $\alpha_v\beta_3$-integrin-targeted nanoparticles. Circulation 108:2270-2274.

39. Morawski, A.M., G.A. Lanza, and S.A. Wickline. 2005. Targeted contrast agents for magnetic resonance imaging and ultrasound. Curr. Opin. Biotechnol. 16:89-92.

40. Ellegala, D.B., H. Leong-Poi, J.E. Carpenter, A.L. Klibanov, S. Kaul, M.E. Shaffrey, J. Sklenar, and J.R. Lindner. 2003. Imaging tumor angiogenesis with contrast ultrasound and microbubbles targeted to $\alpha_v\beta_3$. Circulation 108:336-341.

41. Leong-Poi, H., J. Christiansen, A.L. Klibanov, S. Kaul, and J.R. Lindner. 2003. Noninvasive assessment of angiogenesis by ultrasound and microbubbles targeted to α_v-integrins. Circulation 107:455-460.

42. Leong-Poi, H., J. Christiansen, P. Heppner, C.W. Lewis, A.L. Klibanov, S. Kaul, and J.R. Lindner. 2005. Assessment of endogenous and therapeutic arteriogenesis by contrast ultrasound molecular imaging of integrin expression. Circulation 111:3248-3254.

43. Shohet, R.V., S. Chen, Y.T. Zhou, Z. Wang, R.S. Meidell, R.H. Unger, and P.A. Grayburn. 2000. Echocardiographic destruction of albumin microbubbles directs gene delivery to the myocardium. Circulation 101:2554-2556.

44. Frangioni, J.V. 2003. In vivo near-infrared fluorescence imaging. Curr. Opin. Chem. Biol. 7:626-634.

45. Spibey, C.A., P. Jackson, and K. Herick. 2001. A unique charge-coupled device/xenon arc lamp based imaging system for the accurate detection and quantitation of multicolour fluorescence. Electrophoresis 22:829-836.

46. Montet, X., V. Ntziachristos, J. Grimm, and R. Weissleder. 2005. Tomographic fluorescence mapping of tumor targets. Cancer Res. 65:6330-6336.

47. Chen, X., P.S. Conti, and R.A. Moats. 2004. In vivo near-infrared fluorescence imaging of integrin $\alpha_v\beta_3$ in brain tumor xenografts. Cancer Res. 64:8009-8014.

48. Wang, W., S. Ke, Q. Wu, C. Charnsangavej, M. Gurfinkel, J.G. Gelovani, J.L. Abbruzzese, E.M. Sevick-Muraca, and C. Li. 2004. Near-infrared optical imaging of integrin $\alpha_v\beta_3$ in human tumor xenografts. Mol. Imaging 3:343-351.

49. Sunkuk, K., K. Shi, J.P. Houston, W. Wei, W. Qingping, L. Chun, and E.M. Sevick-Muraca. 2005. Imaging dose-dependent pharmacokinetics of an RGD-fluorescent dye conjugate targeted to $\alpha_v\beta_3$ receptor expressed in Kaposi's sarcoma. Mol. Imaging 4:75-87.

50. Burnett, C.A., J. Xie, J. Quijano, Z. Shen, F. Hunter, M. Bur, K.C. Li, and S.N. Danthi. 2005. Synthesis, in vitro, and in vivo characterization of an integrin $\alpha_v\beta_3$-targeted molecular probe for optical imaging of tumor. Bioorg. Med. Chem. 13:3763-3771.

51. Achilefu, S., S. Bloch, M.A. Markiewicz, T. Zhong, Y. Ye, R.B. Dorshow, B. Chance, and K. Liang. 2005. Synergistic effects of light-emitting probes and peptides for targeting and monitoring integrin expression. Proc. Natl. Acad. Sci. USA. 102:7976-7981.

52. Michalet, X., F.F. Pinaud, L.A. Bentolila, J.M. Tsay, S. Doose, J.J. Li, G. Sundaresan, A.M. Wu, et al. 2005. Quantum dots for live cells, in vivo imaging, and diagnostics. Science 307:538-544.

53. Cai, W., D. Shin, Y. Wu, O. Gheysens, Q. Cao, S.S. Gambhir, S.X. Wang, and X. Chen. RGD peptide-labeled NIR quantum dot for in vivo cancer imaging. Nat. Biotechnol. (Submitted).

54. Rolland, A., B. Collet, R. Le Verge, and L. Toujas. 1989. Blood clearance and organ distribution of intravenously administered polymethacrylic nanoparticles in mice. J. Pharm. Sci. 78:481-484.

55. Peremans, K., B. Cornelissen, B. Van Den Bossche, K. Audenaert, and C. Van de Wiele. 2005. A review of small animal imaging planar and pinhole spect Gamma camera imaging. Vet. Radiol. Ultrasound 46:162-170.

56. Janssen, M.L., W.J. Oyen, I. Dijkgraaf, L.F. Massuger, C. Frielink, D.S. Edwards, M. Rajopadhye, H. Boonstra, et al. 2002. Tumor targeting with radiolabeled $\alpha_v\beta_3$ integrin binding peptides in a nude mouse model. Cancer Res. 62:6146-6151.

57. Janssen, M., C. Frielink, I. Dijkgraaf, W. Oyen, D.S. Edwards, S. Liu, M. Rajopadhye, L. Massuger, et al. 2004. Improved tumor targeting of radiolabeled RGD peptides using rapid dose fractionation. Cancer Biother. Radiopharm. 19:399-404.

58. Janssen, M., W.J. Oyen, L.F. Massuger, C. Frielink, I. Dijkgraaf, D.S. Edwards, M. Radjopadhye, F.H. Corstens, and O.C. Boerman. 2002. Comparison of a monomeric and dimeric radiolabeled RGD-peptide for tumor targeting. Cancer Biother. Radiopharm. 17:641-646.

59. Sadeghi, M.M., S. Krassilnikova, J. Zhang, A.A. Gharaei, H.R. Fassaei, L. Esmailzadeh, A. Kooshkabadi, S. Edwards, et al. 2004. Detection of injury-induced vascular remodeling by targeting activated $\alpha_v\beta_3$ integrin in vivo. Circulation 110:84-90.

60. Meoli, D.F., M.M. Sadeghi, S. Krassilnikova, B.N. Bourke, F.J. Giordano, D.P. Dione, H. Su, D.S. Edwards, et al. 2004. Noninvasive imaging of myocardial angiogenesis following experimental myocardial infarction. J. Clin. Invest. 113:1684-1691.

61. Haubner, R., H.J. Wester, U. Reuning, R. Senekowitsch-Schmidtke, B. Diefenbach, H. Kessler, G. Stocklin, and M. Schwaiger. 1999. Radiolabeled $\alpha_v\beta_3$ integrin antagonists: a new class of tracers for tumor targeting. J. Nucl. Med. 40:1061-1071.

62. Haubner, R., W.A. Weber, A.J. Beer, E. Vabuliene, D. Reim, M. Sarbia, K.F. Becker, M. Goebel, et al. 2005. Noninvasive visualization of the activated $\alpha_v\beta_3$ integrin in cancer patients by positron emission tomography and [18F]galacto-RGD. PLoS Med. 2:e70.

63. Chen, X., M. Tohme, R. Park, Y. Hou, J.R. Bading, and P.S. Conti. 2004. Micro-PET imaging of $\alpha_v\beta_3$-integrin expression with ^{18}F-labeled dimeric RGD peptide. Mol. Imaging 3:96-104.

64. Wu, Y., X. Zhang, Z. Xiong, Z. Cheng, D.R. Fisher, S. Liu, and X. Chen. 2005. MicroPET imaging of glioma α_v-integrin expression using ^{64}Cu-labeled tetrameric RGD eptide. J. Nucl. Med. 46:1707-1718.

65. Sharma, V., G.D. Luker, and D. Piwnica-Worms. 2002. Molecular imaging of gene expression and protein function in vivo with PET and SPECT. J. Magn. Reson. Imaging 16:336-351.

66. Haubner, R., H.J. Wester, F. Burkhart, R. Senekowitsch-Schmidtke, W. Weber, S.L. Goodman, H. Kessler, and M. Schwaiger. 2001. Glycosylated RGD-containing peptides: tracer for tumor targeting and angiogenesis imaging with improved biokinetics. J. Nucl. Med. 42:326-336.

67. Haubner, R., H.-J. Wester, W.A. Weber, C. Mang, S.I. Ziegler, S.L. Goodman, R. Senekowitsch-Schmidtke, H. Kessler, and M. Schwaiger. 2001. Noninvasive imaging of $\alpha_v\beta_3$ integrin expression using ^{18}F-labeled RGD-containing glycopeptide and positron emission tomography. Cancer Res. 61:1781-1785.

68. Haubner, R., B. Kuhnast, C. Mang, W.A. Weber, H. Kessler, H.J. Wester, and M. Schwaiger. 2004. [18F]Galacto-RGD: synthesis, radiolabeling, metabolic stability, and radiation dose estimates. Bioconjug. Chem. 15:61-69.

69. Beer, A.J., R. Haubner, M. Goebel, S. Luderschmidt, M.E. Spilker, H.J. Wester, W.A. Weber, and M. Schwaiger. 2005. Biodistribution and pharmacokinetics of the $\alpha_v\beta_3$-selective tracer ^{18}F-galacto-RGD in cancer patients. J. Nucl. Med. 46:1333-1341.

70. Sutcliffe-Goulden, J.L., M.J. O'Doherty, P.K. Marsden, I.R. Hart, J.F. Marshall, and S.S. Bansal. 2002. Rapid solid phase synthesis and biodistribution of ^{18}F-labelled linear peptides. Eur. J. Nucl. Med. Mol. Imaging 29:754-759.

71. Ogawa, M., K. Hatano, S. Oishi, Y. Kawasumi, N. Fujii, M. Kawaguchi, R. Doi, M. Imamura, et al. 2003. Direct electrophilic radiofluorination of a cyclic RGD peptide for in vivo $\alpha_v\beta_3$ integrin related tumor imaging. Nucl. Med. Biol. 30:1-9.

72. Chen, X., R. Park, A.H. Shahinian, M. Tohme, V. Khankaldyyan, M.H. Bozorgzadeh, J.R. Bading, R.A. Moats, et al. 2004. ^{18}F-labeled RGD peptide: initial evaluation for imaging brain tumor angiogenesis. Nucl. Med. Biol. 31:179-189.

73. Chen, X., R. Park, A.H. Shahinian, J.R. Bading, and P.S. Conti. 2004. Pharmacokinetics and tumor retention of ^{125}I-labeled RGD peptide are improved by PEGylation. Nucl. Med. Biol. 31:11-19.

74. Gottschalk, K.E. and H. Kessler. 2002. The structures of integrins and integrin-ligand complexes: implications for drug design and signal transduction. Angew. Chem. Int. Ed. Engl. 41:3767-3774.

75. Chen, X., E. Sievers, Y. Hou, R. Park, M. Tohme, R. Bart, R. Bremner, J.R. Bading, and P.S. Conti. 2005. Integrin $\alpha_v\beta_3$-targeted imaging of lung cancer.

Neoplasia 7:271-279.

76. Chen, X., C. Plasencia, Y. Hou, and N. Neamati. 2005. Synthesis and biological evaluation of dimeric RGD peptide-paclitaxel conjugate as a model for integrin-targeted drug delivery. J. Med. Chem. 48:1098-1106.

77. Mammen, M., S. Chio, and G.M. Whitesides. 1998. Polyvalent interactions in biological systems: implications for design and use of multivalent ligands and inhibitors. Angew. Chem. Int. Ed. Engl. 37:2755-2794.

78. Zhang, X., Z. Xiong, X. Wu, W. Cai, J.R. Tseng, S.S. Gambhir, and X. Chen. Quantitative PET imaging of tumor integrin $\alpha_\nu\beta_3$ expression with [^{18}F]FRGD2. J. Nucl. Med. (In press).

79. Logan, J. 2000. Graphical analysis of PET data applied to reversible and irreversible tracers. Nucl. Med. Biol. 27:661-670.

80. Kawatsu, S., T. Kato, A. Nagano-Saito, K. Hatano, K. Ito, and T. Ishigaki. 2003. New insight into the analysis of 6-[^{18}F]fluoro-L-DOPA PET dynamic data in brain tissue without an irreversible compartment: comparative study of the Patlak and Logan analyses. Radiat. Med. 21:47-54

81. Thibault, G. 2000. Sodium dodecyl sulfate-stable complexes of echistatin and RGD-dependent integrins: a novel approach to study integrins. Mol. Pharmacol. 58:1137-1145.

82. Anderson, C.J., L.A. Jones, L.A. Bass, E.L. Sherman, D.W. McCarthy, P.D. Cutler, M.V. Lanahan, M.E. Cristel, et al. 1998. Radiotherapy, toxicity and dosimetry of copper-64-TETA-octreotide in tumor-bearing rats. J. Nucl. Med. 39:1944-1951.

83. Pauwels, S., R. Barone, S. Walrand, F. Borson-Chazot, R. Valkema, L.K. Kvols, E.P. Krenning, and F. Jamar. 2005. Practical dosimetry of peptide receptor radionuclide therapy with ^{90}Y-labeled somatostatin analogs. J. Nucl. Med. 46(Suppl 1):92S-98S.

84. Chen, X., Y. Hou, M. Tohme, R. Park, V. Khankaldyyan, I. Gonzales-Gomez, J.R. Bading, W.E. Laug, and P.S. Conti. 2004. Pegylated Arg-Gly-Asp peptide: ^{64}Cu labeling and PET imaging of brain tumor $\alpha_\nu\beta_3$-integrin expression. J. Nucl. Med. 45:1776-1783.

85. Posey, J.A., M.B. Khazaeli, A. DelGrosso, M.N. Saleh, C.Y. Lin, W. Huse, and A.F. LoBuglio. 2001. A pilot trial of Vitaxin, a humanized anti-vitronectin receptor (anti $\alpha_\nu\beta_3$) antibody in patients with metastatic cancer. Cancer Biother. Radiopharm. 16:125-132.

86. Patel, S.R., J. Jenkins, N. Papadopolous, M.A. Burgess, C. Plager, J. Gutterman, and R.S. Benjamin. 2001. Pilot study of vitaxin-an angiogenesis inhibitor-in patients with advanced leiomyosarcomas. Cancer 92:1347-1348.

87. Gambhir, S.S., J. Czernin, J. Schwimmer, D.H. Silverman, R.E. Coleman, and M.E. Phelps. 2001. A tabulated summary of the FDG PET literature. J. Nucl. Med. 42:1S-93S.

Address correspondence to:

Xiaoyuan Chen
Molecular Imaging Program at Stanford (MIPS)
Department of Radiology and Bio-X Program
Stanford University School of Medicine
1201 Welch Road, Rm. P095
Stanford, CA 94305-5484, USA
e-mail: shawchen@stanford.edu

Micro-PET Imaging of $\alpha_v\beta_3$-Integrin Expression with ^{18}F-Labeled Dimeric RGD Peptide

Xiaoyuan Chen, Michel Tohme, Ryan Park, Yingping Hou, James R. Bading, and Peter S. Conti

University of Southern California

Abstract

The α_v integrins, which act as cell adhesion molecules, are closely involved with tumor invasion and angiogenesis. In particular, $\alpha_v\beta_3$ integrin, which is specifically expressed on proliferating endothelial cells and tumor cells, is a logical target for development of a radiotracer method to assess angiogenesis and anti-angiogenic therapy. In this study, a dimeric cyclic RGD peptide E[c(RGDyK)]$_2$ was labeled with ^{18}F ($t_{1/2}$ = 109.7 min) by using a prosthetic 4-[^{18}F]fluorobenzoyl moiety to the amino group of the glutamate. The resulting [^{18}F]FB-E[c(RGDyK)]$_2$, with high specific activity (200–250 GBq/µmol at the end of synthesis), was administered to subcutaneous U87MG glioblastoma xenograft models for micro-PET and autoradiographic imaging as well as direct tissue sampling to assess tumor targeting efficacy and in vivo kinetics of this PET tracer. The dimeric RGD peptide demonstrated significantly higher tumor uptake and prolonged tumor retention in comparison with a monomeric RGD peptide analog [^{18}F]FB-c(RGDyK). The dimeric RGD peptide had predominant renal excretion, whereas the monomeric analog was excreted primarily through the biliary route. Micro-PET imaging 1 hr after injection of the dimeric RGD peptide exhibited tumor to contralateral background ratio of 9.5 ± 0.8. The synergistic effect of polyvalency and improved pharmacokinetics may be responsible for the superior imaging characteristics of [^{18}F]FB-E[c(RGDyK)]$_2$. *Mol Imaging* (2004) 3, 96–104.

Introduction

Tumor angiogenesis, the formation of new blood vessels or the growth of blood vessels between a tumor and surrounding tissue, is a complex process regulated through a precise balance of pro-angiogenic and anti-angiogenic molecules, which involves complex interactions between extracellular matrix molecules, proteolytic enzymes, and cell adhesion molecules on endothelial cells (ECs) [1,2]. As most solid tumors are angiogenesis dependent, the ability to develop molecular imaging methods for evaluating angiogenesis is of vital importance to understand the complex process and to monitor target specific anti-angiogenic treatment efficacy. Inhibition of the activity of any of the key regulators in the angiogenic cascade is expected to block tumor angiogenesis. Integrin adhesion receptors regulate cell survival, proliferation, motility, and differentiation through their ability to transduce signals into and out of the cells and to engage in reciprocal interactions with other cellular receptors [3]. The cell surface adhesion and signaling receptor $\alpha_v\beta_3$ integrin, which is highly expressed in tumor cells of various origin and activated ECs in growing tumors but not on normal cells and quiescent ECs, has been identified as a marker for angiogenic vascular tissue and potentially can be used as a target for diagnostic and therapeutic agents aimed at tumor angiogenesis [4].

Two α_v-integrin antagonists—vitaxin, a humanized antibody [5], and cilengitide [6], a cyclic peptide mimicking the RGD ligand recognition peptidic domain common to α_v-integrin ligands—are in phase II clinical trials [4]. Due to their better pharmacokinetics and oral bioavailability, small synthetic heterocyclic inhibitors are also being developed as successors to peptide-derived agents [7]. Other strategies include radiolabeled cyclic RGD peptides for internal radiotherapy [8], and combination of integrin antagonists and radioimmunotherapy for enhanced therapeutic synergy [9]. The ability to rapidly and accurately detect tumor growth and metastasis is of great importance for implementation of tailored therapeutic regimens [10]. We and others have recently labeled cyclic RGD peptides with ^{18}F [11–17] and ^{64}Cu [14] for positron emission tomography (PET) imaging of $\alpha_v\beta_3$-integrin expression in murine tumor models.

The conjugation labeling of small cyclic RGD peptides with the prosthetic labeling group 4-[^{18}F]fluorobenzoyl significantly increased lipophilicity of the peptide and led to unfavorable hepatobiliary excretion and rapid tumor washout of the resulting PET tracer [11,12,14]. The clinical potential of this type of radiotracer is thus limited due to unfavorable biodistribution, including

very high activity accumulation in the lower abdomen [11,12,14]. Haubner et al. [15,16] inserted a sugar moiety between the 2-[^{18}F]fluoropropionate moiety and the ε-amino group of the cyclic RGD peptide c(RGDfK) lysine residue. The increased hydrophilicity upon glycosylation, rapid excretion, adequate metabolic stability, and the low estimated radiation dose of this radiopharmaceutical endows it with potential for application in human studies. We applied a different approach to improve the in vivo pharmaokinetic profile of ^{18}F-labeled RGD peptide through PEGylation [13]. The ^{18}F-labeled PEG-RGD peptide has significantly improved tumor retention relative to [^{18}F]FB-RGD without compromising the desirably rapid clearance of radioactivity from liver and kidneys. Additionally, decreased biliary excretion minimized intestinal retention of the activity and increased tumor-to-nontumor ratios [13].

Specific recognition of a peptide by a given receptor depends on the specific configuration of the peptide side-chain with regard to its ability to fit in the receptor binding sites. A multimeric peptide with two or more monomeric units connected via semi-rigid molecular linkers may achieve improved binding avidity and specificity through multiple, weakly cooperative interactions [18]. It was recently reported that dimeric and multimeric cyclic RGD peptides have higher receptor binding affinity in vitro [19] and better tumor retention in vivo [19,20]. This is presumably due to polyvalency, which gives rise to an enhanced binding and steric stabilization [21]. The aim of the study presented here was to compare the tumor targeting and in vivo kinetics of the ^{18}F-labeled dimeric RGD peptide [^{18}F]FB-E[c(RGDyK)]$_2$ to that of its monomeric analog, [^{18}F]FB-c(RGDyK).

Materials and Methods

Materials

All reagents, unless otherwise specified, were of analytical grade and commercially obtained. Cyclic RGD peptide c(RGDyK) was synthesized via solution cyclization of the fully protected linear pentapeptide H-Gly-Asp(OtBu)-D-Tyr(OtBu)-Lys(Boc)-Arg(Pbf)-OH, followed by TFA deprotection [22]. FB-c(RGDyK) was prepared earlier by our group [14]. Dimeric RGD peptide E[c(RGDyK)]$_2$ was prepared by coupling Boc-Glu-OH with two equivalents of monomeric RGD peptide c(RGDyK) followed by TFA cleavage [23]. No-carrier-added [^{18}F]F$^-$ was produced via the [18]O(p,n)[18]F reaction by bombarding a [^{18}O]water target (95% enrichment, Isonics, Golden, CO) with 11 MeV protons using a Siemens RDS-112 negative ion cyclotron. Semi-preparative, reversed-phase HPLC was accomplished on a Waters

515 chromatography system with a 486 tunable absorbance detector and model 1015-DC-P single-channel radiation detector from Carroll and Ramsey Associates (Berkeley, CA). Version 7.2.1 Labtech Notebook/XE software (Andover, MA) was used to record chromatograms. Purification was performed on a Vydac protein and peptide column (218TP510, 5 μm, 250 × 10 mm). The flow was 5 mL/min, with the mobile phase starting from 95% solvent A (0.1% TFA in water) and 5% solvent B (0.1% TFA in acetonitrile) (0–2 min) to 35% solvent A and 65% solvent B at 32 min. The analytical HPLC method was performed using the same gradient system, but with a Vydac 218TP54 column (5 μm, 250 × 4.6 mm) and flow of 1 mL/min. The absorbance was monitored at 218 nm.

[^{19}F]FB-E[c(RGDyK)]$_2$

As a reference standard, [^{19}F]FB-E[c(RGDyK)]$_2$ containing the 4-[^{19}F]fluorobenzoyl moiety was synthesized by coupling E[c(RGDyK)]$_2$ with N-succinimidyl 4-fluorobenzoate (SFB) under slightly basic condition. In brief, SFB 2.4 mg (10 μmol) in 500 μL acetonitrile was added to E[c(RGDyK)]$_2$ 2.7 mg (2 μmol) dissolved in Na$_2$HPO$_4$ buffer 1500 μL (pH = 8.7) and allowed to stand at room temperature for 2 hr. The reaction was quenched by adding 50 μL TFA and followed by semi-preparative HPLC purification. Matrix-assisted laser desorption/ionization–time of flight mass spectrometry (MALDI-TOF) of [^{19}F]FB-E[c(RGDyK)]$_2$: m/z = 1472.9 for [M + H]$^+$ (C$_{66}$H$_{90}$FN$_{19}$O$_{19}$); the retention time was 17.3 min from analytical HPLC; the purity was 99%, and the yield was 76%.

Radiolabeling E[c(RGDyK)]$_2$ with [18]F

E[c(RGDyK)]$_2$ was labeled with ^{18}F by conjugation coupling with N-succinimidyl 4-[^{18}F]fluorobenzoate ([^{18}F]SFB). [^{18}F]SFB with a specific activity of 200–250 GBq/μmol [14] was dissolved in acetonitrile (1 mL) and added to E[c(RGDyK)]$_2$ (200 μg, 0.15 μmol) dissolved in Na$_2$HPO$_4$ buffer (1 mL, pH = 8.7). The reaction was continued for 30 min at 45°C until most of SFB had reacted according to radio-TLC (eluent CH$_2$Cl$_2$/EtOAc = 4:1). Final purification was accomplished by C$_{18}$ reversed-phase chromatography (detection modes: radioactivity and UV at 218 nm). HPLC fractions containing the activity were combined and evaporated with a stream of argon to remove acetonitrile. The pH of the resultant aqueous solution was adjusted to 7.0 with 0.1 N NaOH. This solution was passed through an activated Waters C$_{18}$ Sep-Pak cartridge, washed with water and eluted with 200 μL portions of 80% ethanol. The ethanol fractions were pooled and evaporated to a small volume. The activity was reconstituted in phosphate-buffered saline

and passed through a 0.22-μm Millipore filter into a sterile multidose vial for use in animal experiments.

Receptor Binding Assay

Primary human brain capillary endothelial cells (HBCECs) were isolated, characterized, and grown in RPMI-1640 medium with 10% FBS in 5% CO_2 at 37°C as previously described [24]; the cells were used between passages 5 and 14. ^{125}I-c(RGDyK) (specific activity 1700 Ci/mmol) was prepared via the chloramine-T method according to a reported procedure [21]. For competitive integrin receptor binding assay studies, Costar 24-well plates were seeded with 2×10^5 BCEC cells/well for 2 hr and then rinsed twice with binding buffer (50 mM Tris, pH 7.4, 150 mM NaCl, 2 mM $CaCl_2$, 1 mM $MgCl_2$, 1 mM $MnCl_2$, and 0.1% bovine serum albumin) [24]. The plate was incubated with ^{125}I-c(RGDyK) in the presence of increasing concentrations of different RGD peptide analogues (0–1000 nM). The total incubation volume was adjusted to 400 μL. After the cells were incubated for 2 hr at 4°C, the supernatant was removed, and the cells were washed twice with cold binding buffer and then solubilized with 0.5% SDS. Radioactivity was determined using a NaI(Tl) gamma counter (Packard, Meriden, CT). The IC_{50} values were calculated by fitting the data by nonlinear regression using GraphPad Prism (GraphPad Software, San Diego, CA). Experiments were carried out with triplicate samples.

Tumor Models

Animal experiments were conducted under a protocol approved by the USC Institutional Animal Care and Use Committee (IACUC). Female athymic nude mice (nu/nu) obtained from Harlan (Indianapolis, IN) at 4–5 weeks of age were injected subcutaneously in the right front leg with 2×10^6 U87MG glioblastoma cells suspended in 150 μL Eagle's minimum essential medium (EMEM). When the tumors reached 0.4–0.6 cm in diameter (14–18 days after implant), the mice were used for biodistribution and micro-PET imaging experiments.

Biodistribution

Nude mice bearing subcutaneously xenografted human glioblastoma U87MG tumors were injected intravenously with approximately 740 kBq (20 μCi) of [^{18}F] FB-E[c(RGDyK)]₂. Animals were euthanized at 30 min, 1 hr, 2 hr, and 4 hr postinjection. Blood, tumor, and the major organs and tissues were collected, wet-weighed, and counted in a gamma-counter (Packard). The percent-injected dose per gram (%ID/g) was determined for each sample. For each mouse, radioactivity of the tissue samples was calibrated against a known aliquot of the injectate and normalized to body mass of 20 g. Values are quoted as mean ± standard deviation (SD) for a group of four animals. Receptor-mediated localization of the radiotracer was investigated by intravenous injection of 10 mg/kg of c(RGDyK) mixed with [^{18}F]FB-E[c(RGDyK)]₂ into four mice bearing the U87MG tumor. The mice in this group were sacrificed at 1 hr pi.

Micro-PET Imaging Studies

PET imaging was performed with a micro-PET R4 rodent model scanner (Concorde Microsystems, Knoxville, TN). The scanner has a computer-controlled bed, and 10.8 cm transaxial, 8 cm axial field of view (FOV), and an intrinsic resolution of 1.85 mm at the center of the FOV. It has no septa and operates exclusively in 3-D list mode. The raw list mode data were 3-D histogrammed without smoothing into single-frame sonogram files and reconstructed into images via the Ordered Subsets Expectation Maximization (OSEM) method. The spatial resolution obtained with this reconstruction method ranged from 1.9 to 2.3 mm. Regions of interest were drawn around areas of maximum tracer uptake. The mice were injected with 150 μCi of [^{18}F]FB-E[c(RGDyK)]₂ via the tail vein, anesthetized with ketamine/xylazine at 1 hr pi and then centered in the FOV of the micro-PET. Mice were scanned for 15 min, and the raw data were framed into one static frame without attenuation correction. The micro-PET was calibrated in terms of absolute activity concentration (nCi/cc) by imaging a plastic bottle approximating the dimensions of a mouse body and filled with a known concentration of [18]F.

Whole-Body Autoradiography

Autoradiography was performed using a Packard Cyclone Storage Phosphor Screen system (Downers Grove, IL) and a Bright 5030/WD/MR cryomicrotome (Hacker Instruments, Fairfield, NJ). In order to correlate the results obtained from micro-PET and whole-body autoradiography, tumor-bearing mice were sacrificed under ketamine/xylazine anesthesia at 1 hr pi, followed by micro-PET imaging and subsequently cryosectioning for autoradiography. This procedure was followed in order to eliminate the possibility of change in tracer biodistribution between micro-PET and autoradiography. Immediately after micro-PET scanning, the euthanized mouse was frozen in dry ice and isopropyl alcohol bath for 2 min. The body was then embedded in 4% carboxymethyl cellulose (CMC) (Aldrich, Milwaukee, WI) in water mixture within a stainless steel mold. The mold was placed in the dry ice and isopropyl alcohol bath for 5 min and then into a −20°C freezer for 1 hr. The walls

of the mold were then removed, and the frozen block was mounted in the cryomicrotome. The block was cut into 50 μM sections, and desired sections were digitally photographed and then captured for autoradiography. The sections were transferred into a chilled film cassette containing a Super Resolution screen (spatial resolution 0.1 mm; Packard) and kept there overnight at −20°C. Screens were laser-scanned with the Packard Cyclone.

Statistical Analysis

The data are expressed as mean ± SD. Means were compared using one-way analysis of variance (ANOVA) and Student's t test. A p value of < .05 was considered significant.

Results

Radiosynthesis

Labeling of dimeric RGD peptide E[c(RGDyK)]$_2$ using [18F]SFB as a prosthetic group resulted in [18F]FB-E[c(RGDyK)]$_2$ (Figure 1) of high radiochemical purity (> 99%) according to analytical HPLC. The decay- corrected yield of [18F]FB-PEG-RGD, counted from [18F]SFB, ranged from 20% to 30% (in three preparations). The specific radioactivity of [18F]SFB was estimated by radio-HPLC to be 200–250 GBq/μmol at the end of synthesis (EOS) (or 300–400 GBq/μmol at end of bombardment [EOB]), based upon 9.25 GBq (250 mCi) of starting [18F]F$^-$. For micro-PET studies, the injected dose of 5.55 MBq (150 μCi) contained approximately 30–40 ng of [18F]FB-E[c(RGDyK)]$_2$. For biodistribution studies, the injected dose of 0.74 MBq (20 μCi) was composed of 4–5 ng of radioactive [18F]-labeled RGD dimer.
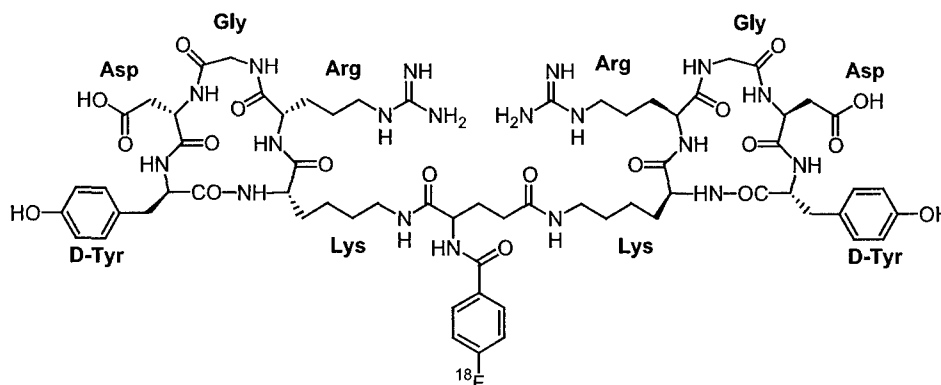
Receptor Binding Studies

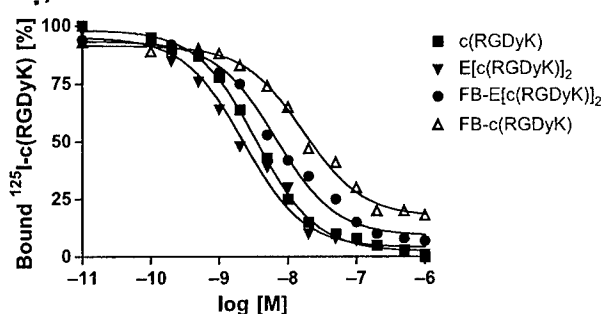All RGD peptide analogues tested in the displacement assays showed the expected sigmoid curves (Figure 2). The dimeric RGD peptide E[c(RGDyK)]$_2$ showed higher binding affinity (IC$_{50}$ = 2.3 ± 0.7 nM) for HBCECs as compared to the monomeric analogue c(RGDyK) (IC$_{50}$ = 3.5 ± 0.3 nM). Modification of the RGD peptides with the 4-fluorobenzoyl group somewhat decreased their binding avidity, with the IC$_{50}$ values for FB-c(RGDyK) and FB-E[c(RGDyK)]$_2$ being 16.9 ± 0.5 nM and 6.7 ± 0.5 nM, respectively.

Biodistribution

The biodistribution of [18F]-labeled dimeric RGD peptide ([18F]FB-E[c(RGDyK)]$_2$) in female nude mice bearing subcutaneous U87MG glioblastoma tumors are shown in Figure 3. Data were obtained at 30 min, 1 hr, 2 hr, and 4 hr postinjection. Tumor weights ranged from 0.3 to 0.5 g. The tracer showed rapid blood clearance, with initial blood radioactivity concentration of 0.81 ± 0.09 %ID/g at 30 min pi, and only 0.09 ± 0.1 %ID/g at 4 hr pi. Tumor uptake was rapid and high (6.79 ± 0.05 %ID/g at 30 min pi) with some tumor washout observed with time (uptake declined to 4.27 ± 1.04 and 2.04 ± 0.5 %ID/g, at 2 and 4 hr pi, respectively). Tumor-to-blood activity concentration ratio peaked at 4 hr (23 ± 2). Systemic clearance occurred predominately by renal excretion. Biodistribution data for [18F]FB-E[c(RGDyK)]$_2$ and [18F]FB-RGD [12,14] are compared in Figure 4. Tumor uptake of dimeric RGD was significantly higher than that of monomeric RGD at all time points (p < .001). At 2 hr after tracer administration, tumor uptake of [18F]FB-E[c(RGDyK)]$_2$ was 4.27 ± 1.04 %ID/g compared with only 1.56 ± 0.35 %ID/g for [18F]FB-RGD. Liver accumulation of monomeric RGD peptide was higher than that of dimeric RGD peptide (p < .001) at 30 min (2.50 ± 0.18 %ID/g for [18F]FB-RGD and 1.34 ± 0.18 %ID/g for [18F]FB-E[c(RGDyK)]$_2$), but the difference diminished with time. Renal uptake of the dimeric RGD peptide was significantly higher than that of the monomeric RGD peptide at all time points

Figure 1. Schematic structure of [18F]FB-E[c(RGDyK)]$_2$ (MW = 1473). [18F]-labeling was carried out via acylation of the amino group at the glutamate residue.

Figure 2. *In vitro displacement of ^{125}I-c(RGDyK) by c(RGDyK) (■), FB-c(RGDyK) (▼), E[c(RGDyK)]₂ (●), and FB-[c(RGDyK)]₂ (△) in HBCECs. Values are the mean of three determinations.*

examined. Consequently, the tumor-to-kidney ratio for the monomeric RGD peptide was higher than for the dimeric RGD peptide (2.8 ± 0.4 for [^{18}F]FB-RGD and 1.4 ± 0.2 for [^{18}F]FB-E[c(RGDyK)]₂ at 2 hr pi, respectively). It is also noteworthy that intestinal uptake of the dimeric RGD peptide was significantly lower than that of the monomeric RGD peptide. Coinjection of [^{18}F]FB-E[c(RGDyK)]₂ with 10 mg/kg of c(RGDyK) resulted in decreased uptake at 1 hr pi in all dissected tissues except the kidneys. The most pronounced reduction of uptake (4.27 ± 1.04 to 0.45 ± 0.11 %ID/g) occurred in tumor (Figure 5). A similar phenomenon has also been observed with other radiolabeled RGD peptides [8,11–16,22].
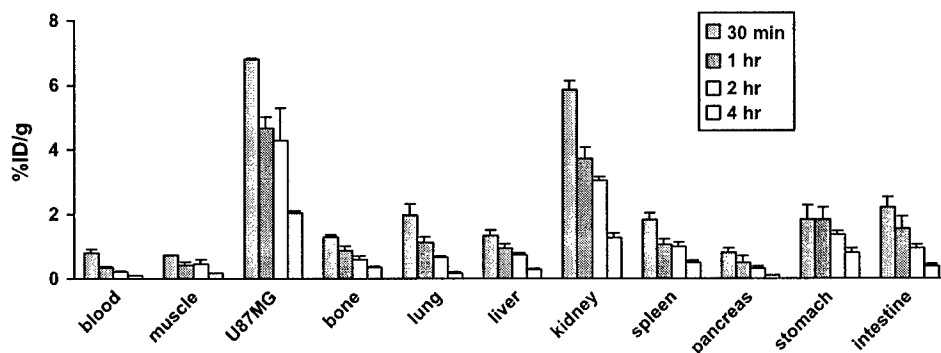
Micro-PET and Autoradiography

A 2-D projection micro-PET image (15 min static single frame beginning at 60 min after intravenous injection of 150 μCi of [^{18}F]FB-E[c(RGDyK)]₂) of a mouse bearing U87MG tumor on the right front leg is shown in Figure 6A. The tumor was clearly visible, with high contrast to contralateral background (ratio: 9.5 ± 0.8). Prominent uptake was also observed in the gallbladder and urinary bladder. Liver uptake was significantly lower than tumor uptake ($p < .001$), and activity accumulation in the kidneys was slightly higher than in tumor, which

agreed well with the data obtained from direct tissue sampling. Notice that, at the time of imaging, the activity in the intestinal tracts was very low, resulting in a very high-quality image and favorable tumor-to-nontumor ratios. As expected, no activity accumulation was observed in the normal brain, presumably due to a low level of αᵥ-integrin expression in the intact blood–brain barrier [21,25]. As a comparison, 2-D projection micro-PET image in the presence of [^{18}F]FB-RGD (15 min static scan at 1 hr postinjection of 150 μCi of monomeric RGD peptide radiotracer) is shown in Figure 6B. U87MG tumor on the right hind leg was visible with contrast to contralateral background, however, excessive activity accumulation in the intestinal tracts eliminated its possibility to visualize tumors in the lower abdomen [12,14].
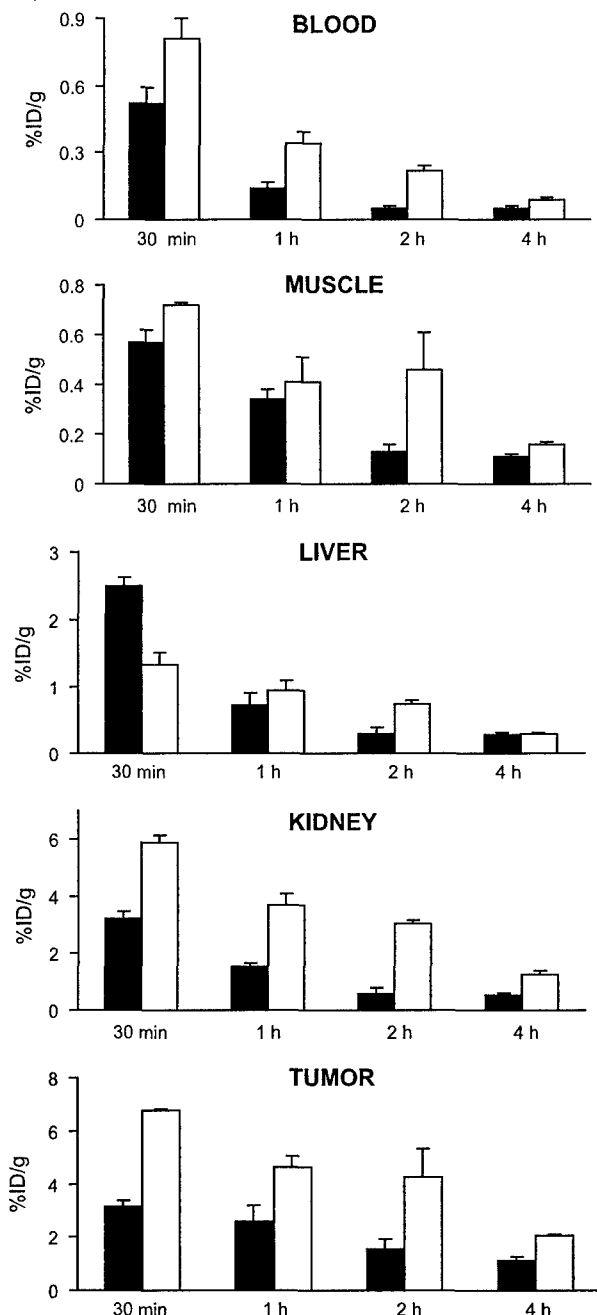
Quantification of tumor and major organ activity accumulation in micro-PET scans was performed on coronal views using regions of interest (ROIs) that encompassed entire organs. Uptake in the U87MG tumor, liver, and kidneys was calculated as 4.4 ± 0.6, 0.9 ± 0.1, and 3.6 ± 1.2 %ID/g, respectively. These results were in good agreement with the biodistribution data obtained at 1 hr pi except for the tumor, which was underestimated due to partial volume effect. For one mouse, micro-PET images obtained following injection of [^{18}F]FB-E[c(RGDyK)]₂ were compared with subsequent high-resolution (0.1 mm) autoradiography. Figure 7 compares a coronal micro-PET slice (thickness 1.2 mm) including the U87MG xenograft (Figure 7, left) with a corresponding autoradiographic section (thickness 0.05 mm, Figure 7, right); correlations between the regions of high uptake observed in the micro-PET scan and autoradiography were clearly demonstrated.

Discussion

This study demonstrates that ^{18}F-labeled dimeric RGD peptide [^{18}F]FB-E[c(RGDyK)]₂ has significantly improved tumor targeting efficacy, in particular, higher

Figure 3. *Biodistribution of [^{18}F]FB-E[c(RGDyK)]₂ in athymic nude mice bearing subcutaneous U87MG glioblastoma tumors (% ID/g: % injected dose per gram).*
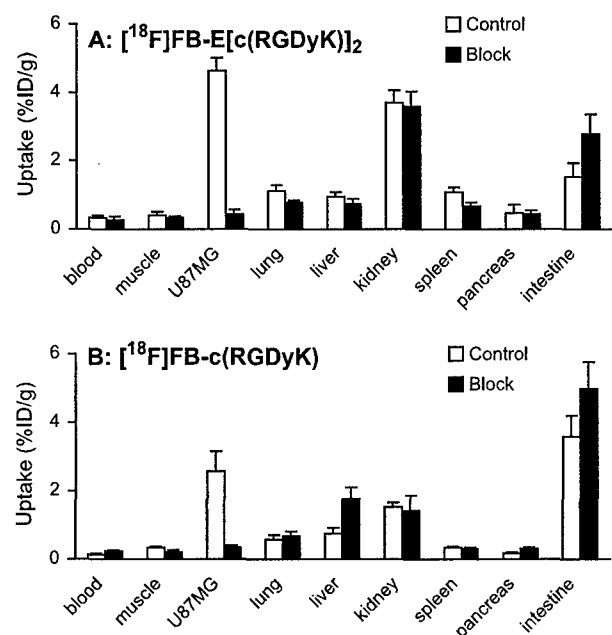
Figure 4. *Comparison of the biodistribution data of [^{18}F]FB-E[c(RGDyK)]$_2$ (□) and [^{18}F]FB-c(RGDyK) (■) in athymic nude mice with subcutaneous U87MG tumors.*

tumor uptake and prolonged tumor retention, compared to the monomeric RGD peptide analogue, [^{18}F]FB-c(RGDyK). Imaging of $\alpha_v\beta_3$-integrin positive U87MG glioblastoma tumor in an intact mouse using a high-resolution micro-PET scanner resulted in strong contrast between tumor and normal tissues at 1 hr after injection of [^{18}F]FB-E[c(RGDyK)]$_2$.
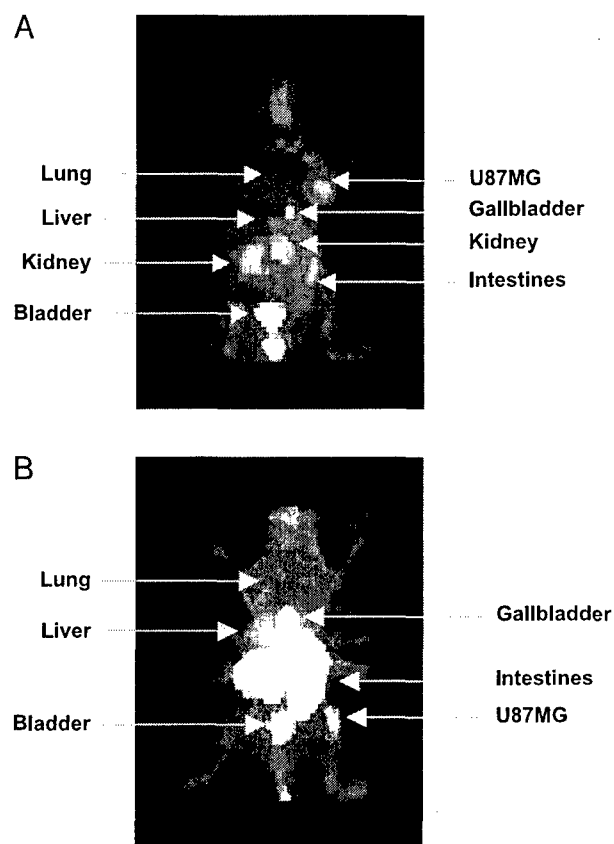
Dysangiogenesis is involved in most of the major human pathologies [25]. Angiogenic properties of tumors are considered to be critical determinants of

the potential for growth and metastasis. Angiogenic therapies have received a great deal of attention in recent years; methods to identify the angiogenic phenotypes of tumors and evaluate the efficacy of these therapies would be of great significance. Integrin receptors are implicated in many pathological processes, such as osteoporosis, misregulated angiogenesis (e.g., rheumatoid arthritis or retinopathy), thrombosis, and inflammation, as well as tumor growth and tumor metastasis [26]. Overexpression of $\alpha_v\beta_3$ integrin on the cell surfaces of tumor cells and activated ECs compared with resting ECs suggests the application of suitably labeled $\alpha_v\beta_3$ antagonists for imaging of receptor density levels in $\alpha_v\beta_3$-positive tumors. Potential antagonists include antibodies, cyclic RGD peptides, peptidomimetics of the confined RGD sequence, or small molecules. However, genetic ablation of α_v integrins in mice has been associated with enhanced pathological angiogenesis [27]. This seemingly paradoxical finding implies that the exact role of α_v in tumor angiogenesis is yet to be established. It is possible that α_v integrins are negative regulators of angiogenesis and that the drugs targeting them may be acting as agonists rather than antagonists [28].

Glioblastoma multiforme, the most malignant astroglial-derived tumor, grows as an adherent mass and locally invades normal brain [29]. Both brain capillary and brain tumor cells express high levels of $\alpha_v\beta_3$ and $\alpha_v\beta_5$ integrins in vitro and in vivo [30], as also observed in

Figure 5. *Biodistribution of [^{18}F]FB-E[c(RGDyK)]$_2$ (A) and [^{18}F]FB-c(RGDyK) (B) in the absence (control) and presence (block) of 10 mg/kg nonradioactive monomeric RGD peptide c(RGDyK) at 1 h pi in athymic nude mice with subcutaneous U87MG tumors.*

Figure 6. *(A) 2-D projection of U87MG bearing mouse 60 min after injection of 150 μCi of [18F]FB-E[c(RGDyK)]2 (15 min static image). Activity in the kidneys and urinary bladder reflects the renal excretion of the radiolabeled peptide. (B) 2-D projection of U87MG tumor-bearing mouse 60 min after injection of 150 μCi of [18F]FB-c(RGDyK) (15 min static image).*
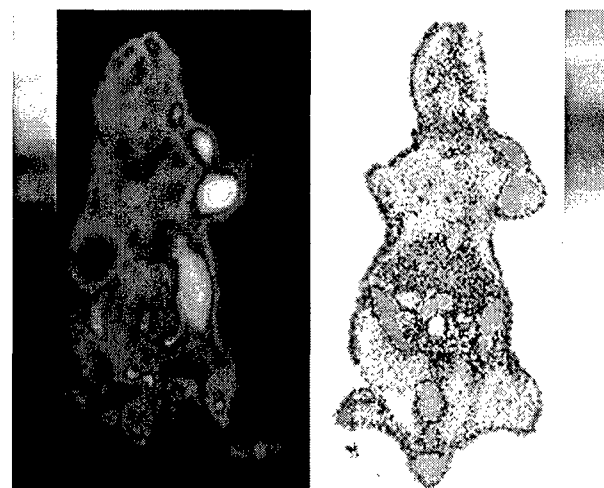
human brain tumor specimens [31]. EMD 121974, c(RGDf[NMe]V), an α_v-integrin antagonist, detaches both the α_v-integrin-expressing brain capillary and brain tumor cells from the matrix proteins vitronectin and tenascin, resulting in significant apoptosis of both cell types [32]. Also, daily administration of EMD 121974 inhibited growth of a glioblastoma (U87MG) cell line xenotransplanted into the forebrain of nude mice resulting in increased survival [32]. Suitably labeled RGD peptide may be used to visualize brain tumor growth, quantify integrin receptor expression, and follow anti-integrin treatment efficacy, as well as to develop more potent anti-integrin drugs based on the tracer targeting ability and in vivo kinetics.

Because of the very precise design of their configuration, modification and labeling of peptidomimetics and small molecule antagonists of $\alpha_v\beta_3$ integrin usually eliminate the receptor binding characteristics of such ligands. Furthermore, the lipophilicity of these types of ligands further limits their applicability for diagnostic imaging of $\alpha_v\beta_3$-integrin expression. On the other hand, cyclic RGD peptides, with suitable metabolic stability

and nanomolar binding affinity for $\alpha_v\beta_3$ integrin, are ideal for development of suitably labeled probes for tumor visualization, $\alpha_v\beta_3$-integrin quantification in vivo, and assessment of anti-integrin treatment efficacy. Cyclic RGD peptides have been labeled with 18F [11–17] and 64Cu [14] for PET, and 111In and 99mTc [8,19,33,34] for SPECT imaging studies. In addition, antibodies have been attached to the surface of microbubbles and liposomes for contrast-enhanced ultrasound [35] and magnetic resonance imaging [36] of tumor angiogenesis, respectively.

Although γ-emitting radiolabels are more readily available and in general have longer half-lives relative to β^+-emitting radionuclides, PET cameras have much higher sensitivity, better spatial resolution, and more accurate attenuation correction, and therefore better quantitative accuracy, than SPECT scanners [37]. The acquisition of higher count statistics is particularly valuable for detecting the fewest possible cells per unit volume with the least amount of radioactivity. We expect PET imaging with the 18F-labeled dimeric RGD peptide described here to provide higher sensitivity and resolution for early tumor detection and assessment of tumor treatment efficacy than SPECT imaging with 111In- and 99mTc-labeled peptide analogs.

18F-labeled monomeric RGD peptides, labeled either via electrophilic [17] or nucleophilic [11–14] substitution, have encountered the problems of rapid tumor washout and unfavorably high hepatobiliary excretion. Insertion of a sugar amino acid between the F-18 label and the RGD ligand increased the hydrophilicity of the peptide, which brought about improved in vivo pharma-

Figure 7. *Left: Micro-PET scan (15 min single frame) of U87MG tumor-bearing mouse sacrificed 1 hr after injection of 150 μCi of [18F]FB-E[c(RGDyK)]2. Right: Digital autoradiograph of the section containing tumor. Tumors were visualized in the right upper leg (arrows).*

cokinetics of the resulting PET tracer. An alternative to this sialidation/glycosylation approach is to introduce a poly(ethylene glycol) moiety into the original lipophilic radiotracer ([18F]FB-RGD). The PEGylated peptide [18F]FB-PEG-RGD has improved bioavailability, increased stability toward enzymatic degradation and solubility under physiological conditions compared with [18F]FB-RGD [13]. In this study, dimeric RGD peptide E[c(RGDyK)]$_2$ labeled with [18F] through the 4-fluorobenzoyl moiety showed both renal and hepatobiliary excretion pathways, resulting in significant activity accumulation in the gallbladder, kidneys, and urinary bladder (Figure 6B). The affinity and specificity of the radiotracer for α_v integrins and relatively slow blood clearance of the radiotracer might be responsible for the prominent tumor retention.

It has been proposed by several groups that the receptor binding characteristics of dimeric and multimeric RGD peptides would be better than that of monomeric RGD peptide based upon polyvalency [18]. Simultaneous binding of multiple RGD motifs within a single molecule to one integrin or binding of multiple integrins to a single multimeric RGD peptide induces cooperativity, entropically enhanced affinity, and steric stabilization [18]. Immobilized human placental $\alpha_v\beta_3$-receptor ELISA assays have indicated a more avid binding of the dimer than the monomeric RGD analogue [19]. Dimeric RGD peptide E[c(RGDfK)]$_2$ has thus been conjugated with 1,4,7,10-tetraazadodecane-N,N',N'',N-tetraacetic acid (DOTA) and labeled with ^{90}Y and ^{111}In [22], and with hydrazinonicotinamide (HYNIC) for ^{99m}Tc [19]. It has been demonstrated that uptake of the dimer is higher than that of the monomer in most organs and tissues, but kidney uptake is also higher for the dimer [19]. Because kidneys received the highest radiation dose among normal tissues and seems to be the dose-limiting organ for the dimeric RGD peptide tracer, further modification of the radioligand is thus needed to obviate too high a renal dose.

Maintenance of integrin receptor binding affinity was previously tested in HBCECs, which are known to express high levels of $\alpha_v\beta_3$ and $\alpha_v\beta_5$ integrins [30]. Dimeric RGD peptide revealed higher integrin receptor affinity than the monomeric analog. Fluorobenzoyl group labeling decreased the receptor binding affinity in vitro for both monomeric and dimeric RGD peptides, which might be attributed to the added hindrance upon substitution of the primary amines. In the current study, higher uptake of [18F]FB-E[c(RGDyK)]$_2$ as compared to [18F]FB-c(RGDyK) (Figure 4) might be attributed to more effective reabsorption of the dimeric RGD peptide and its

major metabolite into the negatively charged proximal renal tubular cells than that of the monomeric RGD analogue [8,19]. Whether the increased tumor targeting of dimeric RGD peptide was due to cooperative binding or pharmacological effects remains to be determined since there is no direct evidence about whether the spatial arrangement and separation of two RGD moieties is optimal for multiple cell surface integrin binding.

Receptor-specific tumor uptake of [18F]FB-E[c (RGDyK)]$_2$ was demonstrated by effective blocking of activity accumulation in U87MG glioblastoma xenograft resulting from coinjection of the radiotracer with monomeric RGD peptide c(RGDyK), which reportedly has high affinity and specificity for $\alpha_v\beta_3$ integrin [22]. It is unclear at this stage whether the visualization of the tumor is du to enhanced integrin expression on the neovasculature or enhanced integrin expression on tumor cells. Further validation of the noninvasive PET imaging requires correlation of the magnitude of tumor uptake with receptor density, which can be determined independently using antibodies that are specific to human $\alpha_v\beta_3$ integrin (U87MG tumor cells) and to mouse α_v and/or β_3 integrin (ECs). In order to address the ultimate goal of imaging in patients, model systems with intermediate integrin expression and negative controls should also be studied in order to represent the full extent of human presentations. Since PEGylation of monomeric RGD peptide significantly improved in vivo kinetics of the RGD peptide without compromising tumor-targeting efficacy [13,22], we expect that PEGylation may further enhance integrin targeting and improve the biodistribution of the dimeric RGD peptide tracer.

Acknowledgments

References

[1] Tonini T, Rossi F, Claudio PP (2003). Molecular basis of angiogenesis and cancer. *Oncogene.* **22**:6549–6556.

[2] Brower V (1999). Tumor angiogenesis—New drug on the block. *Nat Biotechnol.* **17**:963–968.

[3] Miranti CK, Brugge JS (2002). Sensing the environment: A historical perspective on integrin signal transduction. *Nat Cell Biol.* **4**:E83–E90.

[4] Tucker GC (2003). Alpha v integrin inhibitors and cancer therapy. *Curr Opin Investig Drugs.* **4**:722–731.

[5] Gutheil JC, Campbell TN, Pierce PR, Watkins JD, Huse WD, Bodkin DJ, Cheresh DA (2000). Targeted antiangiogenic therapy

for cancer using Vitaxin: a humanized monoclonal antibody to the integrin $a_v\beta_3$. *Clin Cancer Res.* **6**:3056–3061.

[6] Smith JW (2003). Cilengitide Merck. *Curr Opin Investig Drugs.* **4**:741–745.

[7] Kumar CC, Malkowski M, Yin Z, Tanghetti E, Yaremko B, Nechuta T, Varner J, Liu M, Smith EM, Neustadt B, Presta M, Armstrong L (2001). Inhibition of angiogenesis and tumor growth by SCH221153, a dual $\alpha_v\beta_3$ and $\alpha_v\beta_5$ integrin receptor antagonist. *Cancer Res.* **61**:2232–2238.

[8] Janssen ML, Oyen WJ, Dijkgraaf I, Massuger LF, Frielink C, Edwards DS, Rajopadhye M, Boonstra H, Corstens FH, Boerman OC (2002). Tumor targeting with radiolabeled $\alpha_v\beta_3$ integrin binding peptides in a nude mouse model. *Cancer Res.* **62**: 6146–6151.

[9] Burke PA, DeNardo SJ, Miers LA, Lamborn KR, Matzku S, DeNardo GL (2002). Cilengitide targeting of $\alpha_v\beta_3$ integrin receptor synergizes with radioimmunotherapy to increase efficacy and apoptosis in breast cancer xenografts. *Cancer Res.* **62**:4263–4272.

[10] Liu S, Robinson SP, Edwards DS (2003). Integrin $\alpha_v\beta_3$ directed radiopharmaceuticals for tumor imaging. *Drugs of the Future.* **28**:551–564.

[11] Chen X, Shahinian AH, Park R, Bozorgzadeh MH, Bading JR, Conti PS (2003). ^{18}F-labeled cyclic RGD peptide for PET imaging of tumor angiogenesis. *J Nucl Med.* **44**:47P.

[12] Chen X, Park R, Shahinian AH, Tohme M, Khankaldyyan V, Bozorgzadeh MH, Bading JR, Moats R, Laug WE, Conti PS (2004). ^{18}F-Labeled RGD peptide: Initial evaluation for imaging brain tumor angiogenesis. *Nucl Med Biol.* **31**:179–89.

[13] Chen X, Park R, Hou Y, Khankaldyyan V, Gonzales-Gomez I, Tohme M, Bading JR, Laug WE, Conti PS (In press). MicroPET imaging of brain tumor angiogenesis with ^{18}F-labeled PEGylated RGD peptide. *Eur J Nucl Med Mol Imaging.*

[14] Chen X, Park R, Tohme M, Bading JR, Conti PS (2004). [18]F and ^{64}Cu-labeled RGD peptide for imaging breast cancer in mice with microPET. *Bioconjugate Chem.* **15**:41–49.

[15] Haubner R, Wester HJ, Weber WA, Mang C, Ziegler SI, Goodman SL, Senekowitsch-Schmidtke R, Kessler H, Schwaiger M (2001). Noninvasive imaging of $\alpha_v\beta_3$ integrin expression using ^{18}F-labeled RGD-containing glycopeptide and positron emission tomography. *Cancer Res.* **61**:1781–1785.

[16] Haubner R, Kuhnast B, Mang C, Weber WA, Kessler H, Wester H-J, Schwaiger M (2004). [^{18}F]Galacto-RGD: Synthesis, radiolabeling, metabolic stability, and radiation dose estimates. *Bioconjugate Chem.* **15**:61–69.

[17] Ogawa M, Hatano K, Oishi S, Kawasumi Y, Fujii N, Kawaguchi M, Doi R, Imamura M, Yamamoto M, Ajito K, Mukai T, Saji H, Ito K (2003). Direct electrophilic radiofluorination of a cyclic RGD peptide for in vivo $\alpha_v\beta_3$ integrin related tumor imaging. *Nucl Med Biol.* **30**:1–9.

[18] Marshall GR (2001). Peptide interactions with G-protein coupled receptors. *Biopolymers.* **60**:246–277.

[19] Thumshirn G, Hersel U, Goodman SL, Kessler H (2003). Multimeric cyclic RGD peptides as potential tools for tumor targeting: Solid-phase peptide synthesis and chemoselective oxime ligation. *Chemistry.* **9**:2717–2725.

[20] Janssen M, Oyen WJ, Massuger LF, Frielink C, Dijkgraaf I, Edwards DS, Radjopadhye M, Corstens FH, Boerman OC (2002). Comparison of a monomeric and dimeric radiolabeled RGD-peptide for tumor targeting. *Cancer Biother Radiopharm.* **17**:641–646.

[21] Mammen M, Chio SK, Whitesides GM (1998). Polyvalent interactions in biological systems: Implications for design and use of multivalent ligands and inhibitors. *Angew Chem Int Engl.* **37**:2755–2794.

[22] Chen X, Park R, Shahinian AH, Bading JR, Conti PS (2004). Pharmacokinetics and tumor retention of ^{125}I-labeled RGD peptide are improved by PEGylation. *Nucl Med Biol.* **31**:11–19.

[23] Liu S, Cheung E, Ziegler MC, Rajopadhye M, Edwards DS (2001). [90]Y and ^{177}Lu labeling of a DOTA-conjugated vitronectin receptor antagonist useful for tumor therapy. *Bioconjugate Chem.* **12**: 559–568.

[24] Stins MF, Gilles F, Kim KS (1997). Selective expression of adhesion molecules on human brain microvascular endothelial cells. *J Neuroimmunol.* **76**:81–90.

[25] Folkman J (2003). Fundamental concepts of the angiogenic process. *Curr Mol Med.* **3**:643–651.

[26] Ruegg C, Mariotti A (2003). Vascular integrins: Pleiotropic adhesion and signaling molecules in vascular homeostasis and angiogenesis. *Cell Mol Life Sci.* **60**:1135–1157.

[27] Reynolds LE, Wyder L, Lively JC, Taverna D, Robinson SD, Huang X, Sheppard D, Hynes RO, Hodivala-Dilke KM (2002). Enhanced pathological angiogenesis in mice lacking β_3 integrin or β_3 and β_5 integrins. *Nat Med.* **8**:27–34.

[28] Hynes RO (2002). A reevaluation of integrins as regulators of angiogenesis. *Nat Med.* **8**:918–921.

[29] Gladson CL, Cheresh DA (1991). Glioblastoma expression of vitronectin and the $\alpha_v\beta_3$ integrin. Adhesion mechanism for transformed glial cells. *J Clin Invest.* **88**:1924–1932.

[30] Taga T, Suzuki A, Gonzalez-Gomez I, Gilles FH, Stins M, Shimada H, Barsky L, Weinberg KI, Laug WE (2002). Alpha v-integrin antagonist EMD 121974 induces apoptosis in brain tumor cells growing on vitronectin and tenascin. *Int J Cancer.* **98**:690–697.

[31] Tonn JC, Wunderlich S, Kerkau S, Klein CE, Roosen K (1998). Invasive behaviour of human gliomas is mediated by interindividually different integrin patterns. *Anticancer Res.* **18**: 2599–2605.

[32] MacDonald TJ, Taga T, Shimada H, Tabrizi P, Zlokovic BV, Cheresh DA, Laug WE (2001). Preferential susceptibility of brain tumors to the antiangiogenic effects of an α_v integrin antagonist. *Neurosurgery.* **48**:151–157.

[33] Van Hagen PM, Breeman WA, Bernard HF, Schaar M, Mooij CM, Srinivasan A, Schmidt MA, Krenning EP, de Jong M (2000). Evaluation of a radiolabelled cyclic DTPA-RGD analogue for tumour imaging and radionuclide therapy. *Int J Cancer.* **90**: 186–198.

[34] Su ZF, Liu G, Gupta S, Zhu Z, Rusckowski M, Hnatowich DJ (2002). In vitro and in vivo evaluation of a Technetium-99m-labeled cyclic RGD peptide as a specific marker of $\alpha_v\beta_3$ integrin for tumor imaging. *Bioconjug Chem.* **13**:561–570.

[35] Leong-Poi H, Christiansen J, Klibanov AL, Kaul S, Lindner JR (2003). Noninvasive assessment of angiogenesis by ultrasound and microbubbles targeted to α_v-integrins. *Circulation.* **107**: 455–460.

[36] Sipkins DA, Cheresh DA, Kazemi MR, Nevin LM, Bednarski MD, Li KC (1998). Detection of tumor angiogenesis in vivo by $\alpha_v\beta_3$-targeted magnetic resonance imaging. *Nat Med.* **4**:623–626.

[37] Chatziioannou AF, Cherry SR, Shao Y, Silverman RW, Meadors K, Farquhar TH, Pedarsani M, Phelps ME (1999). Performance evaluation of microPET: A high-resolution lutetium oxyorthosilicate PET scanner for animal imaging. *J Nucl Med.* **40**: 1164–1175.

In vivo Near-Infrared Fluorescence Imaging of Integrin $\alpha_v\beta_3$ in Brain Tumor Xenografts

Xiaoyuan Chen,[1,2] Peter S. Conti,[1] and Rex A. Moats[3]

[1]PET Imaging Science Center, University of Southern California Keck School of Medicine, Los Angeles, California; [2]Molecular Imaging Program at Stanford, Stanford University, Stanford, California; and [3]Departments of Pediatrics, Radiology, and Pathology, Children's Hospital Los Angeles, Los Angeles, California

ABSTRACT

Noninvasive visualization of cell adhesion molecule $\alpha_v\beta_3$ integrin expression in vivo has been well studied by using the radionuclide imaging modalities in various preclinical tumor models. A literature survey indicated no previous use of cyanine dyes as contrast agents for in vivo optical detection of tumor integrin. Herein, we report the integrin receptor specificity of novel peptide-dye conjugate arginine-glycine-aspartic acid (RGD)-Cy5.5 as a contrast agent in vitro, in vivo, and ex vivo. The RGD-Cy5.5 exhibited intermediate affinity for $\alpha_v\beta_3$ integrin ($IC_{50} = 58.1 \pm 5.6$ nmol/L). The conjugate led to elevated cell-associated fluorescence on integrin-expressing tumor cells and endothelial cells and produced minimal cell fluorescence when coincubated with c(RGDyK). In vivo imaging with a prototype three-dimensional small-animal imaging system visualized subcutaneous U87MG glioblastoma xenograft with a broad range of concentrations of fluorescent probe administered via the tail vein. The intermediate dose (0.5 nmol) produces better tumor contrast than high dose (3 nmol) and low dose (0.1 nmol) during 30 minutes to 24 hours postinjection, because of partial self-inhibition of receptor-specific tumor uptake at high dose and the presence of significant amount of background fluorescence at low dose, respectively. The tumor contrast was also dependent on the mouse viewing angles. Tumor uptake of RGD-Cy5.5 was blocked by unlabeled c(RGDyK). This study suggests that the combination of the specificity of RGD peptide/integrin interaction with near-infrared fluorescence detection may be applied to noninvasive imaging of integrin expression and monitoring anti-integrin treatment efficacy providing near real-time measurements.

INTRODUCTION

Integrins $\alpha_v\beta_3$ and $\alpha_v\beta_5$ seem to play a critical role in regulating tumor growth and metastasis as well as tumor angiogenesis (1–5). Although only minimally expressed in quiescent blood vessels and normal cells, α_v integrins are significantly up-regulated in sprouting tumor vessels and solid tumor cells of various origins (4, 5), and their expression levels correlate well with the aggressiveness of the disease (6–8). Antibodies, small inhibitory peptides, and nonpeptide antagonists of α_v-integrins have thus been developed as potential antiangiogenic strategies (1, 9–11).

The ability to noninvasively visualize and quantify α_v-integrin level in vivo would allow us to understand the intrinsic relationship between α_v-integrin expression and tumor growth and spread, to evaluate anti-integrin treatment efficacy, and to develop new integrin antagonists of high potency (12, 13) with pertinent in vivo pharmacokinetics. With a similar aim in mind, researchers have labeled a series of monomeric and dimeric cyclic arginine-glycine-aspartic acid (RGD)

peptides with different radionuclides for positron emission tomography (PET; refs. 14–17) and single-photon emission computed tomography (SPECT; 18, 19) imaging of α_v-integrin expression in various preclinical xenograft models, with tumor targeting efficacy and in vivo kinetics profiles being a factor of the receptor binding affinity and hydrophilicity, as well as of the metabolic stability of the radiotracers.

Although radionuclide imaging modalities are characteristic of high sensitivity and noninvasiveness, they often suffer from poor spatial and temporal resolution. Another characteristic of PET imaging, in particular, is the need for a local cyclotron to generate short-lived positron emitting radionuclides and a synthetic unit to produce the biologically useful probes. A relatively inexpensive, robust, and straightforward way of measuring integrin levels at least in a relative manner that also provides the possibility of semiquantitative evaluation would greatly aid the study of tumor biology. Optical imaging, which uses neither ionizing radiation nor radioactive materials, is emerging as a complement to nuclear imaging methods. The major limitation of light is the high absorption and scattering that occur in biological tissues and, thus, the limited penetration of the light through the body. However, in small animals, the required path-length of light is much shorter, which makes the use of optics more feasible. The ease of using short acquisition times also allows the collection of multiple time points and examinations in the same animal. Near-infrared (NIR) fluorescence imaging, in particular, is expected to have a major impact in biomedical imaging of specific targeting. In general, biological tissues exhibit a high photon absorbance in both the visible wavelength range (350–700 nm; secondary to hemoglobin, tissue pigments, and so forth) and in the infrared range (> 900 nm; secondary to lipids and water). However, in the NIR region (700–900 nm) the absorbance spectra for all biomolecules reach minima. Hence, NIR fluorescence light offers a unique advantage for the imaging of pathophysiological states (20). Thus, we chose the widely used Cy5.5 dye for our optical imaging studies.

NIR fluorescent dye Cy5.5 has proved to be a promising contrast agent for the in vivo demarcation of tumors by several groups (21–24). This dye has absorbance maximum at 675 nm and emission maximum at 694 nm, and can be detected in vivo at subnanomole quantities and at depths sufficient for experimental or clinical imaging depending on the NIR fluorescence image acquisition technique. In this study, we report in vivo NIR fluorescence imaging of integrin $\alpha_v\beta_3$-positive U87MG glioblastoma model targeted by a RGD-Cy5.5 conjugate. We demonstrate receptor specificity and long-lasting tumor accumulation of this fluorescent probe in human primary tumor cells in mouse xenografts.

MATERIALS AND METHODS

Materials. Cyclic RGD peptide [(c(RGDyK); M_r 617.6] was synthesized via solution cyclization of the fully protected linear pentapeptide H-Gly-Asp(OtBu)-D-Tyr(OtBu)-Lys[tert-butoxycarbonyl (Boc)]-Arg[2,2,4,6,7-pentamethyldihydrobenzofuran-5-sulfonyl (Pbf)]-OH, followed by trifluoroacetic acid deprotection (25). Cy5.5 monofunctional N-hydroxysuccinimide (NHS) ester (Cy5.5-NHS) and ^{125}I-labeled echistatin labeled by the lactoperoxidase method to a specific activity of 2.000 Ci/mmol were purchased from Amersham Biosciences (Piscataway, NJ). Echistatin was purchased from Sigma

(St. Louis, MO). Chromalux HB microplates were obtained from Dynex Technologies (Chantilly, VA).

Synthesis and Characterization of RGD-Cy5.5. Cyclic RGD peptide [c(RGDyK); 3 mg, 4.84 μmol] dissolved in 1 mL of 0.1 mol/L sodium borate (Na$_2$B$_4$O$_7$) buffer (pH = 8.3) was mixed with Cy5.5-NHS (5.6 mg, 5 μmol) in H$_2$O (1 mL) in the dark at 4°C. After stirring overnight in the dark at 4°C, we quenched the reaction by adding 200 μL of 5% acetic acid (HOAc). The purification of the crude product was carried out on a semipreparative reversed-phase high-performance liquid chromatography (HPLC) system (Waters 515 chromatography system with a 486 tunable absorbance detector). Version 7.2.1 Labtech Notebook/XE software (Andover, MA) was used to record chromatograms. Purification was performed on a Vydac protein and peptide column 218TP510 (5 μm, 250 × 10 mm). The flow was 5 mL/minute, with the mobile phase starting from 95% solvent A (0.1% trifluoroacetic acid in water) and 5% solvent B (0.1% trifluoroacetic acid in acetonitrile; 0 to 2 minutes) to 35% solvent A and 65% solvent B at 32 minutes. The analytic HPLC method was performed with the same gradient system but with a Vydac 218TP54 column (5 μm, 250 × 4.6 mm) and flow was 1 mL/minute. The absorbance was monitored at 218 nm. The peak containing the RGD-Cy5.5 conjugate was collected, lyophilized, redissolved in saline at a concentration of 1 mg/mL, and stored in the dark at −80°C until use.

Solid-Phase Receptor Binding Assay. The standard assay was carried out as described previously with modifications (26). Microtiter-2 96-well plates were coated with 100 μL-per-well integrin $\alpha_v\beta_3$ (500 ng/mL) in coating buffer [25 mmol/L Tris–HCl (pH 7.4), 150 mmol/L NaCl, 1 mmol/L CaCl$_2$, 0.5 mmol/L MgCl$_2$, and 1 mmol/L MnCl$_2$] for 16 hours at 4°C, and the wells were blocked for 2 hours with 200 μL blocking buffer (coating buffer in the presence of 1% radioimmunoassay grade bovine serum albumin). The plate was washed twice with binding buffer (coating buffer in the presence of 0.1% bovine serum albumin) and then was incubated with ^{125}I-labeled echistatin (0.06 nmol/L) in the presence of different concentrations of RGD peptide (0.1 nmol/L to 5 μmol/L) at room temperature for 3 hours. After incubation, the plate was washed three times with binding buffer, and the radioactivity was solubilized with 2 mol/L boiling NaOH and was subjected to gamma-counting (Packard, Meriden, CT). Nonspecific binding of ^{125}I-labeled echistatin to $\alpha_v\beta_3$ was determined in the presence of 100 nmol/L echistatin. The IC_{50} values were calculated by nonlinear regression analysis with the GraphPad Prism computer-fitting program (GraphPad Software, Inc., San Diego, CA). Each data point is a result of the average of triplicate wells.

Cell Lines. Human glioblastoma cell line U87MG was obtained from American Type Culture Collection (Manassas, VA) and was maintained at 37°C in a humidified atmosphere containing 5% CO$_2$ in Iscove's modified Dulbecco's medium and 5% fetal bovine serum (Life Technologies, Inc., Grand island, NY). Primary human brain capillary endothelial cells (HBCECs) were isolated, characterized, and grown in RPMI 1640 with 10% fetal bovine serum in 5% CO$_2$ at 37°C.

Tumor Xenografts. Animal procedures were performed according to a protocol approved by the University of Southern California Institutional Animal Care and Use Committee. Female athymic nude mice (*nu/nu*), obtained from Harlan (Indianapolis, IN) at 4 to 6 weeks of age, were given injections subcutaneously in the right foreleg with 5 × 10^6 U87MG glioblastoma cells suspended in 100 μL of PBS. When the tumors reached 0.4 to 0.6 cm in diameter (14–21 days after implant), the tumor-bearing mice were subject to *in vivo* imaging studies.

Confocal Microscopy. We used a Leica TCS SP1 confocal optics, Ar ion (488 nm), Kr ion (568 nm), and HeNe (633 nm) lasers on a Leica DM IRBE microscope stand with HCX PL APO CS 63 ×/1.40 NA oil immersion objective lens, pinhole 1.0 Airy units, nominal Z resolution 236 nm, image (310 × 310-nm pixel size, medium speed, ~1 second per scan frame, 512 × 512 pixel image format, with 8 frame averaging. For laser confocal microscopy, cells grown on 35-mm MatTek imaging dishes (Cat no. P35G-0-14-C, Ashland, MA) were washed with PBS and then were incubated at 37°C in the presence of 100 nmol/L RGD-Cy5.5 for 1 hour. Afterward, cells were washed in ice-cold PBS and were examined with a TD488/568/633 dichroic beam splitter, simultaneous 488-nm excitation and photomultiplier tube-1 (PMT1) 522-to-578 nm emission for autofluorescence, 633-nm excitation, and PMT2 685-to-765 nm emission for RGD-Cy5.5 and both lasers for (nonconfocal) bright-field transmitted light. PMT1 and 2 were operated at high gain (1167 and 1054 V, respectively) and were offset adjusted such that the no-light

noise floor was above gray value zero. There was no autofluorescence in PMT2 (Cy5.5 channel).

In vivo Optical Imaging System. *In vivo* fluorescence imaging was performed with a prototype Xenogen IVIS three-dimensional small-animal *in vivo* imaging system (Xenogen, Alameda, CA), with both bioluminescence and fluorescence capabilities. The Xenogen instrument is a temperature-controlled, light-tight box with a cryogenically cooled back-illuminated digital charge-coupled device (CCD) camera, and anesthesia inlet and nose cone and gas outlet. For fluorescence a 150-W tungsten-halogen lamp is used with a light guide to a six-position excitation filter wheel. A second filter wheel, with large aperture to accommodate the camera, has six emission positions. Images and measurements of fluorescent signals were acquired and analyzed with Living Image software. An optimized Cy5.5 filter set was used for acquiring RGD-Cy5.5 fluorescence *in vivo*. Identical illumination settings (lamp voltage, filters) were used for all images, and fluorescence emission was normalized to photons per second per centimeter squared per steradian (p/s/cm^2/sr), as is common in bioluminescence imaging. Mice were given injections via tail vein with different amounts of RGD-Cy5.5 (0.1 to 3 nmol) and were anesthetized with 2 to 3% isoflurane (Abbott Laboratories) before they were placed in the Xenogen and imaged at various time points postinjection with a sampling of multiple angles while remaining sedated. A mouse that received an injection of 0.5 nmol of RGD-Cy5.5 was euthanized at 4 hours postinjection, the tumor and major tissue and organs were dissected, and fluorescence image was obtained.

Data Processing and Statistics. All of the data are given as means ± SD of *n* independent measurements. Statistical analysis was performed with a Student's *t* test. Statistical significance was assigned for *P* values < 0.05. For determining tumor contrast, mean fluorescence intensities and mean fluorescence intensities of the tumor (T) area at the right shoulder of the animal and of the corresponding area [normal tissue (N)] at the left shoulder were calculated by the region-of-interest function of Living Image software (Xenogen) integrated with Igor (Wavemetrics, Lake Oswego, OR). Dividing T by N yielded the contrast between tumor tissue and normal tissue.

RESULTS

Synthesis and Characterization of RGD-Cy5.5. The schematic molecule structure of c(RGDyK)-Cy5.5 conjugate (*RGD-Cy5.5*) is shown in Fig. 1. The NHS ester of the NIR fluorophore Cy5.5 is reacted with the ϵ-amino group of the lysine residue and purified by semipreparative HPLC. The absorption and fluorescence emission characteristics of RGD-Cy5.5 conjugate were similar to those of free Cy5.5, as apparent from the spectra measured in H$_2$O, except that the emission maximum slightly blue shifted from 694 nm (Cy5.5-NHS ester) to 690 nm (RGD-Cy5.5 conjugate). The yield of RGD-Cy5.5 conjugate was typically 70 to 75% as calculated with $\epsilon_{678\,nm}$ = 250,000 (mol/L)$^{-1}$cm^{-1}. The retention time on analytical HPLC was 16.6 minutes. Matrix-assisted laser desorption/ionization–time-of-flight mass spectrometry (MALDI-TOF MS): m/z = 1518.4 for [M + H]$^+$ (calculated M_r for C$_{68}$H$_{83}$N$_{11}$O$_{21}$S$_4$, 1518.7), m/z = 1536.4 for [M + Na]$^+$, and m/z = 1556.4 for [M + K]$^+$.
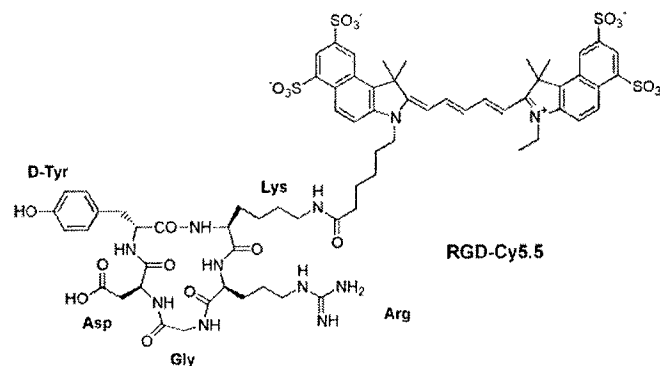

Fig. 1. Schematic structure of the RGD-Cy5.5 conjugate.

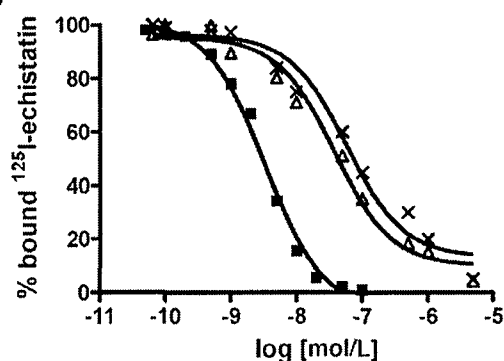Fig. 2. Competition of specific binding of ^{125}I-labeled echistatin with unlabeled echistatin (■), c(RGDyK) (△), and c(RGDyK)-Cy5.5 (✕) to purified $\alpha_v\beta_3$ integrin as determined with the solid-phase receptor assay. All of the points were done in triplicate. Cy5.5 conjugation did not significantly decrease the receptor binding affinity of the resulting fluorescent cyclic RGD peptide.

Receptor Binding Studies. To determine whether Cy5.5 conjugation had any effect on $\alpha_v\beta_3$ integrin receptor binding characteristics of the cyclic RGD peptide c(RGDyK), we measured the IC_{50} values of the RGD peptide analogues in competitive-type experiments. Binding of cold echistatin, c(RGDyK), and RGD-Cy5.5 competed with ^{125}I-labeled echistatin in a concentration-dependent manner (Fig. 2). Modification of the RGD peptide with Cy5.5 somewhat decreased its receptor binding avidity, with the IC_{50} values for c(RGDyK) and RGD-Cy5.5 being 37.5 ± 3.4 nmol/L and 58.1 ± 5.6 nmol/L, respectively.

To demonstrate that the RGD-Cy5.5 conjugate can act as a specific ligand for $\alpha_v\beta_3$ integrin receptor, the binding and subcellular localization of cyanine dye-labeled RGD peptide were incubated with U87MG tumor cells and HBCECs that are known to overexpress $\alpha_v\beta_3$ integrin. Negligible signals were detected in both cell lines when cells were incubated with Cy5.5 dye (data not shown). Receptor-mediated endocytosis of the RGD-Cy5.5 conjugate was observed by confocal laser-scanning microscopy in both cell types (Fig. 3A, C and F, H). Binding of RGD-Cy5.5 to both cell types was completely blocked by coincubation of the conjugate and c(RGDyK; 1 μmol/L; Fig. 3D, I).

In vivo **Fluorescence Imaging with RGD-Cy5.5.** Figure 4A shows typical NIR fluorescence images of athymic nude mice bearing subcutaneous U87MG glioblastoma tumor after intravenous injection of 3 nmol of RGD-Cy5.5. The whole animal became fluorescent immediately after injection, and the subcutaneous U87MG tumor could be clearly delineated from the surrounding background tissue from 30 minutes to 24 hours postinjection with maximum contrast occurring ~4 hours postinjection. Significantly, the amount of fluorescence was still detectable in the tumor at 48 hours after contrast injection (data not shown). The fluorescence intensities defined as photons per second per centimeter squared per steradian ($p/s/cm^2/sr$) in the tumor and the normal tissues as a function of time are depicted in Fig. 5. The tumor uptake reached a maximum at 2 hours postinjection and slowly washed out over time. On the other hand, normal tissue had rapid uptake and relatively rapid clearance. The dose dependence of tumor-to-normal tissue contrast was also measured (Fig. 5). Substantial difference in tumor contrast was observed from 30 minutes to 4 hours postinjection The mice that were given injections of 3-nmol fluorescent probe had the lowest tumor contrast, whereas those with the 0.5-nmol probe had the highest tumor contrast. The mice injected with the 0.1-nmol probe had intermediate contrast. The difference diminished at the 24-hour time point. The tumor contrast was significantly higher at 60° than at 0° for both control and block animals.

To validate the specificity of the targeting process, we performed a blocking experiment. The control mice were each given injections of 0.5 nmol of RGD-Cy5.5, and those as in the blocking experiment were each given coinjections of 0.5 nmol of RGD-Cy5.5 and 10 mg/kg unlabeled RGD peptide (~300 nmol). Tumor-to-normal tissue ratios at different viewing angles (0°, 45°, and 60°) were measured (Table 1) and typical NIR fluorescence images of U87MG-tumor-bearing mice mounted at 60° are shown in Fig. 4B (*left*, control; *right*, block). Unlabeled RGD peptide successfully reduced tumor contrast from 3.34 ± 0.38 to 1.43 ± 0.34 (Table 1). Furthermore, *ex vivo* evaluation of excised organs at 4 hours postinjection (Fig. 4C) showed that the compound was predominantly taken up by the U87MG tumor, with both tumor fluorescence intensity and contrast significantly higher than those obtained from *in vivo* imaging ($P < 0.0001$).

Fig. 3. Specific binding and endocytosis of the Cy5.5-labeled cyclic RGD peptide c(RGDyK). Confocal laser-scanning microscopy images of U87MG human glioblastoma (A–E) and HBCECs (F–J) incubated for 1 hour at 37°C in the presence of 100 nmol/L RGD-Cy5.5 with (D–E, I–J) or without (A–C, F–H) blocking dose of nonfluorescent RGD peptide c(RGDyK). 10 μmol/L. A, F NIR fluorescence images of U87MG (A) and HBCECs (F); B, G, direct visualization of U87MG (B) and HBCECs (G); C, H, merged images of A/B and F/G, respectively. D, I, complete blocking of NIR fluorescence of both U87MG cells (D) and HBCECs (I), demonstrating the high $\alpha_v\beta_3$ integrin specificity of the conjugate. E, J, direct visualization of U87MG (E) and HBCECs (J) under blocking condition.

Fig. 4. *A, in vivo* fluorescence imaging of sub-cutaneous U87MG glioblastoma tumor-bearing athymic nude mice after intravenous injection of RGD-Cy5.5 conjugate. Dye-labeled RGD peptide was administered at a dose of 3 nmol/mouse via a lateral tail vein. All NIR fluorescence images were acquired with a 120-second exposure time (f/stop = 4) at 10 and 30 minutes (min) and at 1, 2, 4, and 24 hours (h) and are normalized to the 10-minute (*10 min*) dorsal image. *Arrow,* the position of the tumor. Fluorescence signal from Cy5.5 was pseudo-colored red. *B,* representative NIR images (60° mounting angle) of mice bearing subcutaneous U87MG tumor on the right shoulder demonstrating blocking of RGD-Cy5.5 (0.5 nmol) uptake in the tumors by coinjection with c(RG-DyK), 10 mg/kg. Pseudo-color fluorescence images of tumor-bearing mice were acquired 4 hours after intravenous injection of RGD-Cy5.5 (*left, Experiment*) or RGD-Cy5.5 + RGD (*right, Block*). *C,* representative images of dissected organs of a mouse bearing U87MG tumor sacrificed 4 hours after intravenous injection of RGD-Cy5.5 at a dose of 0.5 nmol equivalent Cy5.5/mouse. *1,* U87MG tumor; *2,* muscle; *3,* pancreas; *4,* liver; *5,* kidney; *6,* spleen; *7,* lung.

10 min   30 min   1 h   2 h   4 h   24 h

A

Experiment   Block

B   **C**

DISCUSSION

The emergence of molecular imaging, as a result of unprecedented advances in molecular and cell biology and the availability of a cohort of molecular probes that are highly target specific, as well as the successful development of small-animal imaging instrumentation, allows noninvasive visualization of molecular events within living subjects. This emergence thus bridges the divide between the established findings from

Table 1 *Tumor-to-normal tissue ratios at 3 hours postinjection of control (0.5 nmol RGD-Cy5.5) and block (0.5 nmol RGD-Cy5.5 + 100 nmol RGD) mice at different mounting angles*

Mounting angle (°)	Control	Block
0	2.13 ± 0.28	0.85 ± 0.17
45	3.02 ± 0.45	1.33 ± 0.26
60	3.34 ± 0.38	1.43 ± 0.34

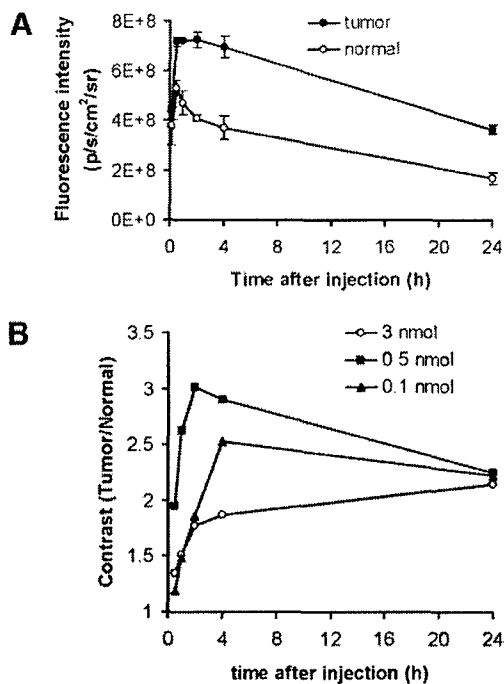NOTE. The data are denoted as mean ± SD ($n = 3$).

A

B

Fig. 5. *A,* quantification and kinetics of *in vivo* targeting character of RGD-Cy5.5 conjugate. Fluorescence intensity was recorded as photons per second per centimeter squared per steradian (*p/s/cm²/sr*). Tumor fluorescence washout was slower than that in the normal tissue. *B,* dose-dependent tumor contrast (tumor-to-normal tissue ratio) as a function of time[hour (*h*)] after administration: ○, 3 nmol; ■, 0.5 nmol; ▲, 0.1 nmol. The tumor contrast with intermediate dose (0.5 nmol) was significantly higher than for that with both high dose (3 nmol) and low dose (0.1 nmol) at all time points examined. [*E,* power (number, 10).]

in vitro and cell culture assays and the clinical settings for disease interventions (27, 28). Molecular imaging has its root in nuclear medicine, which focuses on the management of patients through the use of injected radiotracers in conjunction with imaging technologies such as PET and SPECT (29). The underlying principle can now be tailored to other imaging modalities such as optical imaging (30).

Up-regulation of α_v integrins ($\alpha_v\beta_3$ and $\alpha_v\beta_5$) in tumor cells and tumor vasculature, relative to normal surrounding tissues, permits the preferential delivery of suitably labeled integrin antagonists to the receptor-positive tumors. Previous studies with radiolabeled cyclic RGD peptides demonstrated the site-specific localization of the tracers in the appropriate receptor-positive tumor cells and tumor vessels (14–19). Finding of these studies also showed a good correlation between the magnitude of tumor uptake and receptor expression levels. In our study, we described the selective retention of NIR dye Cy5.5-conjugated RGD peptide in tumors *in vivo*. Conjugation of Cy5.5 to RGD peptide did not have significant effect on the optical properties of Cy5.5 nor on the receptor binding affinity and specificity of the RGD peptide. Our optical imaging method now allows researchers to confirm the results of the radionucleotide studies with a complementary method.

Optical imaging strategies come from the recent development of targeted bioluminescence probes, fluorescent proteins, and exogenous fluorescent probes. The very sensitive, cryogenically cooled CCD camera allows for acquiring a fluorescence image superimposed on a gray-scale photographic image of the small animal with overlay and imaging analysis software. Although the Xenogen imaging system is sensitive enough to visualize the mice and delineate the tumor from background when as low as 0.1 nmol of dye-coupled RGD peptide was administered, the tumor contrast [fluorescence intensities of the

tumor (T) to those of normal tissue (N)] was significantly lower than that obtained by applying 0.5 nmol dye molecules ($P < 0.001$). The low T-to-N ratio at very "low dose" may be attributed to the interference of relatively high background fluorescence and Rayleigh and Raman scattering (31). It is not surprising that "high dose" (3 nmol) administration of fluorescent probe had the lowest tumor contrast at all of the time points examined. It is possible that partial self-inhibition of receptor-specific uptake in U87MG tumor had occurred during the imaging studies at such a high dose. The similar phenomenon was also observed in receptor-targeted radionuclide imaging (32). It is also noticeable that tumor fluorescence intensity and tumor contrast had significant difference at different mouse viewing angles. NIR fluorescence intensity is known to be a function of optical path-length between excitation light and target (33). The uneven character of the mouse and tumor surfaces as well as differences in skin thickness may also be responsible for different tumor contrast at different viewing angles.

Because of the limited tissue penetration ability of Cy5.5 dye, we are successful only in detecting the subcutaneous tumors; the same probe was unable to noninvasively visualize orthotopic U87MG glioblastoma implanted in the mouse forebrain although the dissected tissue indicated tumor-specific uptake of the fluorescent probe (data not shown). NIR fluorescence imaging probes that emit at longer wavelength, with considerably lower autofluorescence, lower tissue scattering, and more photon penetration into living tissue (34) may be desirable for intracranial lesion detection. Likewise, fluorescent impurities are significantly reduced with longer excitation and detection wavelength. Significantly less tumor contrast measured by noninvasive in vivo imaging (Fig. 4A) was observed than that directly measured by imaging the dissected tissues (Fig. 4C). Zaheer et al. (33) compared the osteoblastic activity; imaging with and without skin resulted in an intensity attenuation of 44%. This may be attributed to the loss of excitation and emission light density by penetrating the skin in addition to the scatter caused by the skin. It is expected that an NIR dye with longer excitation and emission wavelengths and an appropriate filter set will reduce the interference from the background and, thus, improve the tumor contrast and attain deeper penetration for visualization of deep-lying tumors and organs. The use of an optical coupling medium and/or tomographic imaging (35) may also be helpful to minimize the effects of skin scattering.

The receptor-mediated binding of Cy5.5-labeled RGD peptide to $\alpha_v\beta_3$ integrin was tested both in vitro and in vivo. Incubation of U87MG glioma cells and HBCECs in the presence of uncoupled Cy5.5 dye did not change the fluorescence signal of the cells (data not shown). However, RGD-Cy5.5 conjugate massively increased the fluorescence intensity of the cells, and the fluorescence was completely lost when the cells were incubated with a blocking dose of uncoupled RGD peptide (Fig. 2). The fluorescence signal was initially distributed over the cell surface and most likely associated with the plasma membrane, whereas prolonged incubation time resulted in endocytosis, with most of the fluorescence accumulated in the perinuclear region and disappeared almost completely from the membrane. The fluorescent dye conjugate also indicated integrin-specific tumor uptake, because the tumor contrast ablation was observed in a blocking experiment. It has been reported that some cyanine dyes are capable of tumor accumulation without conjugation with a specific targeting molecule (36), this may partially explain why the tumor contrast was not completely blocked by unconjugated RGD peptide (Fig. 4B). The residual contrast in the blocking experiment is probably due to accumulation in the extracellular space with some nonspecific binding. Simple blocking experiments demonstrate only that the uptake is tumor specific and saturable in a qualitative manner. Additional studies to correlate the magnitude of tumor uptake (signal

brightness) with tumor receptor density distribution by immunohistochemistry and/or Western blotting are needed to validate the feasibility of noninvasive optical imaging to visualize α_v-integrin expression level in vivo.

Direct image of dissected tissues and organs revealed very good tumor-to-nontumor tissue ratios (Fig. 4C). The tumor-to-muscle ratio was almost twice as much as that observed from in vivo imaging at the same time point, simply because of more effective fluorescence detection without the interference from the skin. However, the quantification of ex vivo imaging of excised organs and tissues may not be a true reflection of tissue distribution of the RGD-Cy5.5 conjugate. The uptake in the liver and kidneys may be underestimated if the tracer was partially degraded and not detectable by the CCD camera because of the loss of fluorescence of the metabolites. Double labeling of RGD peptide with Cy5.5 and ^{125}I, and analyzing the biodistribution of this construct under the same conditions to correlate the fluorescence quantification and tissue activity accumulation of the conjugate, are required to confirm the ex vivo results.

In conclusion, our study successfully used the RGD peptide-$\alpha_v\beta_3$ integrin system to introduce a highly sensitive and semiquantitative NIR fluorescence imaging technique for tumor detection in preclinical animal models. To our knowledge, this is the first example of noninvasive imaging of integrin expression with optical modality. This approach provides the opportunity for rapid and cost-effective structure-activity studies to screen newly developed probes, before the more costly radionuclide-based imaging studies. A noninvasive imaging paradigm to image angiogenesis could provide a significant benefit to patient segmentation with cancer as well as with cardiovascular disease. Further development of more potent $\alpha_v\beta_3$ integrin antagonists for labeling Cy5.5 and other red-absorbing fluorescent dyes are now in progress for better tumor targeting and visualization of deep-lying tissues. The use of a time-domain optical imaging platform (e.g., low-intensity pulsed laser source), instead of continuous wave technique (e.g., tungsten light source), to obtain tomographic (three-dimensional) images and to subtract autofluorescence background based on their different fluorescence life time is also being explored.

ACKNOWLEDGMENTS

REFERENCES

1. Jin H, Varner J. Integrins: roles in cancer development and as treatment targets. Br J Cancer 2004;90:561–5.
2. Nisato RE, Tille JC, Jonczyk A, Goodman SL, Pepper MS. $\alpha_v\beta_3$ and $\alpha_v\beta_5$ integrin antagonists inhibit angiogenesis in vitro. Angiogenesis 2003;6:105–19.
3. Hodivala-Dilke KM, Reynolds AR, Reynolds LE. Integrins in angiogenesis: multi-talented molecules in a balancing act. Cell Tissue Res 2003;314:131–44.
4. Cairns RA, Khokha R, Hill RP. Molecular mechanisms of tumor invasion and metastasis: an integrated view. Curr Mol Med 2003;3:659–71.
5. Felding-Habermann B. Integrin adhesion receptors in tumor metastasis. Clin Exp Metastasis 2003;20:203–213.
6. Gasparini G, Brooks PC, Biganzoli E, et al. Vascular integrin $\alpha_v\beta_3$: a new prognostic indicator in breast cancer. Clin Cancer Res 1998;4:2625–34.
7. Vonlaufen A, Wiedle G, Borisch B, Birrer S, Luder P, Imhof BA. Integrin $\alpha_v\beta_3$ expression in colon carcinoma correlates with survival. Mod Pathol 2001;14:1126–32.
8. Bello L, Francolini M, Marthyn P, et al. $\alpha_v\beta_3$ and $\alpha_v\beta_5$ integrin expression in glioma periphery. Neurosurgery 2001;49:380–9.
9. Shimaoka M, Springer TA. Therapeutic antagonists and conformational regulation of integrin function. Nat Rev Drug Discov 2003;2:703–16.
10. Hamm CW. Anti-integrin therapy. Annu Rev Med 2003;54:425–35.

11. Kumar CC. Integrin $\alpha_v\beta_3$ as a therapeutic target for blocking tumor-induced angiogenesis. Curr Drug Targets 2003;4:123–31.

12. McQuade P, Knight L. Radiopharmaceuticals for targeting the angiogenesis marker $\alpha_v\beta_3$. Q J Nucl Med 2003;47:209–20.

13. Haubner RH, Wester HJ, Weber WA, Schwaiger M. Radiotracer-based strategies to image angiogenesis. Q J Nucl Med 2003;47:189–99.

14. Chen X, Park R, Tohme M, Shahinian AH, Bading JR, Conti PS. MicroPET and autoradiographic imaging of breast cancer α_v-integrin expression using [18]F- and ^{64}Cu-labeled RGD peptide. Bioconjug Chem 2004;15:41–9.

15. Chen X, Park R, Shahinian AH, et al. ^{18}F-labeled RGD peptide: initial evaluation for imaging brain tumor angiogenesis. Nucl Med Biol 2004;31:179–89.

16. Haubner R, Kuhnast B, Mang C, et al. [^{18}F]Galacto-RGD: synthesis, radiolabeling, metabolic stability, and radiation dose estimates. Bioconjug Chem 2004;15:61–9.

17. Haubner R, Wester HJ, Weber WA, et al. Noninvasive imaging of $\alpha_v\beta_3$ integrin expression using ^{18}F-labeled RGD-containing glycopeptide and positron emission tomography. Cancer Res 2001;61:1781–5.

18. Janssen ML, Oyen WJ, Dijkgraaf I, et al. Tumor targeting with radiolabeled $\alpha_v\beta_3$ integrin binding peptides in a nude mouse model. Cancer Res 2002;62:6146–1.

19. Janssen M, Oyen WJ, Massuger LF, et al. Comparison of a monomeric and dimeric radiolabeled RGD-peptide for tumor targeting. Cancer Biother Radiopharm 2002;17:641–6.

20. Becker A, Hessenius C, Licha K, et al. Receptor-targeted optical imaging of tumors with near-infrared fluorescent ligands. Nat Biotechnol 2001;19:327–33.

21. Ballou B, Fisher GW, Deng JS, Hakala TR, Srivastava M, Farkas DL. Cyanine fluorochrome-labeled antibodies in vivo: assessment of tumor imaging using Cy3, Cy5, Cy5.5, and Cy7. Cancer Detect Prev 1998;22:251–7.

22. Weissleder R, Tung CH, Mahmood U, Bogdanov A Jr. In vivo imaging of tumors with protease-activated near-infrared fluorescent probes. Nat Biotechnol 1999;17:375–8.

23. Ke S, Wen X, Gurfinkel M, et al. Near-infrared optical imaging of epidermal growth factor receptor in breast cancer xenografts. Cancer Res 2003;63:7870–5.

24. Petrovsky A, Schellenberger E, Josephson L, Weissleder R, Bogdanov A Jr. Near-infrared fluorescent imaging of tumor apoptosis. Cancer Res 2003;63:1936–42.

25. Chen X, Park R, Shahinian AH, Bading JR, Conti PS. Pharmacokinetics and tumor retention of ^{125}I-labeled RGD peptide are improved by PEGylation. Nucl Med Biol 2004;31:11–19.

26. Kumar CC, Nie H, Rogers CP, et al. Biochemical characterization of the binding of echistatin to integrin $\alpha_v\beta_3$ receptor. J Pharmacol Exp Ther 1997;283:843–53.

27. Weissleder R, Mahmood U. Molecular imaging. Radiology 2001;219:316–33.

28. Massoud TF, Gambhir SS. Molecular imaging in living subjects: seeing fundamental biological processes in a new light. Genes Dev 2003;17:545–80.

29. Blasberg RG, Gelovani J. Molecular-genetic imaging: a nuclear medicine-based perspective. Mol Imaging 2002;1:280–300.

30. Choy G, Choyke P, Libutti SK. Current advances in molecular imaging: noninvasive in vivo bioluminescent and fluorescent optical imaging in cancer research. Mol Imaging 2003;2:303–12.

31. Buschmann V, Weston KD, Sauer M. Spectroscopic study and evaluation of red-absorbing fluorescent dyes. Bioconjug Chem 2003;14:195–204.

32. Chen X, Park R, Hou Y, et al. MicroPET and autoradiographic imaging of GRP receptor expression with ^{64}Cu-DOTA-[Lys[3]]bombesin in human prostate adenocarcinoma xenografts. J Nucl Med 2004;45:1390–7.

33. Zaheer A, Lenkinski RE, Mahmood A, Jones AG, Cantley LC, Frangioni JV. In vivo near-infrared fluorescence imaging of osteoblastic activity. Nat Biotechnol 2001;19:1148–54.

34. Quaresima V, Matcher SJ, Ferrari M. Identification and quantification of intrinsic optical contrast for near-infrared mammography. Photochem Photobiol 1998;67:4–14.

35. Ntziachristos V, Bremer C, Graves EE, Ripoll J, Weissleder R. Fluorescence imaging with near-infrared light: new technological advances that enable in vivo molecular imaging. Eur Radiol 2003;13:195–208.

36. Licha K, Riefke B, Ntziachristos V, Becker A, Chance B, Semmler W. Hydrophilic cyanine dyes as contrast agents for near-infrared tumor imaging: synthesis, photophysical properties and spectroscopic in vivo characterization. Photochem Photobiol 2000;72:392–8.

Integrin $\alpha_v\beta_3$–Targeted Imaging of Lung Cancer[1]

Xiaoyuan Chen*,[†], Eric Sievers[‡], Yingping Hou[†], Ryan Park*, Michel Tohme*, Robert Bart[‡], Ross Bremner[‡], James R. Bading* and Peter S. Conti*

*Molecular Imaging Science Center, Department of Radiology, University of Southern California, Los Angeles, CA 90033, USA; [†]Molecular Imaging Program at Stanford (MIPS), Stanford University School of Medicine, 300 Pasteur Drive, Edwards Building, Room 354, Stanford, CA 94305-5344, USA; [‡]Department of Cardiothoracic Surgery, University of Southern California, Los Angeles, CA 90033, USA

Abstract

A series of radiolabeled cyclic arginine–glycine–aspartic acid (RGD) peptide ligands for cell adhesion molecule integrin $\alpha_v\beta_3$–targeted tumor angiogenesis targeting are being developed in our laboratory. In this study, this effort continues by applying a positron emitter ^{64}Cu-labeled PEGylated dimeric RGD peptide radiotracer ^{64}Cu-DOTA-PEG-E[c(RGDyK)]$_2$ for lung cancer imaging. The PEGylated RGD peptide indicated integrin $\alpha_v\beta_3$ avidity, but the PEGylation reduced the receptor binding affinity of this ligand compared to the unmodified RGD dimer. The radiotracer revealed rapid blood clearance and predominant renal clearance route. The minimum nonspecific activity accumulation in normal lung tissue and heart rendered high-quality orthotopic lung cancer tumor images, enabling clear demarcation of both the primary tumor at the upper lobe of the left lung, as well as metastases in the mediastinum, contralateral lung, and diaphragm. As a comparison, fluorodeoxyglucose (FDG) scans on the same mice were only able to identify the primary tumor, with the metastatic lesions masked by intense cardiac uptake and high lung background. ^{64}Cu-DOTA-PEG-E[c(RGDyK)]$_2$ is an excellent positron emission tomography (PET) tracer for integrin-positive tumor imaging. Further studies to improve the receptor binding affinity of the tracer and subsequently to increase the magnitude of tumor uptake without comprising the favorable *in vivo* kinetics are currently in progress.

Neoplasia (2005) **7**, 271–279

Introduction

Lung cancer is the leading cause of cancer death for both men and women, killing more people than breast, prostate, colon, and pancreas cancers combined [1]. The major histologic types of lung cancer are squamous cell carcinoma, adenocarcinoma, large cell carcinoma (referred to as non small cell carcinoma, or NSCLC) and small cell lung carcinoma (SCLC). Early detection and treatment may lead to improved survival for some types of lung cancer [2]. Even patients with the earliest surgical stage (T_1N_0) have disseminated disease between 15% and 30% of the time [3]. Chemotherapy, surgery, and radiation therapy have been shown to control symptoms and improve quality of life; there remains no standard optimal therapy regimen for NSCLC [4]. The mechanisms of resistance to drug and radiation therapy are poorly understood [5]. Despite significant progress, the molecular events underlying the development of lung cancer are largely unknown. No drug has been found useful in the prevention of lung cancer [6]. Although there are proven means of early diagnosis available for lung cancer, whether these techniques are effective in terms of improving patient survival or outcome remains unknown [7].

Lung cancer diagnosis based on histopathology requires fine-needle biopsy, bronchoscopy, or open-lung biopsy to differentiate benign from malignant lesions, before and often after surgical resection or radiation therapy of the primary tumor lesions. Bronchoscopy, including bronchial washings and brushing, has a sensitivity of 65% for malignancy, and transbronchial biopsy increases the sensitivity to 80% for lesions that are accessible. Pneumothorax and associated morbidity can occur following these invasive procedures. Conventional anatomic imaging techniques such as chest X-ray, computed tomography (CT) scans, bone scans, or magnetic resonance imaging (MRI) can neither accurately stage the disease when metastases occurs without anatomic change, nor differentiate between malignant and nonmalignant tumors. Fluorodeoxyglucose positron emission tomography (FDG-PET) imaging, which visualizes glucose utilization by lung cancer cells, is increasingly used for the management of patients with lung cancer, especially those with NSCLC. FDG-PET quantifies a specific cellular process, namely, phosphorylation of 2-deoxyglucose by hexokinase. The technique

provides highly sensitive and specific data for the diagnosis, staging, and restaging of NSCLC, without the need for a biopsy, and is now well accepted by most physicians as an effective complement to existing imaging modalities [8–10]. FDG-PET may also evolve as a predictor of response after local or systemic treatment [11].

Although assessment of tissue metabolism using the tracer FDG provides useful imaging of lung neoplasms, it is relatively nonspecific and is usually less useful for imaging tumors that have very low growth rates, or as a guide for delivery of specific molecular therapy. The development of tracers that target specific molecular or genetic abnormalities, which are the basis of lung cancer, is therefore essential for the development and utility of clinically relevant PET procedures that can be use to assess the efficacy of therapeutic drugs designed to treat those abnormalities. The goals are: to allow early detection and characterization of the disease, to provide more timely and direct assessments of treatment effects, and to obtain more fundamental understanding of the disease process. The rapidly expanding knowledge of the molecular pathogenesis of lung cancer indicates that respiratory epithelial cells require many genetic alterations to become invasive, leading to metastatic cancer. In addition, most solid tumors are angiogenesis-dependent [12]. Antiangiogenic therapy has been shown to prevent tumor growth and even to cause tumor regression in various tumor models including lung cancer [13]. NSCLC growth, angiogenesis, invasion, and metastases to specific organs are dependent on an orchestrated series of events that include: cellular transformation; establishment of a proangiogenic environment; tumor cell proliferation, invasion, and entry into the circulation; and tumor cell trafficking and metastatic tumor growth in specific organs [14]. Cell adhesion receptors of the integrin family, which are responsible for a wide range of cell–extracellular matrix (ECM) and cell–cell interactions, have been well studied in many tumor types including brain, breast, skin, and ovarian tumors. However, little is known regarding the function of integrins in lung cancer growth and metastasis [15].

Due to its high expression on tumor vasculature and tumor cells compared to resting endothelial cells and normal tissues, $\alpha_v\beta_3$ integrin is an excellent target for integrin-targeted interventions [16,17]. It has been shown that $\alpha_v\beta_3$ integrin antagonists, such as monoclonal antibodies, arginine–glycine–aspartic acid (RGD) peptides, and small molecules, block angiogenesis and tumor growth by selectively promoting apoptosis of vascular endothelial cells [16–18]. The development of noninvasive methods to visualize and quantify α_v integrin expression in vivo appears to be crucial for the success of antiangiogenic therapy based on integrin antagonism [17,19]. A number of molecular probes have been developed for MRI [20,21], PET [22–30], single-photon computed tomography (SPECT) [31–35], and ultrasound [36] imaging applications.

^{64}Cu-labeled RGD peptides are of particular interest because ^{64}Cu [$t_{1/2}$ = 12.8 h; 40% β^- (656 keV); 19% β^+ (600 keV); 38% EC] is an attractive radionuclide for both PET imaging and targeted radiotherapy of cancer [37].
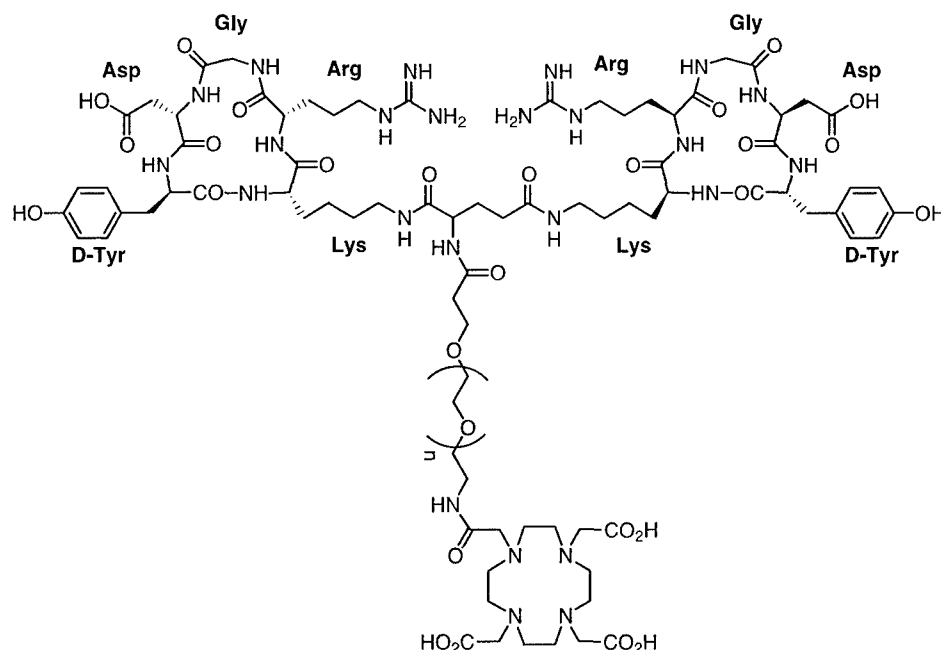
We first coupled monomeric RGD peptide c(RGDyK) with the macrocyclic chelator, 1,4,7,10-tetraazacyclododecane-N,N',N'',N'''-tetraacetic acid (DOTA), and labeled the RGD-DOTA conjugate with ^{64}Cu for tumor targeting. The radiotracer showed intermediate tumor uptake but also high retention in liver and kidney [23]. Introduction of a bifunctional poly(ethylene glycol) (PEG; M_W = 3,400) moiety between DOTA and RGD led to significantly improved in vivo kinetics of the resulting radiotracer ^{64}Cu-DOTA-PEG-RGD compared to that of ^{64}Cu-DOTA-RGD [25]. We also observed that a dimeric RGD peptide E[c(RGDyK]$_2$ with higher integrin binding affinity, when conjugated with DOTA and labeled with ^{64}Cu, yielded almost twice as much uptake in tumors, as well as significantly increased renal activity accumulation compared to the monomeric analogue [27]. In this study, we sought to extend this effort by examining integrin expression in lung cancer using noninvasive PET imaging and a novel radiotracer—^{64}Cu-labeled PEGylated dimeric RGD peptide ^{64}Cu-DOTA-PEG-E[c(RGDyK)]$_2$ (Figure 1).

Materials and Methods

Materials and Analyses

DOTA was purchased from Macrocyclics, Inc. (Dallas, TX). N-hydroxysulfonosuccinimide (SNHS), 1-ethyl-3-[3-(dimethylamino)propyl]carbodiimide (EDC), and Chelex 100 (50–100 mesh) were obtained from Aldrich (St. Louis, MO). Heterofunctional PEG (M_W 3400), t-Boc-NH-PEG-CO$_2$NHS, was obtained from Nektar, Inc. (San Carlos, CA). Cyclic RGD peptide c(RGDyK) was synthesized through solution cyclization of the fully protected linear pentapeptide, H-Gly-Asp(OtBu)-D-Tyr(OtBu)-Lys(Boc)-Arg(Pbf)-OH, followed by TFA deprotection [22–24]. Dimeric RGD peptide E[c(RGDyK)]$_2$ was prepared by coupling Boc-Glu-OH with two equivalents of monomeric RGD peptide c(RGDyK) followed by TFA cleavage [26,27]. Radio-thin layer chromatography (TLC) was performed using MKC18F plates (Whatman, Clifton, NJ), a Bioscan system 200, and Winscan (Washington, DC) software, version 2.2. Reversed-phase extraction C-18 SepPak cartridges were obtained from Waters (Milford, MA). ^{64}Cu was produced on a CS-15 biomedical cyclotron at THE Washington University School of Medicine by the ^{64}Ni(p,n)^{64}Cu nuclear reaction [37]. Chromalux HB microplates were obtained from Dynex Technologies (Chantilly, VA). [^{125}I]echistatin labeled by the lactoperoxidase method to a specific activity of 2000 Ci/mmol was from Amersham Biosciences (Piscataway, NJ). Echistatin was purchased from Sigma (St. Louis, MO).

Semipreparative reversed-phase high-performance liquid chromatography (HPLC) was accomplished on a Waters 515 chromatography system with a 486 tunable absorbance detector. Version 7.2.1 Labtech Notebook/XE software (Andover, MA) was used to record chromatograms. Purification was performed on a Vydac protein and peptide column 218TP510 (5 μm, 250 × 10 mm). The flow was 5 ml/min, with the mobile phase starting from 95% solvent A (0.1% TFA in water) and 5% solvent B (0.1% TFA in

Figure 1. *Schematic structure of DOTA-PEG-E[c(RGDyK)]₂. Heterobifunctional PEG (M$_W$ = 3400) links to DOTA carboxylate group through the N-terminus and to the glutamate amino group of the dimeric RGD peptide through the C-terminus.*

acetonitrile) (0–2 min) to 35% solvent A and 65% solvent B at 32 minutes. The analytical HPLC method was performed with the same gradient system, but with a Vydac 218TP54 column (5 μm, 250 × 4.6 mm) and flow of 1 ml/min. UV absorbance was monitored at 218 nm.

Chemistry and Radiochemistry

t-Boc-NH-PEG-E[c(RGDyK)]₂ conjugate   t-Boc–protected PEG succinimidyl ester (t-Boc-NH-PEG-CO₂NHS, M_W = 3400), 30 mg (ca. 8.8 μmol), dissolved in acetonitrile (2 ml); E[c(RGDyK)]2, 16 mg (ca. 11.8 μmol), dissolved in water (2 ml); and 0.2 M Na₂B₄O₇ buffer (pH = 8.3), 2 ml, were mixed together and incubated overnight at 4°C. The reaction was quenched by adding 5% HOAc (0.5 ml) and the entire mixture was then subjected to several semipreparative HPLC purifications. Removal of the mobile phase gave the product as a lyophilized solid. Yield: 30 mg (ca. 70% based on PEG).

NH₂-PEG-E[c(RGDyK)]₂   Twenty milligrams of t-Boc-NH-PEG-E[c(RGDyK)]₂ conjugate was dissolved in 2 ml of 95% TFA and allowed to stand at room temperature for 2 h. Most of the TFA was then removed by rotary evaporator (equipped with a CO₂/acetone cold finger, oil pump, and acid trap). The residue was triturated with ice-cold ether (10 ml) to precipitate the crude peptide. Semipreparative HPLC purification followed by lyophilization gave the unprotected RGD–PEG conjugate. Yield: 15 mg (ca. 75%).

DOTA-PEG-E[c(RGDyK)]₂   DOTA was activated *in situ* by EDC with a DOTA:EDC:SNHS molar ratio of 10:5:4 [23]. NH₂-PEG-E[c(RGDyK)]₂ (10 mg, ca. 2.1 μmol) dissolved in 2 ml of water was cooled to 4°C and added to the DOTA-

OSSu reaction mixture (20 μmol; calculated based on SNHS) and the pH was adjusted to 8.5 with 1 N NaOH. The reaction was allowed to incubate overnight at 4°C. The DOTA-PEG-E[c(RGDyK)]₂ conjugate was purified by semipreparative HPLC and characterized by analytical HPLC and matrix-assisted laser desorption/ionization time-of-flight mass spectroscopy (MALDI-TOF MS). Yield: 6.5 mg (ca. 60%). The peak containing the RGD conjugate was collected, lyophilized, and dissolved in H₂O at a concentration of 1 mg/ml for use in radiolabeling reactions.

⁶⁴Cu radiolabeling   ⁶⁴CuCl₂ (5 mCi, decay-corrected) was diluted with 400 μl of 0.1 N NaOAc (pH 5.5) and then added to DOTA-PEG-E[c(RGDyK)]₂ (25 μg). The reaction mixture was incubated at 50°C for 50 minutes and then terminated by adding 5 μl of 10 mM EDTA solution. Radiochemical yield was determined by radio-TLC using Whatman MKC18F TLC plates as the stationary phase and 70:30 MeOH:10% NaOAc as the eluent. ⁶⁴Cu-DOTA-PEG-E[c(RGDyK)]₂ was purified on a C-18 SepPak cartridge, using 85% ethanol as the elution solvent. Radiochemical purity (RCP) was determined by radio-TLC or radio-HPLC. The ethanol was evaporated, and the activity was reconstituted in phosphate-buffered saline and passed through a 0.22-μm Millipore (Billerica, MA) filter into a sterile multidose vial for use in animal experiments.

Receptor Binding Assay

Affinity of echistatin and RGD peptides for α$_v$β₃ integrin on the surface of NSCLC NCI-H1975 cells was determined by competitive binding experiments using ¹²⁵I-labeled echistatin as a radioligand as described in the literature, with modifications [38]. In brief, NCI-H1975 cells were harvested, washed

twice with PBS, and resuspended (2×10^6 cells/ml) in binding buffer (20 mM Tris, pH 7.4, 150 mM NaCl, 2 mM CaCl$_2$, 1 mM MgCl$_2$, 1 mM MnCl$_2$, and 0.1% BSA). Ninety-six–well multiscreen DV plates (filter pore size: 0.65 μm; Millipore) were incubated with [^{125}I]echistatin (50,000 cpm/well) in the presence of increasing concentrations of different RGD peptide analogues (0–1000 nM). The total incubation volume was adjusted to 200 μl. After the cells were incubated for 3 hours at room temperature, the plate was filtered through a multiscreen vacuum manifold and washed twice with cold binding buffer. The hydrophilic PVDF filters were collected and the radioactivity was determined using a NaI(TI) gamma counter (Packard, Meriden, CT). The best-fit IC$_{50}$ values for the NCI-H1975 cells were calculated by fitting the data by nonlinear regression using GraphPad Prism (GraphPad Software, Inc., San Diego, CA). Experiments were carried out with triplicate samples.

In Vivo Model

The University of Southern California Institutional Animal Care and Use Committee approved the animal study described herein. All animals received humane care in compliance with the "Guide for the Care and Use of Laboratory Animals" published by the National Institutes of Health.

Six-week–old severe combined immunodeficient (SCID-bg male mice; Harlan Sprague Dawley, Inc., Indianapolis, IN) mice were housed in polycarbonate cages (five per cage) in a room lit for 12 hours each day and maintained at 27°C for 2 days prior to injection. Teklad (4%) diet (Harlan Teklad, Madison, WI) and tap water were provided ad libitum. In preparation for injection, human female lung adenocarcinoma cells NCI-H1975 (American Type Culture Collection, Manassas, VA) were cultured in RPMI 1640 supplemented with 10% fetal bovine serum (GIBCO, Carlsbad, CA) until 90% confluent. Cells were trypsinized, washed, centrifuged, and resuspended to a concentration of 2×10^6 cells/30 μl in RPMI 1640 (cell passages 35 ± 3). Mice were anesthesized by titrating isoflurane inhalant. A 1-cm axillary incision allowed left lung visualization through intercostal muscles and pleura. NCI-H1975 cell suspension was injected through a 27-gauge needle into the left upper lobe at the fourth intercostal space under direct visualization. The incision was closed using 4.0 absorbable suture, and mice were allowed to recover [39]. Mice were subjected to microPET imaging and whole-body digital autoradiography (WBDA) studies at 4 weeks after implantation.

Biodistribution

Male SCID-bg mice bearing subcutaneous NCI-H1975 tumors ($n = 3$ per time point) were injected with ^{64}Cu-DOTA-PEG-E[c(RGDyK)]$_2$ (10 μCi activity in 150 μl of saline) through the tail vein. The animals were euthanized at 0.5, 1, 2, 4, and 24 hours postinjection. The blocking experiment was performed by coinjecting the radiotracer with a saturating dose of c(RGDyK) (10 mg/kg) and was sacrificed at 1 hour postinjection. Following euthanasia, blood, tumor, and major organs and tissues were collected, wet-weighed, and counted in a γ-counter (Packard). Percent injected dose per gram (% ID/g) was calculated by comparison with standards representing the injected dose per animal. Values are quoted as mean ± standard deviation (SD). To compare the in vivo kinetics of ^{64}Cu-DOTA-PEG-E[c(RGDyK)]$_2$ and ^{64}Cu-DOTA-E[c(RGDyK)]$_2$, biodistribution studies of both tracers were performed in female athymic nude mice at 30-minute, 1-hour, 2-hour, 4-hour, and 24-hour time points (10 μCi activity for each animal; $n = 4$ per time point).

MicroPET Imaging and WBDA

PET imaging was performed on a microPET R4 rodent model scanner (Concorde Microsystems, Inc., Knoxville, TN). The scanner has a computer-controlled bed, and 10.8 cm transaxial and 8 cm axial field of view (FOV). It has no septa and operates exclusively in 3D list mode. All raw data were first sorted into 3D sinograms followed by maximum a posteriori (MAP) reconstruction based on a Bayesian formulation, which combines accurate modeling of the coincidence detection process with statistical priors on the PET images [40]. At 4 weeks postinoculation, orthotopic tumor-bearing mice were anesthetized by intraperitoneal injection of ketamine/xylazine solution, placed in a spread-supine position on a cardboard slat, and injected with 200 μCi of [^{18}F]FDG into the tail vein at a volume of 150 μl. The mice were scanned for 10 minutes starting from 30 minutes after FDG injection. The same mice were intravenously injected with 300 μCi of ^{64}Cu-DOTA-PEG-E[c(RGDyK)]$_2$ and sacrificed at 1 hour postinjection by cervical dislocation under ketamine/xylazine anesthesia and placed near the center of the FOV of the microPET, where the highest image resolution and sensitivity are available. The mice were scanned for 20 minutes followed by whole-body autoradiography, using a Packard Cyclone Storage Phosphor Screen system (Downers Grove, IL) and a Bright 5030/WD/MR cryomicrotome (Hacker Instruments, Fairfield, NJ) [22]. Regions of interest (ROI) for microPET imaging were drawn over subcutaneous, orthotopic, and metastatic tumors on decay-corrected whole-body coronal images. The counts per pixel per minute obtained from the ROIs were converted to counts per milliliter per minute by using a system calibration factor obtained from scanning a cylinder phantom in the microPET scanner. The uptake index [ROI (μCi/ml)/injected dose (μCi) × 100%] of tissues and organs of interest was compared with the percent injected dose per gram value obtained from direct tissue sampling after the microPET imaging. Quantification of autoradiographic images was validated by correlating the ROIs in tissues [as detector light units (DUL)/mm^2] with direct gamma counter assays of the tissue samples removed from the frozen block ($n = 3$). A linear relationship between tissue percent injected dose per gram and autoradiography image intensity was observed, and the conversion factor thus obtained and used for autoradiography quantification [41].

Statistical Analysis

The data were expressed as mean ± SD. One-way analysis of variance (ANOVA) was used for statistical evaluation. Means were compared using Student's t-test. P values < .05 were considered significant.

Results

Preparation of PEGylated Dimeric RGD Conjugate and Radiolabeling

The synthetic scheme of DOTA-PEG-E[c(RGDyK)]$_2$ is shown in Figure 2. The PEGylated conjugate was obtained by solution synthesis through an active ester protocol in 30% overall yield calculated from t-Boc-NH-PEG-CO$_2$NHS. Each intermediate was characterized by analytical HPLC and molecular weight measurement by MALDI-TOF MS. The HPLC (under the conditions described in the Materials and Methods section) retention times for E[c(RGDyK)]$_2$, t-Boc-NH-PEG-E[c(RGDyK)]$_2$, NH$_2$-PEG-E[c(RGDyK)]$_2$, and DOTA-PEG-E[c(RGDyK)]$_2$ were 13.8, 23.7, 21.4, and 22.8 minutes, respectively. The mass spectrum of PEGylated RGD dimer was characterized by broad peaks due to polydispersiveness of PEG, with an average PEG size ~3400. The molecular weight of the final DOTA-PEG-E[c(RGDyK)]$_2$ was around 5100, indicating a 1:1:1 molar ratio with respect to DOTA, PEG, and E[c(RGDyK)]$_2$. The ^{64}Cu-DOTA-PEG-E[c(RGDyK)]$_2$ was prepared in high specific activity. Typically, 10 μg of peptide was able to bind 1 mCi of ^{64}Cu with > 95% radiochemical yield after 1 hour of incubation in NaOAc buffer (pH = 5.5) as determined by radio-TLC. SepPak separation provided the product with RCP higher than 99%. The specific activity was thus calculated to be around 500 Ci/mmol (decay-corrected).

In Vitro and In Vivo Evaluation

To characterize α$_v$β$_3$ integrin binding properties of the ^{64}Cu-labeled PEGylated dimeric RGD peptide, competitive binding assay studies were performed. Maintenance of binding affinity was shown by competitive binding measurements between [^{125}I]echistatin and the RGD peptide ligands with cultured NCI-H1975 cells (Figure 3). The binding of [^{125}I]echistatin to NCI-H1975 cells was inhibited by various concentrations of echistatin, c(RGDyK), E[c(RGDyK)]$_2$, or DOTA-PEG-E[c(RGDyK)]$_2$, with IC$_{50}$ values of 0.54, 44.8, 11.1, and 84.9 nM, respectively.

Comparison of biodistribution data of ^{64}Cu-DOTA-PEG-E[c(RGDyK)]$_2$ and ^{64}Cu-DOTA-E[c(RGDyK)]$_2$ in the blood, muscle, liver, and kidneys of female athymic nude mice is shown in Figure 4. The PEGylated RGD peptide had similar blood activity as ^{64}Cu-DOTA-E[c(RGDyK)]$_2$ at early time points, but displayed a more rapid blood clearance than ^{64}Cu-DOTA-E[c(RGDyK)]$_2$ after 4 hours postinjection. The PEGylated RGD dimmer indicated significantly lower activity accumulation in the muscle, liver, and kidneys at all time points examined (P < .001). Overall, ^{64}Cu-DOTA-PEG-E[c(RGDyK)]$_2$ was excreted with a faster rate than ^{64}Cu-DOTA-E[c(RGDyK)]$_2$.

In vivo biodistribution studies of ^{64}Cu-DOTA-PEG-E[c(RGDyK)]$_2$ were performed in healthy male SCID-bg mice implanted subcutaneously with human NSCLC tumors grown from NCI-H1975 cells. Table 1 summarizes results of the biodistribution pattern of ^{64}Cu-DOTA-PEG-E[c(RGDyK)]$_2$ in tumor-bearing SCID mice at 0.5, 1, 2, 4, and 24 hours. The PEGylated RGD peptide tracer showed rapid blood clearance (0.57 ± 0.19% ID/g at 30 minutes postinjection and only 0.05 ± 0.01% ID/g at 2 hours postinjection). Highest tumor uptake was observed at 1 hour postinjection (2.64 ± 0.14% ID/g) and some washout was observed (1.15 ± 0.07% ID/g at 24 hours postinjection). Due to the rapid clearance of the radiotracer, good tumor-to-blood and tumor-to-muscle ratios were achieved after 1 hour postinjection. It is also noteworthy to mention that this PEGylated RGD peptide tracer produced a good tumor-to-lung ratio because of low lung activity accumulation. The
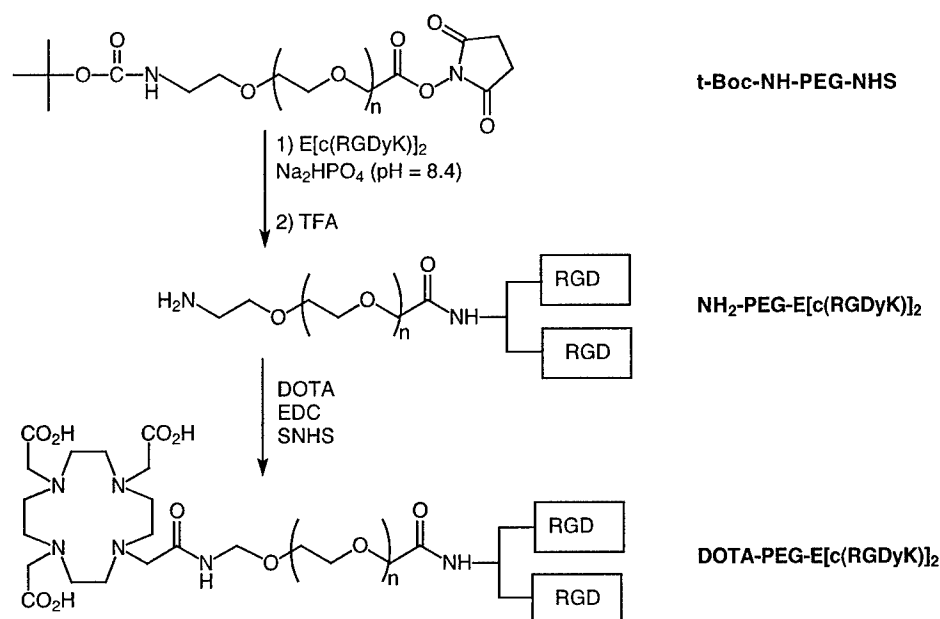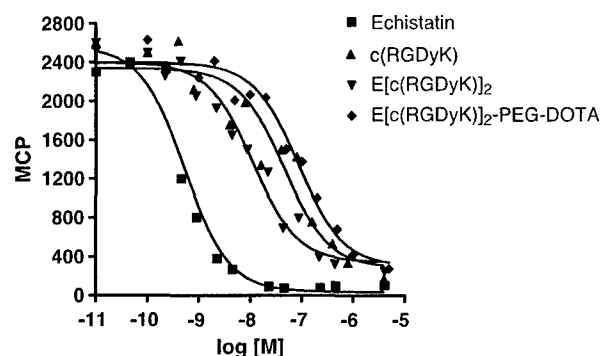

Figure 2. Step-by-step synthesis of the PEGylated dimeric RGD peptide ligand, DOTA-PEG-E[c(RGDyK)]$_2$.

Figure 3. *Competition of specific binding of [^{125}I]echistatin with unlabeled echistatin, c(RGDyK), E[c(RGDyK)]$_2$. and DOTA-PEG-E[c(RGDyK)]$_2$ on integrin $\alpha_v\beta_3$ expressed on the surface of human NSCLC NCI-H1975 cells. All points represent triplicate measurements. PEGylation reduced the receptor binding affinity of the resulting ligand from 11 to 85 nM.*

primary route of clearance of radiolabel from ^{64}Cu-DOTA-PEG-E[c(RGDyK)]$_2$ was through the kidneys into the urine. Only 0.94 ± 0.20% ID/g and 0.90 ± 0.35% ID/g were found in the liver and intestines at 1 hour postinjection, respectively. It is also important to note that there was minimal uptake of ^{64}Cu in organs other than the kidneys, indicating that these normal tissues and organs exhibit little $\alpha_v\beta_3$ integrin expression, which is consistent with previous reports [22–33]. To demonstrate that the ^{64}Cu-DOTA-PEG-E[c(RGDyK)]$_2$ uptake in NCI-H1975 tumor was specific and receptor-mediated, biodistribution studies were performed by coinjection of c(RGDyK) (10 mg/kg) with ^{64}Cu-DOTA-PEG-E[c(RGDyK)]$_2$. An uptake value of 0.68 ± 0.10% ID/g was observed at 1 hour postinjection, which was about four times lower than the

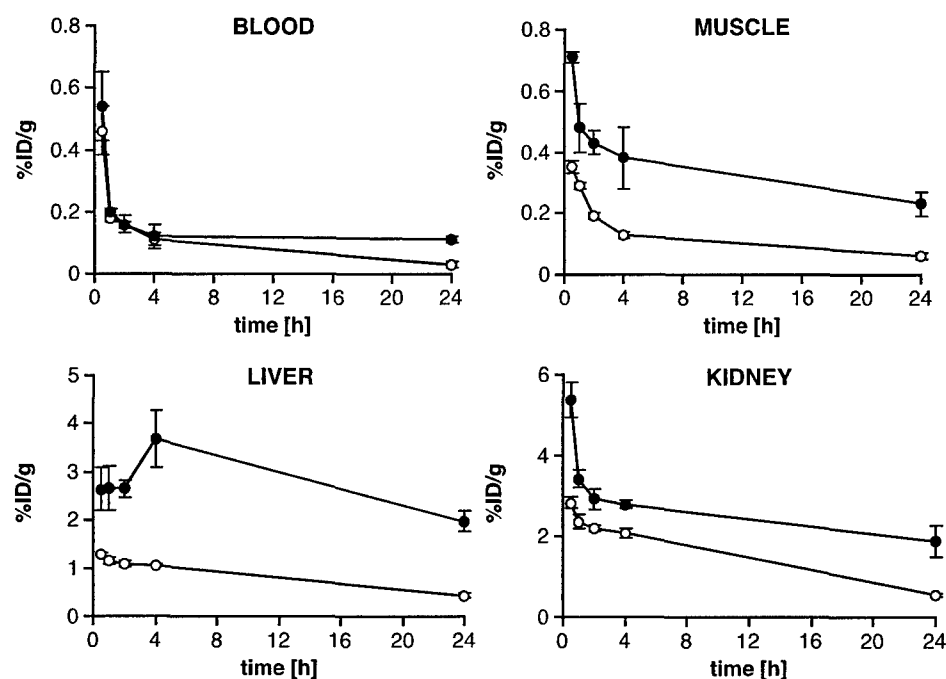tumor uptake of ^{64}Cu-DOTA-PEG-E[c(RGDyK)]$_2$ when no blocking agent was coinjected.

MicroPET and Autoradiography

We used microPET to semiquantitatively image the integrin expression in the orthotopic lung cancer tumor and its metastases. A 2D projection image of a mouse injected 2 hours previously with ^{64}Cu-DOTA-PEG-E[c(RGDyK)]$_2$ (15-minute static scan) is shown in Figure 5. The primary tumor (left upper lobe at the fourth intercostal space) and its metastasis to the contralateral lung were both well visualized. By comparison, an FDG scan on the same mouse identified the primary tumor but failed to visualize any metastasis, probably due to significant nearby myocardial uptake. A coronal section including the primary orthotopic tumor and subcutaneous tumor on the right flank clearly delineates the primary tumor and its metastases to the contralateral lung, mediastinum, and diaphragm. Whole-body autoradiography (100 μm resolution) agreed well with the findings of microPET (Fig. 5). ROI analysis of the FDG-PET images showed a primary tumor-to-muscle ratio of 4.8 and a primary tumor-to-lung ratio of 1.5. SUV. The RGD peptide tracer had much higher tumor-to-background contrast than that of FDG, following the trend of subcutaneous tumor > primary tumor > metastasis (contralateral lung).

Discussion

This study demonstrates that ^{64}Cu-DOTA-PEG-E[c(RGDyK)]$_2$ is an excellent positron-emitting radionuclide tracer for visualization of NSCLC tumor and its metastases based on integrin expression. The high tumor-to-lung contrast is due to

Figure 4. *Comparison of biodistribution data of ^{64}Cu-DOTA-PEG-E[c(RGDyK)]$_2$ (○) and ^{64}Cu-DOTA-E[c(RGDyK)]$_2$ (●) in female athymic nude mice. Error bars denote SD (n = 4).*

Table 1. Biodistribution of ^{64}Cu-Labeled PEGylated Dimeric RGD Peptide (^{64}Cu-DOTA-PEG-E[c(RGDyK)]$_2$) in Male SCID-bg Mice Bearing Subcutaneous NCI-H1975 NSCLC Tumors on the Right Flank.

	0.5 hour	1 hour	2 hours	4 hours	24 hours	1-hour block
Blood	0.57 ± 0.19	0.17 ± 0.02	0.05 ± 0.01	0.04 ± 0.02	0.04 ± 0.01	0.16 ± 0.04
Muscle	0.37 ± 0.05	0.46 ± 0.12	0.22 ± 0.03	0.16 ± 0.03	0.15 ± 0.03	0.81 ± 0.07
Tumor	1.87 ± 0.05	2.64 ± 0.14	1.35 ± 0.06	1.46 ± 0.12	1.15 ± 0.07	0.68 ± 0.10
Skin	0.92 ± 0.05	0.55 ± 0.11	0.56 ± 0.34	0.38 ± 0.09	0.47 ± 0.01	0.31 ± 0.07
Bone	0.56 ± 0.32	0.58 ± 0.14	0.33 ± 0.05	0.33 ± 0.01	0.37 ± 0.08	0.42 ± 0.21
Heart	0.52 ± 0.15	0.31 ± 0.07	0.25 ± 0.02	0.25 ± 0.04	0.23 ± 0.03	0.14 ± 0.05
Lung	1.31 ± 0.35	0.78 ± 0.09	0.51 ± 0.08	0.55 ± 0.05	0.46 ± 0.05	0.48 ± 0.12
Liver	0.83 ± 0.17	0.94 ± 0.20	0.77 ± 0.09	1.01 ± 0.09	0.88 ± 0.01	0.36 ± 0.04
Kidney	3.50 ± 0.54	1.92 ± 0.26	1.63 ± 0.04	1.61 ± 0.17	1.15 ± 0.11	1.33 ± 0.12
Spleen	1.01 ± 0.48	1.23 ± 0.18	0.94 ± 0.06	1.30 ± 0.21	1.15 ± 0.10	0.28 ± 0.04
Pancreas	0.43 ± 0.25	0.29 ± 0.01	0.16 ± 0.01	0.18 ± 0.01	0.18 ± 0.03	0.15 ± 0.12
Stomach	1.25 ± 0.06	1.16 ± 0.22	0.87 ± 0.03	0.90 ± 0.13	0.66 ± 0.11	0.23 ± 0.04
Small intestine	1.30 ± 0.09	0.90 ± 0.35	0.83 ± 0.08	1.02 ± 0.14	0.73 ± 0.05	0.29 ± 0.14
Tumor/blood	3.58 ± 1.43	15.3 ± 1.06	27.9 ± 6.37	36.9 ± 13.1	28.7 ± 3.71	4.64 ± 2.19
Tumor/muscle	5.07 ± 0.69	6.07 ± 1.68	6.17 ± 1.02	8.99 ± 1.59	7.60 ± 0.94	0.83 ± 0.05
Tumor/lung	1.51 ± 0.48	3.41 ± 0.29	2.68 ± 0.51	2.65 ± 0.22	2.45 ± 0.14	1.44 ± 0.33

The data were reported as percent injected dose per gram ± standard deviation at different time points postinjection of 20 μCi radioactivity. A 1-hour blocking experiment was performed with coinjection of 10 mg/kg c(RGDyK) (*n* = 3).
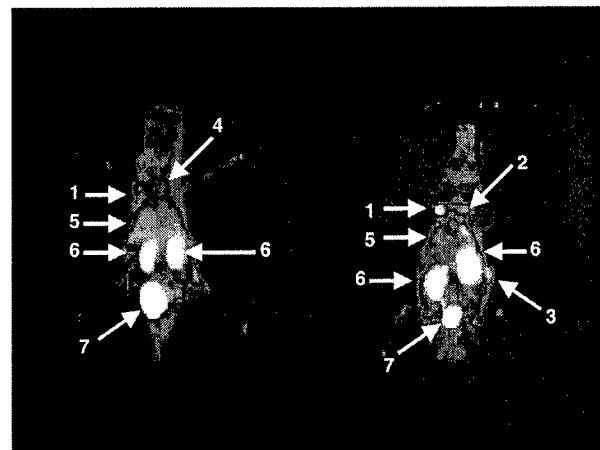
the lack of integrin expression in normal tissues and organs, and consequently minimal nonspecific cardiac and lung activity accumulation with this radiotracer. The same tumor-bearing mouse imaged with FDG showed low tumor contrast and inability to delineate tumor metastases due to intense cardiac uptake.

Most solid tumors are angiogenesis-dependent and, therefore, various antiangiogenic treatment targetings at different molecular mechanisms are being explored [13,42,43]. With growing numbers of antiangiogenic drugs available that target different pathways, it may become useful to select therapeutic regimens based on the molecular characteristics of tumors in individual patients as identified by selective *in vivo* imaging agents. Overexpression of integrin $\alpha_v\beta_3$ on both tumor cells and sprouting tumor vasculature, but not on most normal tissues and resting endothelial cells, presents an excellent target for antiangiogenic interventions [16]. Recent clinical trials and preclinical studies suggest that $\alpha_v\beta_3$ expression correlates positively with tumor metastatic potential and that anti-integin therapy using $\alpha_v\beta_3$ antagonists is most effective with integrin-positive tumors [16,18]. Noninvasive imaging of $\alpha_v\beta_3$ expression is thus of vital importance for patient selection and noninvasive monitoring of anti-integrin treatment efficacy [17,19].
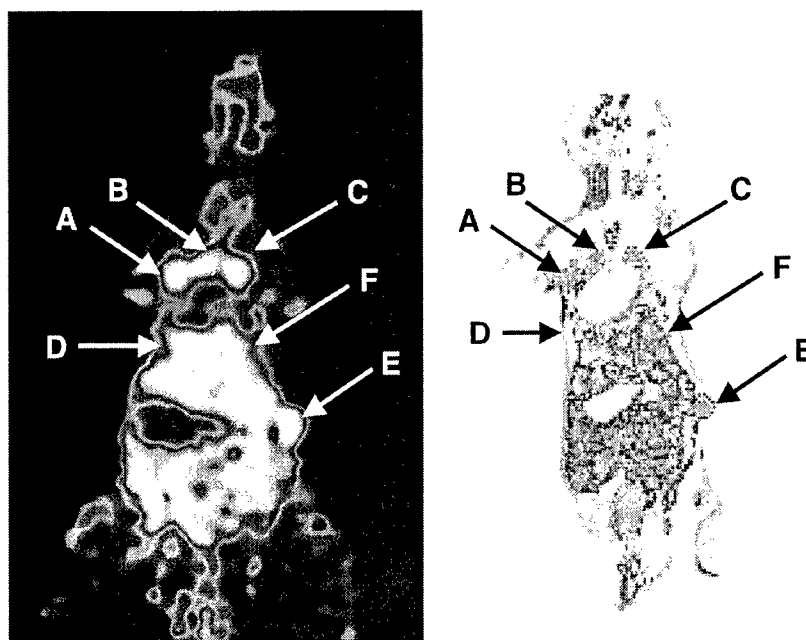
A series of cyclic RGD peptides has been labeled with ^{18}F ($t_{1/2}$ = 109.7 minutes) for PET imaging of tumor integrin expression [22,23,25,26,29,30]. The introduction of a fairly bulky prosthetic ^{18}F labeling group (4-[^{18}F]fluorobenzoyl or 2-[^{18}F]fluoropropionate) to the monomeric RGD peptide results in unfavorable hepatobiliary excretion and rapid tumor washout [22,23]. Inserting an amino sugar [29,30] or PEG [25] moiety between the integrin binding RGD sequence and ^{18}F label increases hydrophilicity and thus improves tumor targeting efficacy and pharmacokinetics of the resulting radiotracers. Recently, it has also been found that an ^{18}F-labeled dimeric RGD peptide with higher receptor binding affinity than the corresponding monomeric counterpart produces significantly increased tumor uptake and shifts

radiolabel clearance from the hepatobiliary route for the monomer to a predominantly renal route for the dimer [26].

Despite the success of ^{18}F-labeled RGD peptides for imaging integrin expression in various preclinical tumor models, it is important also to develop RGD peptides labeled with a radiometal such as ^{64}Cu ($t_{1/2}$ = 12.7 hours) for PET imaging because of the existence of imaging/therapy radionuclide pairs of these metals (i.e., ^{64}Cu/^{67}Cu and ^{86}Y/^{90}Y). Radiotracers labeled with the "imaging" isotope can be used to determine dosimetry and to monitor tumor response for the same ligand labeled with the corresponding therapeutic isotope. With this purpose in mind, we initially conjugated the macrocyclic chelator DOTA with the monomeric RGD

Figure 5. The 2D projection microPET images of SCID-bg mouse bearing both subcutaneous and orthotopic NCI-H1975 tumors. The same mouse was anesthetized and scanned with [^{18}F]FDG (day 1) and ^{64}Cu-DOTA-PEG-E[cRGDyK)]$_2$ (day 2). Left: Fifteen-minute static scan beginning 30 minutes after intravenous injection of 200 μCi of FDG. Right: Fifteen-minute static scan beginning 2 hours after injection of 300 μCi of ^{64}Cu-DOTA-PEG-E[cRGDyK)]$_2$. (1) Primary orthotopic tumor in the upper lobe of the left lung; (2) contralateral lung metastasis; (3) subcutaneous tumor; (4) heart; (5) liver; (6) kidneys; and (7) bladder. Regions identified as tumors were confirmed by cryosectioning and autoradiography following the ^{64}Cu scan (Figure 6).

Figure 6. Left: A coronal image of the same tumor-bearing mouse as shown in Figure 5. Both primary tumors as well as metastases are clearly identified. Right: WBDA of a 50-μm thick section correlating well with the coronal microPET slice shown on the left. (A) Primary orthotopic tumor in the upper lobe of the left lung; (B) local metastasis of the primary tumor; (C) contralateral lung metastasis; (D) metastasis in the diaphragm; (E) subcutaneous tumor; and (F) liver.

peptide c(RGDyK) and evaluated the resulting ^{64}Cu-DOTA-c(RGDyK) radiotracer in the MDA-MB-435 breast cancer xenograft model. Although the monomeric RGD peptide tracer was able to delineate the tumor from background, it also had high activity accumulation in liver. Similar to the ^{18}F-labeled dimeric RGD peptide, the DOTA-conjugated dimeric RGD peptide tracer ^{64}Cu-DOTA-E[c(RGDyK)]$_2$ had almost twice as much tumor uptake and somewhat increased renal uptake compared with the corresponding monomeric RGD peptide tracer ^{64}Cu-DOTA-c(RGDyK). There is no significant difference in blood clearance or liver activity accumulation between the monomeric and dimeric forms. Encouraged by the fact that PEGylation improved tumor targeting efficacy and reduced biliary excretion of the ^{18}F-labeled monomeric RGD peptide [22], we expected that the PEGylated dimeric RGD peptide when labeled with ^{64}Cu would also have improved in vivo kinetics. Indeed, ^{64}Cu-DOTA-PEG-E[c(RGDyK)]$_2$ had similar blood clearance, more rapid renal clearance, and significantly reduced hepatic uptake compared with ^{64}Cu-DOTA-E[c(RGDyK)]$_2$ [27]. However, tumor uptake was also lowered due to the fact that the PEGylated RGD dimer has lower receptor binding affinity than the dimeric RGD peptide (Figure 3). We only tested one bifunctional PEG (M_W = 3400) in this study. We anticipate a systematic investigation of the effect of PEG size and geometry on tumor targeting and biodistribution of the radiolabel in an attempt to develop a radiotracer with high receptor avidity and optimal systemic behavior.

Rapid tumor localization with relatively low normal tissue uptake outside the gut makes ^{64}Cu-DOTA-PEG-E[c(RGDyK)]$_2$ a promising agent for tumor imaging. The proof-of-principle study presented here illustrates the feasibility of NSCLC tumor and metastasis delineation with this radiotracer. It is also striking that the PEGylated dimeric RGD peptide tracer accumulated more specifically than FDG in both primary and metastatic lung tumor lesions. However, the significance of these findings is tempered by the fact that the magnitude of tumor uptake may be too low (less than 3% ID/g) for peptide receptor radiotherapy (PRRT) applications. Further modifications may lead to identification of radiolabeled integrin receptor ligands for both PET imaging and targeted therapy.

Conclusion

The ^{64}Cu-labeled PEGylated dimeric RGD peptide radiotracer was evaluated as an imaging agent for a human NSCLC in which the $\alpha_v\beta_3$ integrin is strongly expressed. On lung cancer cells (NCI-H1975) that express $\alpha_v\beta_3$ integrin, binding of [^{125}I]echistatin was inhibited by the ligand DOTA-PEG-E[c(RGDyK)]$_2$ in a log dose–dependent manner, demonstrating that the ligand is bound to cell surface receptors. IC$_{50}$ value of the PEGylated RGD dimer was lower than the unmodified dimeric RGD peptide, suggesting a weakening of ligand–receptor interaction on PEG modification. The distribution of ^{64}Cu-DOTA-PEG-E[c(RGDyK)]$_2$ in a subcutaneously implanted NCI-H1975 xenograft model showed rapid blood clearance and receptor-specific tumor activity accumulation. Due to limited nonspecific uptake in normal organs and tissues that do not express integrin $\alpha_v\beta_3$, excellent tumor-to-background ratios were obtained at all time points examined. MicroPET and whole-body digital autoradiographic imaging of an orthotopic lung cancer model provided clear delineation of a primary adenocarcinoma nodule as

well as its metastases to the mediastinum, contralateral lung, and diaphragm. The tumor visualization with ^{64}Cu-DOTA-PEG-E[c(RGDyK)]$_2$ was superior to that with the metabolic tracer [^{18}F]FDG, which did not identify the metastatic lesions due to intense cardiac uptake. The *in vivo* data strongly suggest that peptide ligands of this class are promising for imaging integrin expression in lung cancer. Further modifications to increase the magnitude of tumor uptake for integrin-targeted internal radiotherapy are needed.

References

[1] Jemal A, Tiwari RC, Murray T, Ghafoor A, Samuels A, Ward E, Feuer EJ, and Thun MJ (2004). Cancer statistics, 2004. *CA Cancer J Clin* **54**, 8–29.

[2] Mulshine JL, Cuttitta F, Tockman MS, and De Luca LM (2002). Lung cancer evolution to pre-invasive management. *Clin Chest Med* **23**, 37–48.

[3] Park BJ and Altorki NK (2002). Diagnosis and management of early lung cancer. *Surg Clin North Am* **82**, 457–476.

[4] Spira A and Ettinger DS (2004). Multidisciplinary management of lung cancer. *N Engl J Med* **350**, 379–392.

[5] Danesi R, de Braud F, Fogli S, de Pas TM, Di Paolo A, Curigliano G, and Del Tacca M (2003). Pharmacogenetics of anticancer drug sensitivity in non-small cell lung cancer. *Pharmacol Rev* **55**, 57–103.

[6] Sandler AB (2003). Molecular targeted agents in non-small-cell lung cancer. *Clin Lung Cancer* **5**, S22–S28.

[7] Etzioni R, Urban N, Ramsey S, McIntosh M, Schwartz S, Reid B, Radich J, Anderson G, and Hartwell L (2003). The case for early detection. *Nat Rev Cancer* **3**, 243–252.

[8] Line BR and White CS (2004). Positron emission tomography scanning for the diagnosis and management of lung cancer. *Curr Treat Options Oncol* **5**, 63–73.

[9] Seltzer MA, Yap CS, Silverman DH, Meta J, Schiepers C, Phelps ME, Gambhir SS, Rao J, Valk PE, and Czernin J (2002). The impact of PET on the management of lung cancer: the referring physician's perspective. *J Nucl Med* **43**, 752–756.

[10] Rohren EM, Turkington TG, and Coleman RE (2004). Clinical applications of PET in oncology. *Radiology* **231**, 305–332.

[11] Weber V, Petersen WA, Schmidt B, Tyndale-Hines L, Link T, Peschel C, and Schwaiger M (2003). Positron emission tomography in non-small-cell lung cancer: prediction of response to chemotherapy by quantitative assessment of glucose use. *J Clin Oncol* **21**, 2651–2667.

[12] Kirsch M, Schackert G, and Black PM (2004). Metastasis and angiogenesis. *Cancer Treat Res* **117**, 285–304.

[13] Kerbel RS (2004). Antiangiogenic drugs and current strategies for the treatment of lung cancer. *Semin Oncol* **31**, 54–60.

[14] Strieter RM, Belperio JA, Phillips RJ, and Keane MP (2004). Chemokines: angiogenesis and metastases in lung cancer. *Novartis Found Symp* **256**, 173–184.

[15] Smythe WR, LeBel E, Bavaria JE, Kaiser LR, and Albelda SM (1995). Integrin expression in non-small cell carcinoma of the lung. *Cancer Metastasis Rev* **14**, 229–239.

[16] Tucker GC (2003). α_v Integrin inhibitors and cancer therapy. *Curr Opin Invest Drugs* **4**, 722–731.

[17] McQuade P and Knight LC (2003). Radiopharmaceuticals for targeting the angiogenesis marker $\alpha_v\beta_3$. *Q J Nucl Med* **47**, 209–220.

[18] Kumar CC (2003). Integrin $\alpha_v\beta_3$ as a therapeutic target for blocking tumor-induced angiogenesis. *Curr Drug Targets* **4**, 123–131.

[19] Haubner RH, Wester HJ, Weber WA, and Schwaiger M (2003). Radiotracer-based strategies to image angiogenesis. *Q J Nucl Med* **47**, 189–199.

[20] Sipkins DA, Cheresh DA, Kazemi MR, Nevin LM, Bednarski MD, and Li KC (1998). Detection of tumor angiogenesis *in vivo* by $\alpha_v\beta_3$-targeted magnetic resonance imaging. *Nat Med* **4**, 623–626.

[21] Anderson SA, Rader RK, Westlin WF, Null C, Jackson D, Lanza GM, Wickline SA, and Kotyk JJ (2000). Magnetic resonance contrast enhancement of neovasculature with $\alpha_v\beta_3$-targeted nanoparticles. *Magn Reson Med* **44**, 433–439.

[22] Chen X, Park R, Shahinian AH, Tohme M, Khankaldyyan V, Bozorgzadeh MH, Bading JR, Moats R, Laug WE, and Conti PS (2004). ^{18}F-labeled RGD peptide: initial evaluation for imaging brain tumor angiogenesis. *Nucl Med Biol* **31**, 179–189.

[23] Chen X, Park R, Tohme M, Shahinian AH, and Bading PS (2004). MicroPET and autoradiographic imaging of breast cancer α_v-integrin expression using ^{18}F- and ^{64}Cu-labeled RGD peptide. *Bioconjug Chem* **15**, 41–49.

[24] Chen X, Park R, Shahinian AH, Bading JR, and Conti PS (2004). Pharmacokinetics and tumor retention of ^{125}I-labeled RGD peptide are improved by PEGylation. *Nucl Med Biol* **31**, 11–19.

[25] Chen X, Park R, Hou Y, Khankaldyyan V, Gonzales-Gomez I, Tohme M, Bading JR, Laug WE, and Conti PS (2004). MicroPET imaging of brain tumor angiogenesis with ^{18}F-labeled PEGylated RGD peptide. *Eur J Nucl Med Mol Imaging* **31**, 1081–1089.

[26] Chen X, Tohme M, Park R, Hou Y, Bading JR, and Conti PS (2004). MicroPET imaging of $\alpha_v\beta_3$ integrin expression with ^{18}F-labeled dimeric RGD peptide. *Mol Imaging* **3**, 96–104.

[27] Chen X, Liu S, Hou Y, Tohme M, Park R, Bading JR, and Conti PS (2004). MicroPET imaging of breast cancer α_v-integrin expression with ^{64}Cu-labeled dimeric RGD peptides. *Mol Imaging Biol* **6**, 350–359.

[28] Chen X, Hou Y, Tohme M, Park R, Khankaldyyan V, Gonzales-Gomez I, Bading JR, Laug WE, and Conti PS (2004). PEGylated RGD peptide: ^{64}Cu-labeling and PET imaging of brain tumor integrin $\alpha_v\beta_3$ expression. *J Nucl Med* **45**, 1776–1783.

[29] Haubner R, Kuhnast B, Mang C, Weber WA, Kessler H, Wester HJ, and Schwaiger M (2004). [^{18}F]Galacto-RGD: synthesis, radiolabeling, metabolic stability, and radiation dose estimates. *Bioconjug Chem* **15**, 61–69.

[30] Haubner R, Wester HJ, Weber WA, Mang C, Ziegler SI, Goodman SL, Senekowitsch-Schmidtke R, Kessler H, and Schwaiger M (2001). Noninvasive imaging of $\alpha_v\beta_3$ integrin expression using ^{18}F-labeled RGD-containing glycopeptide and positron emission tomography. *Cancer Res* **61**, 1781–1785.

[31] Haubner R, Wester HJ, Burkhart F, Senekowitsch-Schmidtke R, Weber W, Goodman SL, Kessler H, and Schwaiger M (2001). Glycosylated RGD-containing peptides: tracer for tumor targeting and angiogenesis imaging with improved biokinetics. *J Nucl Med* **42**, 326–336.

[32] Haubner R, Wester HJ, Reuning U, Senekowitsch-Schmidtke R, Diefenbach B, Kessler H, Stocklin G, and Schwaiger M (1999). Radiolabeled $\alpha_v\beta_3$ integrin antagonists: a new class of tracers for tumor targeting. *J Nucl Med* **40**, 1061–1071.

[33] Janssen M, Oyen WJ, Massuger LF, Frielink C, Dijkgraaf I, Edwards DS, Radjopadhye M, Corstens FH, and Boerman OC (2002). Comparison of a monomeric and dimeric radiolabeled RGD-peptide for tumor targeting. *Cancer Biother Radiopharm* **17**, 641–646.

[34] Janssen ML, Oyen WJ, Dijkgraaf I, Massuger LF, Frielink C, Edwards DS, Rajopadhye M, Boonstra H, Corstens FH, and Boerman OC (2002). Tumor targeting with radiolabeled $\alpha_v\beta_3$ integrin binding peptides in a nude mouse model. *Cancer Res* **62**, 6146–6151.

[35] van Hagen PM, Breeman WA, Bernard HF, Schaar M, Mooij CM, Srinivasan A, Schmidt MA, Krenning EP, and de Jong M (2000). Evaluation of a radiolabeled cyclic DTPA-RGD analogue for tumor imaging and radionuclide therapy. *Int J Cancer* **90**, 186–198.

[36] Ellegala DB, Leong-Poi H, Carpenter JE, Klibanov AL, Kaul S, Shaffrey ME, Sklenar J, and Lindner JR (2003). Imaging tumor angiogenesis with contrast ultrasound and microbubbles targeted to $\alpha_v\beta_3$. *Circulation* **108**, 336–341.

[37] McCarthy DW, Shefer RE, Klinkowstein RE, Bass LA, Margeneau WH, Cutler CS, Anderson CJ, and Welch MJ (1997). Efficient production of high specific activity ^{64}Cu using a biomedical cyclotron. *Nucl Med Biol* **24**, 35–43.

[38] Kumar CC, Nie H, Rogers CP, Malkowski M, Maxwell E, Catino JJ, and Armstrong L (1997). Biochemical characterization of the binding of echistatin to integrin $\alpha_v\beta_3$ receptor. *J Pharmacol Exp Ther* **283**, 843–853.

[39] Diperna CA, Bart RD, Sievers EM, Ma Y, Starnes VA, and Bremner RM (2003). Cyclooxygenase-2 inhibition decreases primary and metastatic tumor burden in a murine model of orthotopic lung adenocarcinoma. *J Thorac Cardiovasc Surg* **126**, 1129–1133.

[40] Qi J, Leahy RM, Cherry SR, Chatziioannou A, and Farquhar TH (1998). High-resolution 3D Bayesian image reconstruction using the microPET small-animal scanner. *Phys Med Biol* **43**, 1001–1013.

[41] Chen X, Park P, Hou Y, Shahinian AH, Tohme M, Bading JR, and Conti PS (2004). MicroPET and autoradiographic imaging of GRP receptor expression with ^{64}Cu-DOTA-[Lys^3]bombesin in human prostate adenocarcinoma xenografts. *J Nucl Med* **45**, 1390–1397.

[42] Wary KK (2004). Molecular targets for anti-angiogenic therapy. *Curr Opin Mol Ther* **6**, 54–70.

[43] Longo R, Sarmiento R, Fanelli M, Capaccetti B, Gattuso D, and Gasparini G (2002). Anti-angiogenic therapy: rationale, challenges and clinical studies. *Angiogenesis* **5**, 237–256.

Synthesis and Biological Evaluation of Dimeric RGD Peptide–Paclitaxel Conjugate as a Model for Integrin-Targeted Drug Delivery

Xiaoyuan Chen,[†,§,*] Carmen Plasencia,[‡] Yingping Hou,[†] and Nouri Neamati[‡,*]

Department of Radiology and Department of Pharmaceutical Sciences, University of Southern California, Los Angeles, California 90033, and Molecular Imaging Program at Stanford, Department of Radiology, Stanford University, Stanford, California 94305

Targeting drugs to receptors involved in tumor angiogenesis is a novel and promising approach to improve cancer treatment. In this study, we evaluated the antitumor activity of paclitaxel (PTX) conjugated with a bicyclic peptide E[c(RGDyK)]$_2$ (RGD) in a metastatic breast cancer cell line (MDA-MB-435). The cyclic RGD peptide selectively binds to α_v integrin receptors that are highly expressed in metastatic cancer cells. PTX, an antimicrotubule agent, is a potent antitumor agent commonly used in the treatment of advanced metastatic breast cancer. The in vitro results showed that RGD peptide inhibited cell cycle proliferation by arresting cells in G_0/G_1-phase. The PTX–RGD conjugate inhibited cell proliferation with activity comparable to that observed for paclitaxel, both of which were mediated by an arrest of G_2/M-phase of the cell cycle followed by apoptosis. Although the PTX–RGD conjugate showed slightly decreased integrin binding affinity than the unconjugated peptide, it indicated integrin specific accumulation in vivo. ^{125}I-Labeled PTX–RGD showed highest tumor uptake at 2 h postinjection ($2.72 \pm 0.16\%$ID/g) and best tumor/background contrast after 4 h postinjection. Our results demonstrate the potential of tumor-targeted delivery of paclitaxel based on the specific recognition of cell adhesion molecule $\alpha_v\beta_3$ integrin to reduce toxicity and enhance selective killing of cancer cells.

Introduction

The efficacy of chemotherapeutic drugs is limited by low sensitivity for tumor cells and high toxicity to healthy tissues.[1,2] The activity of most chemotherapeutic agents is further limited by the development of drug resistance. Tumor cells are a rapidly changing target because of their genetic instability, heterogeneity, and high rate of mutation, leading to selection and overgrowth of a drug-resistant tumor cell population.[3] To increase the therapeutic index, various drug delivery systems are being developed. Most carriers mainly focus on macromolecules such as monoclonal antibodies, proteins, or peptides. Hybrid molecules designed to bind to specific, overexpressed receptors on tumor cells are an attractive avenue for selective targeting.[4,5]

Angiogenesis, the formation of new blood vessels from preexisting vasculature, is essential for tumor growth and progression.[6,7] Inhibition of angiogenesis has been shown to prevent tumor growth and even causes tumor regression in various experimental models.[8] In contrast to traditional chemotherapeutics, which target all dividing cells, antiangiogenic therapy selectively targets activated endothelial and tumor cells. In early Phase I/II clinical trials, angiogenic modulators have shown modest toxicity, were cytostatic, slowed tumor growth and metastasis, and produced an objective remission.[9] However, antiangiogenic therapy with the aim to normalize tumor vasculature usually is not sufficient to eradicate tumors in the late stage.[8–10] Thus, combinations of antiangiogenic agents with either chemo- or radiation therapy has demonstrated enhanced antitumor activity in multiple tumor systems, and its effectiveness has been shown in breast cancer models.[11–13] The synergy most likely results from the impact of antiangiogenesis that decreases the interstitial tumor pressure leading to improved blood flow with subsequent improved local delivery when given systemically.[13]

The expression of integrin adhesion molecules $\alpha_v\beta_3$ and $\alpha_v\beta_5$ on sprouting capillary cells and their interaction with specific matrix ligands play a key role in angiogenesis and metastasis.[14] The α_v integrin receptors are highly expressed on activated endothelial cells and tumor cells, but not expressed in resting endothelial cells and most normal organ systems, making it a potential target for antiangiogenic strategy. Inhibition of α_v integrin activity by mAbs, cyclic RGD peptides, and peptidomimetics has been shown to induce endothelial apoptosis,[15] inhibit angiogenesis,[16,17] and increase endothelial monolayer permeability.[18] Suitably radiolabeled RGD peptides have also been developed for noninvasive imaging of integrin expression during tumor angiogenesis, growth, and spread.[19–29]
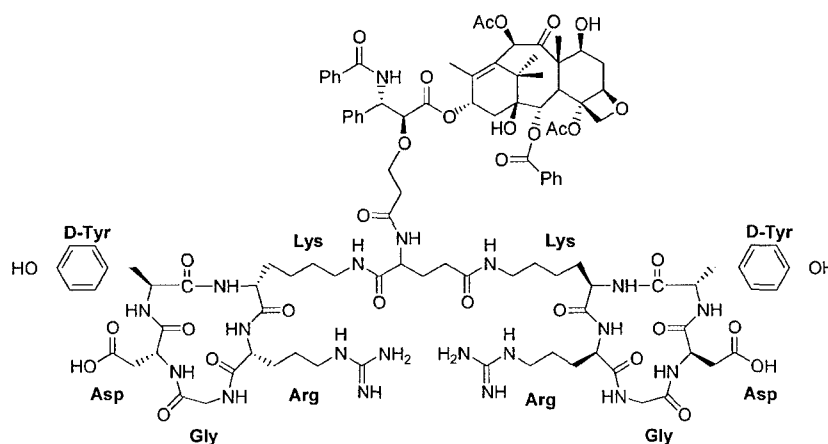
X-ray crystallographic structures of the extracellular segment of $\alpha_v\beta_3$ integrin and its complex with cyclic RGD peptide c(RGDf[NMe]V) revealed electrostatic interactions between the peptide ligand and the $\alpha_v\beta_3$

* Corresponding authors. Xiaoyuan Chen, Ph.D.; Molecular Imaging Program at Stanford, Department of Radiology, Stanford University School of Medicine, 300 Pasteur Dr., Edwards Bldg. R354, Stanford, CA 94305-5344. Phone: (650)725–0950; Fax: (650)736–0234; E-mail: shawchen@stanford.edu. Nouri Neamati, Ph.D.; Department of Pharmaceutical Sciences, School of Pharmacy, University of Southern California, 1985 Zonal Ave., Rm. 304, Los Angeles, CA 90089. Phone: 323-442-2341; Fax: 323-442-1390; E-mail: neamati@usc.edu.
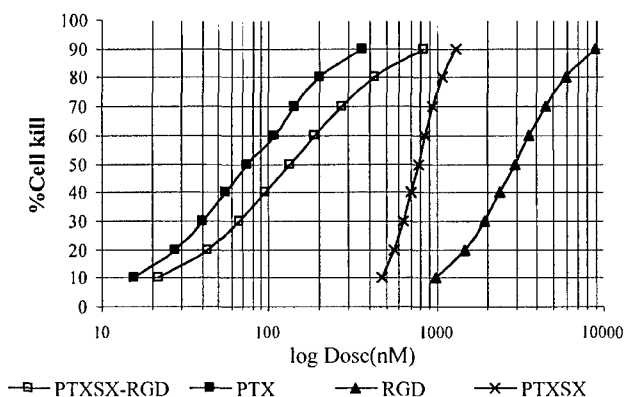   † Department of Radiology, University of Southern California, Los Angeles.
    ‡ Department of Pharmaceutical Sciences, University of Southern California, Los Angeles.
    § Department of Radiology, Stanford University.

Figure 1. Schematic representation of the molecular structure of dimeric RGD peptide–paclitaxel conjugate. The succinate linkage is through the 2′-hydroxy group of paclitaxel and amino group of RGD glutamate residue.

Figure 2. Cytotoxic effect of PTX, PTXSX, PTX–RGD conjugate, and RGD peptide. MDA-MB-435 cells were treated with continuous exposure of each drug for 48 h, and cytotoxicity was assessed by MTT assay as described in the Experimental Section. Data are presented as a measure of percent survival normalized against the untreated population. Each data point is from an average of three to four independent experiments performed in triplicate. IC_{50} values for PTX, PTXSX, PTX–RGD, and RGD are 34 ± 5, 67 ± 9, 134 ± 28, and 2940 ± 15 nM, respectively.
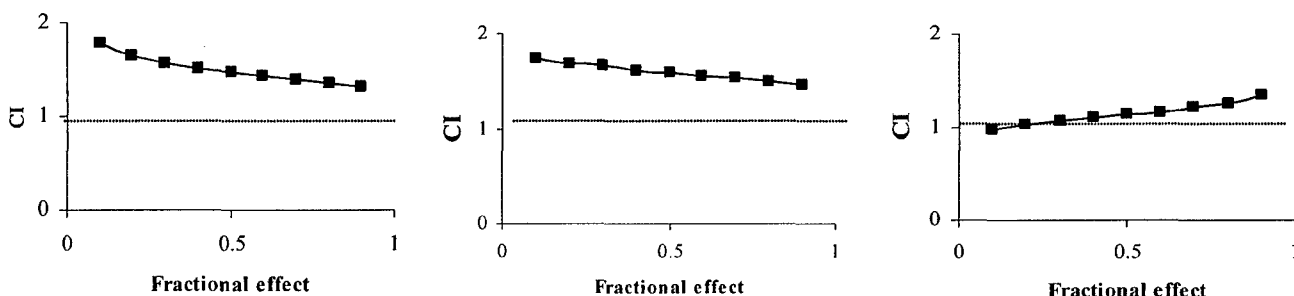
receptor: arginine interacts with two anionic aspartic acid residues in the α-subunit, aspartic acid interacts with divalent metal cation in the metal ion-dependent adhesion site (MIDAS) region of the β-subunit, and glycine forms close contact with the protein. D-Phenylalanine is involved in hydrophobic interactions, while N-methylvaline forms no contact with the protein.[30−32]

Thus, we have changed D-Phe to D-Tyr to increase hydrophilicity, as well as providing the possibility of iodination radiolabeling. N-Methylvaline was changed to lysine to facilitate further modification via the side chain ε-amino group.[19−23,26] It was also recently reported that dimeric and multimeric cyclic RGD peptides have higher receptor binding affinity in vitro[33] and better tumor retention in vivo.[24,25,29] This is presumably due to polyvalency, which gives rise to an enhanced binding and steric stabilization.[34]
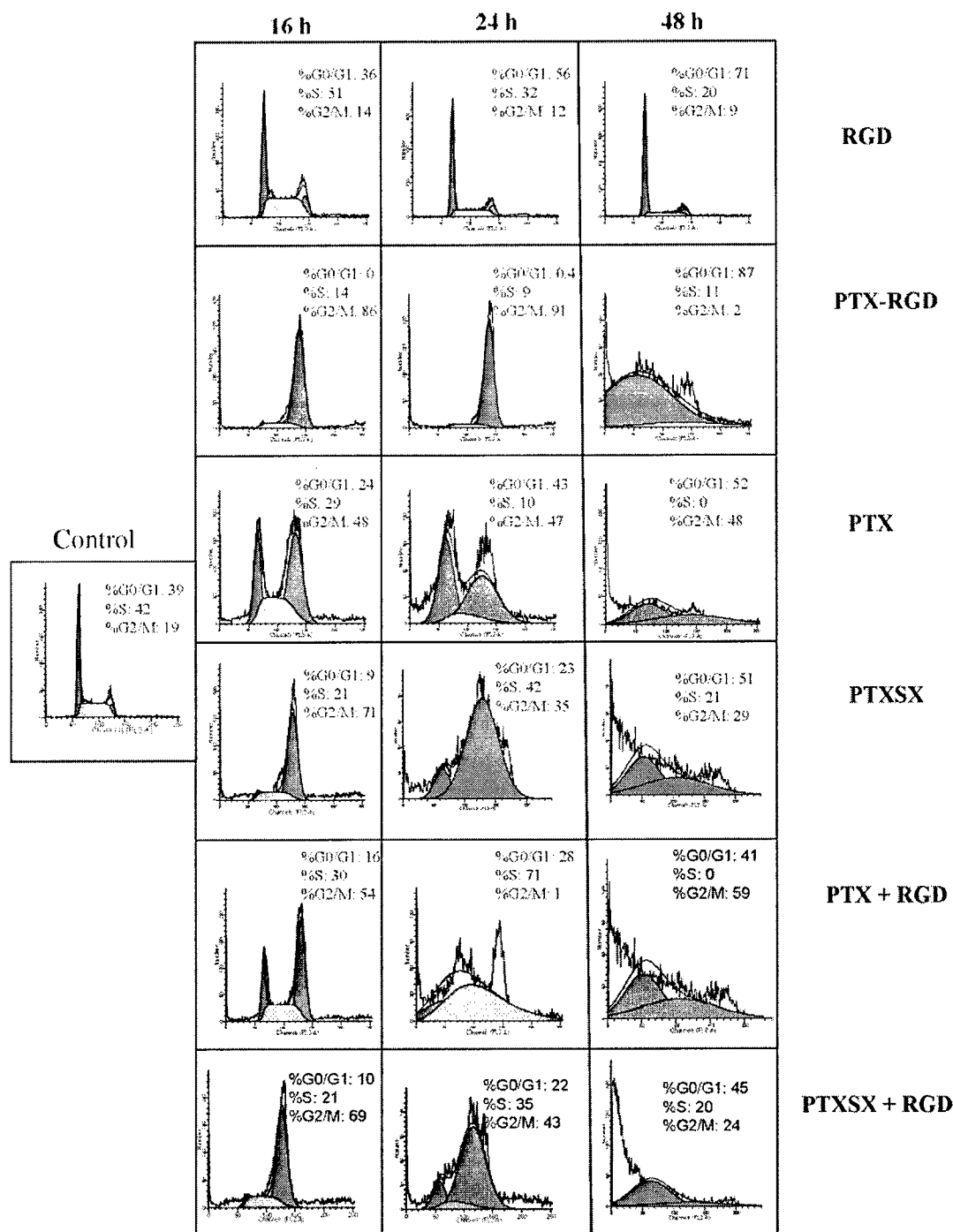
Estrogen-independent breast cancer cell line MDA-MB-435 is known to express high levels of integrin $\alpha_v\beta_3$, and the expression of activated $\alpha_v\beta_3$ integrin has been associated directly with the metastatic and osteolytic potential of MDA-MB-435 breast carcinoma.[25,35,36] In this study, we used dimeric RGD peptide E[c(RGDyK)]₂, a potent α_v-integrin antagonist, as carrier for paclitaxel to specifically target breast cancer cells and tumor blood vessels. The in vitro receptor binding, cytotoxicity, and apoptosis results were observed in the MDA-MB-435 cell line, and biodistribution data was performed in an orthotopic nude mouse breast cancer model.

Results

Synthesis and Characterization. The conjugate of paclitaxel (PTX) with dimeric RGD peptide[37] (Figure 1) was prepared by derivatizing the 2′-hydroxy function of paclitaxel with succinic anhydride, according to reported procedure.[38] The paclitaxel hemisuccinate ester (PTXSX) was activated using EDC and NHS, followed

Figure 3. Combination index (CI) for PTX and RGD combinations. MDA-MB-435 cells were treated with various $IC_{50}:IC_{50}$ ratios of PTX and RGD. (Left panel) PTX+RGD: simultaneous exposure of both drugs for 48 h. (Middle panel) PTX→RGD: cells were pretreated with PTX for 24 h, and then RGD was added for an additional 24 h. (Right panel) RGD→PTX: cells were exposed to RGD for 24 h, and then PTX was added for an additional 24 h. The fractional effect was evaluated by Chou–Talalay method. CI = 1 reflects additive effects, CI > 1 antagonism and CI < 1 synergism.

Figure 4. Flow cytometric analysis of the cell cycle profiles of treated MDA-MB-435 cells. RGD peptide induces cell cycle arrest in G_0/G_1 phase with no apoptosis even at high drug concentration and prolonged exposure. All three PTX derivatives resulted in G_2/M cell cycle arrest with distinct apoptosis (sub-G_0/G_1 population) 24 h after drug treatment.
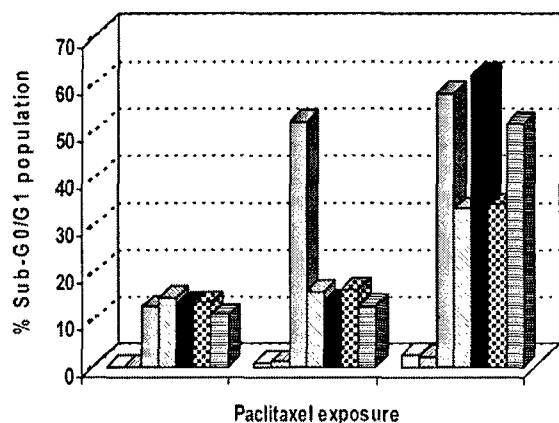
by coupling with RGD peptide glutamate amino group under slightly basic conditions.

Cytotoxicity Assessments. The cytotoxic effect of PTX, PTXSX, RGD, and PTX−RGD conjugate administered as single agents was assessed by MTT (3-(4, 5-dimethylthiazole-2-yl)-2,5-diphenyltetrazoliumbromide) assay[39] in MDA-MB-435 breast cancer cells after 48 h continuous drug exposure (Figure 2). PTXSX with the IC_{50} of 67 ± 9 nM showed similar potency to PTX (IC_{50} = 34 ± 5 nM). However, PTX−RGD conjugate with the IC_{50} value of 134 ± 28 nM was slightly less potent

than free PTX. Cyclic RGD peptide was the least potent (IC_{50} = 2.9 ± 0.1 μM).

Analysis of Drug Combinations. Sequential and concomitant combinations of PTX and RGD peptide were analyzed in MDA-MB-435 cells by the method of Chou and Talalay.[40] We observed that simultaneous (schedule 1) and sequential PTX treatment followed by RGD (PTX → RGD, schedule 2) produced antagonistic effects (CI > 1; Figure 3). However, when cells were exposed to RGD before the addition of PTX (RGD → PTX, schedule 3), an additive effect was observed at all

□ Control □ RGD □ PTX-RGD □ PTX ■ PTXSX ▨ PTX + RGD ▤ PTXSX + RGD

Figure 5. Percentage of sub-G_0/G_1 population determined by flow cytometry. The PTX—RGD conjugate is comparable to that of PTX/RGD combination.

levels of fractional inhibition. As shown in Figure 3, previous exposure to RGD reduced the PTX dose given in combination as compared to PTX administered as a single agent. The cytotoxicity of the simultaneous combination between PTXSX and RGD was also evaluated. In contrast to the data obtained for PTX, a modest synergistic effect was observed for PTXSX and RGD combination (data not shown).

Effect on Cell Cycle Progression. Flow cytometric analysis was performed to analyze the cell cycle perturbations and apoptosis. As expected, RGD administered as a single agent induced cell cycle arrest in G_0/G_1 phase. No apoptotic fraction (as determined by the sub-G_1 peak) was observed even at longer exposures to high concentrations of the drug (IC$_{80}$, Figure 4), which correlates well with the cytostatic effect observed in the drug sensitivity test. A G_2/M cell cycle arrest was observed for PTX, PTXSX, and PTX—RGD conjugate (Figure 4). The appearance of apoptotic cells (as calculated by sub-G_0/G_1 population) was evident at 24 h for all drugs. PTX—RGD conjugate and PTXSX showed similar mitotic arrest and apoptotic cell death to that of PTX. In all cases, the apoptotic events seemed to occur after G_2/M arrest (Figure 5).

Simultaneous combination of PTX, PTXSX, and RGD first induced a slight G_2/M-phase arrest at 16 h followed by the progressive appearance of a sub-G_1 peak characteristic of apoptosis (Figure 5). Levels of apoptotic fractions increased up to 35% and 57% with PTX/RGD and PTXSX /RGD combination, respectively (Figure 5). Our findings also demonstrate that the PTX—RGD conjugate is as efficacious as the combination of PTX or PTXSX and RGD.

Characterization of Drug-Induced Apoptosis. An early event in apoptotic cell death is the translocation of the phosphatidyl-serine (PS) residues to the outer part of the cytoplasmatic cell membrane. In the presence of calcium, rapid high affinity binding of annexin V to PS occurs. PS translocation to the cell surface precedes nuclear breakdown, DNA fragmentation, and the appearance of most apoptosis-associated molecules, making annexin V binding a marker of early-stage apoptosis. By using this method, we determined the ability of PTX—RGD conjugate to induce apoptosis and compared
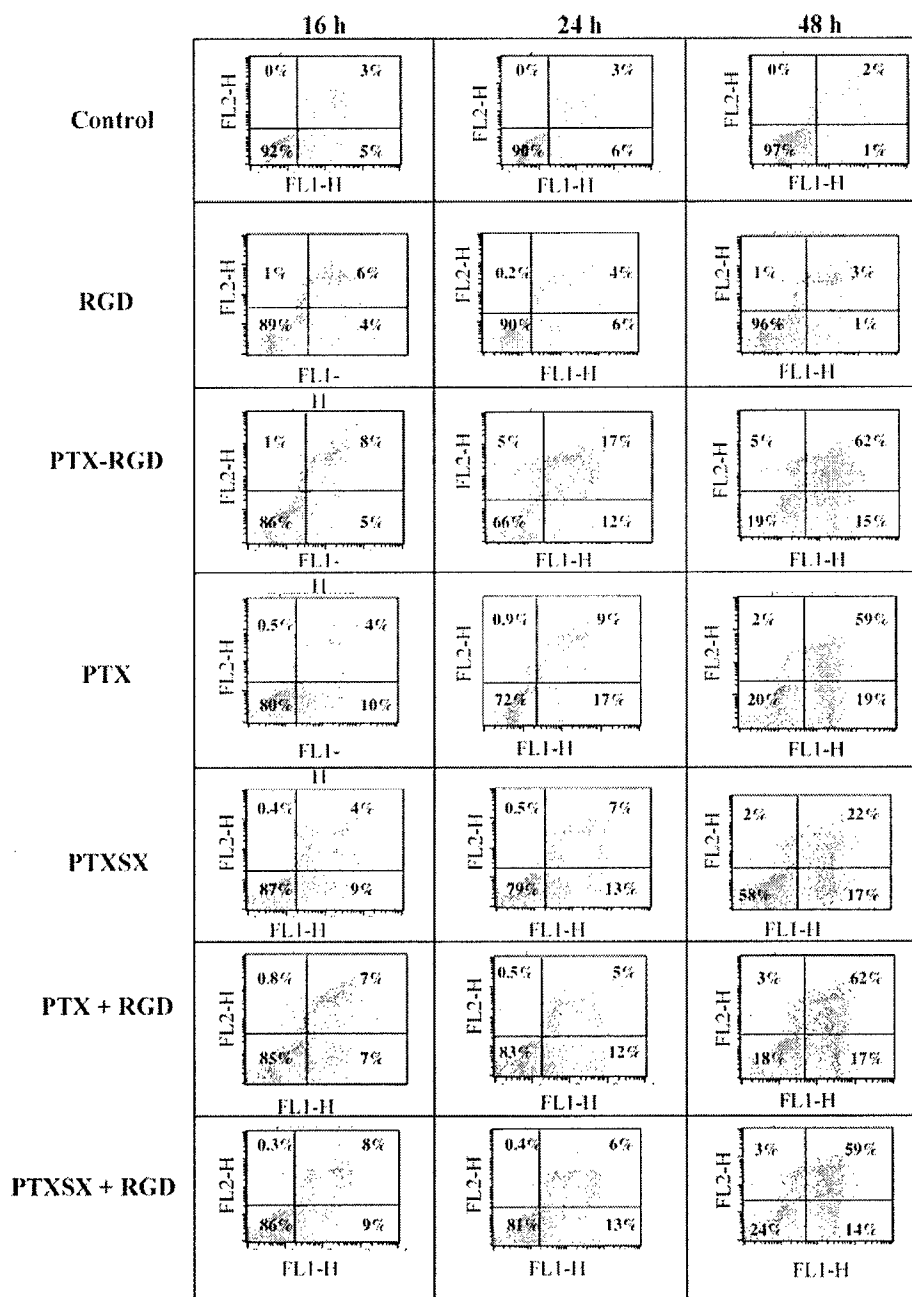
it to the ability of PTX and RGD used as a single agents or in simultaneous combination (PTX+RGD). As shown in Figure 6, PTX—RGD conjugate caused a strong apoptotic effect comparable to that induced by PTX as a single agent. At 24 h, 12% of PTX—RGD conjugate-treated cells appeared to be in early apoptosis as compared to 17% for PTX. An increase in late apoptosis/ necrosis was also apparent at 48 h for both drugs (Figure 6). No significant changes in the percentage of apoptotic cells were observed in RGD treated cells, data that correlates with the results obtained in the cell cycle analysis. Moreover, as we previously observed in the cell cycle profile for the simultaneous combination of PTX and RGD, the presence of RGD significantly reduced the percentage of apoptotic cells as compared to PTX—RGD as a single agent.

Integrin Binding Affinity. To determine whether PTX conjugation alters the receptor affinity of dimeric RGD peptide, competitive binding measurements were performed between ^{125}I-echistatin and the RGD peptide ligands (Figure 7). All ligands tested in these assays showed the expected sigmoid curves. Coupling of a rather bulky PTX moiety with dimeric RGD peptide through the succinate tether did not significantly reduce the receptor avidity of the peptide (IC$_{50}$ values for E[c(RGDyK)]$_2$ and PTX—RGD conjugate were 15.6 and 25.9 nM, respectively).

Biodistribution. To assess the effect of conjugation and the presence of drug moiety on the MDA-MB-435 tumor and normal tissue uptake, the biodistribution of the ^{125}I-labeled conjugate (^{125}I-RGD—PTX) was compared to that of ^{125}I-RGD. Radioiodination of both compounds through a standard Chloramine-T method afforded the labeled molecules as evidenced by radio-HPLC with high specific activity (1500 to 2000 Ci/ mmol). Typical radiochemical yield after HPLC purification for both radioligands was about 50—60% with radiochemical purity over 95%. The labeled RGD and conjugate were injected intravenously (iv) into athymic nude mice carrying orthotopic MDA-MB-435 xenografts. Tissues were removed at different time-points postinjection (pi) and the radioactivity uptakes, expressed in %ID/g were measured (Tables 1 and 2). Both RGD and PTX—RGD conjugate revealed fast blood clearance. Tumor activity accumulation was rapid for ^{125}I-RGD (e.g., 3.85 ± 1.15% ID/g at 30 min pi) and was quickly washed out, resulting in only 1.64 ± 0.24%ID/g at 4 h pi. The maximum tumor uptake for the conjugate appeared at 2 h pi (2.72 ± 0.16%ID/g), and remained constant at 4 h pi (2.37 ± 0.76%ID/g). The best tumor-to-blood and tumor-to-muscle ratios were achieved after 4 h pi. To demonstrate that the RGD and RGD—PTX conjugate uptakes in MDA-MB-435 tumors were specific and receptor mediated, biodistribution studies were performed by co-injecting of c(RGDyK) (10 mg/kg) with the iodinated radiotracers. Uptake values of 0.87 ± 0.17 and 0.42 ± 0.07%ID/g were observed at 1 h pi for RGD and the conjugate, respectively. These values were 4—5 times lower than the tumor uptake of the radiotracers when no blocking agent was co-injected.
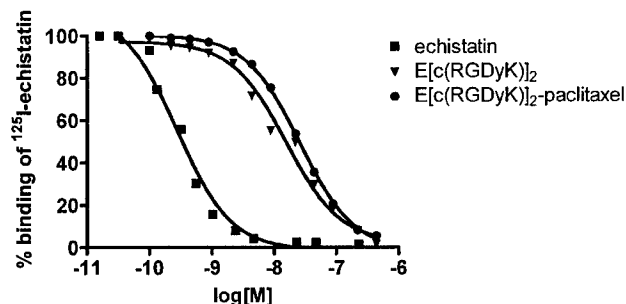
Discussion

In the present work, a dimeric RGD peptide E[c(RGDy-K)]$_2$ was conjugated to paclitaxel (PTX) and evaluated

Figure 6. Apoptosis analysis of MDA-MB-435 cells treated with RGD, PTX–RGD, PTX, PTXSX, and simultaneous combination of PTX and PTXSX with RGD. Cells stained with annexinV/propidium iodide and analyzed by flow cytometry.

for its in vitro antiproliferative effect in comparison with free PTX and for its in vivo tumor-targeting efficacy. We showed that PTX–RGD conjugate inhibits tumor cell growth comparable to that of PTX and PTXSX. PTX–RGD inhibition of cell growth was mediated by cell cycle retention and apoptosis. PTX–RGD blocked cell cycle in G_2/M-phase, with the subsequent disappearance of the G_0/G_1 and S peaks, which was comparably similar to that induced by PTX and PTXSX. The cell cycle arrest induced by these compounds (PTX, PTXSX, and PTX–RGD) was followed by cell death, as determined by annexin V/PI staining. Moreover, PTX–RGD conjugate caused a very strong apoptotic effect. At 24 h, 17% of PTX–RGD conjugate treated cells appeared to be in early apoptosis compared to 9% for PTX. These data is consistent with the increase in the

Figure 7. Competition of specific binding of ^{125}I-echistatin with unlabeled echistatin (■), E[c(RGDyK)]$_2$ (▼), and PTX–E[c(RGDyK)]$_2$ conjugate (●) to MDA-MB-435 cells. Cell-associated radioactivity in the absence of competitor was set at 100%. Values are mean of triplicate assays ± SD. [echistatin: 0.28 nM; RGD: 15.6 nM; RGD–PTX: 25.9 nM].

Table 1. Radioactivity, Expressed as Percent Injected Dose per Gram Tissue in Different Organs and Tumor of MDA-MB-435 Xenograft Model after Intravenous Injection of 2 μCi of ^{125}I-E[c(RGDyK)]$_2$ at 30 min, 1, 2, 4 h, and 1 h Block (with coinjection of 10 mg/kg c(RGDyK)) (n = 4)

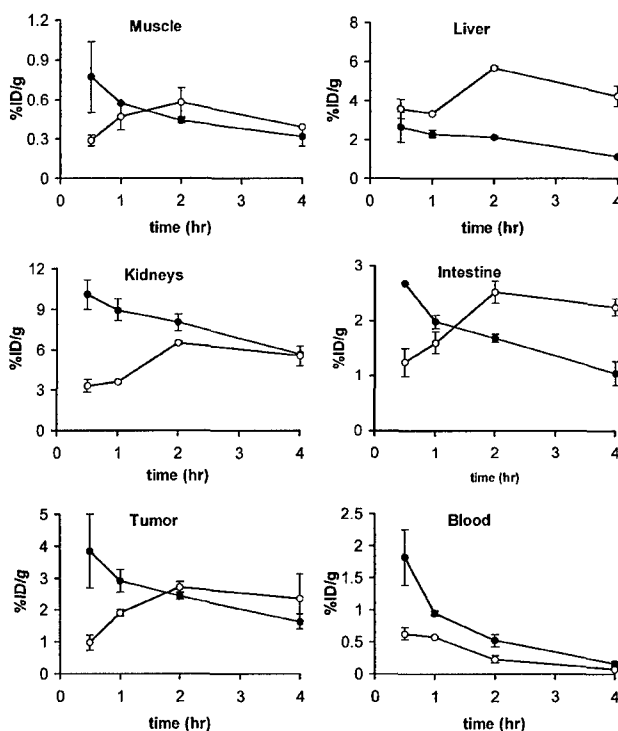|	0.5 h	1 h	2 h	4 h	1 h block
blood	1.82 ± 0.43	0.95 ± 0.04	0.52 ± 0.09	0.16 ± 0.04	1.16 ± 0.31
muscle	0.77 ± 0.23	0.57 ± 0.01	0.44 ± 0.02	0.32 ± 0.07	0.62 ± 0.44
tumor	3.85 ± 1.15	2.91 ± 0.35	2.44 ± 0.10	1.64 ± 0.24	0.87 ± 0.17
bone	1.49 ± 0.63	1.05 ± 0.15	0.81 ± 0.19	0.49 ± 0.14	0.56 ± 0.01
heart	1.28 ± 0.31	0.83 ± 0.01	0.68 ± 0.01	0.36 ± 0.03	0.62 ± 0.14
lung	3.30 ± 0.94	1.99 ± 0.08	1.43 ± 0.15	0.97 ± 0.08	1.47 ± 0.24
liver	2.64 ± 0.77	2.30 ± 0.17	2.11 ± 0.08	1.13 ± 0.05	1.29 ± 0.24
kidney	10.1 ± 1.10	8.95 ± 0.82	8.01 ± 0.64	5.65 ± 0.09	6.43 ± 0.91
spleen	1.96 ± 0.57	1.60 ± 0.07	1.44 ± 0.09	0.85 ± 0.01	0.89 ± 0.37
pancreas	0.57 ± 0.16	0.78 ± 0.09	0.58 ± 0.07	0.34 ± 0.03	0.68 ± 0.01
stomach	5.76 ± 0.89	4.33 ± 0.75	3.20 ± 0.86	1.55 ± 0.54	3.36 ± 0.37
intestines	2.68 ± 0.02	1.98 ± 0.12	1.68 ± 0.07	1.04 ± 0.22	1.74 ± 0.04
tumor/blood	2.09 ± 0.12	3.20 ± 0.44	3.24 ± 0.42	10.9 ± 3.35	0.75 ± 0.21
tumor/muscle	5.03 ± 0.03	5.20 ± 0.71	3.83 ± 0.07	5.16 ± 0.39	1.40 ± 0.49

Table 2. Radioactivity, Expressed as Percent Injected Dose per Gram Tissue in Different Organs and Tumor of MDA-MB-435 Xenograft Model after Intravenous Injection of 2 μCi of ^{125}I-E[c(RGDyK)]$_2$–PTX conjugate at 30 min, 1, 2, 4 h, and 1 h Block (with coinjection of 10 mg/kg c(RGDyK)) (n = 4)

	0.5 h	1 h	2 h	4 h	1 h block
blood	0.63 ± 0.09	0.58 ± 0.01	0.23 ± 0.06	0.07 ± 0.01	0.44 ± 0.05
muscle	0.29 ± 0.04	0.47 ± 0.01	0.58 ± 0.11	0.39 ± 0.01	0.14 ± 0.02
tumor	0.97 ± 0.24	1.91 ± 0.09	2.72 ± 0.16	2.37 ± 0.76	0.42 ± 0.07
bone	1.14 ± 0.01	1.77 ± 0.73	1.81 ± 0.73	0.83 ± 0.12	0.41 ± 0.09
heart	0.81 ± 0.12	0.82 ± 0.05	0.99 ± 0.05	0.81 ± 0.14	0.37 ± 0.01
lung	0.63 ± 0.11	1.55 ± 0.97	2.36 ± 0.97	1.38 ± 0.20	0.95 ± 0.03
liver	3.59 ± 0.48	3.35 ± 0.08	5.66 ± 0.08	4.25 ± 0.52	2.43 ± 0.38
kidney	3.33 ± 0.47	3.61 ± 0.14	6.51 ± 0.14	5.53 ± 0.73	2.32 ± 0.46
spleen	1.04 ± 0.07	1.45 ± 0.24	2.53 ± 0.24	2.14 ± 0.07	0.33 ± 0.06
pancreas	0.34 ± 0.04	0.49 ± 0.05	0.55 ± 0.05	0.48 ± 0.07	0.23 ± 0.01
stomach	1.55 ± 0.02	2.06 ± 0.03	3.08 ± 0.03	2.54 ± 0.12	1.06 ± 0.17
intestines	1.24 ± 0.26	1.60 ± 0.20	2.52 ± 0.20	2.25 ± 0.15	0.45 ± 0.24
tumor/blood	1.52 ± 0.14	3.32 ± 0.21	11.9 ± 2.54	33.4 ± 4.12	0.95 ± 0.17
tumor/muscle	3.32 ± 0.34	4.03 ± 0.21	4.76 ± 0.64	3.01 ± 0.954	3.02 ± 0.36

percentage of sub-G_0/G_1 population as determined by flow cytometry (50% for PTX—RGD versus 20% for PTX and PTXSX at 24 h; Figure 5). These data may suggest

Figure 8. Comparison of biodistribution data for ^{125}I-E[c(RGDyK)]2 (●) and ^{125}I-RGD—PTXSX (O) in orthotopic MDA-MB-435 breast cancer xenograft model. Error bars denote SD (n = 4).

an enhancement of the apoptotic signaling due to the conjugation of RGD to PTX. It is expected that the same conjugate, when applied to integrin negative cancer cells, would not have similar potency due to the lack of integrin-targeted delivery, and internalization of PTX. Further studies are required to support this hypothesis. It is noteworthy that the metabolic stability of PTX—RGD conjugate and PTXSX is unknown. If the RGD conjugate and the paclitaxel hemisuccinate ester are susceptible for enzymatic degradation, the release of free paclitaxel may partially account for the cytotoxic effects observed.

RGD also inhibited cell cycle proliferation by inducing G_0/G_1 arrest with the subsequent disappearance of G_2/M peak. No apoptosis was observed after cell cycle arrest. Therefore, RGD induced inhibition of cell growth was not associated with cell death, despite the alteration of cell adhesion in this cell line (cell detachment, data not shown). The conjugation of RGD to PTX, however, completely abolished the G_0/G_1 arrest induced by RGD, leading to a characteristic G_2/M-phase arrest similar to that induced by PTX. The conjugation also resulted in a decrease in alteration of cell adhesion and a subsequent increase of cell cytoxicity.

Cell cycle-specific action of PTX and RGD supports the rationale for combining both drugs and exploiting them for cancer therapy. Therefore, we evaluated the cytotoxic effects of different combination schedules (concomitant or sequential) between PTX and RGD. We also compared the efficacy of these combinations versus the conjugate. Our results showed that the efficacy of this combination is schedule-dependent. Pretreatment with RGD followed by PTX is more cytotoxic than the

other two schedules (simultaneous RGD + PTX, and reverse sequence, PTX→RGD). Therefore, from our combination studies, we can conclude that RGD possesses schedule-dependent antagonism on the antitumor activity of PTX in vitro, providing a rationale for the administration of two drugs in vivo. Taking into account that PTXSX exhibited similar properties to that of PTX (cytotoxicity, cell cycle retention, and apoptosis induction), we also evaluated the activity of the simultaneous combination of RGD and PTXSX. In contrast to the results with PTX, a synergistic effect was observed in this combination, suggesting that succinate modification improved the ability of PTX to enhance RGD cytotoxicity. Despite the ability of RGD and PTX or PTXSX in combination to inhibit cell growth, they are less effective in cell killing than the PTX−RGD conjugate. A greater percentage of sub-G_0/G_1 population was found when cells were exposed to PTX−RGD conjugate than to the combination of RGD and PTX or PTXSX. The conjugate also produced more early apoptotic cells than the drug combination.

Finally, we also demonstrated that the conjugated PTX did not significantly affect the integrin receptor affinity for RGD peptide, as demonstrated by the integrin binding affinity assays (Figure 7). These data indicate that conjugation could enhance tumor recognition of PTX through integrin receptor binding. The enhanced tumor recognition agrees well with the cytotoxicity of the conjugate observed by the MTT assays. Biodistribution studies also confirmed that PTX−RGD conjugate uptake was receptor-specific and comparable to the RGD uptake. Our results suggest that the presence of RGD peptide may improve the localization and internalization of PTX as well as exert its function as an antiangiogenic compound. Further studies, however, are required to elucidate the molecular mechanisms involved in the activity of this conjugate.

In conclusion, this study demonstrates that a paclitaxel−RGD peptide conjugate can be used as an antitumor agent. By targeting integrin $\alpha_v\beta_3$, it is possible to improve the tumor specificity and cytotoxic effect of paclitaxel, resulting in lower systemic doses to obtain anitumor efficacy and reduced toxicity. It is unknown if and when the free paclitaxel is released during the time course of the assay. The possibility of partial distribution of free drug generated through either extracellular or intracellular proteases cannot be completely ruled out. Nevertheless, an improved therapeutic index could be expected by tumor integrin specific delivery of at least a part of targeted pacliatxel, resulting in lower and therefore less toxic systemic doses that are necessary to obtain antitumor efficacy. Further evaluation of this lead compound in preclinical animal models for tumor growth inhibition and acute toxicity studies is currently in progress.

Experimental Section

Materials. All reagents, unless otherwise specified, were of analytical grade and purchased commercially. *N*-Hydroxysulfonosuccinimide (SNHS) and 1-ethyl-3-[3-(dimethylamino)propyl]carbodiimide (EDC) were obtained from Sigma (St. Louis, MO). Cyclic RGD peptide c(RGDyK) was synthesized via solution cyclization of the fully protected linear pentapeptide H-Gly-Asp(OtBu)-D-Tyr(OtBu)-Lys(Boc)-Arg(Pbf)-OH, followed by TFA deprotection.[19] Dimeric RGD peptide E[c(RG-

DyK)]$_2$ was prepared by coupling Boc-Glu-OH with 2 equiv of monomeric RGD peptide c(RGDyK) followed by TFA cleavage.[24,25,37] PTX-2′-succinate (PTXSX) was prepared by reacting PTX (Hande Tech, Houston, TX) with equal molar amount of succinic anhydride in pyridine.[38] ^{125}I-Echistatin labeled by the lactoperoxidase method to a specific activity of 2000 Ci/mmol was purchased from Amersham Biosciences (Piscataway, NJ). Echistatin was purchased from Sigma (St. Louis, MO). Purified human integrin $\alpha_v\beta_3$ in Triton-100 formulation was obtained from Chemicon International (Temecula, CA).

E[c(RGDyK)]$_2$−PTX Conjugate. To a solution of PTXSX (5 mg, 5.25 μmol) in 50% CH$_3$CN (2 mL) and EDC (1 mg, 5.5 μmol) in water (500 μL) was added 0.1 N NaOH to adjust the pH to 5.0. SNHS (1.1 mg, 5 μmol) was then added to the stirring mixture on an ice-bath, and 0.1 N NaOH was further added to adjust the pH to 5.5. The reaction was allowed to proceed for 30 min at 4 °C. To the active ester PTXSX-OSSu prepared in situ was then added dimeric RGD peptide E[c(RGDyK)]$_2$ (13.5 mg, 10 μmol). The reaction was allowed to mix overnight at 4 °C. The purification of the crude product was carried out on a semipreparative reversed-phase HPLC system (Waters 515 chromatography system with a 486 tunable absorbance detector). Version 7.2.1 Labtech Notebook/XE software (Andover, MA) was used to record chromatograms. Purification was performed on a Vydac protein and peptide column 218TP510 (5 μm, 250 × 10 mm). The flow was 5 mL/min, with the mobile phase starting from 70% solvent A (0.1% TFA in water) and 30% solvent B (0.1% TFA in acetonitrile) (0−2 min) to 10% solvent A and 90% solvent B at 32 min. The analytical HPLC method was performed with the same gradient system, but with a Vydac 218TP54 column (5 μm, 250 × 4.6 mm) at a flow rate of 1 mL/min. The absorbance was monitored at 218 nm. The fractions containing the RGD conjugate were collected and lyophilized, and the solid was dissolved in DMSO at a concentration of 10 mg/mL for use in radiolabeling reactions and in vitro assays. MALDI-TOF MS: m/z = 2285.63 for [M + H]$^+$ (C$_{110}$H$_{139}$N$_{20}$O$_{34}$). The retention time on analytical HPLC under the conditions defined in the Experimental Section was 12.5 min, and the yield was 45% with a purity of 97%. The retention times for PTX and PTXSX under the same gradient condition were 16.9 and 17.3 min, respectively.

^{125}I-Radiolabeling. The dimeric RGD peptide and RGD−PTX conjugate were both labeled with ^{125}I using the standard chloramine-T method.[19] The peptide (10−20 μg) was dissolved in 100 μL of phosphate-buffered saline (PBS) (pH 7.4) in a 1.5 mL polypropylene vial. [^{125}I]NaI (1 mCi) was added to the vial, followed by 150 μg of chloramine-T (10 mg/mL in PBS, pH 7.4). After 2 min, the iodination was quenched with 500 μg of Na$_2$S$_2$O$_5$ (10 mg/mL in PBS, pH 7.4). The mixture was diluted with 200 μL of 0.1% TFA and purified by analytical HPLC with collection of 0.5 mL fractions. After the solvent was removed in vacuo, the residue was triturated with water, passed through a C$_{18}$ Sep-Pak column, washed twice with water (2 mL each), and eluted with 2 mL 80% ethanol. The ethanol was removed in vacuo, and the residue was dissolved in PBS (pH 7.4) to obtain solutions with activity concentration of 1.85 MBq/mL. The solution was passed through a 0.22 μm Millipore filter into a sterile multidose vial for use in animal experiments. Radiochemical yields of ^{125}I-E[c(RGDyK)]$_2$ and ^{125}I-RGD−PTX ranged from 50 to 60%, and radiochemical purity was over 95%.

Cell Culture. Estrogen-negative breast cancer cell line MDA-MB-435 was obtained from Dr. Francis Markland (Department of Biochemistry and Molecular Biology, University of Southern California) and was maintained as monolayer cultures in Leibovitz's L-15 medium with 2 mM L-glutamine supplemented with 10% v/v fetal bovine serum. At confluency, the cells were washed with Dulbecco's PBS and incubated at 37 °C for 5 min with trypsin−EDTA. Subsequently, the cells were detached and resuspended in new medium. All subsequent experiments were performed using cells in exponential growth.

Cytotoxicity Assay. The sensitivity of MDA-MB-435 cells

to drug was determined by MTT (3-(4,5-dimethylthiazole-2-yl)-2,5-diphenyltetrazoliumbromide) assay.[39] Briefly, 4×10^3 cells/well were seeded in 96-well plates and allowed to attach overnight. Serial dilutions of each drug were added for 48 h. An MTT solution (at a final concentration of 0.5 mg/mL) was then added to each well, and cells were incubated for 4 h at 37 °C. After removal of the media, DMSO was added to dissolve the crystals, and the absorbance was measured at 570 nm. All assays were performed in triplicate. Doses for each fraction of survival (ranging from 10% to 90% of cell viability) were determined by median-effect line method. IC_{50} (dose of each drug that inhibits 50% of cell growth) was used for the combination analysis.

Drug Combination Studies. To define the best combination between PTX and RGD, three different schedules of administration were performed: (1) PTX + RGD (48 h), (2) PTX (48 h) → RGD (24 h), and (3) RGD (48 h) → PTX (24 h). Cell viability for each combination was assessed by MTT assay and data were analyzed by Chou and Talalay method.[40] Briefly, the analyses of combined drug effects were performed in each experiment with serial dilutions of both drugs administered at doses that typically correspond to $^1/_4$, 1/2, 1, 1.5, and 3 times the individual IC_{50} values. Fractional survival was then calculated by dividing the number of cells in drug-treated plates by the number of cells in control plates. Data were subsequently analyzed by the method of Chou and Talalay.[40] By using this method it is possible to calculate the doses of the individual drugs and the combination required to produce varying levels of cytotoxicity. For each level of cytotoxicity, a parameter called the combination index (CI) is then calculated according to the following equation: $CI_f = D_1/(D_f)_1 + D_2/(D_f)_2 + \lambda D_1 D_2/(D_f)_1(D_f)_2$,[39] where D_1 and D_2 are the concentrations of the combination required to produce survival f. $(D_f)_1$ and $(D_f)_2$ are the concentrations of the individual drugs required to produce f. The value for λ was set to one or zero depending on whether the drugs are assumed to be mutually nonexclusive or mutually exclusive, respectively, in their action. According to this method, synergism is indicated by a CI < 1, antagonism by a CI > 1, and additivity by CI = 1.

Cell Cycle Analysis. Cell cycle perturbations induced by RGD, PTX, PTXSX, PTX—RGD conjugate or the combination of PTX and RGD were analyzed by propidium iodide (PI) DNA staining. Briefly, exponentially growing MDA-MB-435 cells were treated with IC_{80} doses of each drug (sequential combinations) for 24, 48, and 72 h. At the end of each treatment, cells were collected and washed with PBS after a gentle centrifugation at 200*g* for 5 min. Cells were thoroughly suspended in 0.5 mL of PBS and fixed in 70% ethanol for at least 2 h at 4 °C. Ethanol-suspended cells were then centrifuged at 200*g* for 5 min and washed twice in PBS to remove residual ethanol. For cell cycle analysis, the pellets were suspended in 1 mL of PBS containing 0.02 mg/mL of PI, 0.5 mg/mL of DNase-free RNase A and 0.1% of Triton X-100 and incubated at 37 °C for 30 min. Cell cycle profiles were studied using a FACScan flow cytometer (Becton Dickinson, San Jose, CA) and data were analyzed by ModFit LT software (Verity Software House Inc).

Apoptosis Assay. To quantify the drug-induced apoptosis, annexin V/PI staining was performed followed by flow cytometry. Briefly, after drug treatments (IC_{80} for each drug for 72 h), both floating and attached cells were collected and subjected to annexin V/PI staining using annexin V-FITC Apoptosis Detection Kit (BioVision, Palo Alto, CA) according to the protocol provided by the manufacturer. In cells undergoing apoptosis, annexin V binds to phosphatidylserine which is translocated from inner to outer leaflet of the cytoplasmatic membrane.[41] PI is used to distinguish between viable, early apoptotic, and necrotic or late apoptotic cells.[42,43] The resulting fluorescence was measured by flow cytometry using a FACScan flow cytometer (Becton Dickinson, San Jose, CA).

Receptor Binding Assay. Binding affinity of the dimeric RGD peptide—PTX to $\alpha_v\beta_3$ integrin on the surface of MDA-MB-435 cells was determined in competitive binding experiments using ^{125}I-labeled echistatin as radioligand as described in the literature with modifications.[44] In brief, MDA-MB-435

cells were harvested, washed twice with PBS, and resuspended (2×10^6 cells/mL) in binding buffer (20 mM Tris, pH 7.4, 150 mM NaCl, 2 mM $CaCl_2$, 1 mM $MgCl_2$, 1 mM $MnCl_2$, 0.1% BSA). 96-well multiscreen DV plate (filter pore size: 0.65 μm, Millipore, Billerica, MA) was incubated with ^{125}I-echistatin (50 000 cpm/well) in the presence of increasing concentrations of different RGD peptide analogues (0–1000 nM). The total incubation volume was adjusted to 200 μL. After the cells were incubated for 3 h at room temperature, the plate was filtered through multiscreen vacuum manifold and washed twice with cold binding buffer. The hydrophilic PVDF filters were collected, and the radioactivity was determined using NaI(Tl) gamma counter (Packard, Meriden, CT). The best-fit IC_{50} values for the MDA-MB-435 cells were calculated by fitting the data by nonlinear regression using GraphPad Prism (GraphPad Software, Inc., San Diego, CA). Experiments were carried out with triplicate samples.

Animal Model. All animal experiments were performed in compliance with the Guidelines for the Care and Use of Research Animals established by the University of Southern California's Animal Studies Committee. Female athymic nude mice (*nu/nu*) were obtained from Harlan (Indianapolis, IN) at 4–6 weeks of age and were kept under sterile conditions. The MDA-MB-435 cells were harvested and suspended in sterile PBS at a concentration of 5×10^7 viable cells/mL. Viable cells (5×10^6) in sterile PBS (100 μL) were injected orthotopically in the right mammary fat pad. Palpable tumors appeared by day 10–14 post-implantation. The tumors were allowed to grow 4–5 weeks until 0.5–1 g in weight. Tumor growth was followed by caliper measurements of perpendicular measures of the tumor. The weight in mg was estimated by the formula: tumor weight = $a(b^2)/2$, where a and b are the tumor length and width respectively in mm.[45]

Biodistribution. Orthotopic MDA-MB-435 tumor-bearing female athymic nude mice ($n = 4$ per time point) were injected with ^{125}I-E[c(RGDyK)]$_2$ or ^{125}I-E[c(RGDyK)]$_2$—PTX via the tail vein. The animals were euthanized at 0.5, 1, 2, and 4 h postinjection. The blocking experiment was performed by coinjecting radiotracer with a blocking dose of c(RGDyK) (10 mg/kg) and sacrificed at 1 h postinjection. Following euthanization, blood, tumor, and the major organs and tissues were collected, wet-weighed, and counted in a γ-counter (Packard). The percent injected dose per gram (% ID/g) were calculated by comparison with standards representing the injected dose per animal. Values are reported as mean $\pm$ standard deviation (SD).

Statistical Analysis. The data are expressed as means $\pm$ SD. One-way analysis of variance (ANOVA) was used for statistical evaluation. Means were compared using Student *t* test. A *P* value of <0.05 was considered significant.

References

(1) Dorr, R. T.; von Hoff, D. D. *Cancer chemotherapy handbook*, 2nd ed.; Appleton and Lange: Norwalk, 1994.

(2) Dombernowsky, P.; Gehl, J.; Boesgaard, M.; Jensen, T. P.; Jensen, B. W.; Ejlertsen, B. Treatment of metastatic breast cancer with PTX and doxorubicin. *Semin. Oncol.* **1995**, *22*(Suppl 15), 13–17.

(3) Esteva, F. J.; Valero, V.; Pusztai, L.; Boehnke-Michaud, L.; Buzdar, A. U.; Hortobagyi, G. N. Chemotherapy of metastatic breast cancer: what to expect in 2001 and beyond. *Oncologist* **2001**, *6*, 133–146.

(4) Langer, M.; Kratz, F.; Rothen-Rutishauser, B.; Wunderli-Allenspach, H.; Beck-Sickinger, A. G. Novel peptide conjugates for tumor-specific chemotherapy. *J. Med. Chem.* **2001**, *44*, 1341–1348.

(5) Safavy, A.; Bonner, J. A.; Waksal, H. W.; Buchsbaum, D. J.; Gillespie, G. Y.; Khazaeli, M. B.; Arani, R.; Chen, D. T.; Carpenter, M.; Raisch, K. P. Synthesis and biological evaluation of PTX—C225 conjugate as a model for targeted drug delivery. *Bioconjugate Chem.* **2003**, *14*, 302–310.

(6) Folkman, J. Tumor angiogenesis. *Adv. Cancer Res.* **1985**, *43*, 175–203.

(7) Jain, R. K. Molecular regulation of vessel maturation. *Nat. Med.* **2003**, *9*, 685–693.

(8) Molema, G. Tumor vasculature directed drug targeting: applying new technologies and knowledge to the development of clinically relevant therapies. *Pharm. Res.* **2002**, *19*, 1251–1258.

(9) Cristofanilli, M.; Charnsangavej, C.; Hortobagyi, G. N. Angiogenesis modulation in cancer research: novel clinical approaches. *Nat. Rev. Drug Discovery* **2002**, *1*, 415–26.

(10) MacDonald, T. J.; Taga, T.; Shimada, H.; Tabrizi, P.; Zlokovic, B. V.; Cheresh, D. A.; Laug, W. E. Preferential susceptibility of brain tumors to the anti-angiogenic effects of an α_v integrin antagonist. *Neurosurgery* **2001**, *48*, 151–157.

(11) Burke, P. A.; DeNardo, S. J.; Miers, L. A.; Lamborn, K. R.; Matzku, S.; DeNardo, G. L. Cilengitide targeting of $\alpha_v\beta_3$ integrin receptor synergizes with radioimmunotherapy to increase efficacy and apoptosis in breast cancer xenografts. *Cancer Res.* **2002**, *62*, 4263–4272.

(12) Sacco, M. G.; Soldati, S.; Mira Cato E.; Cattaneo, L.; Pratesi, G.; Scanziani, E.; Vezzoni, P. Combined effects on tumor growth and metastasis by anti-estrogenic and anti-angiogenic therapies in MMTV-neu mice. *Gene Ther.* **2002**, *9*, 1338–1341.

(13) Jain, R. K. Normalizing tumor vasculature with anti-angiogenic therapy: a new paradigm for combination therapy. *Nat. Med.* **2001**, *7*, 987–989.

(14) Hynes, R. O. A reevaluation of integrins as regulators of angiogenesis. *Nat. Med.* **2002**, *8*, 918–921.

(15) Brooks, P. C.; Montgomery, A. M.; Rosenfeld, M.; Reisfeld, R. A.; Hu, T.; Klier, G.; Cheresh, D. A.Integrin $\alpha_v\beta_3$ antagonists promote tumor regression by inducing apoptosis of angiogenic blood vessels. *Cell* **1994**, *79*, 1157–1164.

(16) Brooks, P. C.; Stromblad, S.; Klemke, R.; Visscher, D.; Sarkar, F. H.; Cheresh, D. A. Anti-integrin $\alpha_v\beta_3$ blocks human breast cancer growth and angiogenesis in human skin. *J. Clin. Investig.* **1995**, *96*, 1815–1822.

(17) Buerkle, M. A.; Pahernik, S. A.; Sutter, A.; Jonczyk, A.; Messmer, K.; Dellian, M. Inhibition of the α_v integrins with a cyclic RGD peptide impairs angiogenesis, growth and metastasis of solid tumors in vivo. *Br. J. Cancer* **2002**, *86*, 788–795.

(18) Qiao, R.; Yan, W.; Lum, H.; Malik, A. B. Arg-Gly-Asp peptide increases endothelial hydraulic conductivity: comparison with thrombin response. *Am J Physiol.* **1995**, *269*, C110–C117.

(19) Chen, X.; Park, R.; Shahinian, A. H.; Bading, J. R.; Conti, P. S. Pharmacokinetics and tumor retention of ^{125}I-labeled RGD peptide are improved by PEGylation. *Nucl. Med. Biol.* **2004**, *31*, 11–19.

(20) Chen, X.; Park, R.; Tohme, M.; Shahinian, A. H.; Bading, J. R.; Conti, P. S. ^{18}F and ^{64}Cu-labeled RGD peptide for imaging breast cancer in mice with microPET. *Bioconjugate Chem.* **2004**, *15*, 41–49.

(21) Chen, X.; Park, R.; Shahinian, A. H.; Tohme, M.; Khankaldyyan, V.; Bozorgzadeh, M. H.; Bading, J. R.; Moats, R.; Laug, W. E.; Conti, P. S. ^{18}F-labeled RGD peptide: initial evaluation for imaging brain tumor angiogenesis. *Nucl. Med. Biol.* **2004**, *31*, 179–189.

(22) Chen, X.; Park, R.; Hou, Y.; Khankaldyyan, V.; Gonzales-Gomez, I.; Tohme, M.; Bading, J. R.; Laug, W. E.; Conti, P. S. MicroPET imaging of brain tumor angiogenesis with ^{18}F-labeled PEGylated RGD peptide. *Eur. J. Nucl. Med. Mol. Imaging* **2004**, *31*, 1081–1089.

(23) Chen, X.; Hou, Y.; Tohme, M.; Park, R.; Khankaldyyan, V.; Gonzales-Gomez, I.; Bading, J. R.; Laug, W. E.; Conti, P. S. PEGylated RGD peptide: ^{64}Cu-labeling and PET imaging of brain tumor angiogenesis. *J. Nucl. Med.* **2004**, *45*, 1776–1783.

(24) Chen, X.; Tohme, M.; Park, R.; Hou, Y.; Bading, J. R.; Conti, P. S. MicroPET imaging of $\alpha_v\beta_3$ integrin expression with ^{18}F-labeled dimeric RGD peptide. *Mol. Imaging* **2004**, *3*, 96–104.

(25) Chen, X.; Liu, S.; Hou, Y.; Tohme, M.; Park, R.; Bading, J. R.; Conti, P. S. MicroPET imaging of breast cancer α_v-integrin expression with ^{64}Cu-labeled dimeric RGD Peptides. *Mol. Imaging Biol.* **2004**, *6*, 350–9.

(26) Chen, X.; Conti, P. S.; Moats, R. A. In vivo near-infrared fluorescence imaging of integrin $\alpha_v\beta_3$ in brain tumor xenografts. *Cancer Res.* **2004**, *64*, 8009–8014.

(27) Haubner, R.; Wester, H. J.; Weber, W. A.; Mang, C.; Ziegler, S. I.; Goodman, S. L.; Senekowitsch-Schmidtke, R.; Kessler, H.; Schwaiger, M. Noninvasive imaging of $\alpha_v\beta_3$ integrin expression using ^{18}F-labeled RGD-containing glycopeptide and positron emission tomography. *Cancer Res.* **2001**, *61*, 1781–1785.

(28) Haubner, R.; Kuhnast, B.; Mang, C.; Weber, W. A.; Kessler, H.; Wester, H. J.; Schwaiger, M. [^{18}F]Galacto-RGD: synthesis, radiolabeling, metabolic stability, and radiation dose estimates. *Bioconjugate Chem.* **2004**, *15*, 61–69.

(29) Janssen, M. L.; Oyen, W. J.; Dijkgraaf, I.; Massuger, L. F.; Frielink, C.; Edwards, D. S.; Rajopadhye, M.; Boonstra, H.; Corstens. F. H.; Boerman, O. C. Tumor targeting with radiolabeled $_v\beta_3$ integrin binding peptides in a nude mouse model. *Cancer Res.* **2002**, *62*, 6146–6151.

(30) Xiong, J. P.; Stehle, T.; Zhang, R.; Joachimiak, A.; Frech, M.; Goodman, S. L.; Arnaout, M. A. Crystal structure of the extracellular segment of integrin $\alpha_v\beta_3$ in complex with an Arg-Gly-Asp ligand. *Science* **2002**, *296*, 151–155.

(31) Xiong, J. P.; Stehle, T.; Diefenbach, B.; Zhang, R.; Dunker, R.; Scott, D. L.; Joachimiak, A.; Goodman, S. L.; Arnaout, M. A. Crystal structure of the extracellular segment of integrin $\alpha_v\beta_3$. *Science.* **2001**, *294*, 339–345.

(32) Gottschalk, K. E.; Kessler, H. The structures of integrins and integrin-ligand complexes: implications for drug design and signal transduction. *Angew. Chem., Int. Ed.* **2002**, *41*, 3767–3774.

(33) Thumshirn, G.; Hersel, U.; Goodman, S. L.; Kessler, H. Multimeric cyclic RGD peptides as potential tools for tumor targeting: solid-phase peptide synthesis and chemoselective oxime ligation. *Chemistry* **2003**, *9*, 2717–2725.

(34) Mammen, M.; Chio, S. K.; Whitesides, G. M. Polyvalent interactions in biological systems: implications for design and use of multivalent ligands and inhibitors. *Angew. Chem., Int.* **1998**, *37*, 2755–2794.

(35) Wong, N. C.; Mueller, B. M.; Barbas, C. F.; Ruminski, P.; Quaranta, V.; Lin, E. C.; Smith, J. W. Alphav integrins mediate adhesion and migration of breast carcinoma cell lines. *Clin. Exp. Metastasis* **1998**, *16*, 50–61.

(36) Harms, J. F.; Welch, D. R.; Samant, R. S.; Shevde, L. A.; Miele, M. E.; Babu, G. R.; Goldberg, S. F.; Gilman, V. R.; Sosnowski, D. M.; Campo, D. A.; Gay, C. V.; Budgeon, L. R.; Mercer, R.; Jewell, J.; Mastro, A. M.; Donahue, H. J.; Erin, N.; Debies, M. T.; Meehan, W. J.; Jones, A. L.; Mbalaviele, G.; Nickols, A.; Christensen, N. D.; Melly, R.; Beck, L. N.; Kent, J.; Rader, R. K.; Kotyk, J. J.; Pagel, M. D.; Westlin, W. F.; Griggs, D. W. A small molecule antagonist of the $\alpha_v\beta_3$ integrin suppresses MDA-MB-435 skeletal metastasis. *Clin. Exp. Metastasis* **2004**, *21*, 119–128.

(37) Liu, S.; Cheung, E.; Ziegler, M. C.; Rajopadhye, M.; Edwards, D. S. ^{90}Y and ^{177}Lu labeling of a DOTA-conjugated vitronectin receptor antagonist useful for tumor therapy. *Bioconjugate Chem.* **2001**, *12*, 559–568.

(38) Deutsch, H. M.; Glinski, J. A.; Hernandez, M.; Haugwitz, R. D.; Narayanan, V. L.; Suffness, M.; Zalkow, L. H. Synthesis of congeners and prodrugs. 3. Water-soluble prodrugs of PTX with potent antitumor activity. *J. Med. Chem.* **1989**, *32*, 788–792.

(39) Alley, M. C.; Scudieron, D. A.; Monks, A.; Hursey, M. L.; Czerwinski, M. J.; Fink, D. L.; Abbot, B. J.; Mayo, J. G.; Shoemaker, R. H. Feasibility of drug screening with panels of human tumour cell lines using microculture tetrazolium assay. *Cancer Res.* **1988**, *48*, 589–601.

(40) Chou, T. C.; Talalay, P. Quantitative analysis of dose–effect relationships: the combined effects of multiple drugs or enzyme inhibitors. *Adv. Enzyme Regul.* **1984**, *22*, 27–55.

(41) White, E. Life, death and the pursuit of apoptosis. *Genes Dev.* **1996**, *10*, 1–15.

(42) Fadok, V. A.; Volker, D. R.; Campbell, P. A.; Cohen, J. J.; Bratton, D. L.; Henson, P. M. Exposure of the phosphatidylserine on the surface of the apoptotic lymphocytes triggers specific recognition and removal by macrophages. *J. Immunol.* **1992**, *148*, 2207–2216.

(43) Frey, T. Correlated flow cytometric analysis of terminal events in apoptosis reveals the absence of some changes in some model systems. *Cytometry* **1997**, *13*, 795–808.

(44) Kumar, C. C.; Nie, H.; Rogers, C. P.; Malkowski, M.; Maxwell, E.; Catino, J. J.; Armstrong, L. Biochemical characterization of the binding of echistatin to integrin $\alpha_v\beta_3$ receptor. *J. Pharmacol. Exp. Ther.* **1997**, *283*, 843–853.

(45) Gieseg, M. A.; Man, M. Z.; Gorski, N. A.; Madore, S. J.; Kaldjian, E. P.; Leopold, W. R. The influence of tumor size and environment on gene expression in commonly used human tumor lines. *BioMed Central Cancer* **2004**, *4*, 35.

Pegylated Arg-Gly-Asp Peptide: ^{64}Cu Labeling and PET Imaging of Brain Tumor $\alpha_v\beta_3$-Integrin Expression

Xiaoyuan Chen, PhD[1]; Yingping Hou, MD[1]; Michel Tohme, MS[1]; Ryan Park, BS[1]; Vazgen Khankaldyyan, BS[2]; Ignacio Gonzales-Gomez, MD[2]; James R. Bading, PhD[1]; Walter E. Laug, MD[2]; and Peter S. Conti, MD, PhD[1]

[1]PET Imaging Science Center, Keck School of Medicine, University of Southern California, Los Angeles, California; and [2]Department of Pediatrics, Children's Hospital Los Angeles, Los Angeles, California

The α_v-integrins, cell adhesion molecules that are highly expressed on activated endothelial cells and tumor cells but not on dormant endothelial cells or normal cells, present an attractive target for tumor imaging and therapy. We previously coupled a cyclic Arg-Gly-Asp (RGD) peptide, c(RGDyK), with 1,4,7,10-tetraazacyclododecane-N,N',N'',N'''-tetraacetic acid (DOTA) and labeled the RGD-DOTA conjugate with ^{64}Cu (half-life, 12.8 h; 19% β⁺) for solid tumor targeting, with high tumor-to-background contrast. The rapid tumor washout rate and persistent liver and kidney retention of this tracer prompted us to optimize the tracer for improved pharmacokinetic behavior. In this study, we introduced a polyethylene glycol (PEG; molecular weight, 3,400) moiety between DOTA and RGD and evaluated the ^{64}Cu-DOTA-PEG-RGD tracer for microPET imaging in brain tumor models. **Methods:** DOTA was activated in situ and conjugated with RGD-PEG-NH$_2$ under slightly basic conditions. $\alpha_v\beta_3$-Integrin-binding affinity was evaluated with a solid-phase receptor-binding assay in the presence of ^{125}I-echistatin. Female nude mice bearing subcutaneous U87MG glioblastoma xenografts were administered ^{64}Cu-DOTA-PEG-RGD, and the biodistributions of the radiotracer were evaluated from 30 min to 4 h after injection. microPET (20 min of static imaging at 1 h after injection) and then quantitative autoradiography were used for tumor visualization and quantification. The same tracer was also applied to an orthotopic U87MG model for tumor detection. **Results:** The radiotracer was synthesized with a high specific activity (14,800–29,600 GBq/mmol [400–800 Ci/mmol]). The c(RGDyK)-PEG-DOTA ligand showed intermediate binding affinity for $\alpha_v\beta_3$-integrin (50% inhibitory concentration, 67.5 ± 7.8 nmol/L [mean ± SD]). The pegylated RGD peptide demonstrated rapid blood clearance (0.57 ± 0.15 percentage injected dose [%ID]/g [mean ± SD] at 30 min after injection and 0.03 ± 0.02 %ID/g at 4 h after injection). Activity accumulation in the tumor was rapid and high at early time points (2.74 ± 0.45 %ID/g at 30 min after injection), and some activity washout was seen over time (1.62 ± 0.18 %ID/g at 4 h after injection). Compared with ^{64}Cu-DOTA-RGD, this tracer showed improved in vivo kinetics, with significantly reduced liver uptake (0.99 ± 0.08 %ID/g vs. 1.73 ± 0.39 %ID/g at 30 min after injection and

0.58 ± 0.07 %ID/g vs. 2.57 ± 0.49 %ID/g at 4 h after injection). The pegylated RGD peptide showed higher renal accumulation at early time points (3.51 ± 0.24 %ID/g vs. 2.18 ± 0.23 %ID/g at 30 min after infection) but more rapid clearance (1.82 ± 0.29 %ID/g vs. 2.01 ± 0.25 %ID/g at 1 h after injection) than ^{64}Cu-DOTA-RGD. The integrin receptor specificity of this radiotracer was demonstrated by blocking of tumor uptake by coinjection with nonradiolabeled c(RGDyK). The high tumor-to-organ ratios for the pegylated RGD peptide tracer (at 1 h after injection: tumor-to-blood ratio, 20; tumor-to-muscle ratio, 12; tumor-to-liver ratio, 2.7; and tumor-to-kidney ratio, 1.2) were confirmed by microPET and autoradiographic imaging in a subcutaneous U87MG tumor model. This tracer was also able to detect an orthotopic brain tumor in a model in which U87MG cells were implanted into the mouse forebrain. Although the magnitude of tumor uptake in the orthotopic xenograft was lower than that in the subcutaneous xenograft, the orthotopic tumor was still visualized with clear contrast from normal brain tissue. **Conclusion:** This study demonstrated the suitability of a PEG moiety for improving the in vivo kinetics of a ^{64}Cu-RGD peptide tracer without compromising the tumor-targeting ability and specificity of the peptide. Systematic investigations of the effects of the size and geometry of PEG on tumor targeting and in vivo kinetics will lead to the development of radiotracers suitable for clinical applications such as visualizing and quantifying α_v-integrin expression by PET. In addition, the same ligand labeled with therapeutic radionuclides may be applicable for integrin-targeted internal radiotherapy.

Key Words: molecular imaging; PET; radiopharmaceuticals; angiogenesis; integrin; Arg-Gly-Asp; ^{64}Cu; pegylation

J Nucl Med 2004; 45:1776–1783

Angiogenesis, the formation and differentiation of blood vessels, plays a key role in tumor growth and metastasis spread and has become the new frontier for tumor control (*1,2*). Angiogenesis is a complex process involving extensive interplay among cells, soluble factors, and extracellular matrix components (*3–11*). Integrins are cell adhesion molecules known to be involved in multiple steps of angiogenesis and metastasis. The function of integrins during tumor angiogenesis has been studied most extensively for $\alpha_v\beta_3$-

integrin and $\alpha_v\beta_5$-integrin, which are highly expressed on activated endothelial cells and tumor cells but not on quiescent vessels and normal cells (12). The expression of $\alpha_v\beta_3$-integrin is required for angiogenesis induced by fibroblast growth factor 2 and tumor necrosis factor α, and the expression of $\alpha_v\beta_5$-integrin is required for angiogenesis induced by vascular endothelial growth factor and transforming growth factor α (13). Monoclonal antibodies, peptides, and peptidomimetic antagonists of α_v-integrins have been shown to block angiogenesis in both preclinical tumor models and phase I and II clinical trials by inhibiting endothelium-specific integrin survival signaling (14,15). The ability to noninvasively visualize and quantify the α_v-integrin expression level during tumor growth and spread as well as during anti-integrin treatment will provide new opportunities to develop individualized therapeutic approaches, to select appropriate patients entering clinical trials for anti-integrin treatment, to establish optimized dosages and dose intervals for effective treatment on the basis of receptor occupancy studies, to detect early antiangiogenic responses and quantitatively evaluate treatment efficacy, and finally to cooptimize imaging and therapy via structure–activity studies.

Arg-Gly-Asp (RGD) peptide antagonists of α_v-integrins have been labeled with different radionuclides for both imaging and therapeutic purposes. Notably, various investigators (16–20) labeled cyclic RGD peptides with ^{18}F (half-life [$t_{1/2}$], 119.7 min; 99% β^+) for microPET imaging in various solid tumor models, and high tumor-to-background contrast was obtained. However, these radiotracers have some drawbacks: the labeling procedure is tedious and relatively inefficient, tumor uptake is modest, and tumor retention time is short. Although the tracers were able to localize α_v-integrin-positive tumors, their utility in reflecting targeted radiotherapy is limited because no therapeutic fluorine isotope is available. Because of the existence of an imaging and therapy radionuclide pair (^{64}Cu/^{67}Cu) for diagnosing and treating cancer, ^{64}Cu-labeled RGD peptides with successful tumor-targeting properties will eventually be able to determine dosimetry and tumor responses to the same ligand labeled with therapeutic amounts of ^{67}Cu for α_v-integrin-mediated internal radiotherapy.

Chen et al. (21) recently described the synthesis of a ^{64}Cu-labeled RGD peptide and microPET imaging of orthotopic MDA-MB-435 breast cancer tumor xenografts, with high tumor-to-contralateral background contrast. However, this tracer also had a rapid tumor washout rate and showed persistent activity accumulation in the liver and kidneys. The unfavorable in vivo pharmacokinetics of this tracer limit the application of a 1,4,7,10-tetraazacyclododecane-N,N',N'',N'''-tetraacetic acid (DOTA)-RGD conjugate for tumor imaging and radiotherapy. Haubner et al. (22) chose to modify the RGD peptide with a glycosylate moiety to increase hydrophilicity and thus reduce blood clearance and reduce hepatobiliary excretion. We have found that poly-

ethylene glycol (PEG) is a suitable tool for modifying the RGD peptide, with improved in vivo kinetics.

Chen et al. (23) recently modified a cyclic RGD peptide, c(RGDyK), by introducing a monomethoxy PEG moiety (mPEG; molecular weight [MW], 2,000) into the lysine ε-amino group. The resulting RGD-mPEG conjugate showed drastically decreased renal uptake and slightly increased liver accumulation compared with the parental RGD peptide. In this study, we inserted a heterobifunctional PEG linker (MW, 3,400) between DOTA and c(RGDyK). The resulting DOTA-PEG-RGD conjugate then was radiolabeled with ^{64}Cu ($t_{1/2}$, 12.8 h; 19% β^+) for microPET imaging studies with both subcutaneous and orthotopic U87MG glioblastoma models.

MATERIALS AND METHODS

Materials

c(RGDyK) was synthetically produced by solution cyclization of fully protected linear pentapeptide H-Gly-Asp(tert-butyloxy)-D-Tyr(tert-butyloxy)-Lys(butoxycarbonyl)-Arg(2,2,4,6,7-pentamethyldihydrobenzofuran-5-sulfonyl)-OH, followed by trifluoroacetic acid (TFA) deprotection in the presence of the free radical scavenger triisopropylsilane (23). RGD-PEG conjugate was prepared by coupling of c(RGDyK) with t-butoxycarbonyl (t-Boc)-protected PEG-succinimidyl ester (MW, 3,400), followed by TFA cleavage (24). ^{64}Cu was produced on a CS-15 biomedical cyclotron at the School of Medicine, Washington University, by the ^{64}Ni(p,n)^{64}Cu nuclear reaction (25). All reagents, unless otherwise specified, were of analytic grade and were commercially available. DOTA was purchased from Macrocyclics, Inc. N-Hydroxysulfosuccinimide (SNHS), 1-ethyl-3-[3-(dimethylamino)-propyl]carbodiimide (EDC), and Chelex 100 (50–100 mesh) were obtained from Aldrich.

Chromalux HB microplates were obtained from Dynex Technologies. ^{125}I-Echistatin, labeled by the lactoperoxidase method to a specific activity of 74,000 GBq/mmol (2,000 Ci/mmol), was obtained from Amersham Biosciences. Echistatin was purchased from Sigma. Purified human $\alpha_v\beta_3$-integrin in a Triton X-100 formulation was obtained from Chemicon International.

Semipreparative reversed-phase high-pressure liquid chromatography (HPLC) was accomplished by use of a Waters 515 chromatography system with a 486 tunable absorbance detector. Purification was performed with a Vydac 218TP510 protein and peptide column (5 μm; 250 × 10 mm). The flow rate was 5 mL/min; the mobile phase was changed from 95% solvent A (0.1% TFA in water) and 5% solvent B (0.1% TFA in acetonitrile) (0–2 min) to 35% solvent A and 65% solvent B at 32 min. The analytic HPLC method was performed with the same gradient system but with a Vydac 218TP54 column (5 μm; 250 × 4.6 mm) and a flow rate of 1 mL/min. The absorbance was monitored at 218 nm. Radio–thin-layer chromatography (TLC) was performed by use of MKC18F plates (Whatman), Bioscan System 200, and Winscan software (version 2.2; BioScan Inc.). Reversed-phase extraction C_{18} SepPak cartridges were obtained from Waters.

Preparation of DOTA-PEG-RGD Conjugate

DOTA was activated in situ by EDC at a molar ratio for DOTA:EDC:SNHS of 10:5:4 (21). RGD-PEG conjugate (8 mg; 2 μmol) dissolved in 1,600 μL of water (5 mg/mL) was cooled to

4°C and added to a DOTA-sulfosuccinimydyl ester (OSSu) reaction mixture (10 µmol; calculated on the basis of SNHS), and the pH was adjusted to 8.5 with 1N NaOH. The reaction mixture was incubated overnight at 4°C. DOTA-PEG-RGD conjugate was purified by semipreparative HPLC. The sample containing the RGD conjugate was collected, lyophilized, and dissolved in H$_2$O at a concentration of 1 mg/mL for use in radiolabeling reactions.

^{64}Cu Radiolabeling

DOTA-PEG-RGD was labeled with ^{64}Cu by the addition of 37–185 MBq (1–5 mCi) of ^{64}Cu (5–25 µg of DOTA-PEG-RGD per 37 MBq of ^{64}Cu) in 0.1N sodium acetate (pH 5.5) buffer and 45 min of incubation at 50°C. The reaction was terminated by the addition of 5 µL of ethylenediaminetetraacetic acid solution (10 mmol/L). The radiochemical yield was determined by radio-TLC with MKC18F TLC plates as the stationary phase and methanol:10% sodium acetate (70:30) as the eluent. ^{64}Cu-DOTA-PEG-RGD was purified by use of a C$_{18}$ SepPak cartridge with 85% ethanol as the elution solvent. Radiochemical purity was determined by radio-TLC or radio-HPLC. The ethanol was evaporated, the activity was reconstituted with phosphate-buffered saline, and the sample was passed through a 0.22-µm Millipore filter into a sterile multidose vial for use in animal experiments.

Octanol–Water Partition Coefficient

About 370 kBq of ^{64}Cu-DOTA-c(RGDyK) or ^{64}Cu-DOTA-PEG-c(RGDyK) in 500 µL of saline were added to 500 µL of octanol in an Eppendorf microcentrifuge tube (Brinkman). The 2 layers were mixed for 10 min at room temperature, the tube was centrifuged at 14,000 rpm for 5 min (model 5415C Eppendorf microcentrifuge; Brinkman), and the counts in 100-µL aliquots of both organic and inorganic layers were determined by use of a γ-counter (Packard). The experiment was repeated 3 times.

Solid-Phase Receptor-Binding Assay

The standard assay was performed as described previously with modifications (26). Microtiter-2 96-well plates (Dynatech Laboratories, Inc.) were coated with α$_v$β$_3$-integrin (500 ng/mL; 100 µL per well) in coating buffer (Tris-HCl [pH 7.4] at 25 mmol/L, NaCl at 150 mmol/L, CaCl$_2$ at 1 mmol/L, MgCl$_2$ at 0.5 mmol/L, and MnCl$_2$ at 1 mmol/L) for 16 h at 4°C. The wells then were blocked for 2 h with 200 µL of blocking buffer (coating buffer with 1% radioimmunoassay-grade bovine serum albumin). The plates then were washed twice with binding buffer (coating buffer with 0.1% bovine serum albumin) and incubated with ^{125}I-echistatin (0.06 nmol/L) in the presence of various concentrations of RGD peptide (0.1 nmol/L–5 µmol/L) at room temperature for 3 h. After incubation, the plates were washed 3 times with binding buffer, and the radioactivity was solubilized with 2N boiling NaOH and subjected to γ-counting. Nonspecific binding of ^{125}I-echistatin to α$_v$β$_3$-integrin was determined in the presence of echistatin at 100 nmol/L. The 50% inhibitory concentrations were calculated by nonlinear regression analysis by use of the GraphPad Prism computer fitting program (GraphPad Software, Inc.). Each data point represents the average value for triplicate wells.

Biodistribution Studies

Animal experiments were conducted under a protocol approved by the University of Southern California Institutional Animal Care and Use Committee. Female athymic nude mice (nu/nu) obtained from Harlan at 4–6 wk of age were injected subcutaneously in the right front leg with 5 × 10^6 U87MG glioblastoma cells suspended in 150 µL of Eagle's minimum essential medium. When the tumors reached 0.4–0.6 cm in diameter (14–18 d after implantation), the mice were used for biodistribution and microPET imaging experiments.

Details of the orthotopic (intracranial) xenotransplant model in nu/nu mice were described previously (27). In brief, 10^5 U87MG tumor cells in 1 µL of RPMI medium were injected through a 33-gauge injection needle over 10 min into the nude mouse (4–6 wk old) forebrain 1.5 mm lateral and 0.5 mm anterior to the bregma and at a depth of 2.5 mm by use of a continuous infusion pump. The needle was removed, the burr hole was closed with bone wax, and the skin incision was closed with dermal glue. Mice were kept under ketamine–xylazine anesthesia during the procedure. This tumor cell number resulted in the growth of tumors in all experimental animals and a highly reproducible growth rate. At 5 wk after injection, when the tumors reached 3 mm or more in diameter, the mice were used for microPET imaging studies.

Nude mice bearing subcutaneously xenografted human U87MG glioblastoma tumors were injected intravenously with approximately 370 kBq (10 µCi) of ^{64}Cu-DOTA-PEG-RGD. Animals were euthanized at 30 min, 1 h, 2 h, and 4 h after injection. Blood, tumors, and major organs and tissues were collected and wet weighed, and counts were determined by use of a γ-counter. The percentage injected dose per gram (%ID/g) was determined for each sample. For each mouse, the radioactivity in the tissue samples was calibrated against a known quantity of the injected compound. Values are reported as mean ± SD for groups of 4 animals. The receptor-mediated localization of the radiotracer was investigated by injection of ^{64}Cu-DOTA-PEG-RGD with c(RGDyK) at 10 mg/kg in a subcutaneous U87MG tumor model. Biodistributions were determined as described above at 1 h after injection for 4 mice per group.

microPET Imaging

PET was performed by use of a microPET R4 rodent model scanner (Concorde Microsystems Inc.). The scanner has a computer-controlled bed and 10.8-cm transaxial and 8-cm axial fields of view. It has no septa and operates exclusively in the 3-dimensional list mode. All raw data were first sorted into 3-dimensional sinograms; this step was followed by Fourier rebinning and 2-dimensional (2D) filtered backprojection image reconstruction by use of a ramp filter with the Nyquist limit (0.5 cycle per voxel) as the cutoff frequency. For the subcutaneous tumor model, each mouse was injected with 14.8 MBq (400 µCi) of ^{64}Cu-DOTA-PEG-RGD via the tail vein, sacrificed at 1 h after injection by cervical dislocation under ketamine–xylazine anesthesia, and placed near the center of the field of view of the microPET scanner, where the highest image resolution and sensitivity are available. The mouse was scanned for 20 min and then subjected to whole-body autoradiography. The raw data were framed into one static frame without attenuation correction. For the orthotopic U87MG tumor model, a 20-min static image was obtained at 1 h after injection. The brain tumor was excised postmortem, fixed in buffered formalin, and embedded in paraffin for hexatoxylin–eosin staining.

Autoradiography

Autoradiography was performed by use of a Packard Cyclone Storage Phosphor Screen system and a Bright 5030/WD/MR cryomicrotome (Hacker Instruments). Immediately after microPET scanning, the sacrificed mice with subcutaneous U87MG tumors were frozen in a dry ice–isopropyl alcohol bath for 2 min. The

bodies then were embedded in 4% carboxymethylcellulose (Aldrich) in water by use of a stainless steel mold. The mold was placed in the dry ice–isopropyl alcohol bath for 5 min and then into a −20°C freezer for 1 h. The walls of the mold were removed, and the frozen block was mounted in the cryomicrotome. The block was cut into sections of 50 μm, and the desired sections were digitally photographed and captured for autoradiography. The sections were transferred into a chilled film cassette containing a Packard Super Resolution Screen (spatial resolution, 0.1 mm) and kept there overnight at −20°C. Screens were laser scanned by use of the Packard Cyclone system.
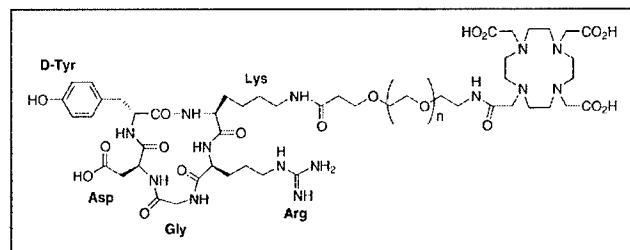
Statistical Analysis

The data were expressed as mean ± SD. A 1-way ANOVA was used for statistical evaluation. Means were compared by use of the Student t test. A P value of <0.05 was considered significant.
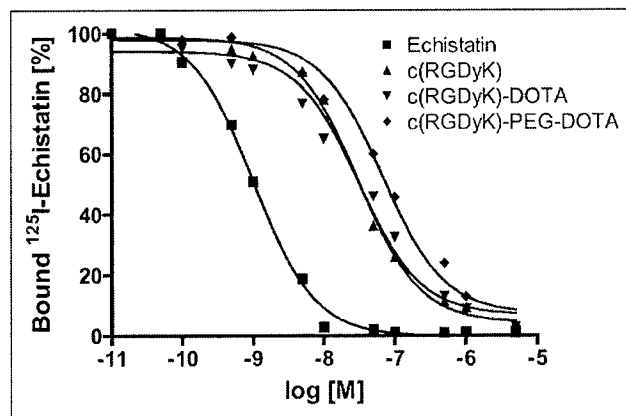
RESULTS

DOTA Conjugation and ^{64}Cu Labeling

The synthesis of PEG-RGD may be performed by coupling of t-Boc-NH-PEG-CO$_2$Su (MW, 3,400) with c(RGDyK), followed by TFA cleavage to unblock the t-Boc protecting group (24). A DOTA-PEG-RGD conjugate (Fig. 1) was produced in the presence of an excess amount of DOTA-OSSu activated in situ. The MW of the DOTA conjugate, evaluated by matrix-assisted laser desorption ionization—time-of-flight mass spectroscopy, increased from 4,000 to 4,400. The mass spectrometry peak was broad (spectrum not shown) because of the polydispersity of PEG (28). The increase in MW, of approximately 400, corresponds to the conjugation of the macrocylic chelator DOTA and is accompanied by the disappearance of amino group reactivity, demonstrated by the 6-trinitrobenzene sulfonic acid reaction (28). Contemporaneously, a slight change in the retention time (from 21.9 min for PEG-RGD to 21.5 min for DOTA-PEG-RGD) and a sharpening of the peak in reversed-phase HPLC elution were found. ^{64}Cu-DOTA-PEG-RGD was prepared at radiochemical purities of about 50%, 80%, 95%, and ≥98% when 5, 10, 15, and 20 μg of peptide per 37 MBq of ^{64}Cu were used. The specific activity of ^{64}Cu-DOTA-PEG-RGD ranged from 14,800 to 29,600 GBq/mmol (400–800 Ci/mmol).

FIGURE 1. Schematic structure of DOTA-PEG-RGD. Heterofunctional PEG (MW, 3,400) is linked to the DOTA carboxylate group through the N terminus and to the lysine side chain ε-amino group of c(RGDyK) through the C terminus.

FIGURE 2. Competition between ^{125}I-echistatin and unlabeled echistatin, c(RGDyK), c(RGDyK)-DOTA, and DOTA-PEG-c(RGDyK) for specific binding to purified $\alpha_v\beta_3$-integrin, as determined by a solid-phase receptor assay. All measurements were made in triplicate. M = molar concentration.
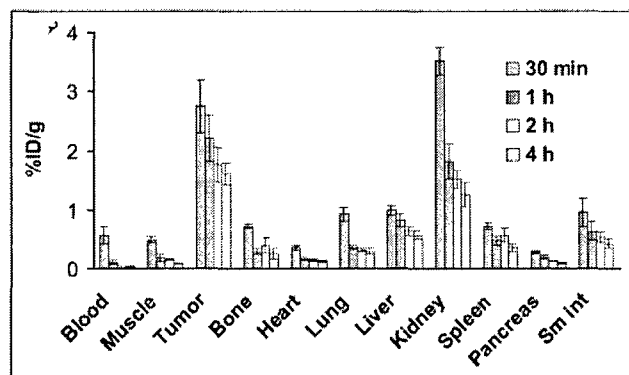
Competitive Displacement and Hydrophilicity Studies

To compare the affinities of c(RGDyK)-DOTA and c(RGDyK)-PEG-DOTA for $\alpha_v\beta_3$-integrin, a competitive displacement study was performed (Fig. 2). The binding of ^{125}I-echistatin to $\alpha_v\beta_3$-integrin was competed for by cold echistatin, c(RGDyK), c(RGDyK)-DOTA, and c(RGDyK)-PEG-DOTA in a concentration-dependent manner. All of the peptides were able to fully suppress the binding of the radioligand to purified human $\alpha_v\beta_3$-integrin. The concentrations required for half-maximal competition (50% inhibitory concentrations) were calculated to be 1.01 ± 0.23 nmol/L for echistatin, 30.3 ± 5.8 nmol/L for c(RGDyK), 31.2 ± 7.4 nmol/L for c(RGDyK)-DOTA, and 67.5 ± 10.5 nmol/L for c(RGDyK)-PEG-DOTA. Both the lead compound c(RGDyK)-DOTA and the pegylated analog c(RGDyK)-PEG-DOTA showed high hydrophilicity, as indicated from octanol–water partition coefficient measurements. LogP values for c(RGDyK)-DOTA and c(RGDyK)-PEG-DOTA were −2.8 ± 0.04 and −2.97 ± 0.30, respectively.

Biodistributions of ^{64}Cu-DOTA-PEG-RGD
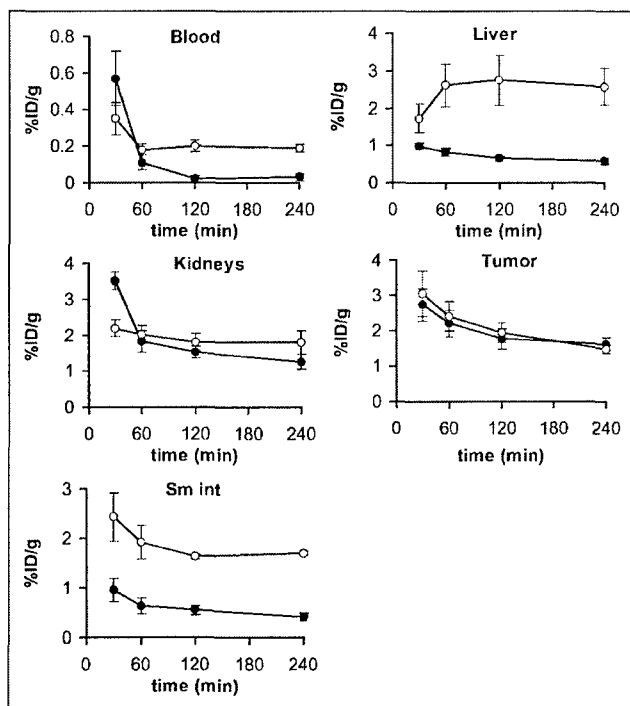
The distributions of radioactivity in selected mouse organs and U87MG glioblastoma xenografts at various times after the administration of ^{64}Cu-DOTA-PEG-RGD are shown in Figure 3. The radiotracer exhibited a rapid decrease in radioactivity over time in blood and most organs. At early time points, the high kidney activity was evidently attributable to the elimination of radiolabeled peptide in the urine. Analogously, radioactivity accumulated in the liver could have been caused by the radioactivity remaining in the blood as well as by partial bile excretion of the agent. The highest tumor uptake of ^{64}Cu-DOTA-PEG-RGD (2.74 ± 0.45 %ID/g) was found at 30 min after injection and decreased to 1.62 ± 0.18 %ID/g at 4 h after injection, suggesting that the ^{64}Cu was present in the tumor up to at least 4 h after injection.

A comparison of the kinetics of excretion of ^{64}Cu-DOTA-PEG-RGD and ^{64}Cu-DOTA-RGD in the blood, liver, kid-

FIGURE 3. Biodistributions of ^{64}Cu-DOTA-PEG-RGD in nude mice bearing subcutaneously xenotransplanted U87MG tumors. The data are reported as mean ± SD (n = 4). Sm int = small intestine.

neys, small intestine, and U87MG tumors is shown in Figure 4. The blood activity of ^{64}Cu-DOTA-PEG-RGD (0.57 ± 0.15 %ID/g) was significantly higher than that of ^{64}Cu-DOTA-RGD (0.35 ± 0.09 %ID/g) at 30 min after injection. The pegylated RGD peptide showed more rapid blood clearance than ^{64}Cu-DOTA-RGD, as the blood activity was as low as 0.02 ± 0.02 %ID/g at 2 h after injection for ^{64}Cu-DOTA-PEG-RGD; the blood activity for ^{64}Cu-DOTA-RGD was 0.20 ± 0.03 %ID/g at 2 h after injection and remained unchanged at 4 h after injection. The kidney uptake of ^{64}Cu-DOTA-PEG-RGD was higher than that of ^{64}Cu-DOTA-RGD at early time points, although the pegy-

FIGURE 4. Comparison of biodistributions of ^{64}Cu-DOTA-PEG-RGD (●) and ^{64}Cu-DOTA-RGD (○) in nude mice. Error bars denote SDs (n = 4). Sm int = small intestine.
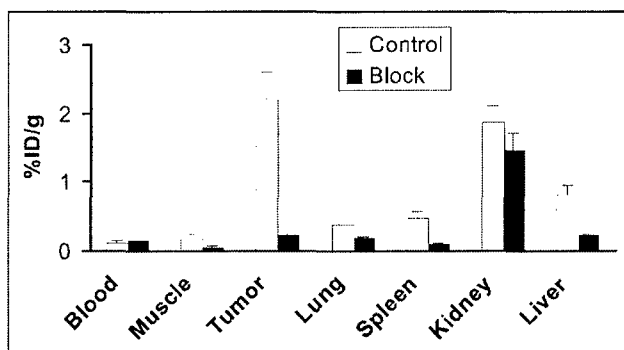
lated RGD peptide showed more rapid renal clearance, resulting in significantly lower kidney activity accumulation at 4 h. The liver uptake of the pegylated RGD peptide was significantly lower than that of ^{64}Cu-DOTA-RGD at all time points. Although the liver uptake of ^{64}Cu-DOTA-RGD increased over time (2.57 ± 0.49 %ID/g at 4 h after injection), ^{64}Cu-DOTA-PEG-RGD liver uptake decreased over time (0.58 ± 0.07 %ID/g at 4 h after injection). Intestinal activity accumulation of the pegylated RGD peptide was significantly higher than that of the lead compound at all time points (P < 0.001). Pegylation had a minimal effect on tumor uptake and clearance.

Coinjection of c(RGDyK) (10 mg/kg) with ^{64}Cu-DOTA-PEG-RGD resulted in a significant decrease in radioactivity in all dissected tissues, except the kidneys (Fig. 5). Uptake in tumors was reduced most dramatically, from 2.21 ± 0.38 %ID/g to 0.22 ± 0.03 %ID/g. The blocking experiment showed that the uptake and retention of ^{64}Cu-DOTA-PEG-RGD were receptor dependent in tumors as well as several normal organs, such as the liver, spleen, and lungs.

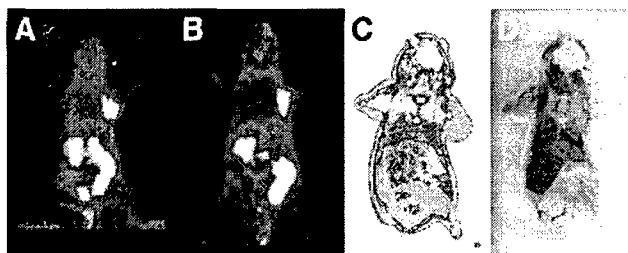## microPET Imaging and Whole-Body Autoradiography

A 2D projection of the microPET image (20-min static single frame) of a female athymic nude mouse bearing an U87MG tumor on the right shoulder at 60 min after intravenous injection of 14.8 MBq (400 μCi) of ^{64}Cu-DOTA-PEG-RGD is shown in Figure 6A. The tumor was clearly visible, with high contrast relative to the contralateral background. Prominent uptake was also observed in the kidneys, intestinal tract, and urinary bladder; these data agreed well with the data obtained from direct tissue sampling. No activity accumulation was observed in the normal brain, probably because of the presence of an intact blood–brain barrier and a low level of α_v-integrin expression.

Quantitation of tumor and major organ activity accumulation in microPET scanning was realized by measuring regions of interest that encompassed the entire organ in the

FIGURE 5. Biodistributions of ^{64}Cu-DOTA-PEG-RGD in the absence and in the presence of c(RGDyK) at 10 mg/kg at 1 h after injection in athymic nude mice with subcutaneous U87MG glioblastoma tumors. Reduced uptake in tumor, liver, muscle, and spleen in the blocking experiment indicated α_v-integrin-mediated localization of ^{64}Cu-DOTA-PEG-RGD in these tissues. Error bars denote SDs (n = 4). Data are mean ± SD (n = 4).
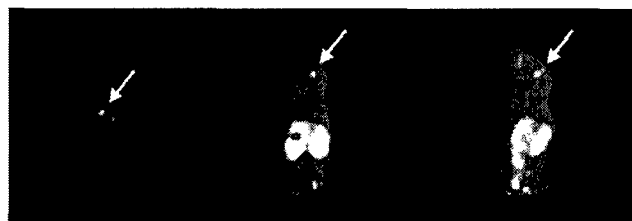
FIGURE 6. (A) 2D projection of U87MG tumor-bearing mouse at 60 min after injection of 14.8 MBq (400 μCi) of ^{64}Cu-DOTA-PEG-RGD (20-min static image). (B) Coronal image of the same tumor-bearing mouse. (C) Digital autoradiograph of the section containing the tumor after microPET imaging. (D) Anatomic photograph of the section.

FIGURE 8. Histopathologic analysis of orthotopically injected U87MG brain tumor cells after microPET imaging. From left to right, panels show original, 4×, and 20× magnification. Tumor size and density of tumor cells were in accordance with volumetric and uptake information obtained from microPET scanning.

coronal orientation. Uptake in U87MG tumors, liver, and kidneys was calculated to be 2.6 ± 0.6, 0.8 ± 0.2, and 2.4 ± 0.5 %ID/g, respectively. These data were in good accordance with the biodistribution data obtained at 1 h after injection. To demonstrate that the uptake detected by microPET scanning of a living mouse corresponded to ^{64}Cu-DOTA-PEG-RGD that had localized appropriately to an integrin-positive tumor after microPET scanning, the mouse was subjected to digital whole-body autoradiography. A comparison of the microPET image encompassing the U87MG tumor xenograft (Fig. 6B) and the corresponding autoradiographic section (Fig. 6C) clearly demonstrated the correlation between the regions of high uptake observed in the scan and autoradiographically detected tumor-associated radioactivity.

microPET imaging was also successful in visualizing an orthotopic U87MG glioblastoma implanted into the mouse forebrain (Fig. 7). Although the absolute tumor uptake $(0.4 \pm 0.1$ %ID/g) was significantly lower than that of the subcutaneous tumor, the tumor-to-brain ratio still reached 4.0 ± 0.5 because of the extremely low background activity accumulation in the normal brain tissue. Histologic staining of the mouse brain (Fig. 8) removed at the end of the scan confirmed the presence and location of the U87MG tumor, which measured 2.9 × 2.8 mm.

DISCUSSION

This study demonstrated that pegylation improves the in vivo kinetics of ^{64}Cu-labeled RGD peptide and that ^{64}Cu-

FIGURE 7. Transaxial, coronal, and sagittal slices (from left to right) of a mouse containing an orthotopically implanted U87MG tumor (arrows). The tumor is about 3 mm in diameter; the tumor-to-brain ratio is 4.0 ± 0.5.

labeled pegylated RGD peptide is able to image a subcutaneous U87MG tumor xenograft and to visualize an orthotopic brain tumor implanted into the mouse forebrain by microPET scanning.

The overexpression of α_v-integrins ($\alpha_v\beta_3$ and $\alpha_v\beta_5$) on solid tumor cells and activated endothelial cells has aroused interest in the development of radiolabeled RGD peptides for imaging and therapy of cancer. Various investigators have shown that ^{18}F-labeled RGD peptides can accumulate in different tumors, such as breast cancer (16,20), brain tumor (17,23), and melanoma and osteosarcoma (18,19). However, the introduction of a prosthetic 4-^{18}F-fluorobenzoyl group to the lysine side chain ε-amino group resulted in unfavorable hepatobiliary excretion, as indicated by high uptake in the gallbladder and intestines; this situation may hamper the imaging of tumor lesions located in the lower abdomen and limit the activity dose that can be administered safely because of whole-body radiation exposure. Haubner et al. demonstrated that substituting a hydrophilic sugar moiety for the lysine resulted in predominant renal clearance for both ^{125}I-labeled (22) and ^{18}F-labeled (18,19) glycosylated RGD peptides. On the other hand, we found that the tumor-targeting ability and in vivo kinetics of an RGD peptide could be substantially improved by introducing a PEG moiety into the lysine side chain amino group. We coupled a c(RGDyK) peptide with mPEG (MW, 2,000) and labeled the c(RGDyK)-mPEG conjugate with ^{125}I. The pegylated RGD peptide resulted in faster blood clearance and lower kidney uptake, without compromising the receptor-targeting ability, than c(RGDyK) (23). We also found that ^{18}F-labeled pegylated RGD (PEG MW, 3,400) resulted in a longer tumor retention time and far less hepatobiliary excretion than the corresponding ^{18}F-labeled RGD (24).

Because no therapeutic fluorine isotope is available, ^{18}F-labeled RGD peptides will not be able to provide direct dosimetry information for integrin-targeted internal radiotherapy. ^{64}Cu with 19% positron emission and 40% β-emission (maximum energy, 578 keV) efficiencies has the potential for both PET and therapy. Chen et al. previously conjugated c(RGDyK) with macrocyclic chelator DOTA and labeled the DOTA-RGD conjugate with ^{64}Cu for PET of breast cancer tumors (21). This tracer showed significant liver uptake. Recent metabolic studies of ^{111}In-diethylenetriaminepentaacetic acid (DTPA)-conjugated polypeptides

indicated that when DTPA was attached to the lysine of the polypeptides, a ^{111}In-DTPA adduct of lysine was generated as the final radiometabolite after lysosomal proteolysis of the parental peptides in the liver (29). We assume that the prominent liver retention after intravenous administration of ^{64}Cu-DOTA-RGD seen here may be ascribed to the combined effects of the transchelation of ^{64}Cu from DOTA to superoxide dismutase (30) in the liver and the persistent localization of the final radiometal metabolite ^{64}Cu-DOTA-lysine within the tissue. Therefore, the practical use of ^{64}Cu as an imaging and therapeutic isotope relies on the development of new chelating agents for Cu(II) that have greater kinetic stability as well as on the prevention of the delivery of negatively charged metabolites to liver nonparenchymal cells via scavenger receptor-mediated endocytosis (31).

Intrigued by the ability of pegylation to improve the tumor-targeting and in vivo kinetics of both [125]I- and ^{18}F-labeled RGD peptides, we extended our study to observe the impact of pegylation on ^{64}Cu-DOTA-RGD. The results of an isolated, immobilized integrin receptor-binding assay indicated that introduction of the PEG moiety at the lysine side chain amino group had a modest influence on $\alpha_v\beta_3$-integrin affinity and selectivity. All of the RGD peptide ligands bound $\alpha_v\beta_3$-integrin with a significantly lower affinity than echistatin, which is folded in a series of irregular loops to form a rigid core stabilized by 4 disulfide bridges (32). It is also worth noting that the introduction of a PEG moiety with an MW of 3,400 significantly reduced the circulatory $t_{1/2}$ of the pegylated radiotracer, in contrast to the results reported for many other pegylated proteins and polypeptides (33). Since the octanol–water partition coefficients of the cyclic RGD peptide and pegylated RGD peptide tracers were similar, the more rapid blood clearance of the pegylated RGD peptide could have been attributable to the fact that this compound showed reduced interactions with blood elements (plasma proteins or blood cells) rather than changes in hydrophilicity on modification.

Both ^{64}Cu-DOTA-RGD and ^{64}Cu-DOTA-PEG-RGD were cleared rapidly from the kidneys. In general, PEG shows little toxicity and is eliminated from the body intact either by the kidneys (for PEG of <30 kDa) or in the feces (for PEG of >20 kDa) (34–36); subsequent reabsorption occurs in the proximal tubular cells, where the pegylated peptide is internalized and degraded in the lysosomes. Following this pathway, the main radiolabeled catabolite of ^{64}Cu-DOTA-PEG-RGD probably is ^{64}Cu-DOTA-PEG-Lys. ^{64}Cu-DOTA-Lys and ^{64}Cu-DOTA-PEG-Lys have the same overall negative charge (−1), but ^{64}Cu-DOTA-PEG-RGD had significantly lower liver uptake and more rapid liver clearance. We assume that the PEG polymer, along with the associated water molecules, acts like a shield to wrap the ^{64}Cu-DOTA chelate and reduces the apparent negative charge, and the negative charge density thus reduces the apparent affinity of the radiometal metabolite for hepatic scavenger receptors. This notion agrees with the phenome-

non in which an increase in the negative charge density of proteins by acylation efficiently increases liver uptake (37).

The features of rapid blood and renal clearance and limited hepatic and biliary excretion permit high signal-to-noise ratios for in vivo imaging soon after injection (1 h). The activities quantified in the mouse tumor, liver, and kidneys were comparable to those obtained by the direct tissue sampling technique. microPET imaging used with the orthotopic U87MG tumor model revealed a good tumor-to-brain ratio; the magnitude of uptake of the orthotopic tumor was about 5 or 6 times lower than that of the subcutaneous tumor. Whether the blood–brain barrier or different integrin expression characteristics of orthotopic brain tumors and subcutaneous tumors are responsible for this difference in uptake needs to be investigated further.

The receptor specificity of the RGD peptide was not significantly affected by the introduction of a PEG moiety and a ^{64}Cu-DOTA radiolabel, because of the invariance of the "kinked" conformation of the pentapeptide (38). The unaltered tumor uptake and clearance and the favorable biokinetics make this radiopharmaceutical suitable for PET of solid tumors that overexpress α_v-integrin and for integrin-targeted internal radiotherapy when therapeutic amounts of [64]Cu- or [67]Cu-labeled pegylated RGD peptide are applied. A radionuclide with PET and therapeutic capacities, such as ^{64}Cu, could be very advantageous, because accurate individualized dosimetry could be obtained for each patient with PET before radiotherapy. The DOTA-PEG-RGD conjugate could also be used with [86]Y ($t_{1/2}$, 14.7 h; 33% β^+) as a surrogate marker to detect the uptake and dosimetry of ^{90}Y-labeled RGD.

We recognize that 2 important issues remain unresolved. The first issue is whether the magnitude of tumor uptake obtained from PET correlates well with the tumor integrin expression level. The ability to measure tumor integrin receptor density noninvasively could have great value in predicting the effectiveness of RGD peptide therapy in patients with brain tumors and other solid tumors that express α_v-integrins. Our recent quantitative analysis of tracer kinetics with the reference tissue sampling technique, which assumes that the radiolabel is not irreversibly trapped within the reference region and that the rate of turnover of the exchanging spaces in both the tumor and the reference tissue is rapid compared with the duration of the time–activity curves (X. Chen, P.S. Conti, unpublished data, 2003), has suggested the feasibility of this reference method (39) for quantifying α_v-integrin receptor density during tumor growth and in response to competition from a nonlabeled RGD peptide or anti-integrin drugs targeted to α_v-integrins. Our future studies will focus on the validation of the results of such an analysis with traditional Western blots and in vitro receptor autoradiography.

The second issue is whether the tumor retention of a suitably labeled RGD peptide is attributable to interactions with α_v-integrins expressed on the neovasculature, on the tumor cells, or on a combination of both cell types. The intrinsic resolution of PET will not allow this question to be

answered directly. In this regard, it is possible that further advances in molecular biology may elucidate subclasses of α_v-integrins present on endothelial cells versus tumor cells, thereby providing an approach for developing more specific diagnostic and therapeutic ligands in the future. In the interim, existing agents may be used to assess overall α_v-integrin activity in tumors.

CONCLUSION

A ^{64}Cu-labeled pegylated RGD peptide was developed for PET imaging of tumor α_v-integrin expression. This new radiotracer was directly compared with ^{64}Cu-DOTA-RGD in vivo, and the results suggested that DOTA-PEG-RGD is a suitable ligand for labeling radiometals that can form stable complexes with the DOTA moiety for both imaging and therapeutic applications. Optimization of this tracer by systematic investigation of the impact of PEG size and geometry and the application of different RGD peptide and peptidomimetic antagonists of α_v-integrins and different chelating agents for Cu(II) may further improve the imaging and therapeutic potentials of the peptides.

ACKNOWLEDGMENTS

REFERENCES

1. Folkman J. Role of angiogenesis in tumor growth and metastasis. *Semin Oncol.* 2002;29(suppl 16):15–18.
2. Brower V. Tumor angiogenesis: new drugs on the block. *Nat Biotechnol.* 1999; 17:963–968.
3. Gasparini G. The rationale and future potential of angiogenesis inhibitors in neoplasia. *Drugs.* 1999;58:17–38.
4. Choi KS, Bae MK, Jeong JW, Moon HE, Kim KW. Hypoxia-induced angiogenesis during carcinogenesis. *J Biochem Mol Biol.* 2003;36:120–127.
5. Jain RK. Tumor angiogenesis and accessibility: role of vascular endothelial growth factor. *Semin Oncol.* 2002;29(suppl 16):3–9.
6. Mignatti P, Rifkin DB. Plasminogen activators and matrix metalloproteinases in angiogenesis. *Enzyme Protein.* 1996;49:117–137.
7. Thorgeirsson UP, Lindsay CK, Cottam DW, Gomez DE. Tumor invasion, proteolysis, and angiogenesis. *J Neurooncol.* 1994;18:89–103.
8. Hood JD, Cheresh DA. Role of integrins in cell invasion and migration. *Nat Rev Cancer.* 2002;2:91–100.
9. Kalluri R. Basement membranes: structure, assembly and role in tumor angiogenesis. *Nat Rev Cancer.* 2003;3:422–433.
10. Yancopoulos GD, Davis S, Gale NW, Rudge JS, Wiegand SJ, Holash J. Vascular-specific growth factors and blood vessel formation. *Nature.* 2000;407:242–248.
11. Vicari AP, Caux C. Chemokines in cancer. *Cytokine Growth Factor Rev.* 2002: 13:143–154.
12. Eliceiri BP, Cheresh DA. The role of α_v integrins during angiogenesis: insights into potential mechanisms of action and clinical development. *J Clin Investig.* 1999;103:1227–1230.
13. Friedlander M, Brooks PC, Shaffer RW, Kincaid CM, Varner JA, Cheresh DA.
14. Definition of two angiogenic pathways by distinct α_v integrins. *Science.* 1995; 270:1500–1502.
15. Kumar CC. Integrin $\alpha_v\beta_3$ as a therapeutic target for blocking tumor-induced angiogenesis. *Curr Drug Targets.* 2003;4:123–131.
16. Kerr JS, Slee AM, Mousa SA. The α_v-integrin antagonists as novel anticancer agents: an update. *Expert Opin Investig Drugs.* 2002;11:1765–1774.
17. Chen X, Shahinian A, Park R, Bozorgzadeh MH, Bading JR, Conti PS. ^{18}F-Labeled cyclic RGD peptide for PET imaging of tumor angiogenesis [abstract]. *J Nucl Med.* 2003;55(suppl 5):271P–272P.
18. Chen X, Park R, Shahinian AH, et al. ^{18}F-Labeled RGD peptide: initial evaluation for imaging brain tumor angiogenesis. *Nucl Med Biol.* 2004;31:179–189.
19. Haubner R, Wester HJ, Weber WA, et al. Noninvasive imaging of $\alpha_v\beta_3$ integrin expression using ^{18}F-labeled RGD-containing glycopeptide and positron emission tomography. *Cancer Res.* 2001;61:1781–1785.
20. Haubner R, Kuhnast B, Mang C, et al. [^{18}F]Galacto-RGD: synthesis, radiolabeling, metabolic stability, and radiation dose estimates. *Bioconjug Chem.* 2004;15:61–69.
21. Ogawa M, Hatano K, Oishi S, et al. Direct electrophilic radiofluorination of a cyclic RGD peptide for in vivo $\alpha_v\beta_3$ integrin related tumor imaging. *Nucl Med Biol.* 2003;30:1–9.
22. Chen X, Park R, Tohme M, Shahinian AH, Bading JR, Conti PS. microPET and autoradiographic imaging of breast cancer α_v-integrin expression using ^{18}F- and ^{64}Cu-labeled RGD peptide. *Bioconjug Chem.* 2004;15:41–49.
23. Haubner R, Wester HJ, Burkhart F, et al. Glycosylated RGD-containing peptides: tracer for tumor targeting and angiogenesis imaging with improved biokinetics. *J Nucl Med.* 2001;42:326–336.
24. Chen X, Park R, Shahinian AH, Bading JR, Conti PS. Pharmacokinetics and tumor retention of ^{125}I-labeled RGD peptide are improved by PEGylation. *Nucl Med Biol.* 2004;31:11–19.
25. Chen X, Park R, Hou Y, et al. microPET imaging of brain tumor angiogenesis with ^{18}F-labeled PEGylated RGD peptide. *Eur J Nucl Med Mol Imaging.* 2004; 31:1081–1089.
26. McCarthy DW, Shefer RE, Klinkowstein RE, et al. Efficient production of high specific activity ^{64}Cu using a biomedical cyclotron. *Nucl Med Biol.* 1997;24:35–43.
27. Kumar CC, Nie H, Rogers CP, et al. Biochemical characterization of the binding of echistatin to integrin $\alpha_v\beta_3$ receptor. *J Pharmacol Exp Ther.* 1997;283:843–853.
28. MacDonald TJ, Taga T, Shimada H, et al. Preferential susceptibility of brain tumors to the antiangiogenic effects of an α_v-integrin antagonist. *Neurosurgery.* 2001;48:151–157.
29. Veronese FM, Saccà B, Polverino de Laureto P, et al. New PEGs for peptide and protein modification, suitable for identification of the PEGylation site. *Bioconjug Chem.* 2001;12:62–70.
30. Franano FN, Edwards WB, Welch MJ, Duncan JR. Metabolism of receptor targeted ^{111}In-DTPA-glycoproteins: identification of ^{111}In-DTPA-ε-lysine as the primary metabolic and excretory product. *Nucl Med Biol.* 1994;21:1023–1034.
31. Bass LA, Wang M, Welch MJ, Anderson CJ. In vivo transchelation of copper-64 from TETA-octreotide to superoxide dismutase in rat liver. *Bioconjug Chem.* 2000;11:527–532.
32. Franssen EJ, Jansen RW, Vaalburg M, Meijer DK. Hepatic and intrahepatic targeting of an anti-inflammatory agent with human serum albumin and neoglycoproteins as carrier molecules. *Biochem Pharmacol.* 1993;45:1215–1226.
33. Calvete JJ, Wang Y, Mann K, Schafer W, Niewiarowski S, Stewart GJ. The disulfide bridge pattern of snake venom disintegrins, flavoridin and echistatin. *FEBS Lett.* 1992;309:316–320.
34. Monfardini C, Veronese FM. Stabilization of substances in the circulation. *Bioconjug Chem.* 1998;9:418–450.
35. Delgado C, Francis GE, Fisher D. The uses and properties of PEG-linked proteins. *Crit Rev Ther Drug Carrier Syst.* 1992;9:249–304.
36. Behr TM, Sharkey RM, Sgouros G, et al. Overcoming the nephrotoxicity of radiometal-labeled immunoconjugates: improved cancer therapy administered to a nude mouse model in relation to the internal radiation dosimetry. *Cancer.* 1997;80(suppl 12):2591–2610.
37. Yamaoka T, Tabata Y, Ikada Y. Distribution and tissue uptake of poly(ethylene glycol) with different molecular weights after intravenous administration to mice. *J Pharm Sci.* 1994;83:601–606.
38. Yamasaki Y, Hisazumi J, Yamaoka K, Takakura Y. Efficient scavenger receptor-mediated hepatic targeting of proteins by introduction of negative charges on the proteins by aconitylation: the influence of charge density and size of the protein molecules. *Eur J Pharm Sci.* 2003;18:305–312.
39. Dechantsreiter MA, Planker E, Matha B, et al. N-Methylated cyclic RGD peptides as highly active and selective $\alpha_v\beta_3$ integrin antagonists. *J Med Chem.* 1999;42:3033–3040.
40. Patlak CS, Blasberg RG. Graphical evaluation of blood-to-brain transfer constants from multiple-time uptake data: generalizations. *J Cereb Blood Flow Metab.* 1985;5:584–590.